

THEORETICAL AND EXPERIMENTAL INVESTIGATION OF RESIDUAL
STRESSES IN ELECTRIC DISCHARGE MACHINING

A THESIS SUBMITTED TO
THE GRADUATE SCHOOL OF NATURAL AND APPLIED SCIENCES
OF
THE MIDDLE EAST TECHNICAL UNIVERSITY

BY

BÜLENT EKMEKÇİ

IN PARTIAL FULFILLMENT OF THE REQUIREMENTS FOR THE DEGREE OF
DOCTOR OF PHILOSOPHY

IN

THE DEPARTMENT OF MECHANICAL ENGINEERING

JANUARY 2004

Approval of the Graduate School of Natural and Applied Sciences.

Prof. Dr. Canan ÖZGEN
Director

I certify that this thesis satisfies all the requirements as a thesis for the degree of Doctor of Philosophy.

Prof. Dr. S. Kemal İDER
Head of the Department

We certify that we have read this thesis and that in our opinion it is fully adequate, in scope and quality, as a thesis for the degree of Doctor of Philosophy.

Prof. Dr. Faruk ARINÇ
Co-Supervisor

Prof. Dr. Abdülkadir ERDEN
Supervisor

Examining Committee in Charge:

Prof. Dr. A. Erman TEKKAYA (Chairman)

Prof. Dr. Abdülkadir ERDEN

Prof. Dr. Faruk ARINÇ

Prof. Dr. Süleyman SARITAŞ

Assoc. Prof. Dr. Hakan GÜR

ABSTRACT

THEORETICAL AND EXPERIMENTAL INVESTIGATION OF RESIDUAL STRESSES IN ELECTRIC DISCHARGE MACHINING

EKMEKÇİ, Bülent

Ph.D. in Mechanical Engineering

Supervisor: Prof. Dr. Abdülkadir ERDEN

Co-Supervisor: Prof. Dr. Faruk ARINÇ

January 2004, 247 pages.

Electric Discharge Machining (EDM) is a process for eroding and removing material by transient action of electric sparks on electrically conductive materials immersed in a dielectric liquid and separated by a small gap. A spark-eroded surface is a surface with matt appearance and random distribution of overlapping craters. It is mechanically hard and stressed close to ultimate tensile strength of the material and sometimes covered with a network of micro cracks. The violent nature of the process leads a unique structure on the machined surface and generates residual stresses due mainly to the non-homogeneity of heat flow and metallurgical transformations.

An extensive experimental study is presented to explore the surface and sub-surface characteristics together with the residual stresses induced by the process. Layer removal method is used to measure the residual stress profile in function of depth beneath. A finite element based model is proposed to determine residual stresses and compared with the experimental results.

The residual stress pattern is found to be unchanged with respect to machining parameters. Thus, a unit amplitude shape function representing change in

curvature with respect to removal depth is proposed. The proposed form is found as a special form of Gauss Distribution, which is the sum of two Gaussian peaks, with the same amplitude and pulse width but opposite center location that is represented by three constant coefficients. In each case, agreement with the proposed form is established with experimental results. Results have shown that these coefficients have a power functional dependency with respect to released energy.

Keywords: Electric Discharge Machining, EDM, Electric Discharge Texturing, EDT, Residual Stresses, Layer Removal Method, Bending Deflection Method, Thermo-Mathematical Modeling.

ÖZ

ELEKTRİKSEL AŞINDIRMA İLE İŞLEMEDE KALINTI GERİLMELERİN TEORİK VE DENEYSEL İNCELENMESİ

EKMEKÇİ, Bülent

Doktora Tezi, Makina Mühendisliği Anabilim Dalı

Tez Yöneticisi: Prof. Dr. Abdülkadir ERDEN

Yardımcı Tez Yöneticisi: Prof. Dr. Faruk ARINÇ

Ocak 2004, 247 sayfa.

Elektriksel Aşındırma ile İşleme (EDM), dielektrik sıvıya batırılmış ve aralarında küçük bir boşlukla ayrılan iletken malzemelerin elektriksel kıvılcımların anlık etkisi ile malzeme kaldırma ve aşındırma işlemidir. Kıvılcımla işlenmiş yüzey mat ve üst üste binen, rast gele dağılmış kraterler görünümündedir. Yüzey, mekanik olarak sert ve yüksek gerilmelere maruzdur ve bazen mikro çatlak ağları ile kaplıdır. İşlemin karmaşık doğası gereği, işlenmiş parçaların yüzeyinde alışılmamış mikro yapılar oluşmakta; ısı akışının homojen olmamasından ve metalürjik dönüşümlerden dolayı da kalıntı gerilmeler meydana gelmektedir.

İşlenmiş yüzey ve yüzey altı karakteristiği işleminden dolayı meydana gelen kalıntı gerilmelerle birlikte yoğun deneysel çalışmalarla sunulmuştur. Kalıntı gerilme profili, yüzeyden itibaren kalınlığın bir fonksiyonu olarak, tabaka kaldırma yöntemi kullanılarak ölçülmüştür. Kalıntı gerilmelerin hesaplanması için sonlu elemanlar yöntemi temel alınarak bir model önerilmiş ve sonuçlar deneysel bulgularla karşılaştırılmıştır.

Kalıntı gerilme profilinin işleme parametrelerindeki göre değişmediği anlaşılmıştır. Bundan ötürü, tabaka kaldırma derinliğine bağlı olarak eğrilik

apında meydana gelen deęişimleri ifade eden bir birim genlik Őekil fonksiyonu nerilmiŐtir. nerilen bu Őekil fonksiyonu,  katsayı ile ifade edilebilen, aynı genlikte ve darbe geniŐliğinde fakat ters merkezli iki Gauss darbesinin toplamı olan, Gauss Daęılım fonksiyonunun zel bir formu Őeklinde bulunmuŐtur. nerilen bu Őekil fonksiyonunun deneysel veriler ile uyumluluęu incelenen her iŐleme koŐulu iin gsterilmiŐtir. Sonular, Őekil fonksiyonu katsayılarının, iŐlem sırasında salınan enerjiyle g fonksiyonel bir iliŐki olduęunu ortaya koymuŐtur.

Anahtar Szckler: Elektriksel AŐındırma ile iŐleme, EDM, Elektriksel AŐındırma ile Przlendirme, EDT, Kalıntı Gerilmeler, Tabaka Kaldırma Yntemi, Eęilme Őehim Yntemi, Termo-Matematik Modelleme.

ACKNOWLEDGEMENTS

The author wish to express his deepest gratitude to his major professor, Dr. Abdülkadir ERDEN, Dr. A. Erman TEKKAYA and Dr. Hakan GÜR for their advice, criticism, and encouragement during the course of this investigation. Gratitude is also expressed to Dr. Faruk ARINÇ and Dr. Süleyman SARITAŞ for their participation as members of the thesis committee.

The author also would like to thank Dr. Oktay ELKOCA from ERDEMİR Iron and Steel Work Co. helped the author obtain the microscopic measurements made in this study.

Mr. Mehmet HALKACI from Konya Selçuk University helped the author prepare the test samples analyzed in this study. Mr. Muhlis BAHARLI and Mr. Yılmaz ÖZTÜRK materially assisted with the construction and development of experimental setup.

Also, the author wishes to thank to staff of Mechanical Engineering Department at Zonguldak Karaelmas University for opening their laboratories and equipments for this study.

To my wife, Nihal, I offer sincere thanks for her unshakable faith in me and her willingness to endure with me the vicissitudes of my endeavors. To my child, İlksen, I thank him for understanding my frequent absences.

This study was supported by Grant No. 2001-03-02-03 from Middle East Technical University Research Program.

TABLE OF CONTENTS

	Page
ABSTRACT.....	iii
ÖZ.....	v
ACKNOWLEDGEMENTS.....	vii
TABLE OF CONTENTS.....	viii
LIST OF TABLES.....	xiii
LIST OF FIGURES.....	xiv
LIST OF SYMBOLS.....	xxiii
CHAPTER	
I. INTRODUCTION.....	1
1.1 Basic Principles of Electric Discharge Machining.....	1
1.1.1 Spark Generator.....	3
1.1.2 Servo System.....	4
1.1.3 Dielectric Circuit.....	4
1.1.4 Mechanical Structure.....	6
1.2 Operation Types of Electric Discharge Machines.....	6
1.2.1 Die Sinking EDM.....	7
1.2.2 Wire EDM.....	7
1.2.3 EDM Milling.....	7
1.2.4 Electric Discharge Grinding.....	7
1.2.5 Electric Discharge Texturing.....	7
1.3 Material Removal Mechanism.....	8
1.3.1 Breakdown (Ignition) Phase.....	9
1.3.2 Discharge Phase.....	10

1.3.3	Erosion (Crater Formation) Phase.....	11
1.4	Characteristic of Electrical Discharge Machined Surfaces.....	12
1.4.1	Surface Topography.....	12
1.4.2	Thermally Influenced Layers.....	12
1.4.3	Residual Stresses	14
1.5	Purpose of the Study.....	16
II.	THEORETICAL MODELS FOR EDM	17
2.1	Introduction.....	17
2.2	Energy Partition between Cathode, Anode and Dielectric Liquid.....	18
2.3	Discharge Channel Radius and Profile.....	18
2.4	Formulation of the Heat Transfer Models.....	20
2.4.1	Heat Transfer Models.....	24
2.4.2	Thermal and Residual Stress Models.....	33
2.5	Electrostatic Field Models for Short Pulse Duration.....	35
III.	ELECTRIC DISCHARGE MACHINED SURFACES.....	38
3.1	Introduction.....	38
3.2	Surface Topography.....	39
3.3	Subsurface Deformations and Metallurgical Structure.....	41
3.3.1	Recast Layer.....	42
3.3.2	Heat Affected Layers.....	44
3.3.3	Thickness of Affected Layers.....	45
3.4	Residual Stresses in EDM.....	46
3.5	Cracking Behavior and its Consequences.....	50
IV.	RESIDUAL STRESSES.....	52
4.1	Introduction.....	52
4.2	Influences of Residual Stresses	53
4.3	Determination of Residual Stresses.....	54

4.4	Residual Stress Measurement.....	55
4.4.1	Mechanical Techniques.....	56
4.4.2	Diffraction Techniques.....	60
4.4.3	Ultrasonic Techniques.....	61
4.4.4	Magnetic Methods.....	62
4.5	Measurement Techniques with Layer Removal Method.....	63
V.	EXPERIMENTAL FACILITIES AND PROCEDURES.....	66
5.1	Introduction.....	66
5.2	Experimental Set Up for Residual Stress Measurement.....	66
5.2.1	Electro Polishing Behavior.....	72
5.4.2	Accuracy and Precision.....	72
5.3	Apparatuses for Topographical and Metallurgical Examinations.....	74
5.4	Apparatuses for Electric Discharge Texturing.....	77
VI.	TOPOGRAPHICAL AND METALLURGICAL PROPERTIES OF EDM'ED SURFACES.....	78
6.1	Introduction.....	78
6.2	Materials.....	78
6.3	Surface Topography.....	79
6.4	Thermally Influenced Layers.....	81
6.5	Hardness Depth.....	103
6.6	X-Ray Diffraction Patterns.....	106
VII.	RESIDUAL STRESS MEASUREMENTS.....	110
7.1	Introduction.....	110
7.2	Measured Data.....	110
7.2.1	Repeatability of the Measurements.....	113
7.2.2	Analysis of Measured Data.....	114
7.2.3	Electro-Chemical Polishing in Affected Layers.....	117
7.3	Parametric Measurements.....	117

7.3.1	Graphite Tool Electrode and De-Ionized Water as Dielectric Liquid.....	121
7.3.2	Copper Tool Electrode and De-Ionized Water as Dielectric Liquid.....	125
7.3.3	Graphite Tool Electrode and Kerosene as Dielectric Liquid.....	129
7.3.4	Copper Tool Electrode and Kerosene as Dielectric Liquid.....	133
VIII.	FINITE ELEMENT ANALYSIS.....	137
8.1	Introduction.....	137
8.2	Single Spark Solution.....	138
8.2.1	Material Model.....	140
8.2.2	Finite Element Mesh.....	142
8.2.3	Results.....	143
	8.2.3.1 Results at the End of Pulse Time.....	144
	8.2.3.2 Residual Stresses.....	147
	8.2.3.3 Time History.....	151
	8.2.3.4 Parametric Simulations.....	158
8.3	A Triple Spark Approach to Simulate EDM'ed Surface.....	159
IX.	DISCUSSION OF THE RESULTS.....	163
9.1	Introduction.....	163
9.2	Surface Topography, Sub-Surface Metallurgy and Damage...	163
9.2.1	Surface Topography.....	163
9.2.2	Cracking.....	164
9.2.3	Sub-Surface Metallurgy and Damage.....	174
	9.2.3.1 Effects of Tool Electrode and Dielectric on White Layer Morphology.....	174
	9.2.3.2 Thermally Affected Layers.....	181
9.3	Residual Stress Measurement.....	182
9.3.1	Layer Removal Method.....	182

9.3.2	Residual Stresses.....	183
9.3.3	A Semi Empirical Approach to Estimate Residual Stresses.....	185
9.4	Finite Element Analysis of EDM.....	187
X.	SUMMARY AND CONCLUSIONS.....	203
	REFERENCES.....	208
	APPENDICES.....	218
A	JPDS-DIFFRACTION DATA FOR ANALYZED X-RAY PATTERNS.....	218
B	RESULT OF PARAMETRIC SIMULATIONS.....	220
C	COMMAND LISTING FOR THE FEM ANALYSIS OF SINGLE SPARK MODEL.....	232
	VITA.....	247

LIST OF TABLES

TABLE

4.1	Characteristic Data of the Different Techniques to Measure Strains and Related Quantities to Evaluate Residual Stresses.....	57
5.1	Average Measured Thickness and Deviation.....	74
6.1	Chemical Compositions of Workpiece Materials (wt.%).....	79
6.2	EDM Test Parameters for Plastic Mold Steel Samples.....	79
6.3	EDT Test Parameters and Roughness.....	81
6.4	Detected Compounds from X-Ray Patterns.....	109
7.1	Machining Parameters for EDM'ed Sample.....	111
7.2	Estimation of Affected Layer Thickness with respect to Electro Chemical Machining Parameters.....	119
7.3	Unit Shape Function Coefficients.....	120
7.4	Gain Coefficients.....	120
8.1	Parametric Simulations.....	140
8.2	Temperature Dependent Thermal Conductivity, Specific Heat and Young's Modulus.....	141
8.3	Temperature Dependent Thermal Expansion Coefficient.....	141
10.1	Affects of Operating Parameters on Cracking, Residual Stresses and Affected Layer Thickness.....	205
A.1	JCPDS-International Center for Diffraction Data, PDF No: 31-0619	218
A.2	JCPDS-International Center for Diffraction Data, PDF No: 06-0696	219
A.3	JCPDS-International Center for Diffraction Data, PDF No: 34-0001	219

LIST OF FIGURES

FIGURES

1.1	Basic Elements of an EDM System.....	3
1.2	Schematic Diagram of the EDM Process Showing the Circle Heat Sources, Plasma Configuration, and Melt Cavities after a Certain Time.....	11
1.3	The Surface of an EDM'ed DIN 1.2738 Steel Specimen Showing Craters, Global Appendages, Pockmarks and Cracks.....	13
1.4	Scanning Electron Micrograph Showing a Cracked Surface of an EDM'ed Micro Alloy Steel Specimen * $I_{av}=4$ A; $t_p= 800 \mu s$ with the Magnification of a) $\times 100$ b) $\times 200$	15
1.5	a) Optical Photomicrograph from Cross Section of an EDM'ed Micro Alloy Steel * $I_{av}=16$ A; $t_p= 1600 \mu s$ b) Representation of Affected Layers after Edge Detection.....	15
2.1	Heat Flow From Spark Channel to Electrode.....	20
2.2	Infinite Plane Source Model.....	25
2.3	Point Source Model.....	26
2.4	Two Dimensional Heat Source Model.....	27
4.1	Illustration of a Stress State Composed of 1 st , 2 nd and 3 rd Kind of Residual Stresses.....	52
4.2	The Necessary Data and Interactions for Predicting Residual Stresses.....	54
4.3	X-ray Diffraction at an Unloaded and a Loaded Single Crystal.....	60
4.4	Schematic Views of Acoustoelastic Measurement Configurations...	61
4.5	Experimental Set Up for the Deflection Method Using Strain Gages	64
4.6	The Specimen for Deflection Method Using Strain Gages.....	64
4.7	Experimental Set Up for the Deflection Method Using Displacement Sensors.....	65
4.8	The Specimen for Deflection Method Using Displacement Sensors	65
5.1	Samples a) Before b) After EDM.....	67
5.2	a) FURKAN EDM 25 Industrial Machine b) A View During Machining.....	68

5.3	a) Magnetic Pump, Sample Holder and Samples b) Electrolytic Bath...	69
5.4	a) Power Supply and Data Acquisition b) Computer.....	70
5.5	a) Measurement Unit b) Dial Indicators on the Unit.....	71
5.6	Schematic Representation of Experimental Set-Up.....	72
5.7	Conditions for the Electro Polishing of Plastic Mold Steel Using Perchloric Acid Based Electrolyte.....	73
5.8	Measurement Deviation of the Measurement Unit.....	73
5.9	JEOL JSM-5600 Scanning Electron Microscope.....	75
5.10	Olympus Metallographic Microscope.....	75
5.11	Future-Tech FM-700 Micro Hardness Tester.....	76
5.12	Roltex-Sarclad Ltd. Industrial Type EDT Machine.....	77
6.1	SEM Pictures of EDM'ed Surfaces: $I_{av}=16A$, Electrode: Graphite, Material: Plastic Mold Steel.....	83
6.2	SEM Pictures of EDM'ed Surfaces: $I_{av}=16A$, Electrode: Graphite, Material: Plastic Mold Steel.	84
6.3	SEM Pictures of EDM'ed Surfaces: $I_{av}=16A$, Electrode: Copper, Material: Plastic Mold Steel.....	85
6.4	SEM Pictures of EDM'ed Surfaces: $I_{av}=16A$, Electrode: Copper, Material: Plastic Mold Steel.....	86
6.5	SEM Pictures of EDM'ed Surfaces: $I_{av}=8A$, Electrode: Graphite, Material: Plastic Mold Steel.....	87
6.6	SEM Pictures of EDM'ed Surfaces: $I_{av}=8A$, Electrode: Graphite, Material: Plastic Mold Steel.	88
6.7	SEM Pictures of EDM'ed Surfaces: $I_{av}=8A$, Electrode: Copper, Material: Plastic Mold Steel.	89
6.8	SEM Pictures of EDM'ed Surfaces: $I_{av}=8A$, Electrode: Copper, Material: Plastic Mold Steel.....	90
6.9	EDT'ed Surfaces of Bands A (a, b), B (c, d) and C (e, f).....	91
6.10	Cross-Sections EDM'ed Plastic Mold Steel Samples $I_{av}=16A$, Dielectric Liquid: Kerosene, Electrode: Graphite.....	92
6.11	Cross-Sections EDM'ed Plastic Mold Steel Samples $I_{av}=16A$, Dielectric Liquid: De-Ionized Water, Electrode: Graphite	93
6.12	Cross-Sections EDM'ed Plastic Mold Steel Samples $I_{av}=16A$, Dielectric Liquid: Kerosene, Electrode: Copper.....	94
6.13	Cross-Sections EDM'ed Plastic Mold Steel Samples $I_{av}=16A$, Dielectric Liquid: De-Ionized Water, Electrode: Copper..	95

6.14	Cross-Sections EDM'ed Plastic Mold Steel Samples I _{av} =8A, Dielectric Liquid: Kerosene, Electrode: Graphite.....	96
6.15	Cross-Sections EDM'ed Plastic Mold Steel Samples I _{av} =8A, Dielectric Liquid: De-Ionized Water, Electrode: Graphite..	97
6.16	Cross-Sections EDM'ed Plastic Mold Steel Samples I _{av} =8A, Dielectric Liquid: Kerosene, Electrode: Copper.....	98
6.17	Cross-Sections EDM'ed Plastic Mold Steel Samples I _{av} =8A, Dielectric Liquid: De-Ionized Water, Electrode: Copper....	99
6.18	Cross-Sections EDM'ed Micro Alloy Steel Samples I _{av} =16A, Dielectric Liquid: Kerosene, Electrode: Copper.....	100
6.19	Cross-Sections of EDT'ed Bands A (a), B (b) and C (c).....	101
6.20	Cross (a) and Tangential (b) Sections of EDT'ed Surfaces.....	101
6.21	Tangential Sections of EDT'ed Bands A (a,b), B (c,d) and C (e,f).	102
6.22	Hardness Depth Profile on Cross-Sectioned Surfaces of EDM'ed Plastic Mold Steel. I _{av} =16A, Dielectric: Kerosene, Tool Electrode: Graphite.....	104
6.23	Hardness Depth Profile on Cross-Sectioned Surfaces of EDM'ed Plastic Mold Steel. I _{av} =16A, Dielectric: Kerosene, Tool Electrode: Copper.....	104
6.24	Hardness Depth Profile on Cross-Sectioned Surfaces of EDM'ed Plastic Mold Steel. I _{av} =16A, Dielectric Liquid: Water, Tool Electrode: Graphite.....	105
6.25	Hardness Depth Profile on Cross-Sectioned Surfaces of EDM'ed Plastic Mold Steel. I _{av} =16A, Dielectric Liquid: Water, Tool Electrode: Graphite.....	105
6.26	Hardness Depth Profile on Cross-Sectioned Surfaces of EDT'ed Bands A,B and C.....	106
6.27	X-Ray Diffraction Patterns of Plastic Mold Steel Samples a) Before EDM b), c) Copper and Graphite Electrodes in Kerosene Dielectric d), e) Copper and Graphite Electrodes in De-Ionized Water (I _{av} =16 A, t _p =800μs).....	107
6.28	X-Ray Diffraction Patterns of EDT Roll Steel Samples a) Before EDT b) Band A c) Band B d) Band C.....	108
7.1	Deflection Curves after Removal of Consecutive Layers.....	111
7.2	Surface Thickness Profiles after Removal of Consecutive Layers..	112
7.3	Change in Radius of Curvature, C(δ), with respect to Removed Layer Thickness, δ.....	112
7.4	Data Cloud and Corresponding Curve Fit.....	113

7.5	Layer Removal.....	114
7.6	Variation of Room and Electrolytic Bath Temperatures.....	118
7.7	Variation in Voltage During Layer Removal.....	118
7.8	Change Curvature with respect to Removed Layer Thickness. (Electrode: Graphite, Dielectric: De-Ionized Water, $I_{av}=16A$).....	121
7.9	Change Curvature with respect to Removed Layer Thickness. (Electrode: Graphite, Dielectric: De-Ionized Water, $I_{av}=8A$).....	121
7.10	Change in Gain with respect to Released Energy. (Electrode: Graphite, Dielectric: De-Ionized Water).....	122
7.11	Residual Stresses in EDM'ed Surface. (Electrode: Graphite, Dielectric: De-Ionized Water, $I_{av}=16A$).....	123
7.12	Residual Stresses in EDM'ed Surface. (Graphite, Dielectric: De-Ionized Water, $I_{av}=8A$).....	123
7.13	Residual Stresses in EDM'ed Surface Through the Thickness. (Electrode: Graphite, Dielectric: De-Ionized Water, $I_{av}=16A$).....	124
7.14	Residual Stresses in EDM'ed Surface Through the Thickness. (Electrode: Graphite, Dielectric: De-Ionized Water, $I_{av}=8A$).....	124
7.15	Change Curvature with respect to Removed Layer Thickness. (Electrode: Copper, Dielectric: De-Ionized Water, $I_{av}=16A$).....	125
7.16	Change Curvature with respect to Removed Layer Thickness. (Electrode: Copper, Dielectric: De-Ionized Water, Water, $I_{av}=8A$).	125
7.17	Change in Gain with respect to Released Energy. (Electrode: Copper, Dielectric: De-Ionized Water).....	126
7.18	Residual Stresses in EDM'ed Surface. (Electrode: Copper, Dielectric: De-Ionized Water, $I_{av}=16A$).....	127
7.19	Residual Stresses in EDM'ed Surface. (Electrode: Copper, Dielectric: De-Ionized Water, $I_{av}=8A$).....	127
7.20	Residual Stresses in EDM'ed Surface Through the Thickness. (Electrode: Copper, Dielectric: De-Ionized Water, $I_{av}=16A$).....	128
7.21	Residual Stress in EDM'ed Surface Through the Thickness. (Electrode: Copper, Dielectric: De-Ionized Water, $I_{av}=8A$).....	128
7.22	Change Curvature with respect to Removed Layer Thickness. (Electrode: Graphite, Dielectric: Kerosene, $I_{av}=16A$).....	129
7.23	Change Curvature with respect to Removed Layer Thickness. (Electrode: Graphite, Dielectric: Kerosene, Water, $I_{av}=8A$).....	129

7.24	Change in Gain with respect to Released Energy (Electrode: Graphite, Dielectric: Kerosene).....	130
7.25	Residual Stresses in EDM'ed Surface. (Electrode: Graphite, Dielectric: Kerosene, $I_{av}=16A$).....	131
7.26	Residual Stresses in EDM'ed Surface. (Electrode: Graphite, Dielectric: Kerosene, $I_{av}=8A$).....	131
7.27	Residual Stresses in EDM'ed Surface Through the Thickness. (Electrode: Graphite, Dielectric: Kerosene, $I_{av}=16A$).....	132
7.28	Residual Stress in EDM'ed Surface Through the Thickness. (Electrode: Graphite, Dielectric: Kerosene, $I_{av}=8A$).....	132
7.29	Change Curvature with respect to Removed Layer Thickness. (Electrode: Copper, Dielectric: Kerosene, $I_{av}=16A$).....	133
7.30	Change Curvature with respect to Removed Layer Thickness. (Electrode: Copper, Dielectric: Kerosene, Water, $I_{av}=8A$).....	133
7.31	Change in Gain with respect to Released Energy. (Electrode: Copper, Dielectric: Kerosene).....	134
7.32	Residual Stresses in EDM'ed Surface. (Electrode: Copper, Dielectric: Kerosene, $I_{av}=16A$).....	135
7.33	Residual Stresses in EDM'ed Surface. (Electrode: Copper, Dielectric: Kerosene, $I_{av}=8A$).....	135
7.34	Residual Stresses in EDM'ed Surface Through the Thickness. (Electrode: Copper, Dielectric: Kerosene, $I_{av}=16A$).....	136
7.35	Residual Stress in EDM'ed Surface Through the Thickness. (Electrode: Copper, Dielectric: Kerosene, $I_{av}=8A$).....	136
8.1	Theoretical Model for Single Spark.....	139
8.2	Temperature Dependent Bilinear Isotropic Hardening.....	141
8.3	Finite Element Mesh in EDM Domain.....	142
8.4	Finite Element Mesh in EDM Domain (Enlarged on the Spark Incident Surface).....	143
8.5	Removed Elements from the Spark Domain at the End of Pulse.....	145
8.6	Temperature Isotherms at the End of Pulse.....	145
8.7	Radial Stress Component (σ_r) at the End of Pulse.....	146
8.8	Axial Stresses Component in z Direction (σ_z) at the End of Pulse...	146
8.9	Shear Stresses Component (σ_{rz}) at the End of Pulse.....	147
8.10	Radial Component of Residual Stresses (σ_r).....	148

8.11	Axial Component of Residual Stresses (σ_z).....	148
8.12	Shear Component of Residual Stresses (σ_{rz}).....	149
8.13	Paths on Working Domain.....	149
8.14	Residual Stresses on Symmetry Path.....	150
8.15	Residual Stresses on Diagonal Path.....	150
8.16	Residual Stresses on Surface Path.....	151
8.17	Variation of Temperature with respect to Time on Symmetry Path.	152
8.18	Variation of Radial Stresses with respect to Time on Symmetry Path. (Beneath the Crater Base)	153
8.19	Variation of Radial Stresses with respect to Time on Symmetry Path. (Away from the Crater Base)	153
8.20	Variation of Temperature with respect to Time on Diagonal Path...	154
8.21	Variation of Radial Stresses with respect to Time on Diagonal Path. (Beneath the Crater Base).....	155
8.22	Variation of Radial Stresses with respect to Time on Diagonal Path (Away from the Crater Base).....	155
8.23	Variation of Temperature with respect to Time on Surface Path.....	156
8.24	Variation of Radial Stresses with respect to Time on Surface Path (Beneath the Crater Base).....	157
8.25	Variation of Radial Stresses with respect to Time on Surface Path (Away from the Crater Base).....	157
8.26	Triple Spark Finite Element Model for EDM.....	159
8.27	Finite Element Mesh for Triple Spark Case (Enlarged).....	160
8.28	Removed Elements at the End of Three Sparks.....	160
8.29	Residual Stress Component of x (σ_x) at the End of Three Sparks....	161
8.30	Residual Stress Component of z (σ_z) at the End of Three Sparks....	161
8.31	Residual Stress Component of y (σ_y) at the End of Three Sparks....	162
9.1	Cracking after EDM a)×200 b)×550 SEM c) Cross-Sectional View Tool Electrode: Graphite, Dielectric: Kerosene; $t_p=1600 \mu s$; $I_{av}=8A$	166
9.2	Cracking after EDM a)×200 b)×550 SEM c) Cross-Sectional View Tool Electrode: Copper, Dielectric: Kerosene; $t_p=1600 \mu s$; $I_{av}= 8A$	167
9.3	Cracking after EDM a)×200 b)×550 SEM c) Cross-Sectional View Tool Electrode: Graphite, Dielectric: Kerosene; $t_p=800 \mu s$; $I_{av}= 8A$	168
9.4	Cracking after EDM a)×200 b)×800 SEM c) Cross-Sectional View Tool Electrode: Copper, Dielectric: Kerosene; $t_p=800 \mu s$; $I_{av}= 8A$	169

9.5	Cracking after EDM a)×200 b) ×550 SEM c) Cross-Sectional View Tool Electrode: Graphite, Dielectric: Kerosene; $t_p=400 \mu\text{s}$; $I_{av}= 8\text{A}$	170
9.6	Cracking after EDM a)×200 b) ×550 SEM c) Cross-Sectional View Tool Electrode: Copper, Dielectric: Kerosene; $t_p=400 \mu\text{s}$; $I_{av}= 8\text{A}$	171
9.7	Boundary Cracking a) Surface b), c) Cross-Sectional Views Tool Electrode: Graphite, Dielectric: De-Ionized Water; $t_p=1600 \mu\text{s}$; $I_{av}= 8\text{A}$..	172
9.8	Boundary Cracking a) Surface b), c) Cross-Sectional Views Tool Electrode: Graphite, Dielectric: De-Ionized Water; $t_p=800 \mu\text{s}$; $I_{av}= 8\text{A}$..	173
9.9	EDM'ed Surfaces of Micro Alloy Steel a) $I_{av}= 16$ b) $I_{av}= 8$ c) $I_{av}= 4$ A. Tool Electrode: Copper, Dielectric: Kerosene; $t_p=800 \mu\text{s}$	175
9.10	Cross-Sectional View of Micro Alloy Steel a) ×100 b) ×200 c) ×800 Tool Electrode: Graphite, Dielectric: Kerosene; $t_p=800 \mu\text{s}$; $I_{av}=16\text{A}$	176
9.11	Cross-Sectional Views of Micro Alloy Steel a) $I_{av}=16\text{A}$; $t_p=50 \mu\text{s}$ b) $I_{av}=16\text{A}$; $t_p=8\mu\text{s}$ c) $I_{av}=4\text{A}$; $t_p=8 \mu\text{s}$; Electrode: Graphite; Dielectric: Kerosene.....	177
9.12	Cross-Sectional Views of Plastic Mold Steel a) White Layer b) Globule Section Tool Electrode: Graphite, Dielectric: Kerosene; $t_p=100 \mu\text{s}$; $I_{av}=16\text{A}$	179
9.13	Hardness Depth Profile after and before Sub-Zero Treatment on Cross-Sectioned Surface of EDT'ed Bands A,B and C.....	181
9.14	Change in Curvature on Cracked Samples.....	185
9.15	Comparison of Finite Element Analysis Results with Measured Residual Stresses ($I_{av}=16\text{A}$, $t_p=100\mu\text{s}$). a) Graphite b) Copper Electrode in De-Ionized Water Dielectric Liquid.....	190
9.16	Comparison of Finite Element Analysis Results with Measured Residual Stresses ($I_{av}=16\text{A}$, $t_p=100\mu\text{s}$). a)Graphite b) Copper Electrode in Kerosene Dielectric Liquid.....	191
9.17	Comparison of Finite Element Analysis Results with Measured Residual Stresses ($I_{av}=16\text{A}$, $t_p=1600\mu\text{s}$). a) Graphite b) Copper Electrode in De-Ionized Water Dielectric Liquid.....	192
9.18	Comparison of Finite Element Analysis Results with Measured Residual Stresses ($I_{av}=16\text{A}$, $t_p=800\mu\text{s}$). a) Graphite b) Copper Electrode in De-Ionized Water Dielectric Liquid.....	193
9.19	Comparison of Finite Element Analysis Results with Measured Residual Stresses ($I_{av}=16\text{A}$, $t_p=400\mu\text{s}$). a) Graphite b) Copper Electrode in De-Ionized Water Dielectric Liquid.....	194
9.20	Comparison of Finite Element Analysis Results with Measured Residual Stresses ($I_{av}=16\text{A}$, $t_p=200\mu\text{s}$). a) Graphite b) Copper Electrode in De-Ionized Water Dielectric Liquid.....	195

9.21	Comparison of Finite Element Analysis Results with Measured Residual Stresses ($I_{av}=16A$, $t_p=200\mu s$). c) Graphite d) Copper Electrode in Kerosene Dielectric Liquid.....	196
9.22	Comparison of Finite Element Analysis Results with Measured Residual Stresses ($I_{av}=16A$, $t_p=50\mu s$). a) Graphite b) Copper Electrode in De-Ionized Water Dielectric Liquid.....	197
9.23	Comparison of Finite Element Analysis Results with Measured Residual Stresses ($I_{av}=16A$, $t_p=50\mu s$). a) Graphite b) Copper Electrode in Kerosene Dielectric Liquid.....	198
9.24	Comparison of Finite Element Analysis Results with Measured Residual Stresses ($I_{av}=16A$, $t_p=25\mu s$). a) Graphite b) Copper Electrode in De-Ionized Water Dielectric Liquid.....	199
9.25	Comparison of Finite Element Analysis Results with Measured Residual Stresses ($I_{av}=16A$, $t_p=25\mu s$). a) Graphite b) Copper Electrode in Kerosene Dielectric Liquid.....	200
9.26	Comparison of Finite Element Analysis Results with Measured Residual Stresses ($I_{av}=16A$, $t_p=8\mu s$). a) Graphite b) Copper Electrode in De-Ionized Water Dielectric Liquid.....	201
9.27	Comparison of Finite Element Analysis Results with Measured Residual Stresses ($I_{av}=16A$, $t_p=8\mu s$). a) Graphite b) Copper Electrode in Kerosene Dielectric Liquid.....	202
B.1	Removed Elements From the Spark Domain at the End of Pulse ($t_p=100\mu s$, $I_{av}=16A$, $R=110\mu m$, $R_w=0.06$, $R_{wp}=0$).....	220
B.2	Temperature at the End of Pulse ($t_p=100\mu s$, $I_{av}=16A$, $R=110\mu m$, $R_w=0.06$, $R_{wp}=0$).....	220
B.3	Radial Component of Residual Stresses (σ_{rr}) ($t_p=100\mu s$, $I_{av}=16A$, $R=110\mu m$, $R_w=0.06$, $R_{wp}=0$).....	221
B.4	Removed Elements from the Spark Domain at the End of Pulse ($t_p=100\mu s$, $I_{av}=16A$, $R=110\mu m$, $R_w=0.1$, $R_{wp}=0$).....	221
B.5	Temperature at the End of Pulse ($t_p=100\mu s$, $I_{av}=16A$, $R=110\mu m$, $R_w=0.1$, $R_{wp}=0$).....	222
B.6	Radial Component of Residual Stresses (σ_r) ($t_p=100\mu s$, $I_{av}=16A$, $R=110\mu m$, $R_w=0.1$, $R_{wp}=0$).....	222
B.7	Removed Elements From the Spark Domain at the End of Pulse ($t_p=100\mu s$, $I_{av}=16A$, $R=110\mu m$, $R_w=0.08$, $R_{wp}=0.001$).....	223
B.8	Temperature at the End of Pulse ($t_p=100\mu s$, $I_{av}=16A$, $R=110\mu m$, $R_w=0.08$, $R_{wp}=0.001$).....	223
B.9	Radial Component of Residual Stresses (σ_r) ($t_p=100\mu s$, $I_{av}=16A$, $R=110\mu m$, $R_w=0.08$, $R_{wp}=0.001$).....	224

B.10	Removed Elements From the Spark Domain at the End of Pulse ($t_p=100\ \mu\text{s}$, $I_{av}=16\text{A}$, $R=110\ \mu\text{m}$, $R_w=0.08$, $R_{wp}=0.002$).....	224
B.11	Temperature at the End of Pulse ($t_p=100\ \mu\text{s}$, $I_{av}=16\text{A}$, $R=110\ \mu\text{m}$, $R_w=0.08$, $R_{wp}=0.002$).....	225
B.12	Radial Component of Residual Stresses (σ_r) ($t_p=100\ \mu\text{s}$, $I_{av}=16\text{A}$, $R=110\ \mu\text{m}$, $R_w=0.08$, $R_{wp}=0.002$).....	225
B.13	Removed Elements From the Spark Domain at the End of Pulse ($t_p=100\ \mu\text{s}$, $I_{av}=16\text{A}$, $R=110\ \mu\text{m}$, $R_w=0.08$, $R_{wp}=0.004$).....	226
B.14	Temperature at the End of Pulse ($t_p=100\ \mu\text{s}$, $I_{av}=16\text{A}$, $R=110\ \mu\text{m}$, $R_w=0.08$, $R_{wp}=0.004$).....	226
B.15	Radial Component of Residual Stresses (σ_r) ($t_p=100\ \mu\text{s}$, $I_{av}=16\text{A}$, $R=110\ \mu\text{m}$, $R_w=0.08$, $R_{wp}=0.004$).....	227
B.16	Removed Elements From the Spark Domain at the End of Pulse ($t_p=100\ \mu\text{s}$, $I_{av}=16\text{A}$, $R=110\ \mu\text{m}$, $R_w=0.08$, $R_{wp}=0.008$).....	227
B.17	Temperature at the End of Pulse ($t_p=100\ \mu\text{s}$, $I_{av}=16\text{A}$, $R=110\ \mu\text{m}$, $R_w=0.08$, $R_{wp}=0.008$).....	228
B.18	Radial Component of Residual Stresses (σ_{rr}) ($t_p=100\ \mu\text{s}$, $I_{av}=16\text{A}$, $R=110\ \mu\text{m}$, $R_w=0.08$, $R_{wp}=0.008$).....	228
B.19	Removed Elements From the Spark Domain at the End of Pulse ($t_p=100\ \mu\text{s}$, $I_{av}=16\text{A}$, $R=95\ \mu\text{m}$, $R_w=0.08$, $R_{wp}=0$).....	229
B.20	Temperature at the End of Pulse ($t_p=100\ \mu\text{s}$, $I_{av}=16\text{A}$, $R=95\ \mu\text{m}$, $R_w=0.08$, $R_{wp}=0$).....	229
B.21	Radial Component of Residual Stresses (σ_{rr}) ($t_p=100\ \mu\text{s}$, $I_{av}=16\text{A}$, $R=95\ \mu\text{m}$, $R_w=0.08$, $R_{wp}=0$).....	230
B.22	Removed Elements From the Spark Domain at the End of Pulse ($t_p=100\ \mu\text{s}$, $I_{av}=16\text{A}$, $R=125\ \mu\text{m}$, $R_w=0.08$, $R_{wp}=0$).....	230
B.23	Temperature at the End of Pulse ($t_p=100\ \mu\text{s}$, $I_{av}=16\text{A}$, $R=125\ \mu\text{m}$, $R_w=0.08$, $R_{wp}=0$).....	231
B.24	Radial Component of Residual Stresses (σ_r) ($t_p=100\ \mu\text{s}$, $I_{av}=16\text{A}$, $R=125\ \mu\text{m}$, $R_w=0.08$, $R_{wp}=0$).....	231

LIST OF SYMBOLS

A	Constant
$A_{1,2}$	Constants
a	Constant
$a_{1,2}$	Constants
b	Electrode radius, m
C	Curvature, 1/m; Constant; Empirical coefficient
$C_{1,2}$	Constants
C^*	Dimensionless curvature
c	Specific heat, J/kg ^o K
c_p	Specific heat under constant pressure, J/kg ^o K
c_s	Specific heat at solid phase, J/kg ^o K
c_l	Specific heat at liquid phase, J/kg ^o K
c_g	Specific heat gaseous state, J/kg ^o K
c'_p	Modified specific heat to account for latent heat of fusion L_m , J/kg ^o K
c''_p	Modified specific heat to account for latent heat of evaporation L_e , J/kg ^o K
d_i	Constants
d_s	Discharge channel diameter, m
E	Elasticity modulus, Pa
E_{EF}	Electric field, V/m
E_R	Total discharge energy, J
E_w	Total energy received by the workpiece, J
E^*	Dimensionless energy
e	Energy per unit mass, J/kg
e_i	Total charge on an ion, C
F	Force, N
g	Energy factor
g^*	Dimensionless energy factor
H	Initial sample thickness, m
h_c	Convection heat transfer coefficient, W/m ^o K
HV_{10}	Vickers Hardness measured with a load of 10g
I	Current, A; Moment of Inertia, m ⁴
I_{av}	Average current, A
J_0	Zeroth order Bessel function
J_1	First order Bessel function
K	Empirical coefficient
k	Thermal conductivity, W/m ^o K
k_l	Thermal conductivity of liquid material at melting temperature, W/m ^o K
k_s	Thermal conductivity of solid material at melting temperature, W/m ^o K
L	Empirical coefficient
l	Length, m

L_e	Latent heat of evaporation, J/kg
L_m	Latent heat of melting, J/kg
M	Empirical coefficient
M_c	Material constant
m	Empirical coefficient
m_i	Mass of an ion, kg
N	Empirical coefficient
n	Empirical coefficient
P	Position (x,y,z) in rectangular coordinates (r,θ,z) in cylindrical coordinates
P_i	Second order polynomial representing deflection curve of a sample after removal of layer i from its surface
Q	Discharge power, W
q	Power density (per unit area), W/m ²
q_{dc}	Critical power density, W/m ²
R	Source (Spark) radius, m
R_w	Energy partition of heat to the workpiece
R_{wp}	Energy partition of pressure to the workpiece
r	Radius coordinate
r_m	Radius of the crater along the melting isothermal, m
\tilde{r}	Dimensionless radius
\tilde{r}_m	Dimensionless radius of the crater along the melting isothermal
S_{HS}	Hot strength value, Pa
T	Temperature, °K
T_s	Spark temperature, °K
T_0	Initial temperature, °K
T_b	Boiling temperature, °K
T_m	Melting temperature, °K
T^*	Equivalent temperature, °K
t	Time, s
\tilde{t}	Dimensionless time
t_p	Pulse (spark) time, s
U_b	Breakdown voltage, V
U_{av}	Average breakdown voltage, V
u	Internal energy per unit mass, J/kg
$V(T)$	Time dependent boundary
z	Depth coordinate
z_m	Depth on a melting isothermal, m
\tilde{z}_m	Dimensionless depth on a melting isothermal
\tilde{z}	Dimensionless depth
α	Thermal diffusivity, m ² s
α_e	Coefficient of expansion, 1/°K
β	Empirical coefficient
ΔT	Temperature increment, °K
δ	Removed layer thickness, m
δ^*	Dimensionless removed layer thickness

ε	Strain
ϕ_0	Reference potential, V
ϕ_w	Electrode potential, V
γ	Empirical coefficient
η	Metal removal efficiency
ϕ	Distance from each point source, m
λ	Wavelength, m
$\lambda_{1,2}$	Constants
ν	Poisson's ratio
Θ	Dimensionless temperature
ρ	Density, kg/m^3 ; Radius of curvature, m
ρ_e	Mass densities at boiling point, kg/m^3
ρ_m	Mass density at melting point, kg/m^3
σ	Stress, Pa
σ_n	Normal stress component, Pa
σ_b	Bending stress component, Pa
σ^{rl}	Stress in a removed layer, Pa
σ^{rs}	Residual stress, Pa
σ^*	Dimensionless Stress
τ	Dummy variable for time, s; Shear stress, Pa
ξ	Distance above from removed layer, m

CHAPTER I

INTRODUCTION

1.1 Basic Principles of Electric Discharge Machining

Electric Discharge Machining (EDM) provides an effective manufacturing technique that enables the production of parts made of hard materials with complicated geometry that are difficult to produce by conventional machining processes. Its ability to control the process parameters to achieve the required dimensional accuracy and finish has placed this machining operation in a prominent position in industrial applications. The absorbing interest for electric discharge machines has resulted in great improvements in its technology. Nowadays, sophisticated electric discharge machines are available for most of machine shop and tool room applications.

EDM can be described as a process for eroding and removing material by transient action of electric sparks on electrically conductive materials immersed in a dielectric liquid and separated by a small gap. It is well known that the main mode of erosion is caused by the thermal effect of an electrical discharge (Zingerman, 1959; Optiz, 1960; Barash and Sri-Ram, 1962; Saito, 1961; Llyod and Warren, 1965; Heuvalman, 1969; Snoeys and Dijck, 1972; Crookall and Khor, 1974; Greene and Alvarez, 1974; Koning et al., 1975; Marty, 1977; Jeswani, 1978; Pandit, 1980; Erden, 1980; Beck, 1981; Pandey and Jilani, 1986; DiBitonto et al., 1989; Madhu et al., 1991). The charge induced on electrodes by a power supply creates a strong electric field. This field is strongest where the electrodes are closest to each other. Molecules and ions of dielectric fluid are polarized and oriented between these two peaks. When the dielectric strength of the liquid in the

gap is exceeded a natural limit, a low resistance discharge channel is formed due to electron avalanche striking to anode and cathode. This collision process transforms their kinetic energy in the form of heat and pressure and released in the solid body. The amount of generated heat within the discharge channel is predicted to be as high as 10^{17} W/m² and thus, could raise electrode temperatures locally up to 20 000 °K even for short pulse durations (McGeough and Rasmussen, 1982). No machining process is known where similar high temperatures can be obtained even in such small dimensions. The pressure increase in the plasma channel forces to expand discharge channel boundaries and decreases the current density across inter-electrode gap. Most of the time, the pressure increase is so high that it prevents evaporation of superheated material on electrode surfaces. Rapid decrease in discharge channel pressure at the end triggers a violent erosion process. Superheated material on the surfaces evaporates explosively. Finally, the surfaces cool down instantaneously, where all vaporized and a fraction of melted material flush away by dielectric liquid in the form of small droplets. Each discharge leaves a tiny crater on the surfaces where the remaining part of the melted material has splashed on it. The surface is observed with globules of debris and chimneys formed by entrapped gases escaping from the re-deposited material (Opitz, 1960; Lloyd and Warren, 1965; Ghabrial, 1972; Walbank, 1980). Applying consecutive spark discharges and driving one electrode towards the other erode the workpiece gradually in a form complementary to that of the tool electrode.

Material removal rate, electrode wear, surface finish, dimensional accuracy, surface hardness, texture and cracking depend on size and morphology of craters formed. Applied current, voltage and pulse duration, thermal conductivity, electrical resistance, specific heat, melting and boiling temperatures of tool electrode and workpiece, size and composition of debris in dielectric liquid can be considered as the main physical parameters effecting the process. Among them, the applied voltage, pulse and pause duration are the parameters that can be easily controlled.

Every EDM machine has the following basic elements (Figure 1.1).

- (i) Spark generator
- (ii) Servo system
- (iii) Dielectric liquid and circulating system
- (iv) Mechanical structure

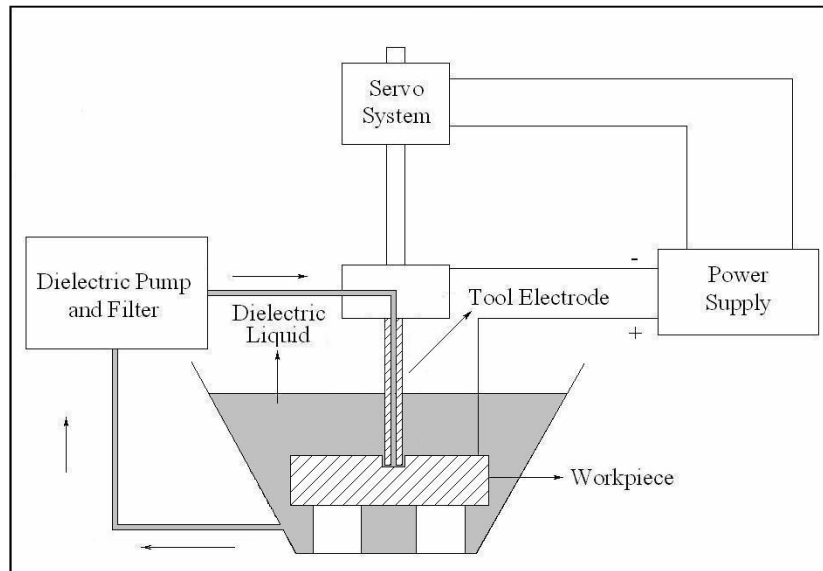


Figure 1.1 Basic Elements of an EDM System (Kögmen, 1993).

1.1.1 Spark Generator

Electrical energy in the form of short duration impulses with a desired shape should be supplied to the inter-electrode gap. Spark generators are used as the source of electrical pulses in EDM. The generators can be distinguished according to the way in which the voltage is transformed and the pulse is controlled. The discharge may be produced in controlled manner by natural ignition and relaxation, or by means of a controllable semiconductor switching elements. Nowadays, sophisticated computer aided spark generators are in use as a result of fast development in electronics industry. These types of generators provide a better means of controlling the physical parameters.

The required energy is in the form of pulses usually in rectangular form. Some studies have shown that application of pulses in the form of trapezoids give a marked improvement in cutting efficiency. Actually, the optimum pulse form to achieve maximum cutting efficiency is not exactly trapezoidal, but the form is very similar (Erden and Kaftanoğlu, 1981).

1.1.2 Servo System

Both tool electrode and workpiece are eroded during the process. Dimensions of the electrodes change considerably with respect to time and the gap between electrodes increases. This changes the required voltage for sparking. Increasing the pulse voltage or decreasing the gap could be the responses to retain machining process. The former is not feasible since most of the electrical energy used for breaking dielectric liquid and producing a discharge channel in it rather than machining, the resulting surface characteristic will be changed continuously, and furthermore, the required voltage for sparking will be increased to the levels that spark generator can not supply. Therefore, the inter electrode gap should be maintained uniformly. This can be achieved by a servo system that keeps up a movement of the electrode towards the workpiece at such a speed that the working gap, and hence, the sparking voltage is unaltered significantly during machining.

1.1.3 Dielectric Circuit

Properties of the dielectric liquid affect machining performance by changing discharging conditions at the spark gap. Most of the investigators have noted that impurities in dielectric liquid have considerable effect on the EDM and the surface quality can be enhanced by adding powder material into it (Erden and Kaftanoğlu, 1980; Erden, 1983; Wong et al., 1998; Chow et al., 2000; Uno et al., 2001; Furutani et al., 2001). Erosion properties of tool and workpiece are determined partly by the discharging medium (Erden, 1977). The medium is composed mainly of dielectric liquid and debris formed due to solidification of

vaporized material in cold dielectric liquid after each discharge either as irregularly shaped particles or hollow spherical particles. In the case of the normal erosion process with sequential discharges, there are very large changes of the machining parameters as a consequence of the existing flushing. Such changes cause large differences in metal removal, accuracy, and surface integrity (Larsson and Wong, 1976; Koenig et al., 1977; Erden, 1982). Therefore, type of the flushing highly depends on the geometrical properties of the machined part. Hence, EDM machines are equipped with necessary pumps, filters and other devices necessary for fluid circulation. Filtration of the liquid is required to keep debris concentration within acceptable limits. There are basically four functions of a dielectric liquid for EDM (Erden and Temel, 1981).

- (i) Physically, the dielectric liquid holds the charge accumulated on the electrodes for a certain time period, determined by spark gap conditions. When the gap conditions are favorable, the liquid allows the electric current to flow with lowest electrical resistivity.
- (ii) The dielectric liquid keeps the discharge in a narrow channel. Power density over the electrode surface is thus increased and machining rate is improved.
- (iii) Heat released during discharge should be immediately removed, since it does not contribute to the erosion. Further, it may cause damage on the electrode surfaces. The dielectric liquid during electric discharge machining should remove the heat from the electrode surfaces as soon as the electric discharge ends.
- (iv) The dielectric liquid is expected to carry the machining products (debris) away from the spark gap to prevent short circuits and therefore prevent damage to the electrodes.

1.1.4 Mechanical Structure

Electric discharge machines have similar construction with conventional drilling and milling machine frames with vertical tool feeding and horizontal workable movements. Since there is not a real contact between electrodes, it may be concluded that frame elements will not sustain much more force as in conventional machining and so simpler design is possible. This is not true since high frontal shock waves are produced at the end of each discharge. Therefore, the frame should be strong enough to overcome these types of stresses and keep its dimensional stability.

1.2 Operation Types of Electric Discharge Machines

EDM enables the machining operation in several ways. Some of these operations are similar to conventional operations such as milling and die sinking. Others have their own characteristic. Different classifications are possible and current developments in its technology add new types of operations due to increase in market demands. A simple and general classification can be given by considering well-known applications such as,

- (i) Die Sinking EDM
- (ii) Wire EDM
- (iii) EDM Milling
- (iv) Electric Discharge Grinding
- (v) Electric Discharge Texturing

1.2.1 Die Sinking EDM

The tool electrode has the complementary form of finished workpiece and literally sinks into the raw material. Complex shapes are possible, more machining time is needed. However, dimensional accuracy is high when compared with wire EDM.

1.2.2 Wire EDM

The electrode is a wire that cuts through the workpiece and is renewed constantly to avoid rupture. The wire is cheaper than complex electrodes used in die sinking EDM. Less material should be removed, which result in less machining time and electrode wear. The operation is possible only for ruled surfaces. The wire may bend during machining and cause substantial shape errors.

1.2.3 EDM Milling

Usually a rotating cylindrical electrode follows a path through the workpiece, yielding the desired final geometry. It is advantageous when large holes or complex geometries are required.

1.2.4 Electric Discharge Grinding (EDG)

In the case where small holes are needed, a relatively large electrode may be reversibly eroded against a sacrificial workpiece. In this case, the polarity between tool electrode and workpiece is reversed so that the material removal predominantly takes place on the electrode.

1.2.5 Electric Discharge Texturing (EDT)

Today, consumer demands on sheet metal products dictate the controlled topographical surface characteristics regarding formability and appearance. The key point to satisfy the needs is the production of the sheet metal with a predefined texture, which can be obtained by the use of textured rolls during both temper and cold rolling. Electric Discharge Texturing (EDT) can be given as an example for an adaptation of established EDM to steel industry to meet texturing demands of rolls surfaces.

A roll is mounted in a lathe together with a texturing head consisting of an array of electrodes connected to one or more servo control units. To form the desired texture on the roll surface, a multi channel pulsed DC power supply provides controlled electrical discharges through the dielectric flowing between the tool electrodes and the roll.

1.3 Material Removal Mechanism

A perfect general theory for EDM can not be constructed since each machining condition has its own particular aspects and involves numerous phenomena, i.e., heat conduction and radiation, phase changes, electrical forces, chemical reactions and plasma formation. In addition, theories of how sparks eroded the workpiece and electrode have never been completely supported by the experimental evidence since it is very difficult to observe the process, scientifically. Thus, most of the published studies are mostly concerned with simplified models of different events of EDM. Development of high-speed computers and comprehensive numerical techniques enabled scientists to include more parameters in their models than before, but still many aspects of the process are unclear and needs further investigations.

Melting, vaporization and even ionization of the electrode materials occur at the point where the discharge takes place. Flushing action of the dielectric liquid pulls away all of the vaporized and some of the melted material. Theoretical models based on one spark can be extended to the machining with some side effects (Erden and Kaftanoğlu, 1980). Generally, the physics of the sparks can be investigated in three phases.

- (i) Breakdown (Ignition) phase
- (ii) Discharge phase
- (iii) Erosion (Crater Formation) phase

Breakdown phase takes a relatively small percent of the total spark time. It varies from few microseconds to several hundreds depending on the discharge conditions. Erosion is observed in the later stages of spark, partly after the discharge has ceased (Erden and Kaftanoğlu, 1980).

1.3.1 Breakdown (Ignition) Phase

Breakdown in liquids is the initial condition for plasma formation. There are several proposed theories, which try to explain the breakdown phase, but consistent results with experiments cannot be obtained. Erden and Kaftanoğlu (1983) have proposed the following synthesis of breakdown theories:

“The impurities in the liquid even without an external electric field, move to and fro, collide with other particles and unite to give larger particles. When an external electric field is applied, this motion is more oriented. Particles move a place of maximum stress (maximum stress occurs around irregularities). The motion is enhanced by the applied field, but resisted by viscous liquid action. As the particle concentration around the stress point increase, particles align themselves along a bridge. This action probably due to the polarization of the particles. They are mostly surrounded by a negative charge, but under an electrical field behave like dipoles. With dipole action and by attractive London Vander Walls forces, particle strings starting from a stress point extending towards the other electrode are formed. These strings increase the electric stress at that point further, and more particles are gathered. The inter-electrode gap is also reduced greatly. It is possible that one of these strings touches the other electrode hence a complete particle bridge is formed. If such a situation occurs, the electrodes are short circuited and current starts to flow along the bridge, but the particles can not carry this current and heat up to high temperatures, boil the surrounding liquid and disperse in to the liquid. Then discharge takes place in the dielectric

liquid vapor. More probable event than this is, that some amount of current as it has been observed in pure liquid, leaks across the electrodes through the strings and particles. This current heats up the liquid by joule heating and in a very short time, vaporize the liquid. This is quite probable since current channel cross section is very small, hence a power density obtained. Thus, a gaseous bridge between the two electrodes is formed. Absorbed gaseous in the liquid and on the electrode surfaces also enhance this formation. As soon as the dielectric vapor bubble is formed, the initial current leakage turn into an electron avalanche, first by electron collision and cold field emission, later by temperature field emission, a discharge develops as in gases. Current increased to high values as the voltage drops. Then discharge phase starts.”

1.3.2 Discharge Phase

Discharge phase of the process is similar to many gas discharges in that a constant current is passed through the plasma. Using shorter pulse duration and dense dielectric liquid alters the macroscopic plasma features, considerably. These changes result in higher erosion rates on electrodes than gas discharges. High-speed photographs from various sources show the spark to be barrel shape with its radius near the cathode being much smaller than that near the anode (Figure 1.2). Thus, the shape of the discharge channels is neither a sphere nor a cylinder (Eubank et al., 1993).

Charged particles collide with the atoms in dielectric liquid and then hit the electrode surfaces. This collision process transforms their kinetic energies to thermal energy and rapidly increases the pressure in the plasma channel due to evaporation of dielectric liquid. The hot spark radiates energy to the surrounding dielectric liquid as well as to metal electrodes. During each time increment, radiation from the vaporized plasma, dissociates, and ionizes a thin cylindrical shell of liquid at this interface causing the mass of the plasma to increase by the

mass of this cylindrical shell (Eubank et al., 1993). The plasma radius increases with time since the high internal plasma pressure is pushing back the high-density dielectric (DiBitonto et al., 1989) and liquid dielectric is converted to plasma at the interface (Patel et al., 1989).

1.3.3 Erosion (Crater Formation) Phase

Before removing the pulse voltage, the superheated electrode material stays in a metastable equilibrium for a short time. When the pulse voltage ceases, a rapid decrease in plasma pressure occurs and erosion process begins. The superheated molten cavities explode violently into the dielectric liquid due to rapid changes in the pressure, and then molten material is rushing back into the volume occupied by the plasma. At this stage, some of the researchers have reported bulk boiling process around the heated section (Dijck and Soneys, 1974; Pandey and Jilani, 1986; Eubank et al., 1993). Most of the evaporated metal cools down very rapidly in the form of irregularly shaped or hollow spherical particles and are flushed away by the dielectric liquid. The remaining part is splashing around together with the melted material and forming a small crater on the electrode surfaces.

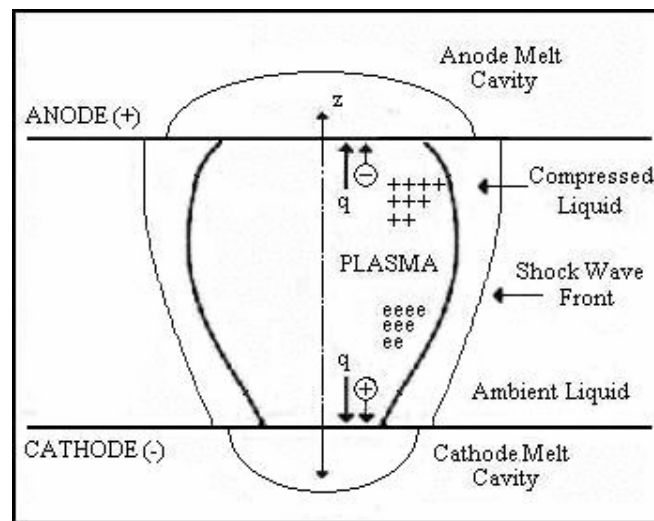


Figure 1.2 Schematic Diagram of the EDM Process Showing the Circle Heat Sources, Plasma Configuration, and Melt Cavities after a Certain Time (Eubank et al., 1993).

1.4 Characteristic of Electrical Discharge Machined Surfaces

1.4.1 Surface Topography

A spark-eroded surface is a surface with a matt appearance and random distribution of overlapping craters. It is mechanically hard and stressed close to the ultimate tensile strength of the material and is often covered with a network of micro cracks (Pandey and Jilani, 1986). The general appearance of a crater formed after sparking is almost the same for the different materials except for the sizes and depth. Sparking leaves a well-defined ridge, which could come only through the deposition of the molten material from the crater. The surface is observed with globules of debris and pockmarks, formed by entrapped gasses escaping from the re-deposited material (Figure 1.3). Global appendages are molten metals, which were expelled randomly during the discharge and later solidified on the electrode surfaces. (Lee et al., 1988). The crack formation (Figure 1.4) is associated with the development of high thermal stresses of the material, as well as with plastic deformation. A dramatic example of a cracked surface due to EDM can be seen on Figure (1.4). The crater sizes increase with pulse energy (Rebello et al., 1998).

1.4.2 Thermally Influenced Layers

The violent nature of the process leads a unique structure on the surfaces of the machined parts. Microscopic observations have shown that unusual phase changes occur since high local temperature is attained during the machining process. No machining process is known that such high temperatures can be obtained even in such small dimensions. The topmost layer is a recast layer formed by resolidification of the molten metal at the base of the craters after the discharge. This layer is found to be heavily alloyed with the pyrolysis products of the cracked dielectric. When pure iron and ferrous alloys are used as workpiece materials, the recast surface layer is often saturated with carbon from the cracked dielectric, as well as other alloying elements introduced via the tool electrode. The material surface is found to be fairly resistant to etching by conventional

metallographic reagents. For this reason, the recast layer on ferrous alloys is often referred to as an unetchable ‘white’ layer. Microhardness measurements have shown that for ferrous alloys, the recast layer generally have a hardness value much higher than that of the underlying matrix and may exceed that attainable by normal quenching techniques. (Optiz, 1960; Brash and Sri Ram, 1962; Lloyd and Warren, 1965; Aleksandrov, 1965; Crookall and Khor, 1974; Koenig and Werheim, 1976; Jeswani and Basu, 1979; Mamalis et al., 1988).

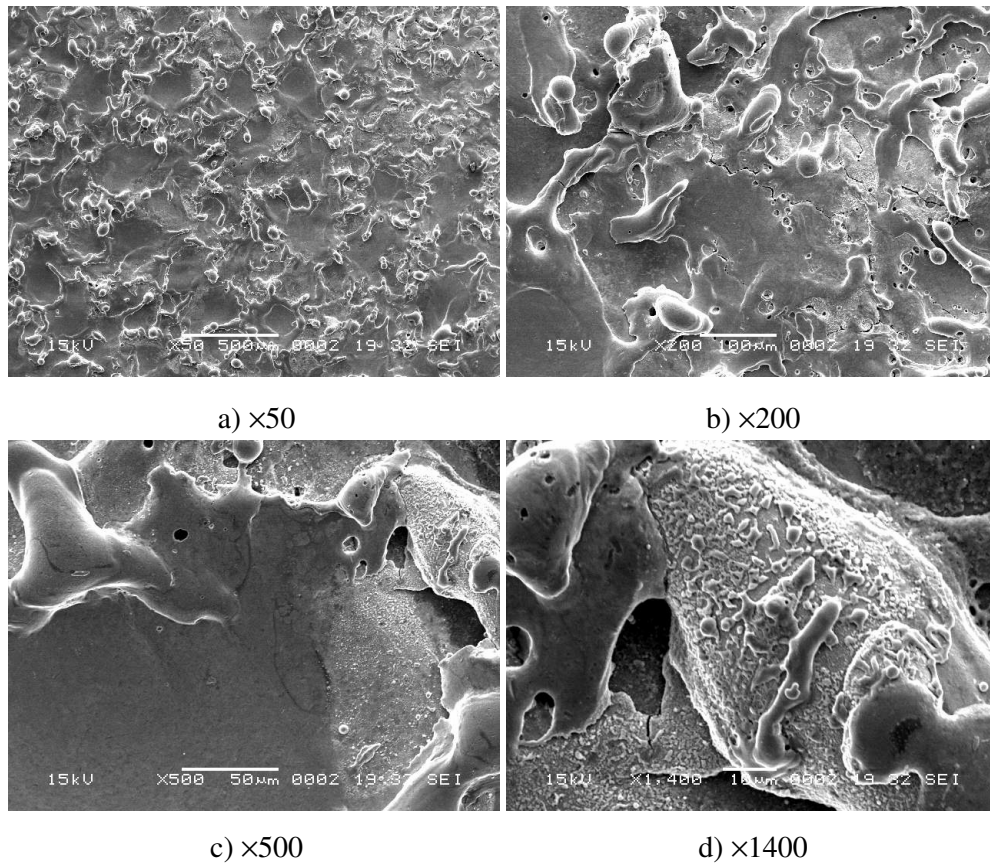


Figure 1.3. The Surface of an EDM'd DIN 1.2738 Steel Specimen Showing Craters, Global Appendages, Pockmarks and Cracks.

Heat effected zone lies below the white layer structure. This layer generally has a tempered microstructure and has a hardness value somewhat less than that of the underlying hardened metal. In a number of studies, an intermediate layer between the recast and the tempered layers was also observed (Lloyd and Warren, 1965; Crookall and Khor, 1974). This layer was found to exhibit a carbon gradient and

contamination of materials from the tool electrode. It is possible that this layer includes part of the melted layer plus a region beyond which diffusion has occurred in solid state. The hardness of this layer is found to be comparable to or, sometimes, slightly higher than that of the recast layer (Lim et al., 1991). Under optical microscope, it generally has a darker appearance than the parent material (Figure 1.5). The bulk of the material beyond the tempered zone remains unaffected by machining.

1.4.3 Residual Stresses

Knowledge about residual stress state, material properties and microstructural changes on the surface and sub-surface layers of metal parts plastically worked by means of electrical sparks is useful for determining the surface integrity to understand the relation between the physical properties of the material and the functional behavior of the machined component.

EDM generates residual stresses due mainly to the non-homogeneity of heat flow and metallurgical transformations. The rapid heating and cooling cycle leads to dramatic structural changes. High thermal contraction rates cause severe slip, twinning and cleavage on or near the crater depending on the crystal structure. In addition shock waves produced from the discharge region may deform the material. These changes accentuate the grain boundary weakness in the epitaxial layer, and grain boundary cracking is often found even in ductile materials (Crookall and Khor, 1974). Investigation of the residual stresses of EDM'ed components revealed their tensile nature, the extremely narrow superficial zone where they appear, their high magnitude at the surface layers, and their increase with increasing pulse energy. (LLyod and Warren, 1965; Crookall and Khor, 1974; Wallbank, 1980).

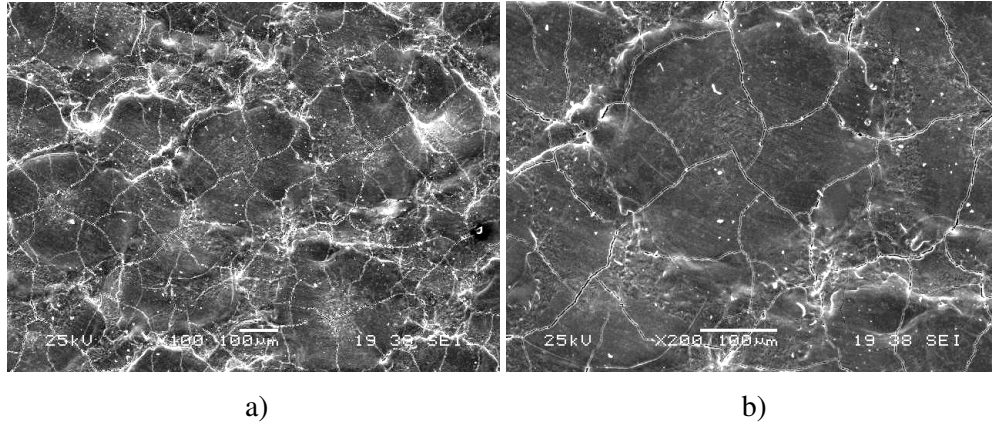


Figure 1.4 Scanning Electron Micrograph Showing a Cracked Surface of an EDM'd Micro Alloy Steel Specimen* $I_{av}=4\text{ A}$; $t_p=800\ \mu\text{s}$ with the Magnification of a) $\times 100$ b) $\times 200$

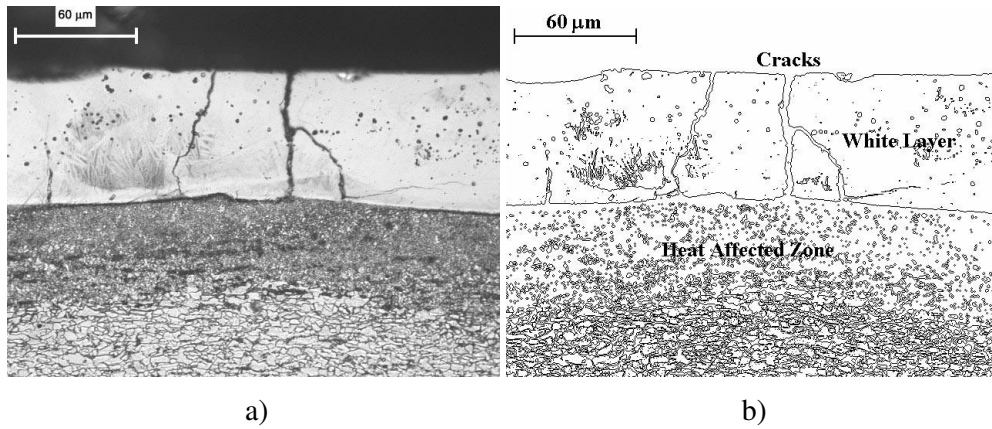


Figure 1.5 a) Optical Photomicrograph from Cross Section of an EDM'd Micro Alloy Steel* $I_{av}=16\text{ A}$; $t_p=1600\ \mu\text{s}$ b) Representation of Affected Layers after Edge Detection.

*Tool Electrode: Copper, Dielectric: Kerosene

1.5 Purpose of the Study

The accurate prediction of the surface damage is highly desirable since EDM is extensively used in areas where high precision is required. Moreover, the surface integrity aspects of EDM'ed surfaces are important to meet the requirements of component performance, longevity, and reliability (Powley, 1982; Gough, 1979). The presence of cracks as well as brittleness of the hardened layer has been reported to reduce the fatigue strength of EDM'ed components (Field and Kahles, 1971; DeVries et al., 1976). This requirement becomes more important when components are exposed to high stresses and high temperatures such as turbine parts and jet engine combustion domes (Dallas, 1979).

In this thesis, an extensive experimental study is presented to explore the surface and sub-surface characteristics together with the residual stress induced by EDM. Analytical studies and a finite element based model are proposed to determine residual stresses with respect to operational parameters and results are compared with experiments.

CHAPTER II

THEORETICAL MODELS FOR EDM

2.1 Introduction

The energy released in the discharge channel is consumed in heating the dielectric, cathode, and anode. The absorbed heat melts and even evaporates a small portion of the electrodes in contact with the spark channel. The electrode surfaces; except the discharge channel, are surrounded by the dielectric liquid and the process takes place in a very short time period. This time period is approximately between 1 and 2000 μ sec depending on the pulse duration selected on the spark generator. Thus, heat transfer cannot take place on the surfaces excluding spark-electrode interface (Zolotykh, 1960; Saito, 1964; Snoeys and Dijck, 1971; Koning et al., 1975; Pandit and Rajurkar, 1980; Erden, 1980; Beck, 1981; Pandey and Jilani, 1986). High plasma pressure developed during sparking prevents bursting of the molten material, but it is believed that a part of the molten material is ejected out of the cavity by mechanical shock generated by the gas bubbles entrapped in the molten crater. The bubble collapses only after termination of the discharge, and the surrounding molten metal is ejected out. (Koning and Zvirin, 1975).

The actual sequence of processes involving sparking, heating, melting, vaporization and the resultant material removal during EDM are complex in nature and not yet fully understood at the microscopic level due to difficulty in its scientific observation. Various theoretical and numerical approaches have been proposed for explaining the basic phenomenon of the EDM process but a

comprehensive quantitative theory concerning the mechanism of material removal cannot be formulated. This section summarizes the attempts for modeling EDM process, available in literature.

2.2 Energy Partition between Cathode, Anode and Dielectric Liquid

The thickness of the layer where heat is generated on the electrode surfaces is very small (Erden, 1980); therefore, it may practically be assumed as a plane heat source. Zingerman (1959) has shown that radiation losses from the discharge channel is negligibly small and therefore, the total discharge energy can be assumed to be dissipated only at the electrodes. Van Dijck and Snoeys (1974) estimated that more than 90% of this heat is conducted into the electrode and less than 10% of the heat is transported from the surface by evaporation of metal during sparking. DiBitonto et al. (1989) have suggested that a constant fraction of total power is transferred to the electrodes. They have used the value 8% as the percentage of heat input is absorbed by the workpiece for their theoretical work. Shankar et al. (1998) have found that the percentage of input heat going into the cathode, anode, and dielectric liquid stabilizes after a small fraction of pulse time. Pulse current and inter electrode gap are found to have a very small effect on their relative values. No comprehensive method has been proposed to calculate the amount of heat input distributed between cathode, anode and dielectric.

2.3 Discharge Channel Radius and Profile

The experimental observations (McGeough and Rasmusen, 1982) showed that the dielectric breakdown process would start only if the electric field is more than a critical value. Drabkina (1951) used the thermodynamic approach to determine spark radius and its variation with temperature. The thermodynamic approach was also used by Lowke and Ludwing (1975) to study the EDM process. Snoeys and Van Dijck (1971) varied heat source diameter and studied its effects on various responses. They analyzed spark radius and its growth rate using three different approaches. Erden (1983) has suggested an empirical relationship for the spark

radius. For a rectangular pulse, the spark radius $R(t)$ depends on time t as it is given in the following expression:

$$R(t) = KQ^m t^n \quad (2.1)$$

Here Q is the discharge power m , n and K are empirical constants. These constants are defined in terms of three parameters that are (L , M and N) determined experimentally for different electrode materials for discharge length l .

$$K = \frac{L}{lM + 0.5N} \quad , \quad m = M + 0.5N \quad , \quad n = N \quad (2.2)$$

Pandey and Jilani (1986) have proposed the following model for calculation of spark radius;

$$T_b = \frac{E_R R}{K \pi^{0.5}} \tan^{-1} \left[\frac{4\alpha t}{R^2} \right]^{0.5} \quad (2.3)$$

where T_b is the boiling temperature, E_R is the total energy released and α is the thermal diffusivity of the electrode material. Applications of the above expressions are limited, as they are valid only for few cases of selected electrode pairs and dielectric.

Eubank et al. (1989) defined the EDM spark to be barrel shaped with its radius near the cathode to be much smaller than that near the anode, and expanded with respect to time. Erden (1993) has shown that the variation of the diameter of discharge channel with time obeyed the integrated Drabkina (1951) equation. Shankar et al. (1998) have found that the spark shape is non cylindrical with the smallest cross section occurring at the middle of a discharge and larger on the cathode spark interface than on the anode spark interface by using finite element method.

2.4 Formulation of Heat Transfer Models

Erden (1977) has studied on thermo-mathematical models in detail. In his work, he defined $Q(t)$ as the rate of heat generation and t_p as the pulse duration. Then he expressed the total energy release as;

$$E_R = \int_0^{t_p} Q(\tau) d(\tau) \quad (2.4)$$

He computed the heat power density ($q(t)$) on the electrode surface by dividing the total power by the discharge channel area at any time (t).

$$q(t) = \frac{Q(t)}{\pi [R(t)]^2} \quad (2.5)$$

As a result, he obtained a time dependent circular area where time dependent power is released (Figure 2.1).

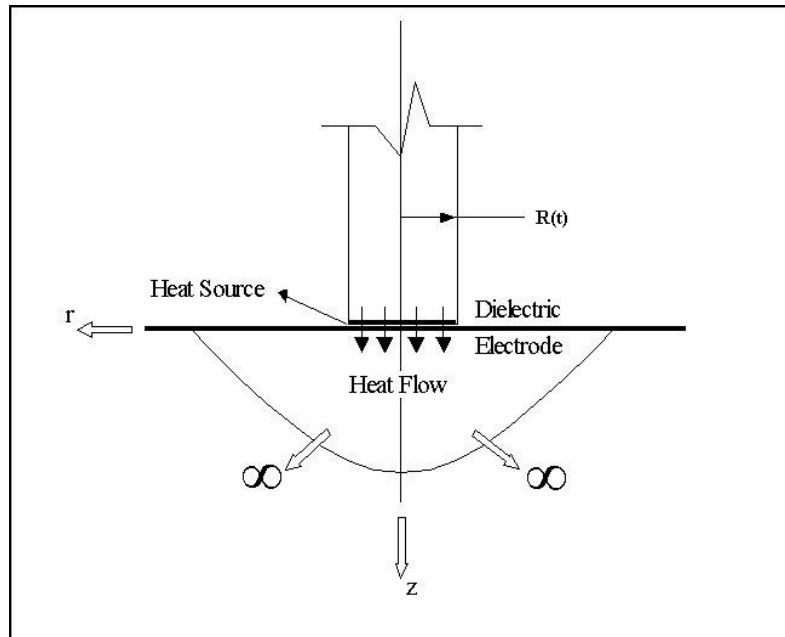


Figure 2.1 Heat Flow From Spark Channel to Electrode (Erden, 1980).

The following assumptions have been carried out for all proposed models unless otherwise is specified.

- a) The electrode material is at much lower temperatures, thus heat flow naturally from discharge channel towards the electrode. It is known that the channel diameter is approximately between 10 μm and 100 μm (Dijck and Snoeys, 1974; Pandey and Jilani, 1986). Such channel dimensions are very low when compared with the dimensions of the electrode. Thus, the electrode can be considered as a semi-infinite body.
- b) Heat conduction into dielectric fluid is negligible compared with that in the metallic electrode and convection in the vapor phase is not significant until the burst of bubbles that contain vapor.
- c) Properties of the material can be considered constant during the discharge and equal in three phases. Since variation of the properties between the solid and the liquid phases are quite moderate and due to the fact that the crater is tiny, the assumption of constant properties seems reasonable (Koning and Zvirin, 1975).
- d) The short times applicable to the process and since the workpiece is immersed in a dielectric fluid, heat transfer at the boundaries can be neglected compared to heat conduction in the metal.

The principle of conservation of energy amounts to an application of the first law of thermodynamics. The first law of thermodynamics applies to a thermodynamic system, which is originally at rest and, after some event; it is finally at rest again. Under these conditions it is stated that the change in internal energy, due to the event, is equal to the sum of the total work done on the system and any heat,

which was added. With this basic law in mind, the statement can be written in analytic form

$$\rho \frac{\partial e}{\partial t} + \rho u_k \frac{\partial e}{\partial x_k} + \rho u_j \frac{\partial u_j}{\partial t} + \rho u_j u_k \frac{\partial u_j}{\partial u_k} = u_j \frac{\partial \sigma_{ij}}{\partial x_i} + \sigma_{ij} \frac{\partial u_j}{\partial x_i} + u_j \rho f_i - \frac{\partial q_j}{\partial x_j} \quad (2.6)$$

The third and fourth terms on the left-hand side and first and third terms on the right-hand side represents mechanical energy of a system. If these terms subtracted from the above equation, we obtain;

$$\rho \frac{\partial e}{\partial t} + \rho u_k \frac{\partial e}{\partial x_k} = \sigma_{ij} \frac{\partial u_j}{\partial x_i} - \frac{\partial q_j}{\partial x_j} \quad (2.7)$$

Increase in temperature around the plasma channel results with evaporation of the dielectric fluid. High pressure induced within the channel prevents evaporation of the superheated metal. When the voltage is removed, the pressure drops suddenly and the superheated metal evaporates explosively (Beck, 1981). At this time interval the variation of density can be neglected and the equation can be simplified by considering constant density throughout the electrode medium. The resulting equation is the law of conservation of thermal energy for differential volumes.

$$\rho c \frac{\partial T}{\partial t} + \nabla \cdot q = V \quad (2.8)$$

If Fourier Law of Conduction is applied to the above equation the result is the heat conduction equation for homogenous isotropic solids and frictionless incompressible fluids.

$$\nabla^2 T + \frac{V}{k} = \frac{1}{\alpha} \frac{\partial T}{\partial t} \quad (2.9)$$

In the above equation $T=T(P,t)$ is the temperature at position P within the material body, and time t , k is the thermal conductivity and α is the thermal diffusivity. The electrode material is assumed to be isotropic. For the problem under consideration $V(T)$ can be defined as follows (Erden and Kaftanoğlu, 1980).

$$V = V(T) \begin{cases} = 0 & , \text{ for } T < T_m & \text{for any } P \\ = -L_m \rho_m, & \text{ for } T = T_m & \text{at } P_m \\ = 0 & , \text{ for } T_b > T > T_m & \text{for any } P \\ = -L_e \rho_e, & \text{ for } T = T_b & \text{at } P_e \end{cases} \quad (2.10)$$

where, P_m and P_e are the location of points reached to the melting and evaporation temperatures of the material, L_m and L_e are the latent heats of melting and evaporation, ρ_m and ρ_e are the mass densities at melting and boiling points.

Initially, the material is at ambient temperature.

$$T(P, 0) = T_0 \quad (2.11)$$

The workpiece is assumed to be as semi-infinite medium. Hence, the temperature can be set as the initial temperature at any time during the process at the outer dimensions P_E .

$$T(P_E, t) = T_0 \quad (2.12)$$

A moving boundary can be set on the liquid-solid interface that the temperature is at melting point.

$$k_l (T_m) \left. \frac{\partial T}{\partial P} \right|_{l, P=P_m} - k_s (T_m) \left. \frac{\partial T}{\partial P} \right|_{s, P=P_m} = -\rho L_m \frac{\partial P_m}{\partial t} \quad (2.13)$$

Here, $k_l(T_m)$ and $k_s(T_m)$ are thermal conductivities of liquid and solid materials at the melting temperature T_m , followed with the temperature gradients at liquid and solid sides of the melting boundary.

The last boundary condition can be set by using heat source term.

$$-k(T) \frac{\partial T}{\partial z} \Big|_{z=0} \begin{cases} q(r,t) & \text{for } r < R \text{ and } 0 \leq t \leq t_p \\ 0 & \text{for } r > R \end{cases} \quad (2.14)$$

The problem can be considered as axis-symmetric since temperature distribution is symmetrical around spark channel axis. Thus, the problem statement can be reduced in two-dimensional form. In addition, Erden (1977) has defined an equivalent temperature T^* which includes melting and evaporating effects. By this way he eliminated negative heat sources and simplified the problem without any approximation.

$$\nabla^2 T^* + = \frac{1}{\alpha} \frac{\partial T^*}{\partial t} \quad (2.15)$$

The boundary condition describing liquid solid interface is dropped by equivalent temperature definition.

So far the basic feature of the problem has not been changed with any approximation. On the other hand, the problem is still difficult to obtain practical solutions. Therefore, several researchers have proposed solutions with additional assumptions and simplifications.

2.4.1 Heat Transfer Models

An infinite plane source can be assumed for very long pulses, resulting in one-dimensional formulation (Figure 2.2). Zolotykh (1971) has applied this model for

a constant surface temperature. This type of problem is also known as Stefan's problem. The depth of molten zone was found as;

$$s(t) = At^{1/2} \quad (2.16)$$

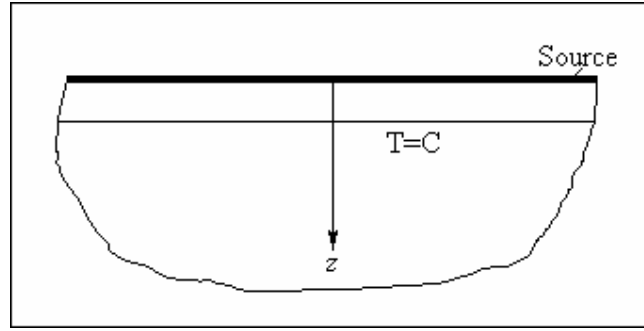


Figure 2.2 Infinite Plane Source Model.

Although the exact solution of the problem can be found such a simple form, determination of the constant A is very difficult. Özışık (1968) has worked on the same problem and gave an approximate solution.

$$A = \left[\frac{12\alpha \left[1 - \left[1 + \frac{2k(T_s - T_m)}{\rho\lambda\alpha} \right]^{1/2} + \frac{2k(T_s - T_m)}{\rho\lambda\alpha} \right]^{1/2}}{5 + \left[1 + \frac{2k(T_s - T_m)}{\rho\lambda\alpha} \right]^{1/2} + \frac{2k(T_s - T_m)}{\rho\lambda\alpha}} \right]^{1/2} \quad (2.17)$$

The Stefan's problem considers a constant surface temperature. If constant surface temperature is replaced with an infinite plane source the solution (Carslaw and Jaeger, 1959; Luikov, 1968) can be found for constant power density at depth z given by the following equation.

$$T(z,t) = \frac{2q}{t} \left(\frac{\alpha t}{\pi} \right)^{1/2} \exp\left(-\frac{z^2}{4\alpha t}\right) - \frac{qz}{k} \operatorname{erf}\left(\frac{z}{2(\alpha t)^{1/2}}\right) \quad (2.18)$$

Carslaw and Jaeger (1959) also worked on point heat source model (Figure 2.3) and found temperature distribution for an instantaneous source.

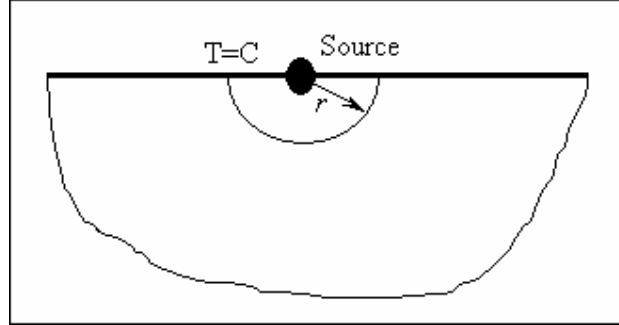


Figure 2.3. Point Source Model.

$$T(r, t) = \frac{E_R}{8\rho(\pi\alpha t)^{3/2}} \exp\left(-\frac{r^2}{4\alpha t}\right) \quad (2.19)$$

Zingerman (1957) worked on the same problem but solved for an active point heat source for a pulse time t_p and any shape of the power function $Q(t)$.

$$T(r, t) = \frac{(\rho c)^{1/2}}{8(\pi k)^{3/2}} \int_0^{t_p} Q(t)(t-\tau)^{-3/2} \exp\left[-\frac{r^2}{4\alpha(t-\tau)}\right] d\tau \quad (2.20)$$

The above equation can be integrated for constant power, as it is the case in pulse generators.

$$T(r, t) = \frac{Q}{2\pi kr} \operatorname{erfc}\left[\frac{r}{2(\alpha t)^{1/2}}\right] \quad (2.21)$$

Erden and Kaftanoğlu (1981) have also studied optimization of energy pulse forms using point heat source model and found that the rectangular pulses are not the optimum shapes for maximum material removal.

Point source can be replaced with a circular one on a semi-infinite cylindrical body. In addition, if heat source radius is taken as constant during sparking, a solvable two-dimensional heat conduction model can be obtained (Figure 2.4). Snoeys and Dijck (1971) have studied on such a model and found the solution in the following form.

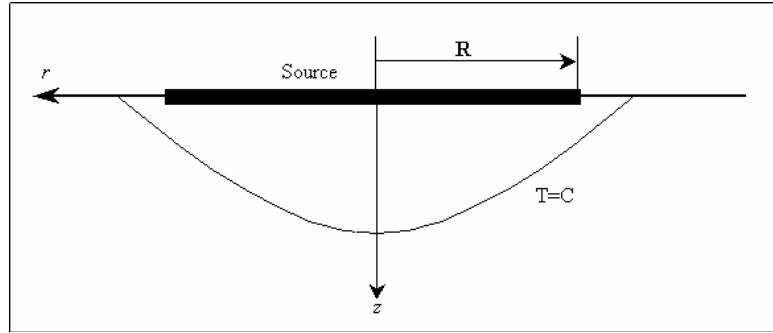


Figure 2.4 Two Dimensional Heat Source Model.

$$T(r, z, t) = \sum_{n=1}^{\infty} \frac{C_n J_0(\lambda_n r)}{2\lambda_n} \left\{ \begin{array}{l} \exp(\lambda_n z) \left[\operatorname{erf} \left(\lambda_n \sqrt{\alpha t} + \frac{z}{2\sqrt{\alpha t}} - 1 \right) \right] \\ + \exp(-\lambda_n z) \left[\operatorname{erf} \left(\lambda_n \sqrt{\alpha t} - \frac{z}{2\sqrt{\alpha t}} + 1 \right) \right] \end{array} \right\} \quad (2.22)$$

Where C_n is defined as

$$C_n = q \frac{2r_s J_1(\lambda_n r_s)}{k \lambda_n b^2 J_1^2(\lambda_n b)} \quad (2.23)$$

Eigenvalues λ_n can be found by finding the roots of $J_0(\lambda_n b) = 0$ for $n=1, 2, \dots, \infty$.

They also proposed the model for finite cylinder with insulated ends instead of semi-infinite cylindrical medium and found that the difference is very small. Carslaw and Jeager (1959) also worked on the same model and obtained the solution in integral form which is actually the same solution obtained by Snoeys and Dijck (1971). Beck (1981) has studied on similar model except the circular heat source replaced with a disc shaped heat source. He also assumed a semi-infinite cylindrical body. His solution is given in the following form.

$$T(r, z, t) = \frac{2qR}{k} \left\{ \frac{B(z, t)R}{b^2} + \sum_{n=1}^{\infty} \frac{A_n(z, t) J_0(\lambda_n r) J_1(\lambda_n R)}{2[\lambda_n b J_0(\lambda_n b)]^2} \right\} \quad (2.24)$$

Similarly eigenvalues λ_n can be found by finding the roots of $J_1(\lambda_n b) = 0$ for $n=1, 2, \dots, \infty$. Functions A_n and B are defined as follows.

$$A_n(z, t) = \exp(-z\lambda_n) \left\{ 1 + \operatorname{erf} \left[\lambda_n (\alpha t)^{1/2} - \frac{z}{2(\alpha t)^{1/2}} \right] \right\} \\ - \exp(z\lambda_n) \operatorname{erf} \left[\lambda_n (\alpha t)^{1/2} + \frac{z}{2(\alpha t)^{1/2}} \right] \quad (2.25)$$

$$B(z, t) = (\alpha t)^{1/2} \operatorname{ierfc} \left[\frac{z}{2(\alpha t)^{1/2}} \right]$$

Pandey and Jilani (1986) suggested a solution for the problem in a simple mathematical form.

$$T(r, z, t) = \frac{qR^2 \sqrt{\alpha}}{k \sqrt{\pi}} \int_0^t \frac{d\tau}{\sqrt{\tau(4\alpha\tau + R^2)}} \exp \left[-\frac{r^2}{(4\alpha\tau + R^2)} - \frac{z^2}{4\alpha\tau} \right] \quad (2.26)$$

Erden and Kaftanoğlu (1980) have considered the problem in different way. They assumed the spark channel interface covered by point sources and equated total energy release to total spark energy. Physically, the model can be visualized as an electron bombardment on the electrode surfaces. They found the temperature distribution in the following manner.

$$T(P, t) = \sum_{i=1}^n M_c \int_0^t \frac{Q_i(\tau)}{(t-\tau)^{3/2}} \exp \left[-\frac{\varphi_i^2}{4(t-\tau)} \right] d\tau \quad (2.27)$$

Here, t is the duration of point source, M_c is a material constant and φ_i is the distance from each point source.

$$M_c = \frac{(\rho c_p)^{\frac{1}{2}}}{8(\pi k)^{\frac{3}{2}}} \quad (2.28)$$

$$\varphi^2 = z^2 + R_i^2 + r^2 - 2R_i r \cos \psi$$

The solution of the explicit equation for constant φ_i and Q_i with respect to time is given as;

$$T(P,T) = \frac{1}{2\pi} \sum_{i=1}^n \frac{Q_i}{k} \operatorname{erfc} \left[\frac{\varphi_i}{2\sqrt{\alpha t}} \right] \quad (2.29)$$

Pandit and Rajurkar (1983) defined a thermal model with the help of a method called Data Dependent Systems (DDS). They obtained EDM surface profiles from actual working conditions and modeled by DDS methodology in the form of a first order stochastic differential equation. They considered the EDM surfaces as a superposition of occasionally overlapping craters with randomly varying depths and positions. This equation of melting isothermal curve is then combined with the heat conduction equation to develop a transient temperature distribution. Carslaw and Jaeger (1959) solution in integral form;

$$T(r, z, t) = \frac{qR}{2k} \int_0^\infty J_0(\lambda r) J_1(\lambda R) \left\{ \begin{array}{l} \exp(-\lambda z) \operatorname{erfc} \left[\frac{z}{2(\alpha t)^{1/2}} - \lambda(\alpha t)^{1/2} \right] \\ - \exp(\lambda z) \operatorname{erfc} \left[\frac{z}{2(\alpha t)^{1/2}} + \lambda(\alpha t)^{1/2} \right] \end{array} \right\} \frac{d\lambda}{\lambda} \quad (2.30)$$

The Transient temperature distribution along $r=0$ axis in the median plane is;

$$T(0, z, t) = \frac{2q(\lambda t)^{1/2}}{k} \left\{ \operatorname{ierfc} \left[\frac{z}{2(\lambda t)^{1/2}} \right] - \operatorname{ierfc} \left[\frac{(z^2 + R^2)^{1/2}}{2(\lambda t)^{1/2}} \right] \right\} \quad (2.31)$$

In non-dimensional form;

$$\Theta(0, \check{Z}, \check{t}) = \frac{4Q}{\theta_m \pi c_p \rho R^3} \frac{1}{\check{t}} \left\{ \text{ierfc} \left[\frac{\check{Z}}{\check{t}} \right] - \text{ierfc} \left[\frac{(\check{Z}^2 + 1)^{1/2}}{\check{t}} \right] \right\} \quad (2.32)$$

The non-dimensional parameters in the above equation are given as;

$$\check{Z} = \frac{z}{R}, \quad \check{r} = \frac{r}{R}, \quad \check{t} = \frac{2(\alpha t)^{1/2}}{R}, \quad \Theta = \frac{T - T_\infty}{T_m - T_\infty} \quad (2.33)$$

Here, R is the heat source radius, α is the thermal diffusivity, T_m and T_∞ are the melting and ambient temperatures. Similarly, θ_m and Q are;

$$\begin{aligned} \Theta_m &= T_m - T_\infty \\ Q &= q(\pi R^2)(t) \end{aligned} \quad (2.34)$$

Here, q is the supply of heat per unit time per unit area.

Similarly, the non-dimensional form of the characteristic crater shape, which represents the melting isothermal, defined by Pandit and Rajurkar (1980) as

$$\check{Z} = \check{Z}_m \left[1 - \exp \left(-4.5 \left(1 - \frac{\check{r}}{\check{r}_m} \right) \right) \right] \quad (2.35)$$

where $\check{Z}_m = z_m / R$, z_m , being the depth at $r=0$ on a melting isothermal, and $\check{r}_m = r_m / R$, r_m , being the radius of the crater along the melting isothermal on the surface, $z=0$. They have approximated the non-dimensional form using the power series expansion of $\text{ierfc}(u)$ and neglecting higher order terms and claimed that the error introduced by such an approximation lies between 4 to 10% melting temperature for values of $\check{Z} < 1$ and $\check{t} \geq 1$. The temperature distribution has been derived as the product of two solutions and found in the following manner.

$$\Theta(\tilde{r}, \tilde{Z}, \tilde{t}) = \frac{\frac{K}{\tilde{t}^2} \left[\frac{\tilde{t}^2}{K\beta} - \tilde{Z} \right]}{\left[1 + \left(\frac{1}{\beta} - 1 \right) \exp \left(-4.5 \left(1 - \frac{\tilde{r}}{\tilde{r}_m} \right) \right) \right]} \quad (2.36)$$

where,

$$\beta = \frac{\tilde{t}^5}{K \left(\tilde{t}^3 - \frac{\tilde{t}^2}{\sqrt{\pi}} + \frac{1}{6\sqrt{\pi}} \right)} \quad (2.37)$$

$$K = \frac{4qt}{c_p \rho R \Theta_m}$$

Assuming that the above temperature distribution is valid in the region of melting point, an expression for \tilde{r}_m can be obtained by substituting proper derivatives of the transient heat conduction equation for cylindrical coordinates in non-dimensional form. The solution has been found in the following form:

$$\tilde{r}_m^2 = 1.75\tilde{t}^2 - \frac{9}{K} \int_0^{\tilde{t}} \frac{\tilde{t}^6}{\left(\tilde{t}^3 - \frac{\tilde{t}^2}{\sqrt{\pi}} + \frac{1}{6\sqrt{\pi}} \right)} d\tilde{t} \quad (2.38)$$

Erden, Arriç and Kögmen (1995) have examined all the models described above, except the infinite plane source assumption, for some practical solutions and found that the heat source diameter is one of the most dominant parameters of the erosion process.

DeBitonto et al. (1989) used point heat source for cathode erosion. In their second paper (Patel et al., 1989) an expanding circle heat source that produce a Gaussian distributed heat flux on the incident surface on the anode material was analyzed by using Carslaw and Jaeger (1959) integral form given in Equation (2.30). The energy flux was given as;

$$q(r) = q_0 \exp\left(-\frac{r^2}{a^2}\right) \quad (2.39)$$

The disk radius a is replaced by R . The energy distribution is then considered uniform over this new radius. Furthermore, they assumed a constant fraction, F_A , of the total power is transferred to the anode. The relation between a and R was given as.

$$R = \frac{a}{\exp(1)} \quad (2.40)$$

They solved the Carslaw and Jaeger's equation using "isotherm migration method". The temperature contributions due to disk radii change with respect to time were summed over discrete disk sizes in the corresponding time interval.

Madhu et al. (1991) have used finite element method to estimate resultant crater shape and calculated the material removal rate. They applied Glarkin finite element formulation to obtain temperature distribution within cylindrical domain. Heat source has been taken as Gaussian heat distribution of power within a spark incident region.

$$q(r) = \frac{2Q}{\pi R^2} \exp\left\{-2\left(\frac{r}{R}\right)^2\right\} \quad (2.41)$$

where, Q is the total power received by the electrode and R is the spark radius. They solved the transient heat conduction problem by using eight noded isoparametric elements for a single discharge and also for a continuous power input. They removed the material regions above the melting temperature to predict the resultant crater shape.

Bhattacharya et al. (1996) have improved the previous finite element model. In this case, they have considered a constant fraction of heat, distributed between tool and workpiece. In addition the latent heat of melting and vaporization are included in following form.

$$\begin{aligned}
c'_p &= c_s + \left(\frac{L_m}{2\Delta T} \right) \\
c''_p &= c_l + \left(\frac{L_e}{2\Delta T} \right)
\end{aligned}
\tag{2.42}$$

where c'_p and c''_p are modified specific heats to account for latent heat of fusion L_m and latent heat of evaporation L_e respectively. c_s and c_l are the specific heats of material in solid and liquid states.

Shankar et al. (1998) solved the field equations for electric potential and temperature in the spark region by using finite element method and employed an integrated approach to handle temperature distribution in the electrodes and dielectric liquid simultaneously.

2.4.2 Thermal and Residual Stress Models

The high temperature gradients generated during EDM result in large localized thermal stresses in a small heat affected zone. Heat transfer models are usually used as the input to estimate these kinds of stresses. Lenz et al. (1975) proposed an approximate model based on temperature distribution and on the thermal stresses, which are created at the end of the discharge. They applied Carslaw and Jaeger's (1959) solution to the radial and thermal stress equation given by Timoshenko and Goodier (1970) with the boundary conditions;

$$\begin{aligned}
r = a & \quad \sigma_{rr} = 0 \\
r = \infty & \quad \sigma_{rr} = 0
\end{aligned}
\tag{2.43}$$

where a corresponds to the radius of a spherical crater. They derived the radial and tangential stresses as;

$$\sigma_{rr} = \frac{2\alpha_e E}{(1-\nu)} \frac{1}{r^3} \int_a^r T(r,t) r^2 dr
\tag{2.44}$$

$$\sigma_{\theta\theta} = \frac{\alpha_e E}{(1-\nu)} \frac{1}{r^3} \int_a^r T(r,t) r^2 dr - \frac{\alpha_e E T(r,t)}{(1-\nu)} \quad (2.45)$$

where E is the modulus of elasticity, ν is the poisson's ratio and α_e is the coefficient of expansion. Rajurkar and Pandit (1984) used the transient temperature distribution developed by DDS analysis to obtain thermal stress expressions. The corresponding boundary conditions were given as;

$$\begin{aligned} r = a & \quad \sigma_{rr} = 0 \\ r = b & \quad \sigma_{rr} = 0 \end{aligned} \quad (2.46)$$

Here, b is the radius up to which thermal stresses can be significant. In this case the solution can be expressed as;

$$\sigma_{rr} = \frac{2\alpha_e E}{(1-\nu)} \frac{1}{r^3} \int_a^r T(r,t) r^2 dr + \frac{2E}{(1-\nu)} \frac{(r^3 - a^3)}{(b^3 - a^3)} \frac{1}{r^3} \int_a^b T(r,t) r^2 dr \quad (2.47)$$

$$\begin{aligned} \sigma_{\theta\theta} = & \frac{\alpha_e E}{(1-\nu)} \frac{1}{r^3} \int_a^r T(r,t) r^2 dr + \frac{\alpha_e E}{(1-\nu)(b^3 - a^3)} \frac{(2r^3 - a^3)}{r^3} \int_a^b T(r,t) r^2 dr \\ & - \frac{\alpha_e E T(r,t)}{(1-\nu)} \end{aligned} \quad (2.48)$$

Temperature distribution is the dimensionalized form of the temperature distribution given in Equation (2.36).

$$T(r,t) = T_\infty + \frac{Q_0}{B} \left[\frac{A}{1 + \{A Q_0 / B (T_m - T_\infty) - 1\} \exp(-4.5(1 - r/r_m))} \right] \quad (2.49)$$

where,

$$\begin{aligned} A = 1 - \frac{a_s}{2\sqrt{\pi\alpha t}} + \frac{a_s^3}{48\alpha t\sqrt{\pi\alpha t}} \\ B = \pi c \rho a_s \alpha t \end{aligned} \quad (2.50)$$

The radial thermal stresses remain compressive, but the tangential ones became tensile and eventually tend to zero. Yadav et al. (2002) worked on a model to

represent thermal stress due to EDM based on the finite element technique. They assumed a Gaussian heat flux distribution as;

$$q_w(r) = \frac{4.45R_w U_b I}{\pi R^2} \exp\left\{-4.5\left(\frac{r}{R}\right)^2\right\} \quad (2.51)$$

where U_b is the breakdown (discharge) voltage, I is the current and R_w is the energy partition to the workpiece and taken as 8% of the total released discharge energy. They have solved the heat conduction equation in a similar manner proposed by Bhattacharya et al. (1996) and then feed the results as input for the calculation of thermal stress.

They have demonstrated the effect of current on the thermal stress distribution along the radial distance and depth. When the current is high, the induced radial, tangential and transverse components of thermal stress are also high and compressive in nature. They have also observed that the value of any stress component increases in the same proportion as increase in current. Das et al. (2003) improved the model to predict the residual stresses that are induced in the workpiece as a result of a single pulse discharge. They used temperature dependent thermo-physical and elastic-plastic material properties for the simulation process. The calculated residual stresses were found high exceeding the ultimate strength of the material and tensile in nature near the surface. Compressive residual stresses have been also detected at some distance below the surface.

2.5 Electrostatic Field Models for Short Pulse Durations

The plasma region itself cannot accommodate the potential drop between the electrodes and a thin layer of charge is formed between the cathode and the plasma. This layer is commonly termed as plasma sheath. During EDM, there is a strong electric field at the cathode since a large potential drop occurs and such a drop is sustained with a thin sheath. The field induces a negative charge on the cathode surface. The negative charge on the surface is pulled outwards by the

field, which leads to a stress distribution on the surface and in turn, inside the metal (Singh and Ghosh, 1999).

It was observed that heat is not responsible for erosion when short pulses are applied (McGeough and Rasmussen, 1982; Luo and Chen, 1990; Erden, 1992; Singh and Ghosh, 1999). Electrode material does not get enough time to heat up and almost no melting takes place (Singh, and Ghosh, 1999). In this case, the material removal is due to electro static force acting on the metal surface. Erden (1992) derived an expression to estimate the critical time for constant power discharges by using critical power density such that mechanical erosion is possible for higher density.

$$t_c = \left[\frac{q\gamma}{Cq_{dc}} \right]^{1/2n} \quad (2.52)$$

Here, $\gamma = 1 - 2M - N$ and $C = L^2 / 1^{2M+N}$. Experimental coefficients M and N can be found by using Equation (2.2).

Singh and Ghosh (1999) have estimated the electrostatic force acting on the metal surface and the stress distribution inside the metal for pulse times less than 5 μ s. They have used plasma fluid equation in one dimension and found the electric field at the cathode as

$$E_{EF}^2(x) = \frac{4}{\epsilon_0} n_{se} e_i \sqrt{\phi_0 \phi_w} \quad (2.53)$$

Here, n_{se} is the ion or electron density, e is the total charge on an ion. ϕ_0 and ϕ_w are the reference and electrode potentials respectively. The stress acting on the electrode surface in the discharge area was given as

$$\sigma = 2\sqrt{2} \left(\frac{I}{\pi R^2} \right) \sqrt{m_i} \left(-\frac{\phi_w}{e_i} \right)^{1/2} \quad (2.54)$$

where, m_i is the mass of an ion. Finally, they have found the stress inside the electrode as

$$\sigma_z(r, z) = \int_0^{r_s} \int_0^{2\pi} \frac{3\sigma z^3 r' d\theta dr'}{2\pi(z^2 + r^2 + r'^2 - 2rr'\cos\theta)^{5/2}} \quad (2.55)$$

It is commonly accepted by all of the researchers that thermal phenomena plays the main role of the material removal in EDM. Except for small pulse durations, in all the proposed mathematical models; electric power, pulse duration, discharge channel diameter and thermal constants of electrode materials are taken as the main parameters.

CHAPTER III

ELECTRIC DISCHARGE MACHINED SURFACES

3.1 Introduction

EDM has proven to be applicable to electrically conductive materials regardless of their physical and metallurgical properties. Technological advances have led to an increasing use of high strength, high hardness materials in manufacturing industries. Thus, the use of this process has increased in recent years since it has the capability of machining hard materials with complicated forms as fine slots and micro holes. However, fracture and fatigue failures generally nucleate at, or near the surface of the component and frequency of surface defects reduce the strength of the material due to the rapid heating and cooling effects induced by the machining process. These properties determine the resultant operational behavior of the machined parts.

Surface quality damage due to machining operations is directly related to the amount of energy used to remove the material. The main factors, which influence machining in EDM, are the spark gap, the electrical parameters (like pulse frequency, current and voltage) the material properties of electrode, workpiece and dielectric fluid like melting point, thermal conductivity and specific heat (Lloyd and Warren, 1965; Brash, 1971; Ghabrial, 1972; Crookall and Khor, 1974; Koning et al., 1975; Toren et al., 1975; Marty, 1977; Erden, 1982; Ramarao and Fruqi, 1982; Haron et al., 2001; Ho and Newman, 2003; Tosun et al., 2003). Therefore, promoting the quality of the process by developing a thorough understanding of the relationship between these parameters and the machined

surface quality has become a major research concern. This section summarizes the previous research activities that attempt to explore such a relationship.

3.2 Surface Topography

A clear characterization of surface topography is essential to predict the quality and functional behavior of surfaces (Crookall and Khor, 1974). Saito (1962) tried to define the relation between the shape of a single discharge crater and the condition of discharge. He found that the inter-electrode gap distance causes the diversity of the size of crater made by the discharge. Lloyd and Warren (1965) have shown that the anode craters take the form of a circular depression independent of crystal orientation and characterized by a raised circumferential lip resulting from the upheaval of metal during the liquid dispersion time. In addition, they found that the crater diameter is approximately constant for the same spark condition. The cathode craters on the other hand were not found truly circular but tend to reflect the symmetry of the crystal faces on which they occur. Greene and Guerreo-Alvarez (1974) used a profilometer imaging technique to accurately measure the volume of the electrode craters on different electrode materials produced by EDM. They showed the effects of high pressure generated during sparking on craters with illustrating radial flow lines near the rim. Radhakrishnan and Achyutha (1980) have found that the general appearance of the crater formed is almost the same for different materials except for their sizes and depth using relocation technique. They reported a well-defined ridge and considered that this was due to the deposition of the molten material from the crater. Wong, Rahman, Lim, Han and Ravi (2003) have worked on a micro EDM which has a single spark generator to study the erosion characteristic from the microcrater size, and found that the shapes of the craters to be more uniform with better defined rim at lower energies ($\leq 50\mu\text{J}$) in contrast to irregular diameters at higher levels.

A practical EDM surface is a random superposition of craters formed by the discrete removal of metal by the effects of successive discharges. Various experimental results and empirical models of surface finish for different operation

types, conditions, dielectric and electrode material combinations of EDM have been published (Saito, 1962; Ramaswami and Raj, 1973; Crookall and Khor, 1974; Jeswani, 1978; Rao and Faruqi, 1982; Lee et al., 1988; Chen and Luo, 1990; Cogun and Savsar, 1990; Aspinwall et al., 1992; Robelo et al., 1998; Chen and Mahdavian, 1999; Chen and Mahdavian, 2000; Tsai and Wang, 2001; Rozenek et al., 2001; Lee and Li, 2001; Halkacı and Erden, 2002; Liu and Huang, 2003; Lee and Tai, 2003; Ghanem et al., 2003; Simao et al., 2003; Guu et al., 2003) It has been observed that there are many process variables that effect the surface finish such as peak current, duration of current pulse, open voltage gap, electrode polarity, thermal properties of the tool, work, and dielectric liquid and debris concentration. Generally, logarithmic trend of curves, representing an increase surface roughness with respect to increased pulse energy, were presented. Large roughness values can be explained by the generation of large craters due to high energy levels. A great deal of effort has been made to improve EDM accuracy and surface roughness for using this process as an ultra precision machining. In the previous section, it was mentioned that the material removal is due to electro static force acting on the metal surface when short pulse duration is applied. In this case, surface roughness values (R_a) less than $0.2 \mu\text{m}$ is possible and a mirror-like surface can be obtained (Mohri and Saito, 1985; Luo et al., 1988; Luo and Chen, 1990).

Studies on various machined surfaces with electron microscopy (Crookall and Khor, 1974; Greene and Alvarez, 1974; Ramarao and Faruqi, 1982; Lee et al., 1988; Thomson, 1989; Rebelo et al., 1998; Ghanem et al., 2003; Lee and Tai, 2003; Lee and Li, 2003) showed that the surface is observed with globules of debris and chimneys formed by entrapped gases escaping from the re-deposited material. Evidently the surface is frozen, virtually instantaneously, when the discharge ceases. However, the shapes of the pockmarks, and particularly their rims, are indicative of their sudden and simultaneous rupture, coinciding with the sharp decrease in pressure as the discharge cut off (Crookall and Khor, 1974).

Another feature on electrical discharge machined surfaces is the abundance of micro-cracks. Amount of thermal energy created and the conductivity of the workpiece determine the cracking behavior of the machined surface. Cracks formed due to thermal stresses in a single discharge tend to follow the pitting arrangements created in the surface by EDM'ing. They normally form closed loops, instead of crossing the material's surface (R. of AGIE, 1987). Tensile stress generated since the melted material contracts more than the unaffected parent material during the cooling process, and when the stress in the surface exceeds the material's ultimate tensile strength (Mamalis et al., 1987; Thomson, 1989; Lee and Tai, 2003). A tension crack usually runs cross-crater. Cracks formed in a crater continue to propagate when another discharge takes place at the neighborhood. It can be noted that intersection points of crack paths usually form perpendicular angles.

3.3 Subsurface Deformations and Metallurgical Structure

The metallurgical characteristic of a crater shows high complexity because of the violent nature of the process. Therefore several questions have been raised about the surfaces such as the depth of affected material and the amount of structural changes.

Microscopic observations have shown that unusual phase changes occur since high local temperatures can be attained during machining process. The local temperature has been estimated more than 12 000 °K (Erden, 1992) which is very high, and it is not known any machining process that such high temperatures can be obtained even in such small dimensions. The molten surface of a spark crater suddenly charged with alloying material from dielectric or possibly from the tool (Optiz, 1960; Brash and Sri-Ram, 1962; Green and Alvarez, 1974; Crookall and Khor, 1974; Ramarao and Fruqi, 1982; Ramulu and Garbini, 1991; Tabrett, 1996) and then quenched by conduction through the crater base and convection by dielectric.

3.3.1 Recast Layer

As reported by many authors (Crookall and Khor, 1974; Massarelli and Marchionni, 1977; Wallbank, 1980), the resolidified layer, usually known as the recast layer, undergoes complex structural changes associated with extremely high cooling rate. Carbide formation was noted on the surface of pure titanium (Lloyd and Warren, 1965), Ti-6Al-4V (Chen et al., 1999) uranium, and zirconium (Lim et al., 1991) in hydrocarbon dielectrics, whereas oxide formation was found on pure titanium (Lloyd and Warren, 1965) and Ti-6Al-4V machined in water (Chen et al., 1999). Qin et al. (2003) have identified a new phase in Ti-46Al-2Cr machined under water dielectric. This phase was found well consistent with FCC structure titanium hydride with lattice parameter of 4.49-4.5 .

Lloyd and Warren (1965) reported high hardness values on the surface of pure titanium. Hung et al. (1994) have studied on cast aluminum metal matrix composite reinforced with silicon carbide particles and found that the surface is softened after EDM. Qu et al. (2003) have analyzed affected layers of WC-Co composites in water dielectric with nanoindentation and found that the recast layer had lower hardness and modulus of elasticity than the bulk material. Lee and Li (2003) have detected the damaged layer on the tungsten carbide by the amount of WC grains and micro-cracks. They have not found any significant difference between the hardness of the affected surface and parent material, which is machined in commercial hydrocarbon dielectric.

Earlier studies on electric discharge machined surfaces on pure iron and ferrous alloys revealed a non-etchable white covering layer, which is far harder than the basic grain structure. The surface of the white layer was found irregular signs of splashing and alloying effect from the electrode material (Optiz, 1960; Brash and Sri-Ram, 1962; Lloyd and Warren, 1965; Crookall and Khor, 1974; Ramulu and Garbini, 1991). This observation gives a sense of how the electrode material affects the workpiece surface quality. So, it was considered that this alloying effect could be used to enhance the surface quality such as reducing residual

stresses by a suitable source of alloying element (Lloyd and Warren, 1965; Crookall and Khor, 1974; Ramulu and Garbini, 1991). The hardness value was found high when compared with the hardness value obtainable by quenching (Lloyd and Warren, 1965). This layer was observed under all machining conditions, including when water is used as dielectric material (Optiz, 1960; Brash and Sri-Ram, 1962; Lloyd and Warren, 1965; Crookall and Khor, 1974).

Lloyd and Warren (1965) obtained a fused outer zone consisting of dendritic austenite and a cementite-austenite eutectic (ledeburite structure of a hypoeutectic white cast iron) when machining with a graphite electrode and in paraffin dielectric under severe conditions or fully austenitic surface followed by an austenite-cementite matrix when machining with a copper electrode under less severe conditions. Optiz (1960) have reported a hypereutectic recast layer in a hot forging steel. Massarelli and Marchionni (1977) reported a similar structure of carbides in an austenite matrix, but stated that different electrodes do not change the morphology of the white layer; only the ratio of the carbide and the austenite phases varies. However, Simao et al. (2003) have reported an increase in white layer hardness when employing powder metallurgy (PM) green compact and sintered TiC/WC/Co electrodes during EDT. They used glow discharge optical emission spectroscopy to analyze surface enrichment/depletion of the modified/alloyed EDT roll surfaces and observed that Ti and W contained in the PM electrodes together with C decomposed from the dielectric fluid during sparking were transferred to the AISI D2 roll surface. Similarly Tsai et al. (2003) have reported Cu and Cr migration to the machined surface from Cr/Cu based composite electrodes. Rebelo et al. (1998) have reported a severe increase in carbon intensity of the surface as nine times greater at the surface than the bulk material by microprobe analysis. Ghanem et al. (2003) have also detected an enrichment in carbon and hydrogen in the outer layer by glow discharge spectrometric (GDS) depth profiling. Increase in carbon content in the surface and sub-surface layers has been attributed by most workers to the pyrolysis of the dielectric, but others have suggested that carbon is assimilated more rapidly from graphite electrodes than from carbonaceous dielectric. Thomson (1989) has

concluded that carbon was absorbed from the dielectric rather than from the electrode. The near surface hardening is more important in the austenitic structure than in the ferritic structure due to solubility of carbon in FCC structure (Ghanem et al., 2003). Rebelo et al. (1998) have shown that Fe_3C cementite was formed on the surface of martensitic steels whereas Cabanillas et al. (2000) have found two different regimes of carbide formation. ϵ -carbide, austenite and martensite for sparks of energy below 0.5 J and cementite, austenite and traces of martensite, Fe_7C_3 , or Fe_5C_2 for higher spark energies on the pure iron in hydrocarbon dielectrics.

Lim et al. (1991) have managed to visualize the recast layer by using unconventional metallographic reagents and showed a variety of microstructures and as a result, they categorized these observations into three main groups according to recast layer thickness. The first type was found around 20 to 50 μm and has a multiplayer structure made up of overlapping layers of similar microstructures. The second type was found ranging 10 to 20 μm and is largely columnar and dendritic in nature. The last type was found having a thickness less than 10 μm and fairly resistant to etching. Thus, could not be described and named as featureless.

3.3.2 Heat Affected Layers

In most cases, a thermally affected layer was often found beneath the recast layer (Optiz, 1960; Lloyd and Warren, 1965; Crookall and Khor, 1974; Bucklow and Cole, 1969; Massarelli and Marchionni, 1977; Wallbank, 1980). It is partly affected by carbon drawn by the dielectric. This layer generally has a tempered microstructure. The hardness value of this layer is often found less than that of the underlying hardened material. In a number of studies, an intermediate layer between the recast and the tempered layers has also been observed (Optiz, 1960; Lloyd and Warren, 1965; Crookall and Khor, 1974; Massarelli and Marchionni, 1977). This layer was found to exhibit a carbon gradient and contamination of materials from the tool electrode. It is possible that this layer includes part of the

melted layer plus a region beyond which diffusion has occurred in solid state under severe machining condition and have a darker appearance than the parent material in optical microscope, suggesting that complex structural changes have taken place. The thickness of this layer increases proportionally with respect to discharge energy, but the chemical composition of the working material greatly affects its appearance. The intermediate layer can be as thick as the white layer. This layer contains a high density of second phase particles, which are larger in size and more rounded than the carbide particles in the parent material (Lee et al., 1988). The hardness of this layer is found to be comparable to or, sometimes, slightly higher than that of the recast layer (Lim et al., 1991). A zone of plastically deformed material has been reported (Bucklow and Cole, 1969) for single-phase materials, which do not undergo complex phase transformations during EDM. This plastically deformed layer has been found in thickness from a few tens to a few hundred micrometers in to the underlying metal. Cleavage and grain boundary cracks, penetrating into the underlying material, have been observed in brittle materials under severe machining conditions (Optiz, 1960; Llyod and Warren, 1965; Lee et al., 1988). The bulk of the material beyond these zones remains unaffected by machining.

3.3.3 Thickness of Affected Layers

Rajurkar and Pandit (1984) have applied DDS analysis to estimate the thickness of the white layer as the amount of material in which the temperatures range from the phase transformation to the melting point of the metal.

$$wlt = p(1 - \eta^{1/3}) - \frac{\tilde{t}^2}{K}(C - \eta^{1/3}) \quad (3.1)$$

where,

$$p = \left(1 - \frac{1}{\tilde{t}\sqrt{\pi}} + \frac{1}{6\tilde{t}^3\sqrt{\pi}} \right) \quad (3.2)$$

K is given in Equation (2.37) and C is the ratio between the phase transformation temperature and the melting temperature. η is the metal removal efficiency.

Pandey and Jilani (1986) used Equation (2.26) to compute the locations of the boundaries of the boiling isotherm, melt isotherm and transformation isotherms. They defined the material between the melting and boiling isotherms as resolidified layer and the material between the melting and transformation isotherms as thermally affected layer. Their comparative studies with experimental data revealed similar results.

Rebelo et al. (1998) suggested the following empirical relations to estimate the white and heat affected layer thickness for previously quenched and tempered martensitic steels.

$$\begin{aligned} wlt &= 148(I_{av}t_p)^{0.34} \\ halt &= 1086(I_{av}t_p)^{0.38} \end{aligned} \quad (3.3)$$

Guu et al. (2003) also proposed a similar relation for AISI D2 tool steel as

$$wlt = 2.93I_{av}^{0.36}t_p^{0.29} \quad (3.4)$$

where, wlt is the white layer thickness and $halt$ is the thickness of heat affected zone.

3.4 Residual Stresses in EDM

EDM generates residual stresses and these being due mainly to the non-homogeneity of heat flow and metallurgical transformations or to localized inhomogeneous plastic deformation respectively. Sharp temperature gradients in the workpiece material cause stresses even more than the yielding point of the material (Brash and Sri-Ram, 1962) and severe slip, twinning and cleavage depending on the crystal structure (Crookall and Khor, 1974). The magnitude and nature of residual stresses significantly influence, as they affect the main material properties.

Earlier attempts to measure residual stresses due to EDM have conducted by Aleksandrov (1965), Aleksandrov and Zolotykh (1958), Barash (1965), Lloyd and Warren (1965). Barash (1965) have investigated residual stresses by discrete layer removal bending deflection method, and found high residual stresses. Llyod and Warren (1965) have measured strains by a foil strain gage. They etched away the surface in tiny (0.0002") steps and measured the corresponding strains obtained from a calibrated high frequency bridge. Tensile residual stresses were found to approach the upper tensile strength of the material at the immediate surface, and then fall rapidly to a relatively low value before giving way to small residual compressive stresses in the core of the material. The measured stress distribution for three different machining times revealed that the stress distribution does not vary with time once the operation of machining has settled down to a steady state. Measurements of residual stresses on different phases have also showed that the general stress distribution is not greatly affected (Llyod and Warren, 1965). Aleksandrov (1965) studied the effects of pulse duration and pulse energy on the formation of residual stresses. Results by Aleksandrov and Zolotykh (1958) indicated that surface finish and depth of surface layer affected depended on a considerable extent upon the pulse duration. The observed residual stresses supported the expected trend and increased by both the pulse duration and pulse energy. Aleksandrov (1965) and Lloyd and Warren (1965) forwarded similar tentative explanations for the formation of residual stresses. The stresses were deemed to arise mainly as a result of the thermal contraction of the resolidified metal, which was not expelled from the craters, onto the relatively unaffected parent metal, inducing plastic deformation and biaxial tensile stress.

Crookall and Khor (1972) measured the residual stresses for tool steel at three different energy levels with pulse duration varying between 75 and 500 μ s. They used the bending deflection method in a continuous manner. In their studies, they measured highest tensile residual stresses of 420 MN/m² about 0.04 mm below the machined surface at the highest energy level of 1.1 J. At lower energy level of 0.5 J but the same pulse duration of 250 μ s, they found that the general extent and

penetration of residual stresses has decreased although a similar value of maximum stress occurs at a decreased depth of 0.015 mm. However, when using RC pulse generators, the general feature is the high near surface stresses, which decrease with distance from the surface, becoming low tensile or even compressive at a depth about 0.1 mm. Also, with increasing capacitance, the general level of the stresses increases. The maximum stress level cannot be detected on the results since the measuring method did not allow measuring stresses just on the surface. Another interesting feature is the difference in stress levels when the surface machined with different type of machine but under similar machining conditions. They have been compared the effect of workpiece material on residual stress by using two different materials, copper and tool steel. The stress level in copper was found lower, and decrease to a low level within about 0.02 mm.

Mamalis et al. (1988) used x-ray diffraction method in parallel beam modification to determine the residual stress profile of EDM'ed microalloyed steel. They detected considerable amount of residual stresses at the sub-surface layer and found that the peak stresses were almost independent of the discharge energy and approaches the ultimate tensile strength of the material. The affect of increase in discharge energy was described as increase in depth where the peak residual stress occurs. This was related to the intensification of the surface cracking with energy. They observed lower stresses for dual phase samples compared to microalloyed one, although the difference in strength between these steels is not significant. They have concluded this situation as the influence of transformation stresses due to phase changes.

Rebelo et al. (1998) also measured residual stress with x-ray diffraction technique and found similar stress pattern for martensitic steels. The residual stress increases from the bulk material to a maximum and then decreases again near to the surface. This decrease is related to crack formation since the residual stresses exceed the fracture strength of the material. They have noticed that the depth of the

maximum stress value corresponds to the average depth of the thermal cracks network induced by EDM.

Kruth and Bleys (2000) measured residual stresses developed during wire EDM by bending deflection method based on continuous material removal. They have observed that, the peak stress is not located at the surface, but somewhat below for roughing. They explained this situation by the fact that the white layer has a lot of cavities and micro-cracks, which cause relaxation of the residual stress as in the study of Mamalis et al. (1988). After reaching the peak stress, the tensile stress decreases and switches to small compressive stress at a certain penetration depth below the surface. The residual stress is in much lower extent and amplitude, and the peak stress is at the top surface under fine machining conditions. They have also observed a clear relaxation of the residual stress with respect to time. The maximum stress decreases considerably in time, whereas the depth of maximum stress and the penetration depth of the tensile stress are unchanged. A possible explanation for the relaxation of stress in time is given as the diffusion of carbon atoms to more favorable positions near dislocations, which reduces the residual stress. To verify this process, they repeated the experiments, but, in order to accelerate the tests, they exposed EDM'ed samples to a higher temperature by placing it in a furnace at 75 °C, which will speed up the stress relaxation. It must be noted that they cannot verify stress relaxation phenomenon for all samples. In some cases, even after several days, no stress relaxation has been observed at all. A satisfying explanation for this different behavior between samples cannot be found, and no significant microstructural difference can be detected.

Ghanem et al. (2003) have studied on martensitic hardenable steels and also on non-hardenable austenitic and ferritic stainless steels. They measured residual stresses with x-ray diffraction and reported a high tensile stress level and a wide profile associated with surface stress relaxation for hardenable steels. Surface stress relaxation has been found even under finishing conditions for non-hardenable steels. However, they were measured the stress pattern only under one machining condition. Therefore, they have not stated any qualitative explanation for the affect of energy level on stress distribution.

Das et al. (2003) modeled EDM process with a finite element method. The model uses process parameters such as power input, pulse duration to predict the transient temperature distribution, liquid and solid state material transformation and residual stresses that are induced in the workpiece as a result of a single discharge which is approximated by the Gaussian heat input model. They used temperature dependent thermo physical material properties for the simulation process and calculated large tensile stresses close to surface where the spark struck. The level of maximum stress has been found higher than the ultimate tensile strength of the material. They have concluded that such stresses induce micro-cracks in white layer.

3.5 Cracking Behavior and its Consequences

Crack formation can be attributed to the presence of thermal and tensile stresses within the machined component. Thermal stresses are produced when an electric discharge heats up the spark incident surface. Tensile stresses are generated since the melted material contracts more than the unaffected parent material. Diffusion of carbon from dielectric liquid and possibly alloying materials from tool electrode can also affect the material contraction rate. When the stress in the surface exceeds the material's ultimate tensile strength, cracks are formed (Lenz and Katz, 1975; Schachrai and Lenz, 1976; Thomson, 1998; Mamalis et al., 1987; Lee et al., 1990). Results from previous studies (Mamalis et al., 1987; Lee et al., 1988; Lee et al., 1990; Lee et al., 1992) have indicated that cracking increases as the pulse energy increases. But, it was stated that maximum crack density actually occurs under the minimum pulse current and maximum pulse on duration (Lee and Tai, 2003). It has been also known that crack density is decreasing in water dielectric (Kruth et al., 2001).

Cracks are initiating from the surface and traveling down perpendicularly toward the parent material. In most cases the cracks terminate within the white layer or just on the interface zone between the white layer and heat affected zone. However, under some critical machining settings, cracks can penetrate to the

parent material. Grain boundary cracking is evident under such circumstances (Lloyd and Warren, 1965).

The fatigue strength of mechanical components is dependent on the properties of the surface and near surface regions (Zeid, 1996; Zeid, 1997). Among the surface defects, cracking was found the most significant since it leads to a reduction in the material resistance to fatigue and corrosion (Lim et al., 1991), especially under tensile loading conditions (Thomson, 1998).

CHAPTER IV

RESIDUAL STRESSES

4.1 Introduction

Residual stresses are self-equilibrating stresses existing in materials under uniform temperature conditions without external loading. Such stresses will be always produced if regions of a material are non-homogeneous plastically deformed in such a permanent manner that strain incompatibilities occur. Residual stresses can be classified in three categories according to the distance or range over where the stresses equilibrated. These are the residual stresses of the 1st, 2nd and 3rd kind (Figure 4.1).

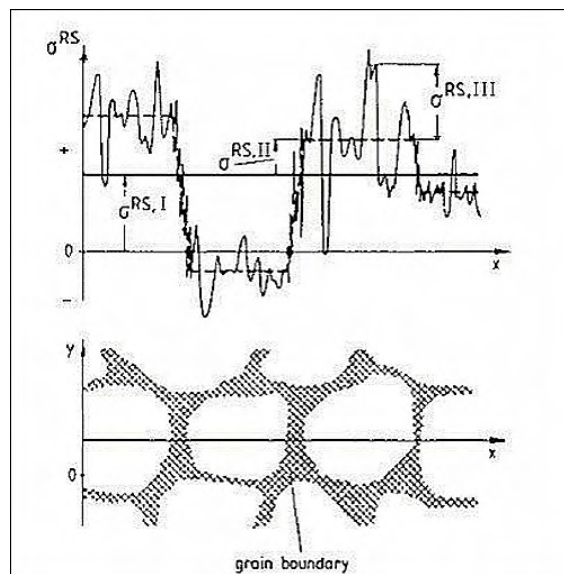


Figure 4.1 Illustration of a Stress State Composed of 1st, 2nd and 3rd Kind of Residual Stresses (Macherauch, 1987).

Residual stresses of the 1st kind are nearly homogeneous across large areas, say several grains of a material and equilibrated within the whole body. This kind of stress is also called as macro residual stresses. Residual stresses of the 2nd kind are nearly homogeneous across microscopic areas, covers a distance of one grain or a part of a grain of a material and the equilibrated across a sufficient number of grains. This kind of residual stresses is also known as structural micro-stresses. Residual stresses of the 3rd kind are inhomogeneous across submicroscopic areas of a material, covers only several atomic distances within a grain and are equilibrated across small part of a grain. This kind of stresses is also called as micro residual stresses. Usually, superposition of residual stresses of the 1st, 2nd and 3rd kind determines the total residual stress state acting at a particular point of a material (Macherauch and Kloos, 1987).

4.2 Influences of Residual Stresses

Residual stresses in a workpiece are a function of its material processing and machining history. Such stresses may improve or impair the functional behavior of a machined part. The machining processes, which generate functional relevant surfaces, have a great importance for the development of the physical state of the surface and the residual stresses in it. For many applications, the properties of a part's surface are dominant for the functional behavior of the whole component (Brinksmeier, 1982).

Residual stresses act in a body without applying forces or moments. Therefore the effect of residual stresses can be found by considering the material behavior under real loading conditions. The main result of residual stresses on a mechanical component is the deformation due to the new state of equilibrium. In addition, for a material which have a characteristic yield point, the residual stresses act like a pre-stress state and changes the level of the yield strength. Finally, the dynamic strength changes considerably. This can be explained as the change in mean residual stress level during cyclic loading.

4.3 Determination of Residual Stresses

The prediction of the stresses requires knowledge on the thermo-mechanical behavior of the material, the external forces to which the material is submitted, the interactions between the thermal and mechanical forces, and the structural transformations of the metal.

The importance of the different properties and interactions (Figure 4.2) will depend on the type of treatment. Interactions can be explained as;

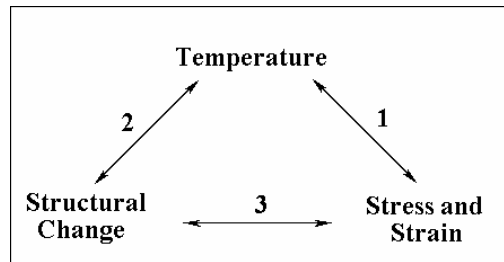


Figure 4.2 The Necessary Data and Interactions for Predicting Residual Stresses.

- 1- Temperature dependency of mechanical properties and deformation due to heat generation.
- 2- Temperature and time dependency of phase transformation and structural dependency of thermal constants.
- 3- Stress and strain dependency of phase transformation and structural dependency of mechanical properties.

Thermo-mechanical behavior of the material is characterized by the dilatation coefficient, density and mechanical properties given in relation to the material temperature and structure.

The main mechanical behaviors used are thermo-elastic, thermo-plastic or thermo-elasto-visco-plastic. Simple elastic behavior becomes quickly limited and cannot account for residual stress effect. Visco-plastic behavior is encountered

principally at high temperatures. Elasto-plastic behavior is most frequently used to characterize a material undergoing treatment.

To calculate the internal stresses in a part, it is necessary to know the external forces. These forces may be,

- (i) Temperature gradients in the part
- (ii) The chemical composition gradients
- (iii) The deformation gradients

The most universal and most practical method of establishing the evaluation of temperature in a part is to solve the heat equation. This requires us to know, heat transfer coefficient, heat flux on the cooled surface, and the thermo-physical constants.

4.4 Residual Stress Measurement

It is not possible to measure residual stresses directly. Always distinct physical quantities have to be measured from which the kinds of residual stresses can be derived. Among them, a distinction has to be made between destructive and non-destructive measuring techniques. However, for a residual stress depth analysis all methods require partial or complete destruction of the specimen. From that reason it is more effective to use a distinction as direct and indirect measuring methods. The residual stress can be analyzed as,

- (i) From microscopic strains, which are released while an amount or part of the stressed material is removed from the body. This is the basis of all mechanical methods exclusively investigating residual stresses by 1st kind and 2nd kind.
- (ii) From lattice strain, where the stressed lattice spacing is determined by diffraction techniques.

- (iii) From propagation velocities of birefringence of ultrasonic waves influenced by residual stresses
- (iv) From magnetic properties and phenomena of the material that influenced by all kinds of residual stresses.

Characteristic items of the mostly applied methods to evaluate residual stresses state are summarized in Table (4.1). These experimental methods for measuring internal stresses are quite reliable. But none of them is able to give the value of transient stresses. For example, the stresses at the moment when they are being generated during the heat treatment or any kind of process result with loading, either in the bulk or at the surface can not be measured (Beck and Ericsson, 1987).

4.4.1 Mechanical Techniques

The first series of methods is based on the destruction of the state of equilibrium of a residual stress in mechanical component. In this way the residual stress can be measured by relaxing it. In this technique, it is only possible to measure the consequences of the stress relaxation. Therefore, the stress relaxation must be determined by an analytical approach or using finite element technique.

The procedure for mechanical methods is as follows;

- (i) Creation of a new stress state by removing material from the analyzed part.
- (ii) Detection of the local change in stress by measuring the strain or displacement.
- (iii) Calculation of the residual stresses as a function of strain measured using the elastic theory.

Techniques	Measuring Quantities	Required Data	Surface Condition	Smallest Analyzed Area	Evaluated Stress	Accuracy of Evaluated Stress	Evaluation of Stress Gradient	Equipment Measuring Time	Applications
Mechanic	Layer Removal	Young Modulus Poisson's Ratio Calibration Functions	Suitable for Applications of Strain Gages	1.8 mm dia	I. Kind	$\pm 10 \text{ N/mm}^2$	Possible	Strain Gage Measuring Device, Depending on the extent of Measurement	All Kinds of Components If Geometrical Conditions are Fulfilled
	Sectioning						Variation of Hole Drilling Depth		
	Hole Drilling						Variation of Ring Notch Depth		
	Ringcore								
Diffraction	X-Rays	X-ray Elastic Constants, Lattice Parameter of Stress Free Material State in Special Cases	Roughness (Arithmetical Mean) $< 2 \times$ Average Penetration Depth	0.2 mm dia. x Penetration Depth	I.+II. Kind, Separation is possible in Special Cases, Measurable in Each Phase of Heterogeneous Materials with Sufficient Volume Content	$\pm 10 \text{ N/mm}^2$ max.	Variation of Wavelength and/or Etching Depth	X-Ray, Synchrotron or Neutron-Ray Source, Diffractometer. Min. 10 Hours per Stress Component	All Kinds of Components and Materials with at least One Crystalline Phase of Sufficient Volume Content
	Synchrotron Radiation						Shifting of in Steps of 0.5 mm		
	Neutron Rays			0.5x0.25x10 mm ³ Volume					

Table 4.1 Characteristic Data of the Different Techniques to Measure Strains and Related Quantities to Evaluate Residual Stresses (Hauk et al., 1987)

Techniques	Measuring Quantities	Required Data	Surface Condition	Smallest Analyzed Area	Evaluated Stress	Accuracy of Evaluated Stress	Evaluation of Stress Gradient	Equipment Measuring Time	Applications
Ultrasonic	Propagation Velocity	Velocity of L-, S-, SH and Surface Waves	Roughness < 0.1 x Ultrasonic Wavelength with $0.3 \leq \lambda \leq 5$ mm	30 mm ² Probe Area	I. Kind	$\pm 3\%$ of Stress Value ± 5 N/mm ² max.	If Microstructure is Known Alteration of Frequency of Surface Waves for Analyzing Depths Between 0.3 and 5 mm	Ultrasonic and Time of Flight Measuring Device, 1 to 2 Minutes Per Stress Value	Components of Metallic and Ceramic Materials Increasing Efforts are Necessary in case of Pronounced Textures
	Time of Flight	Shear Modulus and III. Order Elastic Constants							
	Dispersion	In Textured States Dispersion of Velocity and/or Time of Flight of S-Grain Size							
Magnetic	Magnetoinductive	Incremental Permeability vs H _t (Tangential Magnetic Field Strength)	Roughness < 0.1 x Probe dia. Surface Preparations are not Necessary	1 mm ²	I+II+III. Kind, Depending on Calibration Procedure	Reproducibility about 10%	Variation of Analyzed Frequency with Particular Consideration of Microstructure and Texture	Multiparameter Micromagnetic Device, 1 second Per Measuring Quantity	Components of Ferromagnetic Material, Excluded Regions which cannot be Exited Magnetically
	Magneto-Elastic	The Measured Ferromagnetic Quantities have to be Calibrated by X-Ray or by Strain Gage Measurement		50 mm ²					
	Ferro-Magnetic	Amplitude of the Acoustic Barkhausen Noise vs H _t Amplitude of the Magnetic Barkhausen Noise vs H _t		0.1 mm ²					

Table 4.1 (cont'd)

The most useful techniques are as follows,

- (i) Hole drilling method
- (ii) Ring core technique
- (iii) Layer method
- (iv) Sectioning method

Applying hole drilling or the ring core method for residual stress determinations, strains that occur in the neighborhood of the hole or the ring core due to a partial release of residual stresses will be measured. From these values, by the aid of Young's modulus and Poisson's ratio as well as calibration coefficients or calibration functions of the material, residual stresses can be calculated with considering the applied strain gage configurations.

The principle of layer removal method depends on the balance of internal stresses and moments when residual stresses are gradually removed from the material by thin layers using chemical or electro chemical machining. The resultant strains or deflections due to rebalancing of internal stresses are measured to calculate residual stresses from elastic theory. In general, residual stresses in the outmost surface layers of components cannot be determined easily.

If sectioning techniques are used, the equilibrium conditions for stresses and moments have to be considered. The stressed object is sectioned and the stress is relaxed. In any case, averaged strain values will be measured according to the amount of the removed material, which determines the magnitude of stress release. Residual stress values analyzed by any mechanical method can be falsified with plasticity effects when high quantities of stresses exist. Improper sectioning and strong residual stress gradients beneath the surface also may lead to some uncertainties in the results.

4.4.2 Diffraction Techniques

Diffraction techniques can only be applied to crystalline materials or to crystalline phases in material, respectively. In any case, a sufficient amount of crystalline material is necessary to determine residual lattice strains.

Residual stress analysis by x-ray diffraction depends upon the measurement of lattice strains. Therefore, distances between atoms must be known. Bragg described x-ray diffraction as a selective reflection according to the law.

$$\lambda = 2d \sin \theta \quad (4.1)$$

Where λ is the wavelength of x-rays, d is the lattice spacing and θ is the diffraction angle. Figure (4.3) shows the diffraction at a single crystal with and without loading.

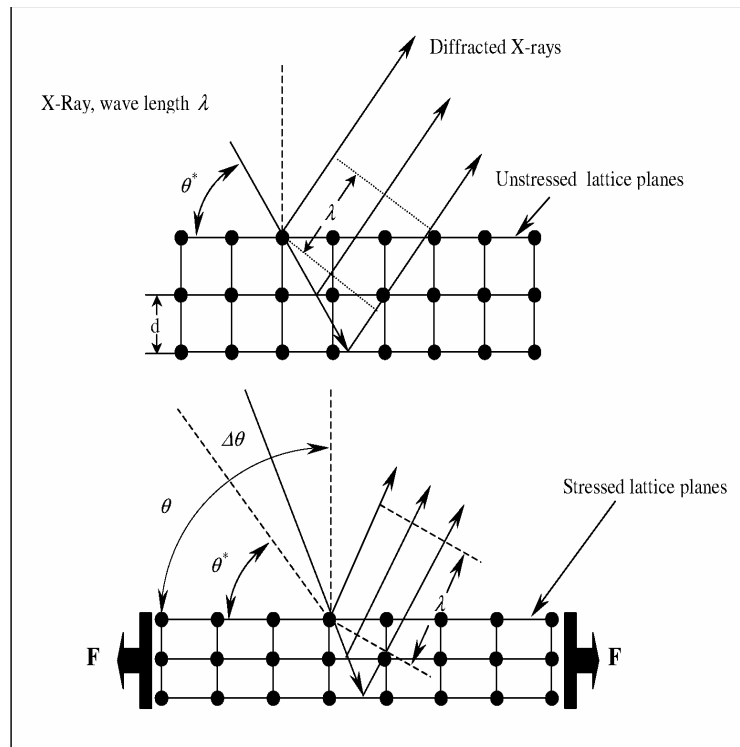


Figure 4.3 X-Ray Diffraction at an Unloaded and a Loaded Single Crystal (Brinksmeler et al., 1982).

The diffraction angle θ^* in the unstressed condition has to be increased to $(\theta^* + \Delta\theta)$ in order to receive interference with a maximum intensity at the detector in the loading condition.

4.4.3 Ultrasonic Techniques

Ultrasonic methods are based on the acoustic elastic effect according to which residual stress states influence the velocity of sound. Although residual stress influence on this quantity is only of some 0.1 %, the effect can be measured precisely. Variation of the wave velocity due to residual stresses can be conceptually described with the following relation.

$$V = V_0 + K\sigma \quad (4.2)$$

Here, V_0 is the velocity of a wave in an unstressed medium, σ is the stress and K is a material dependent parameter known as the acoustoelastic constant.

Several ultrasonic techniques using different types of ultrasonic waves have been developed. Special combinations of different wave types or waves with different directions of propagation and polarization yield different measuring procedures, which are independent of the path length of sound (Figure 4.4).

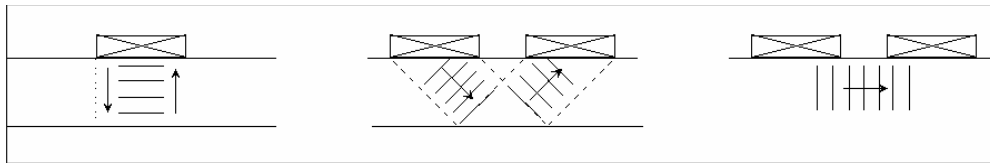


Figure 4.4 Schematic Views of Acoustoelastic Measurement Configurations.

A primary advantage of ultrasonic technique is to obtain information about stresses in the interior of the material. The velocity shift is proportional to the average stress in the region through which the waves propagate. Ultrasonic techniques can easily be applied. No special surface treatments are necessary. No

difficulties arise with field applications. Measuring times are approximately about one minute.

4.4.4 Magnetic Methods

It has been long known there is an interaction between the magnetization and elastic strain in ferromagnetic materials. Experiments conducted almost a century ago confirmed that a piece of steel wire, when magnetized, will be elongated in the direction of magnetization; when stretched, will be magnetized in the direction of stretching.

This phenomenon is caused by magnetostriction, the spontaneous lattice strain resulting from the alignment of atomic magnetic moments in certain crystallographic directions. Spontaneous magnetostriction may be positive or negative. It is parallel to magnetization within magnetically ordered regions called domains. The magnetization is uniform within a domain, equal in magnitude to the saturation value and directed along one of easy directions. Within each grain there may be several domains.

Magnetostrictive strain within each domain causes dimensional changes in the material when domains reorder under applied magnetic field. To minimize the stored plastic energy, domain magnetization vectors in iron with positive magnetostriction prefer to align themselves parallel to tensile stress axis, and perpendicular to compressive stress axis. The alignment effect in turn causes changes in the net magnetization of the material when stress is applied.

Magnetic stress testing methods rely on this interaction between strain and magnetization. These methods are restricted in their applicability to ferromagnetic materials and ferro-magnetic phases of heterogeneous materials. Since ferro-magnetic quantities are strongly influenced by all microstructural changes, magnetic residual stress measurement can only be performed in a simple way if no changes of the real state of microstructure occur. Contrary to diffraction and

ultrasonic methods, the relationship between micromagnetic quantities and residual stresses are quite complex. Residual stresses on sheets, tubes, have been performed successfully by this method and have a large capacity for automation. Usual measuring times are smaller than one second.

4.5 Measurement Techniques with Layer Removal Method

Mechanical methods are based on measurement of deflection after partial removal of stress layers by a mechanical action. One of the appropriate mechanical techniques to measure residual stresses produced by EDM is the layer removal method. It was claimed that residual stress measurement with this method has many advantages over other techniques (Crookall, 1974). In this method, stressed layers are removed successively and resulting strains or deformations are measured. Since the resulting deformations of analyzed part can be related to stresses in removed layer due to equilibrium of forces and moments, residual stresses can be determined.

One of the most appropriate machining process to remove stressed layers from an analyzed part is electro-chemical polishing since it does not add any additional stress component and it is possible to obtain a mirror like surface finish, which is highly desirable for the measurements. Parameters involved in this process are anode-cathode distance, applied potential, current, and electrolyte composition. It was expected to measure removal rate continuously, but up to this time, a feasible technique to measure sample thickness cannot be found due to harsh environmental conditions. Hence, the thickness can be measured discretely after pre-defined machining time intervals or volume of metal removed by electro-polishing can be related to the electrical charge passed. However, in this case material removal rate should be linear.

Brinksmeier et al. (1982) have suggested an experimental set up for continuous measurement of residual stresses using strain gages (Figure 4.5). But in such an arrangement it is very difficult to protect strain gages against harmful action of

electrolyte and such coatings can be strengthen the specimen. In addition, temperature of electrolyte should be carefully monitored and controlled against any possible shift effect on strain gages and material removal rate.

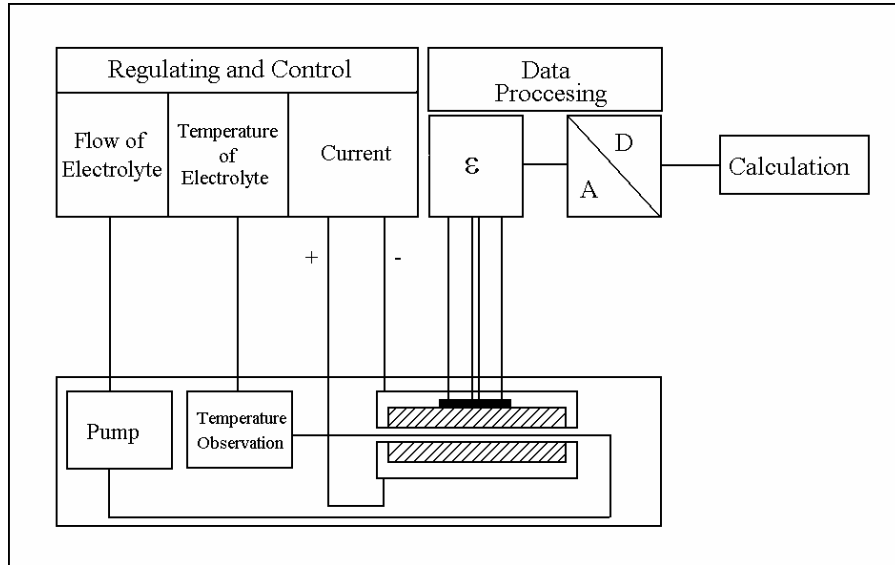


Figure 4.5 Experimental Set Up for the Deflection Method Using Strain Gages (Brinksmeier, 1982).

The derivation of residual stresses from experimental data can be found in standard elasticity work. If the principal directions of the residual stresses are known, and strain gages are used to measure principle strains, the stresses can be calculated (Figure 4.6).

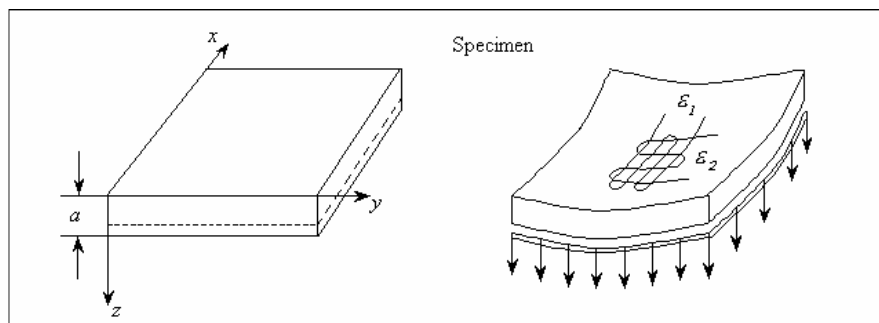


Figure 4.6 The Specimen for Deflection Method Using Strain Gages (Brinksmeier et al., 1982).

Crookall and Khor (1972) and Kruth et al. (2002) have measured deflection over the electrolyte bath by using a light arm connected to sample (Figure 4.7). The deflection of which occurs as a change of radius δR , which is related to the moment M producing it by the simple bending relationship (Figure 4.8). They used experimental calibration data for the material removal rate and claimed that the removal rate is linear with respect to time.

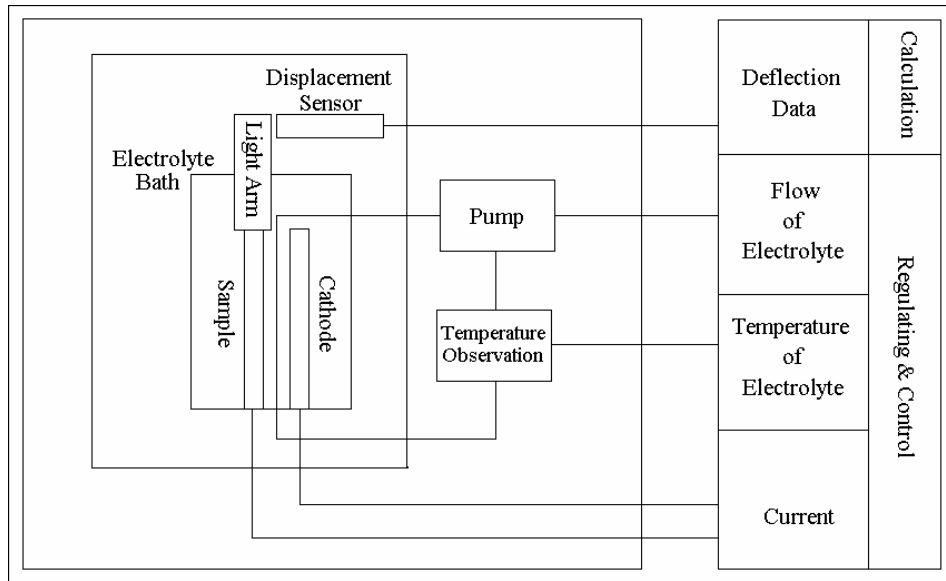


Figure 4.7 Experimental Set Up for the Deflection Method Using Displacement Sensors.

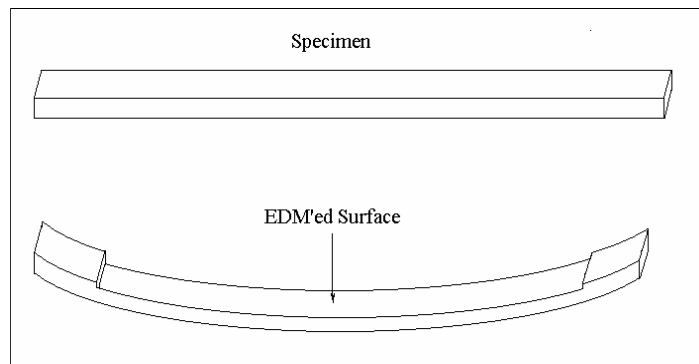


Figure 4.8 The Specimen for Deflection Method Using Displacement Sensors.

CHAPTER V

EXPERIMENTAL FACILITIES AND PROCEDURES

5.1 Introduction

The main objective of this study is to investigate residual stresses on EDM'ed surfaces and to explore the relational dependence with operational parameters. Discrete measurement of deflections after removal of layers from EDM'ed surface by electro-chemical polishing is applied for residual stress measurements. Topographical examinations are conducted with an electron microscope and an optical microscope is used to examine subsurface metallurgical changes. Affected layer hardness values are measured with a micro hardness tester and finally x-ray diffraction patterns are used to identify metallurgical phases due to EDM. This section gives a detailed description of the experimental apparatuses used and procedures applied to the resultant data.

5.2 Experimental Set Up for Residual Stress Measurement

Plastic mold steel (DIN 1.2738) samples whose dimensions are $10 \times 70 \times 2.5$ mm in width, length and thickness (Figure 5.1a) respectively are stress relieved prior to electric discharge machining to ensure stress free condition. They are heated up to $600\text{ }^{\circ}\text{C}$ for 1 hour and cooled down slowly. One of the surface is EDM'ed with a FURKAN EDM 25 industrial machine (Figure 5.2) on a rectangular working area of 10×50 mm (Figure 5.1b). The generator produced rectangular pulses at average currents of $I_{av}=1, 2, 4, 8, 16$ A and at durations $t_p=6, 12, 25, 50, 100, 200, 400, 800, 1600$ μs . After machining, a stainless steel cathode and sample anode is

fixed from its one end with a plastic holder to give a uniform gap about 2 mm where the machined surface of the anode positioned towards the cathode (Figure 5.3a). Then the holder is immersed in 5% perchloric acid, 80% ethanol and 15% distilled water mixture (Figure 5.3b). A constant current of 12 A is applied (Figure 5.4) for a short time period depending on the EDM conditions of the sample. Circulation of electrolyte is maintained during the removal process to stabilize bath temperature by a magnet pump (Figure 5.3a). Room and electrolyte bath temperatures together with the applied voltage are monitored and recorded to a computer via HP 34970A data acquisition unit (Figure 5.4). Finally, sample is removed from the electrolytic bath (Figure 5.3b) to measure its thickness and deflection. A special unit is designed (Figure 5.5a) for this purpose and equipped with an interface for data acquisition. In this unit, two 1/1000 mm digital dial indicators and one digital caliper are fixed on a precision cross table (Figure 5.5b) with an appropriate sample handler. 45 measurements are taken from midline of the sample. Electro chemical machining and measurements on analyzed sample are repeated up to the unaffected deflection depth is reached. Schematic illustration of the set up for layer removal is shown in Figure 5.6.

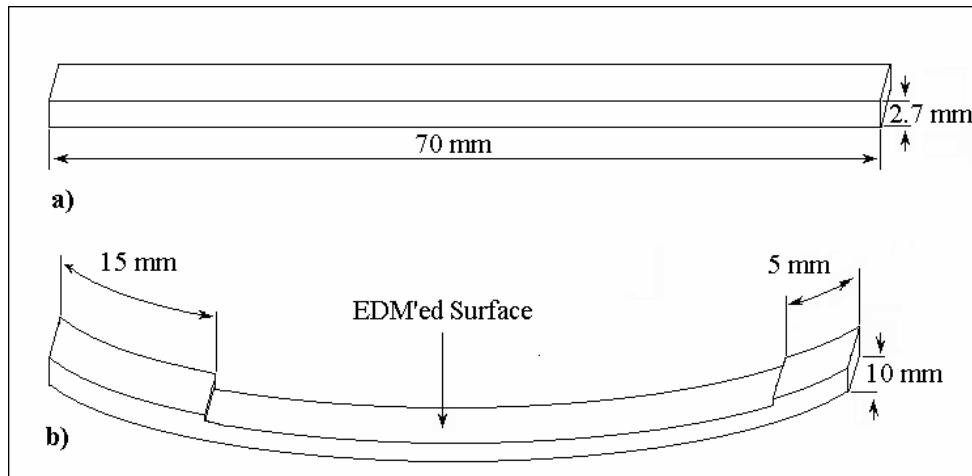
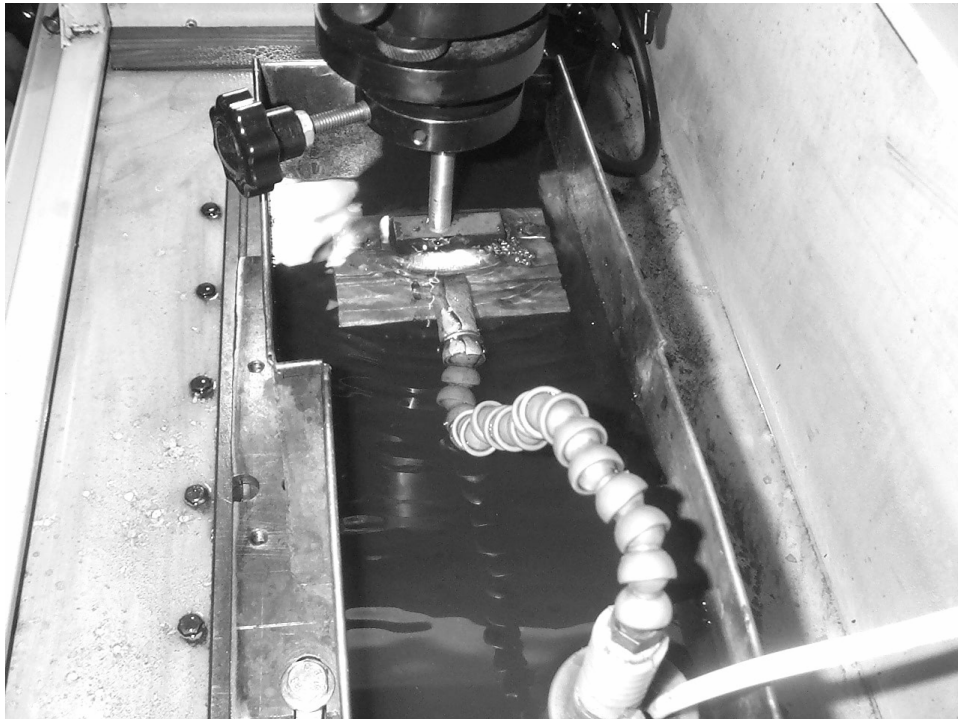


Figure 5.1 Samples a) Before b) After EDM.

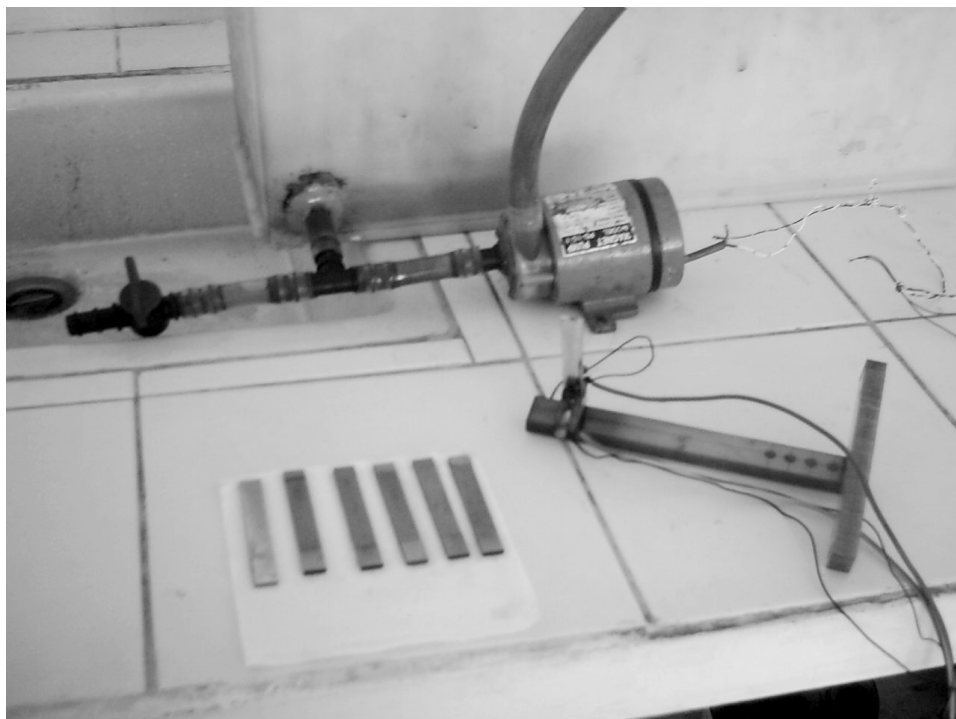


a)

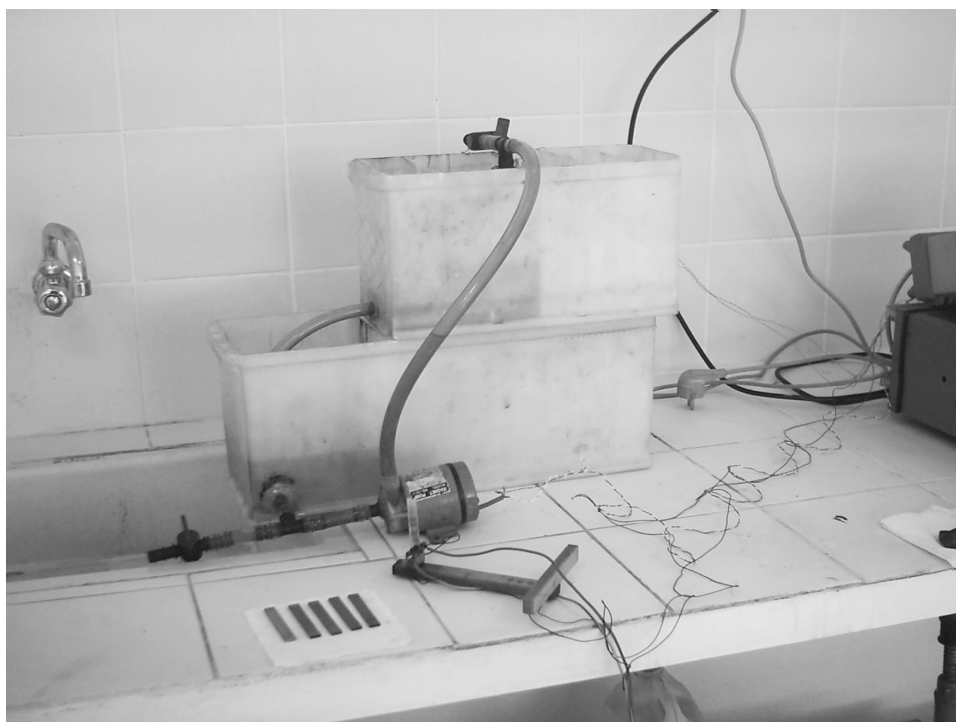


b)

Figure 5.2 a) FURKAN EDM 25 Industrial Machine b) A View During Machining.



a)



b)

Figure 5.3 a) Magnetic Pump, Sample Holder and Samples b) Electrolytic Bath.

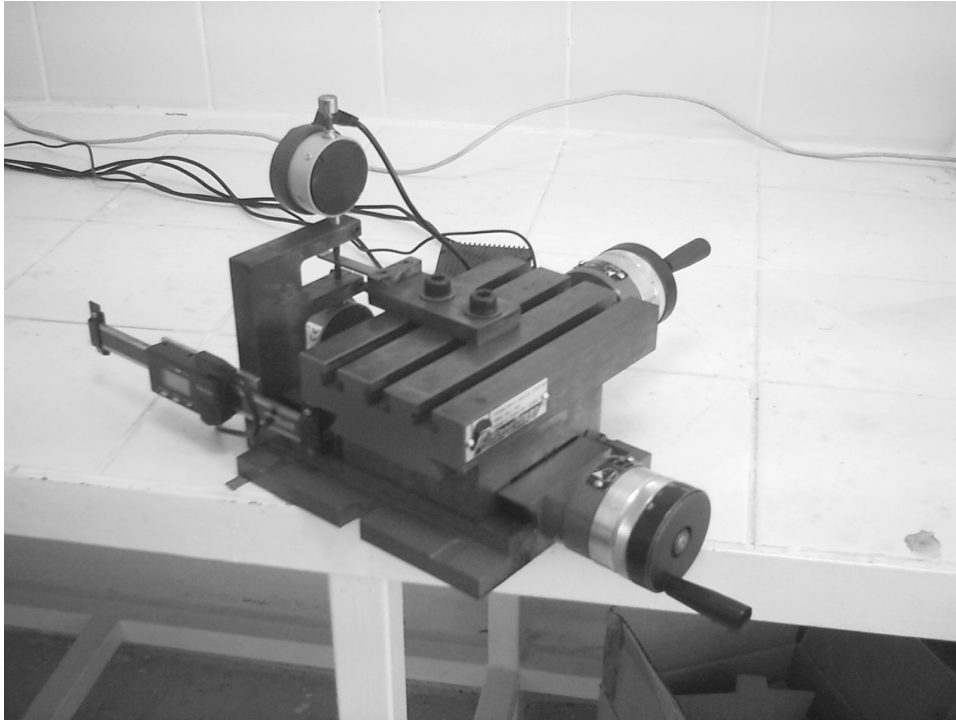


a)



b)

Figure 5.4 a) Power Supply and Data Acquisition b) Computer.



a)



b)

Figure 5.5 a) Measurement Unit b) Dial Indicators on the Unit.

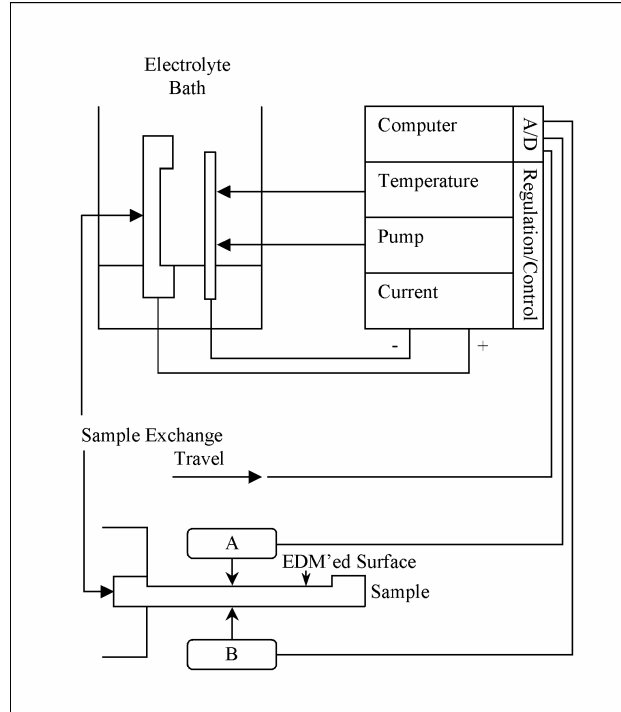


Figure 5.6 Schematic Representation of Experimental Set-Up.

5.2.1 Electro Polishing Behavior

The electro-polishing behavior of the specimen material is investigated experimentally (Figure 5.7). Up to voltage V_1 a matt surface is produced, but in the region $V_1 - V_3$ current density changed little with voltage and a better electro polished surface is obtained. A mirror like surface finish is obtained under high current settings beyond V_3 .

5.2.2 Accuracy and Precision

The thickness of a non-machined sample is measured 12 times with the designed equipment to figure out the measurement errors. Total error due to sample misalignment and dial indicators measurement deviation is found to be $\pm 3\mu\text{m}$ for point measurements (Figure 5.8). The average thickness values obtained after one scan from the midline of the specimen revealed less than $\pm 1\mu\text{m}$ span of error (Table 5.1) with respect to the first scan.

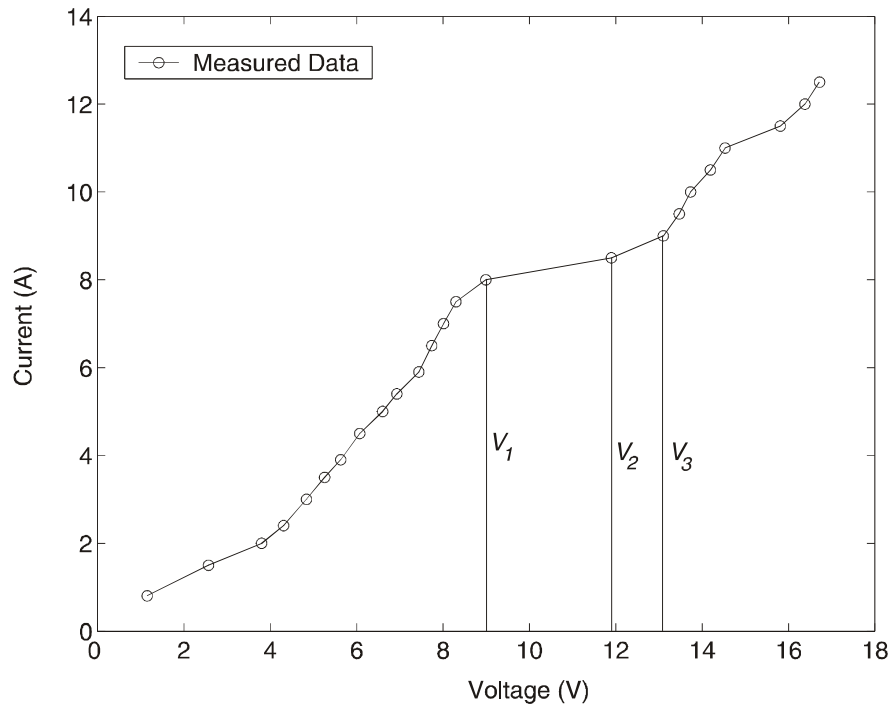


Figure 5.7 Conditions for the Electro Polishing of Plastic Mold Steel Using Perchloric Acid Based Electrolyte.

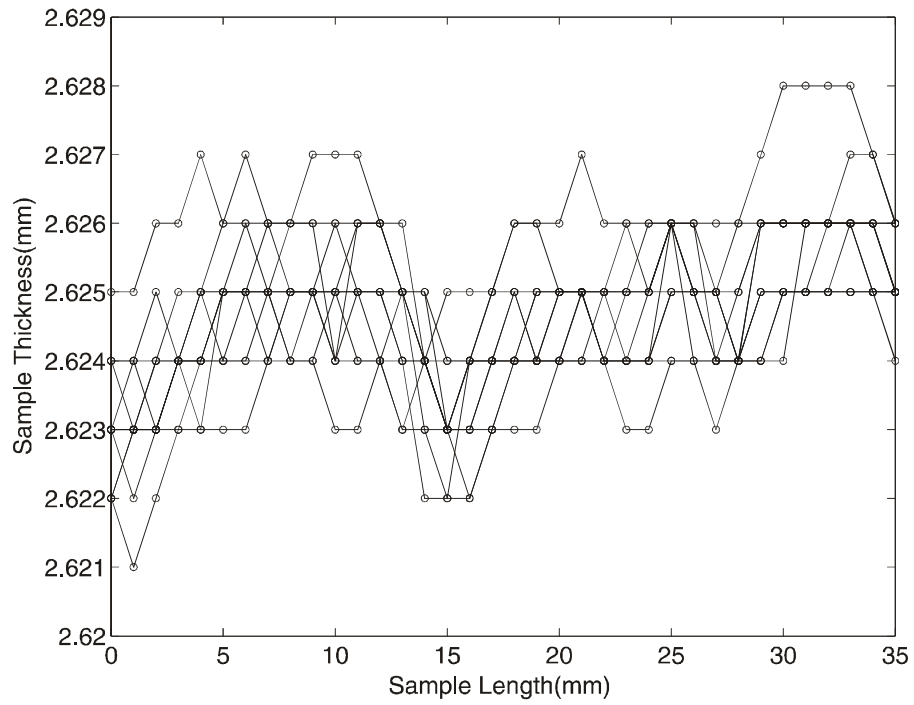


Figure 5.8 Measurement Deviation of the Measurement Unit.

Table 5.1 Average Measured Thickness and Deviation

No	Average Thickness (μm)	Deviation (μm)
1	2623	0,000
2	2624	0,422
3	2624	0,089
4	2624	0,467
5	2623	0,467
6	2624	0,489
7	2623	0,089
8	2624	0,911
9	2624	0,667
10	2624	0,600
11	2624	0,178
12	2624	0,444

5.3 Apparatuses for Topographical and Metallurgical Examinations

Topographic examinations is performed with a JEOL JSM-5600 scanning electron microscope (Figure 5.9). Samples are prepared using conventional metallographic techniques on both radial and tangential sections, in which thermally affected layers can be observed normally, and tangentially to magnify adjacent heat affected zones. These observations are performed on Olympus model metallographic microscope (Figure 5.10). Microstructural sections are etched with nital reagent in order to reveal thermally effected zones. Microhardness depth profile measurements are made on a Future-Tech FM-700 hardness tester (Figure 5.11) using a Vickers indenter with a load of 10 g and an indentation time of 15 s. X-ray diffraction patterns are obtained with a SHIMADZU XRD-6000. Data are collected using Cu-K α radiation ($\lambda=1.5405$) in the range on $10 \leq 2\theta \leq 120$. The phases are identified from searches in the JPDS (International Center for Diffraction Data) databases.

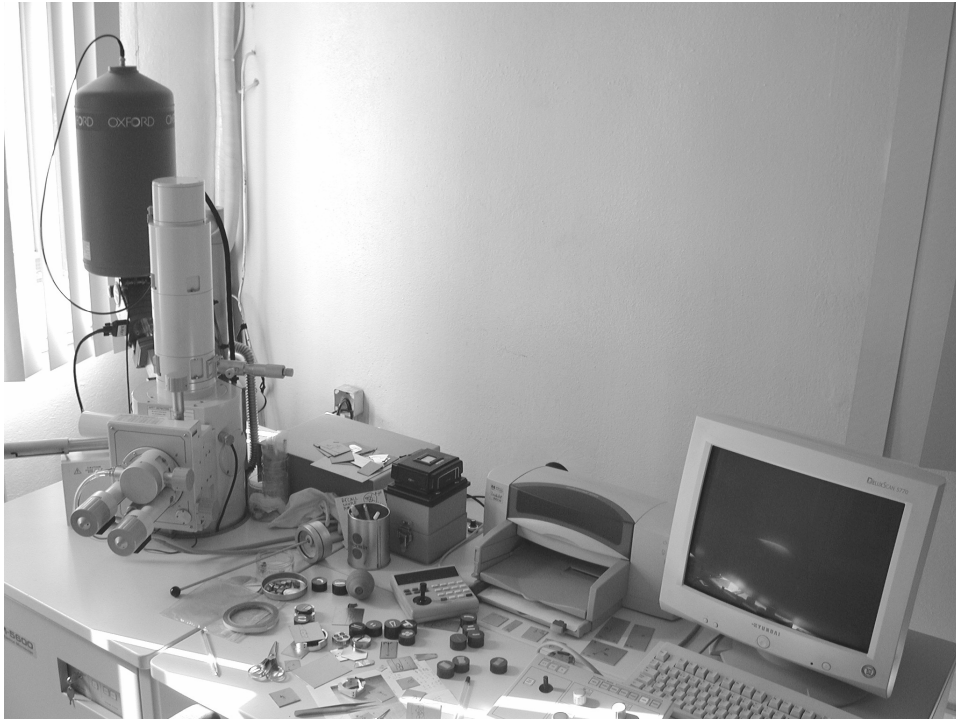


Figure 5.9 JEOL JSM-5600 Scanning Electron Microscope.

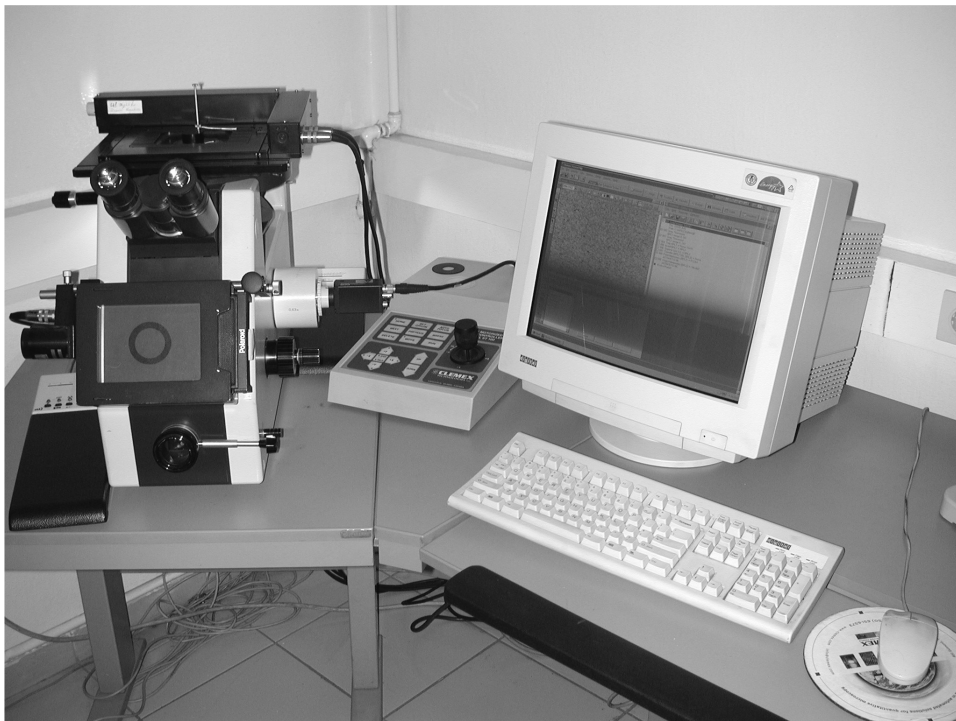


Figure 5.10 Olympus Metallographic Microscope.



Figure 5.11 Future-Tech FM-700 Micro Hardness Tester.

5.4 Apparatuses for Electrical Discharge Texturing

Temper mill work roll (3%Cr forged steel) used in this study is produced with electro-slag re-melted and forged and finally double induction hardened up to 30mm with 86 ShC (HV). The mill roll is textured with a Roltex-Sarclad Ltd. industrial type EDT machine shown in Figure (5.12). Three different textured bands on the same roll are produced under analyzed operation parameters. Surface roughness is measured on site using a portable Mahr Perthometer M2 (cut-off length of 2.5 mm and peak count setting level of 0.5 μm). Samples of the bands are cut from the roll by using a cutting saw. A precision cut-off disc (Struers Accutom-2 Precision Saw) is used to extract small specimens for further examinations. Sub-zero treatment of textured samples is performed in liquid nitrogen to explore any occurrence of retained austenite within thermally effected layers.

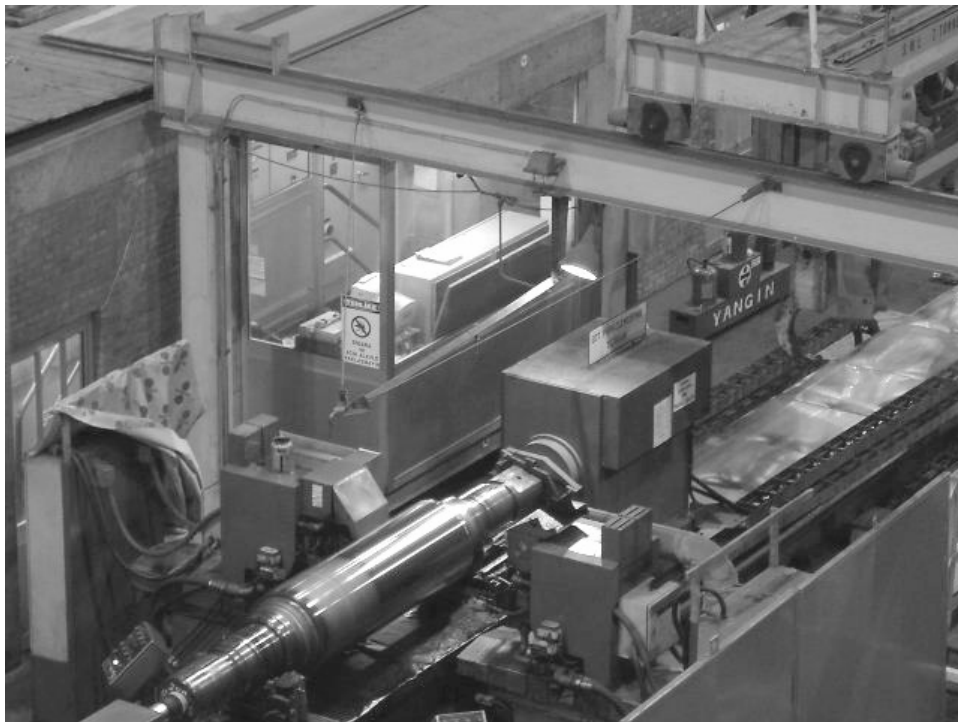


Figure 5.12 Roltex-Sarclad Ltd. Industrial Type EDT Machine.

CHAPTER VI

TOPOGRAPHICAL AND METALLURGICAL PROPERTIES OF EDM'ED SURFACES

6.1 Introduction

In this section, metallurgical and topographical properties of EDM'ed surfaces are presented. Scanning electron microscope is used to demonstrate topographical features of machined surfaces. Thermally affected layers are illustrated by using optical microscope. Hardness values of these layers are measured with a microhardness tester and metallurgical phases are analyzed with an x-ray diffractometer.

6.2 Materials

Micro alloyed (X60/API 5L) and plastic mold steel samples (DIN 1.2738) are machined with a RAM type EDM for different energy levels and pulse time. Commercial kerosene and de-ionized water is used as dielectric liquid. Copper and graphite are selected as the tool electrode. Temper mill work roll (3%Cr Forged Steel) surface is textured with an EDT machine, which is used on continuous hot-dip galvanizing line at Ereğli Iron and Steel Works Co. The electrode material used is high phosphorus braze, dielectric liquid is, ESSO Somentor 43. Chemical compositions of sample material are given in Table (6.1).

6.3 Surface Topography

The high temperature gradients within spark incident area and a violent explosive removal process results with randomly overlapped craters on the EDT'ed surface.

Table 6.1 Chemical Compositions of Workpiece Materials (wt.%).

Material	C	Cr	Cu	Mn	Mo	Nb	Ni	Si
Micro Alloy Steel	0,09	0,024	0,018	1,48	0,04	0,048	-	0,33
Plastic Mold Steel	0,38	2.0	-	1.5	0.2	-	1.1	0,30
Mill Roll Steel	0.86	3.42	-	0.50	0.31	-	0.18	0.56

The depth and diameters of the craters produced after sparking varies with respect to released energy, which can be described as the product of applied potential, current and pulse time. Figures (6.1-6.8) illustrate SEM photographs of EDM'ed plastic mold steel surfaces obtained under several operational conditions (Table 6.2). All the samples are machined under positive polarity. The photographs are placed to represent decreased pulse time settings from top to bottom. First columns in these figures show samples machined in kerosene and the other in de-ionized water as dielectric liquid.

Table 6.2 EDM Test Parameters for Plastic Mold Steel Samples

Pulse Time (μ s)	1600	800	400	200	100	50	25	8
Average Current (A)	16				8			
Dielectric Liquid	Commercial kerosene				De-ionized water			
Tool Electrode	Graphite				Copper			

Globules of debris and chimneys formed by entrapped gases escaping from the re-deposited material are found as essential features for all EDM'ed samples. Evidently the surface is frozen, virtually instantaneously, when the discharge ceases. The shapes of the pockmarks, and particularly their rims, are indicative of their sudden and simultaneous rupture, coinciding with the sharp decrease in pressure as the discharge cut off as stated before (Crookall and Khor, 1972). Increase in pulse duration produces larger crater sizes (Figure 6.1-6.8). Decrease

in average pulse current generates shallow craters (Figure 6.5, 6.6) where its diameters are slightly less than that of the high current setting (Figure 6.1, 6.2). Unstable operational conditions are observed at high pulse durations when water is used as dielectric liquid. Machining became stable at pulse durations lower than 400 μ s when average pulse current is equal to 16A. When 8A pulse current applied, stable machining conditions are reached at pulse durations lower than 200 μ s. The affect of unstable machining condition can be visualized as deep cavities presumably due to electric arcs (Figure 6.1, 6.3, 6.5, 6.7). However, an extensive change in surface topography is not essential if graphite is used as tool electrode (Figure 6.1, 6.2, 6.6, 6.8). A considerable decrease in number of appendages due to bulk boiling is observed when copper is used as tool electrode (Figure 6.4, 6.8).

Long pulse duration dramatically increase the amount of surface damage. Cracking is observed on the sample, which is machined at 1600 μ s pulse duration and 16A pulse current and using kerosene as dielectric liquid. The number of cracks decreased significantly at 800 μ s pulse duration (Figure 6.1). In spite of this, at pulse current of 8A and pulse duration of 1600 μ s indicates a dramatic increase in number of cracks. Moreover it increases much more at pulse duration of 800 μ s (Figure 6.5). General topographical features of EDM'ed micro alloy steel surfaces are found analogous with the findings stated above.

The affects of EDT operating parameters on surface topography of textured temper mill rolls are also analyzed experimentally. Three different textured bands on same roll are produced under analyzed operation parameters (Table 6.3) with same roll surface speed of 8 mm/min and axial feed rate of 30 mm/min. Operation parameters are selected as to give maximum and minimum practical peak count and average roughness respectively. These parameters are taken from the previous practical values.

Table 6.3 EDT Test Parameters and Roughness

Zone	Pulse Time (μs)	Average Current (A)	Ra (μm)	Pc (μm)
A	12	15	1,91	110
B	17	28	3,69	82
C	45	15	4,08	67

SEM photographs obtained under the given operational conditions are illustrated in Figure 6.9. Increase in energy level produces larger crater dimension that leads to increased average surface roughness, but decreased peak counts on the textured roll surface (Table 6.3). This can be explained as the lower number of rims that surround craters within unit length in high energy levels. It is possible to come with un-machined local areas at low energy levels. The straight lines represent the residuals from the previous grinded roll surface (Figure 6.9a,b). Cracks are visible at randomly spaced locations at high energy levels (Figure 6.9e,f). This is the indication of highly stressed layers due to thermal loading.

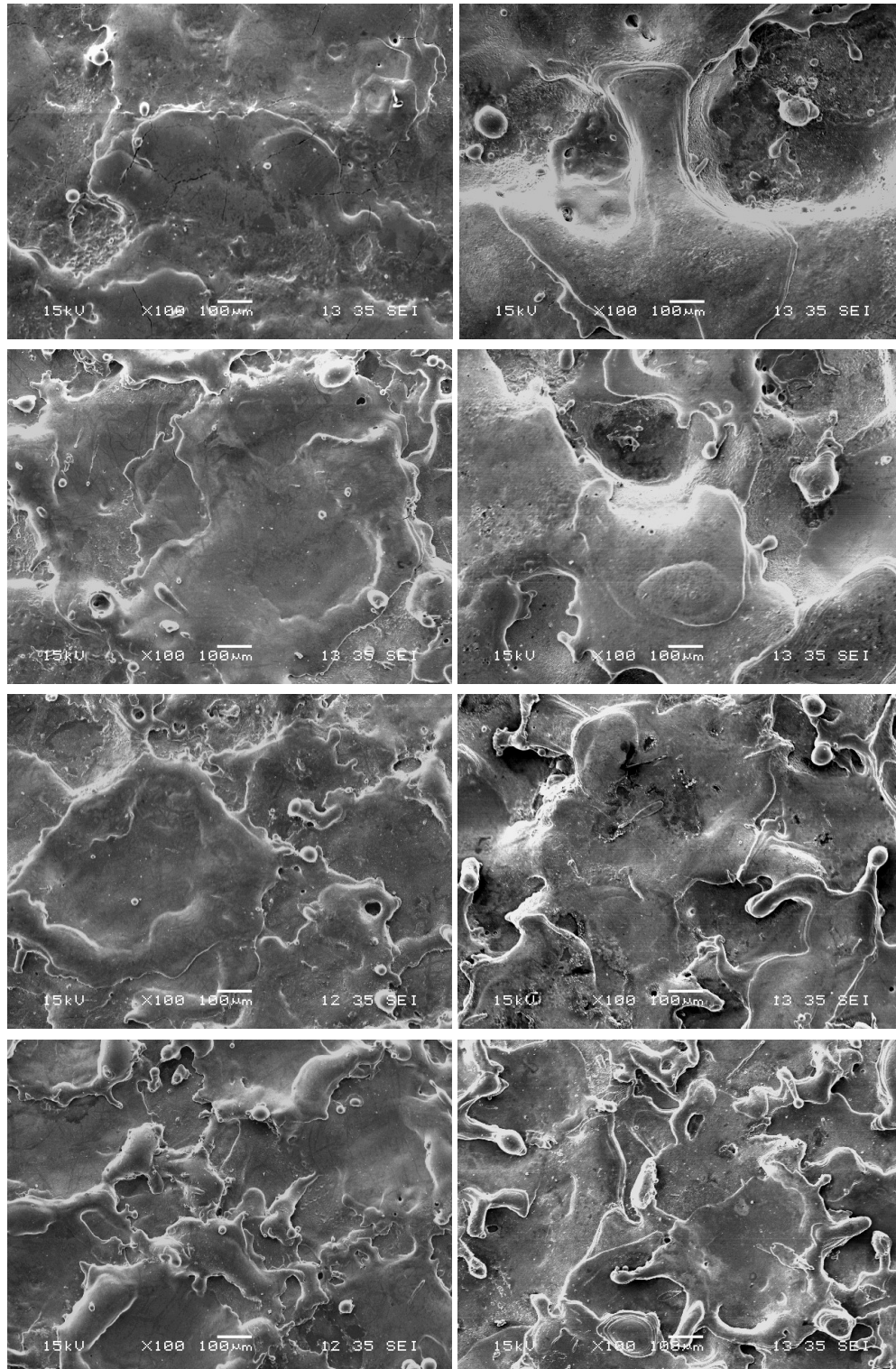
6.4 Thermally Influenced Layers

Thermally affected layers are generated in subsurface when producing surfaces with EDM. Figures from 6.10 to 6.17 show cross sectional views of EDM'ed plastic mold steel samples. In all operational cases (Table 6.2) white layer thickness is found highest at the longest pulse duration of 1600 μs . Variation in white layer thickness with respect to pulse duration seems to follow one term power functional tend for all cases. Overlapped crater bases and their rims can be distinguished with thicker white layer formations at rims and thinner at bases. Dielectric liquid and tool electrode used during machining are found to be effective on piled white layer formation at crater rims. Such a formation is evident when graphite is used as tool electrode and kerosene as dielectric liquid (Figure 6.10, 6.14). A slight decrease in this formation can be deduced when copper is used as tool electrode (Figure 6.10, 6.12, 6.14, 6.16). A recognizable decrease is evident when water is used as dielectric liquid (Figure 6.11, 6.13, 6.15, 6.17). Lowest amount of unevenness of white layer is found especially when copper is used as tool electrode (Figure 6.13, 6.17).

Extraordinary surface defects are found on samples machined by using graphite electrode in water dielectric at 1600 and 800 μ s pulse duration with 8A pulse current (Figure 6.15). These parameters match with the unstable operating conditions as stated earlier. In this case, cracks penetrating into core of the material are apparent. Except this, no crack formation is observed when water is used as dielectric liquid (Figure 6.11, 6.13, 6.15, 6.17). High crack densities are evident at high pulse durations in kerosene dielectric liquid (Figure 6.10, 6.12, 6.14, 6.16).

A non-melted but heat affected zone due to high thermal gradients is found beneath the white layer. In most cases a dark heat affected intermediate layer is visible. This layer is found much more thinner than the white layer. Micro alloy steel samples are found to have thicker dark affected layer (Figure 6.18). In this case, thickness of this layer is comparable with white layer thickness. Structural changes within white layer are also seems more complicated than in plastic mold steel presumably due to presence of micro alloyed elements in the samples. Similar findings are also evident on EDT'ed mill roll surfaces (Figure 6.19).

Appearances of affected layers in cross sectional views are related to their appearances in tangential section of EDT surfaces (Figure 6.20). The first layer in heat-affected zone is considered as composed from a hard untempered martensite (UTM) followed with a dark layer described as overtempered martensite (OTM). Surface bands of A, B and C (Table 6.3) shows a clear decrease in affected-layer thickness (Figure 6.21). Circular appearance of the dark layer can be visualized clearly in this perspective.

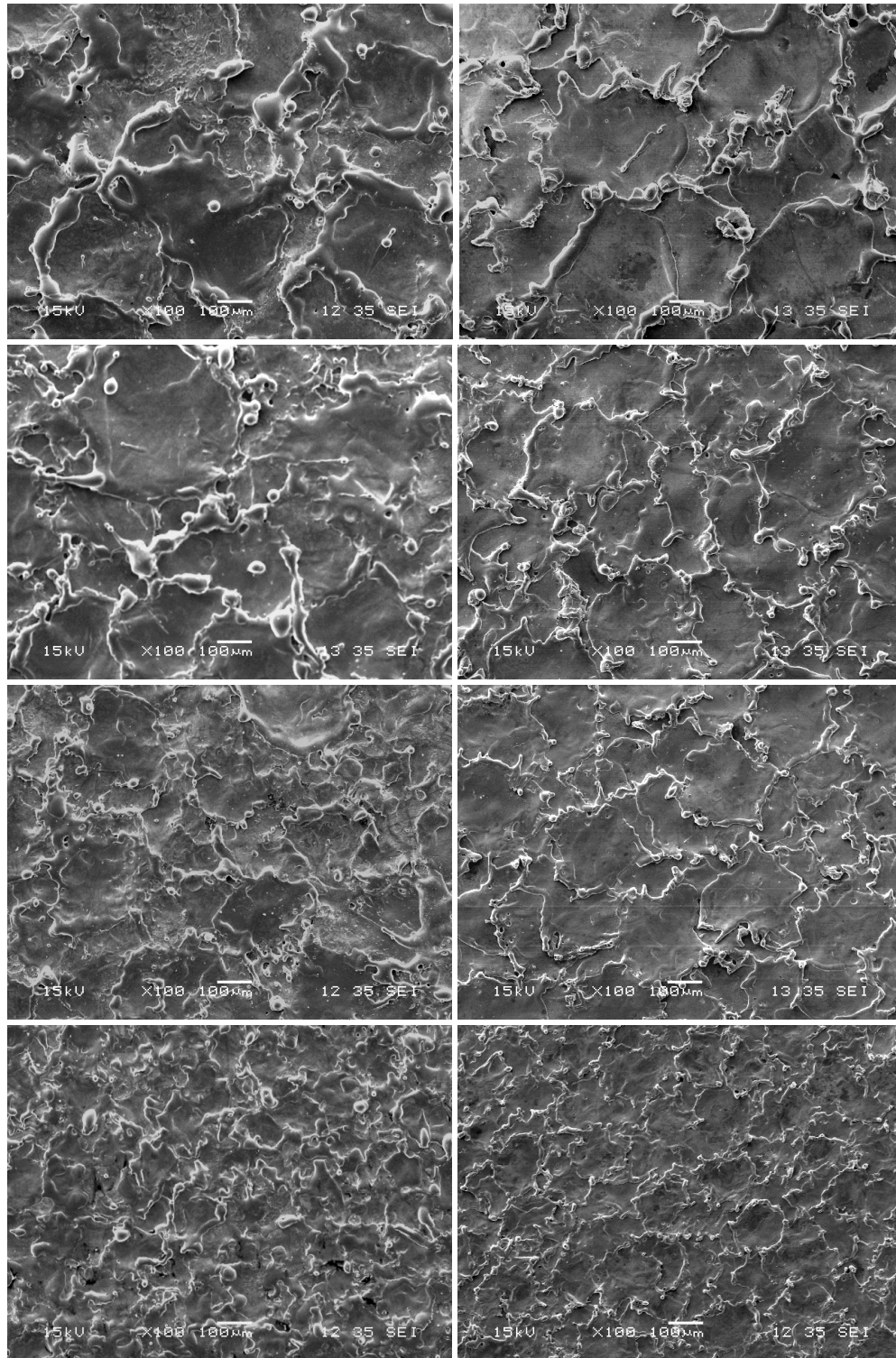


Dielectric Liquid: Kerosene

Dielectric Liquid: De-ionized Water

$t_p=1600, 800, 400$ and $200 \mu s$ from top to bottom for each row respectively

Figure 6.1 SEM Pictures of EDM'd Surfaces: $I_{av}=16A$, Electrode: Graphite, Material: Plastic Mold Steel.

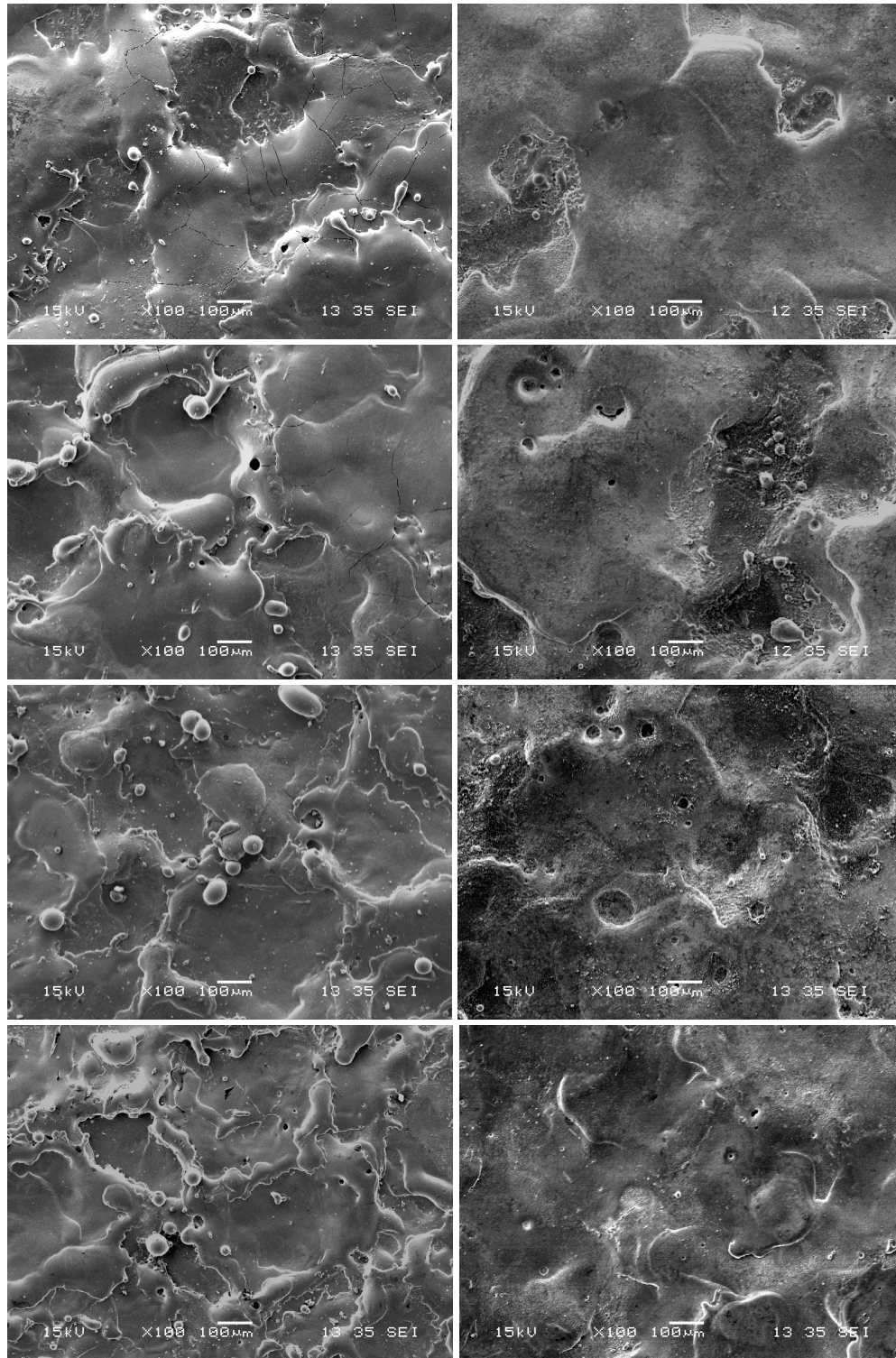


Dielectric Liquid: Kerosene

Dielectric Liquid: De-ionized Water

$t_p=100, 50, 25$ and $8 \mu\text{s}$ from top to bottom for each row respectively

Figure 6.2 SEM Pictures of EDM'd Surfaces: $I_{av}=16\text{A}$, Electrode: Graphite, Material: Plastic Mold Steel.

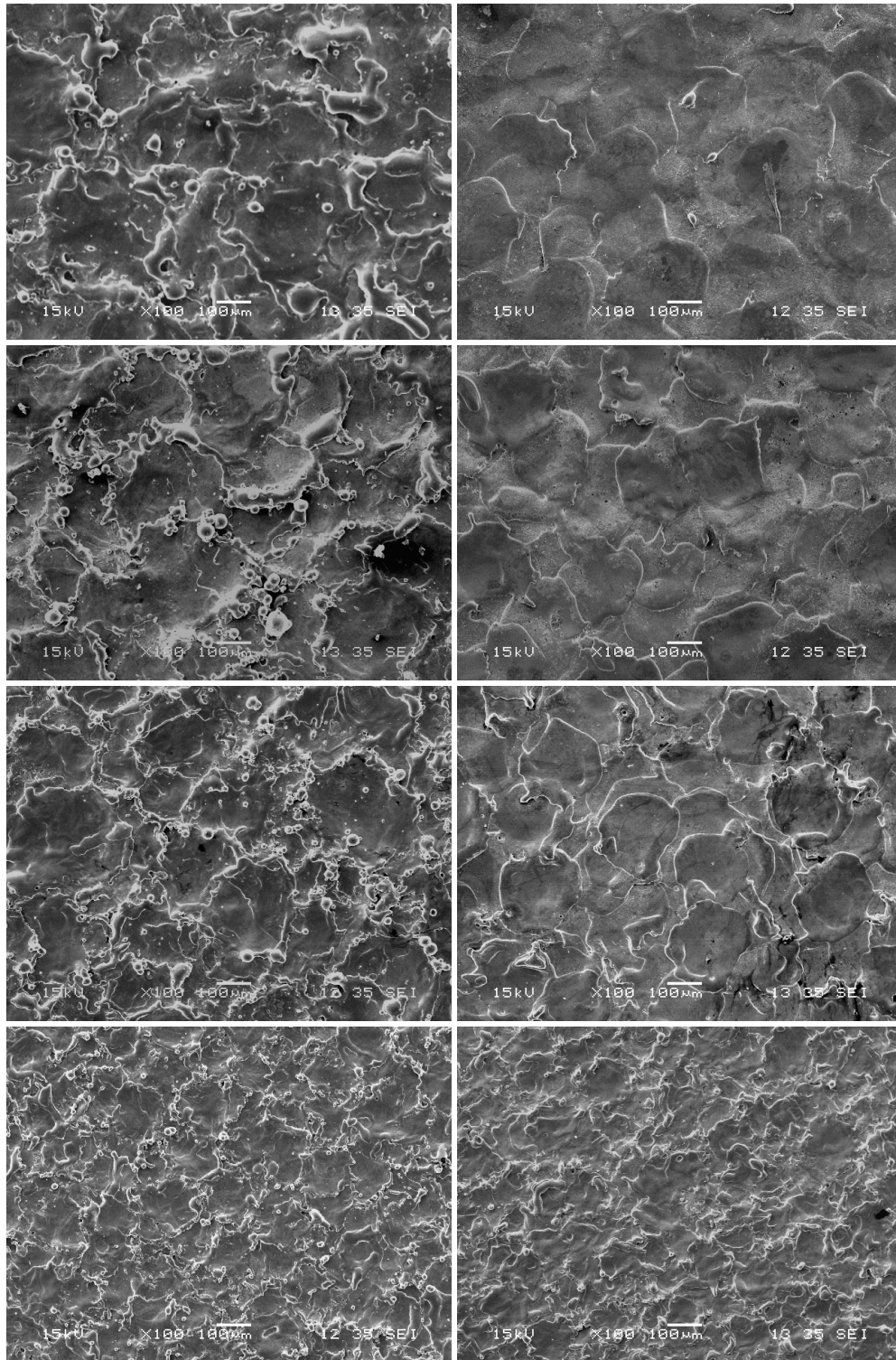


Dielectric Liquid: Kerosene

Dielectric Liquid: De-ionized Water

$t_p=1600, 800, 400$ and $200 \mu s$ from top to bottom for each row respectively

Figure 6.3 SEM Pictures of EDM'ed Surfaces: $I_{av}=16A$, Electrode: Copper, Material: Plastic Mold Steel.

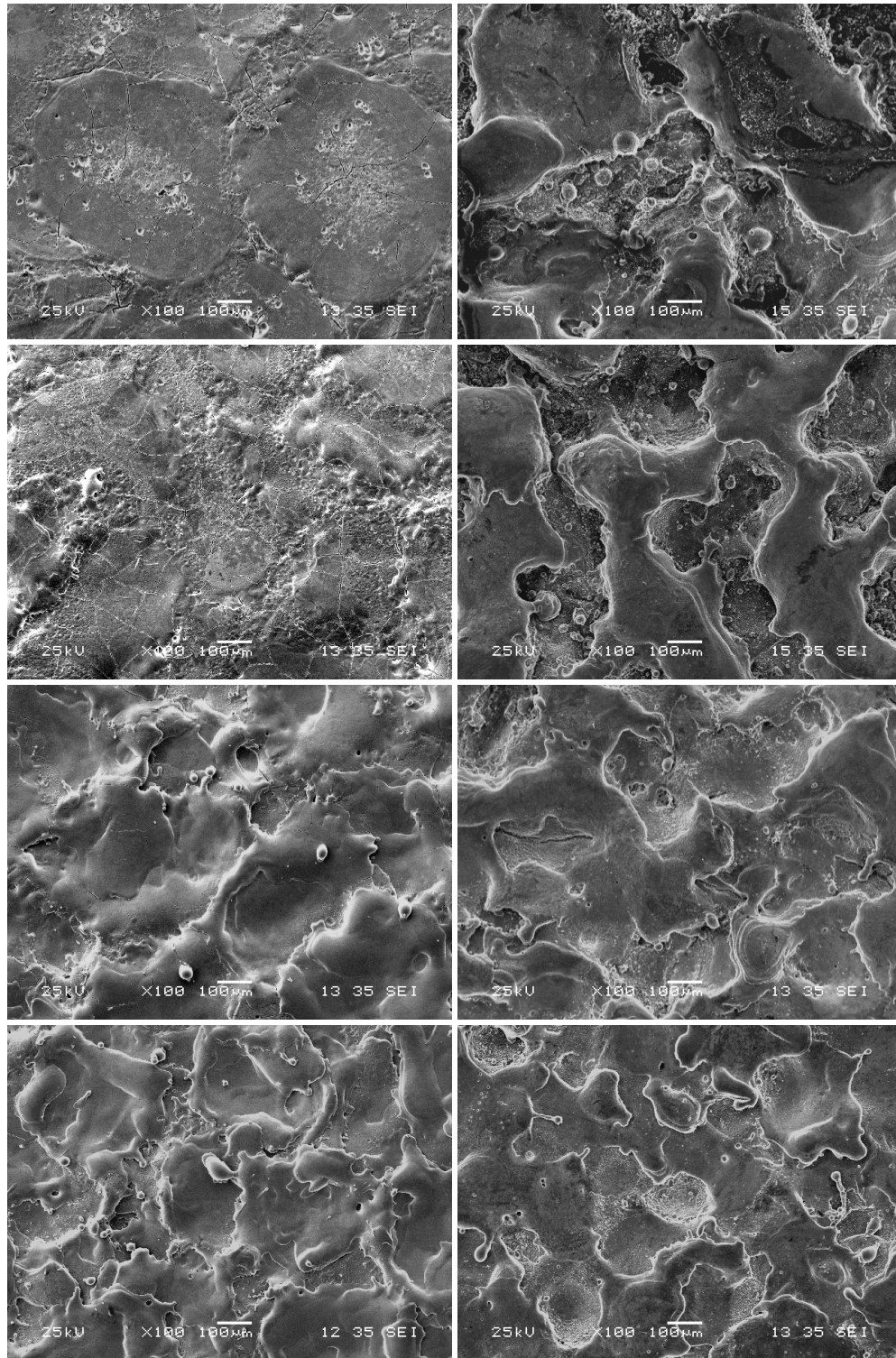


Dielectric Liquid: Kerosene

Dielectric Liquid: De-ionized Water

$t_p=100, 50, 25$ and $8 \mu\text{s}$ from top to bottom for each row respectively

Figure 6.4 SEM Pictures of EDM'd Surfaces: $I_{av}=16\text{A}$, Electrode: Copper, Material: Plastic Mold Steel.

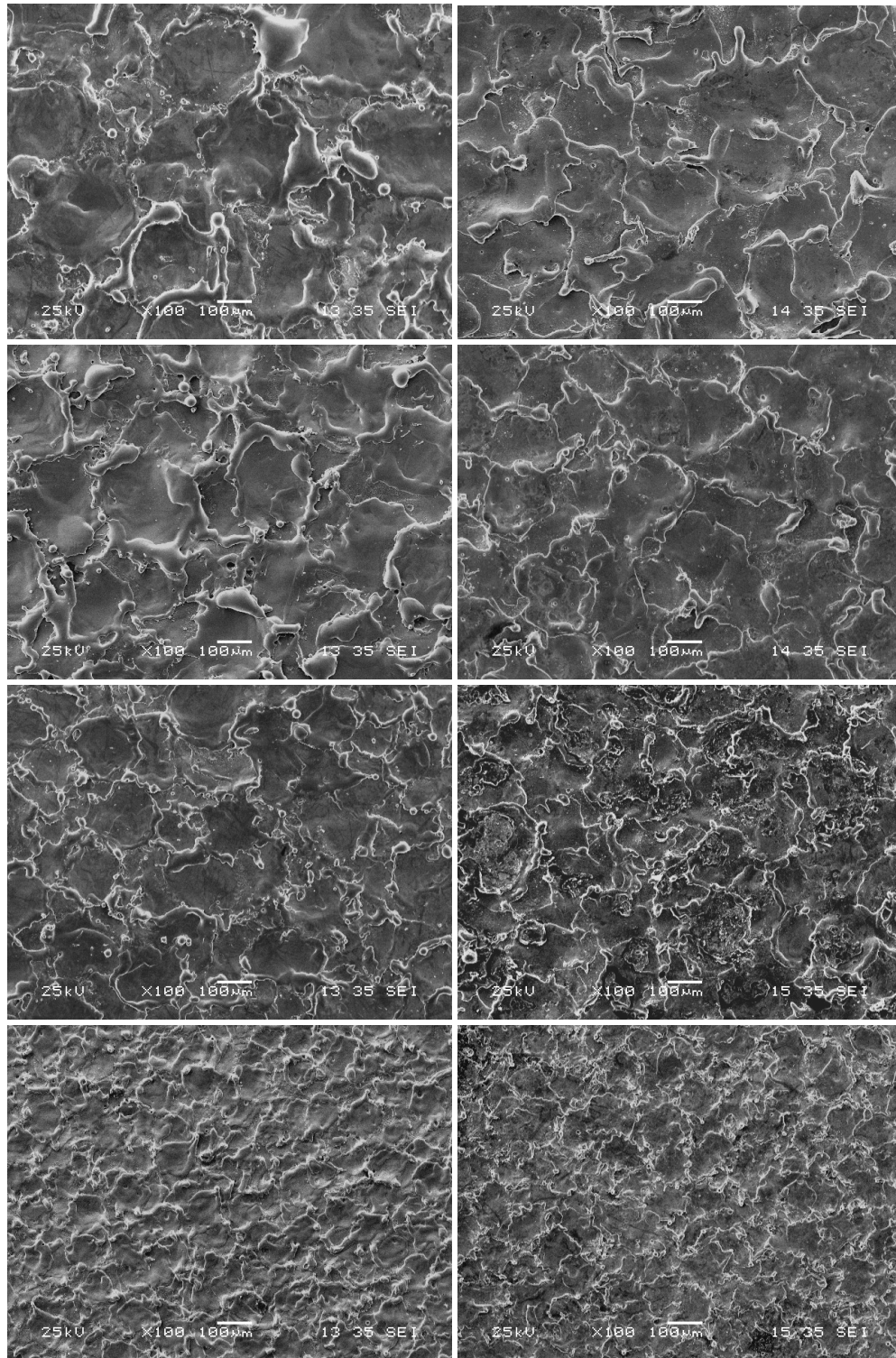


Dielectric Liquid: Kerosene

Dielectric Liquid: De-ionized Water

$t_p=1600,800,400$ and $200 \mu s$ from top to bottom for each row respectively

Figure 6.5 SEM Pictures of EDM'ed Surfaces: $I_{av}=8A$, Electrode: Graphite, Material: Plastic Mold Steel.

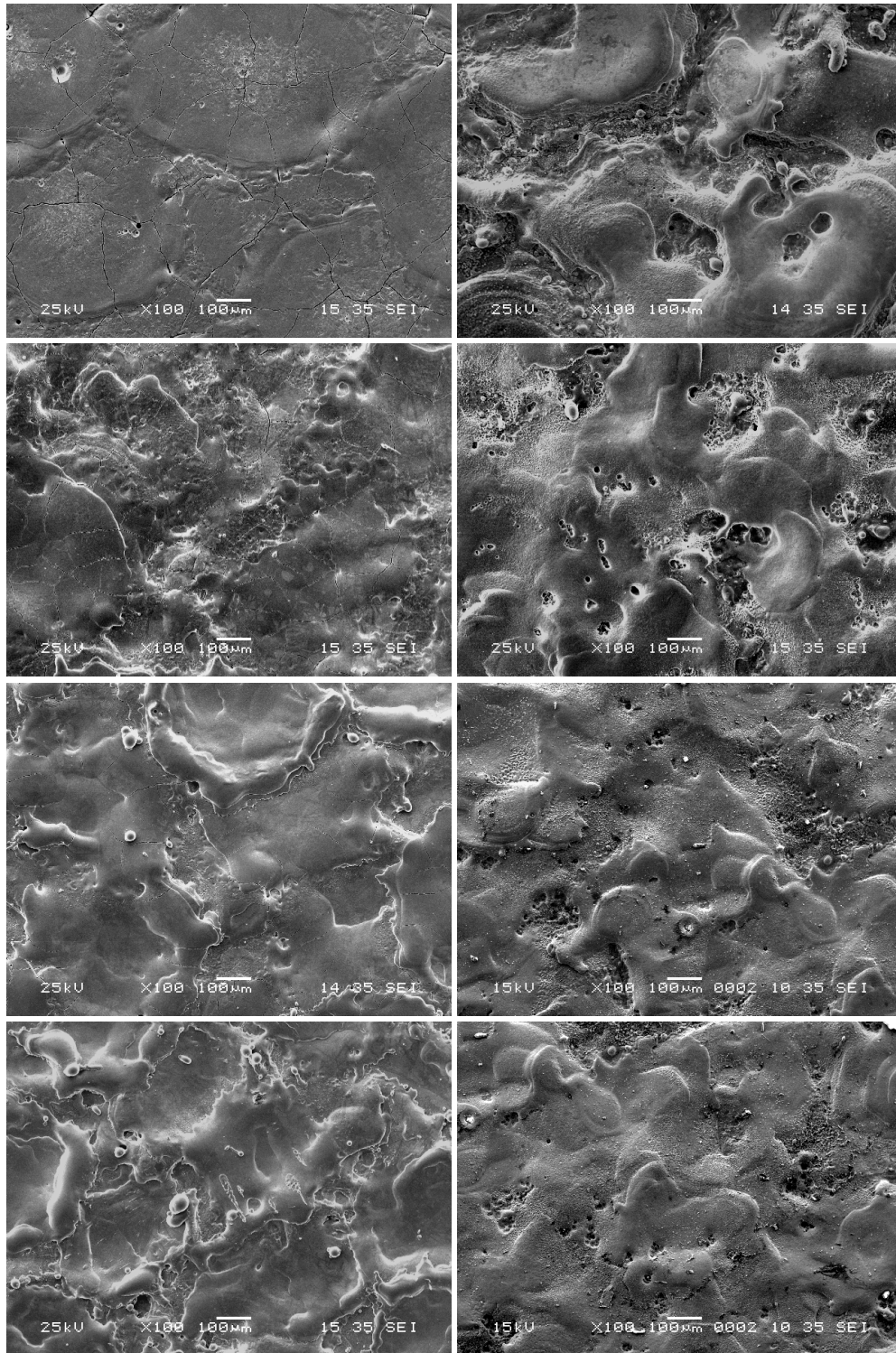


Dielectric Liquid: Kerosene

Dielectric Liquid: De-ionized Water

$t_p=100, 50, 25$ and $8 \mu\text{s}$ from top to bottom for each row respectively

Figure 6.6 SEM Pictures of EDM'ed Surfaces: $I_{av}=8\text{A}$, Electrode: Graphite, Material: Plastic Mold Steel.

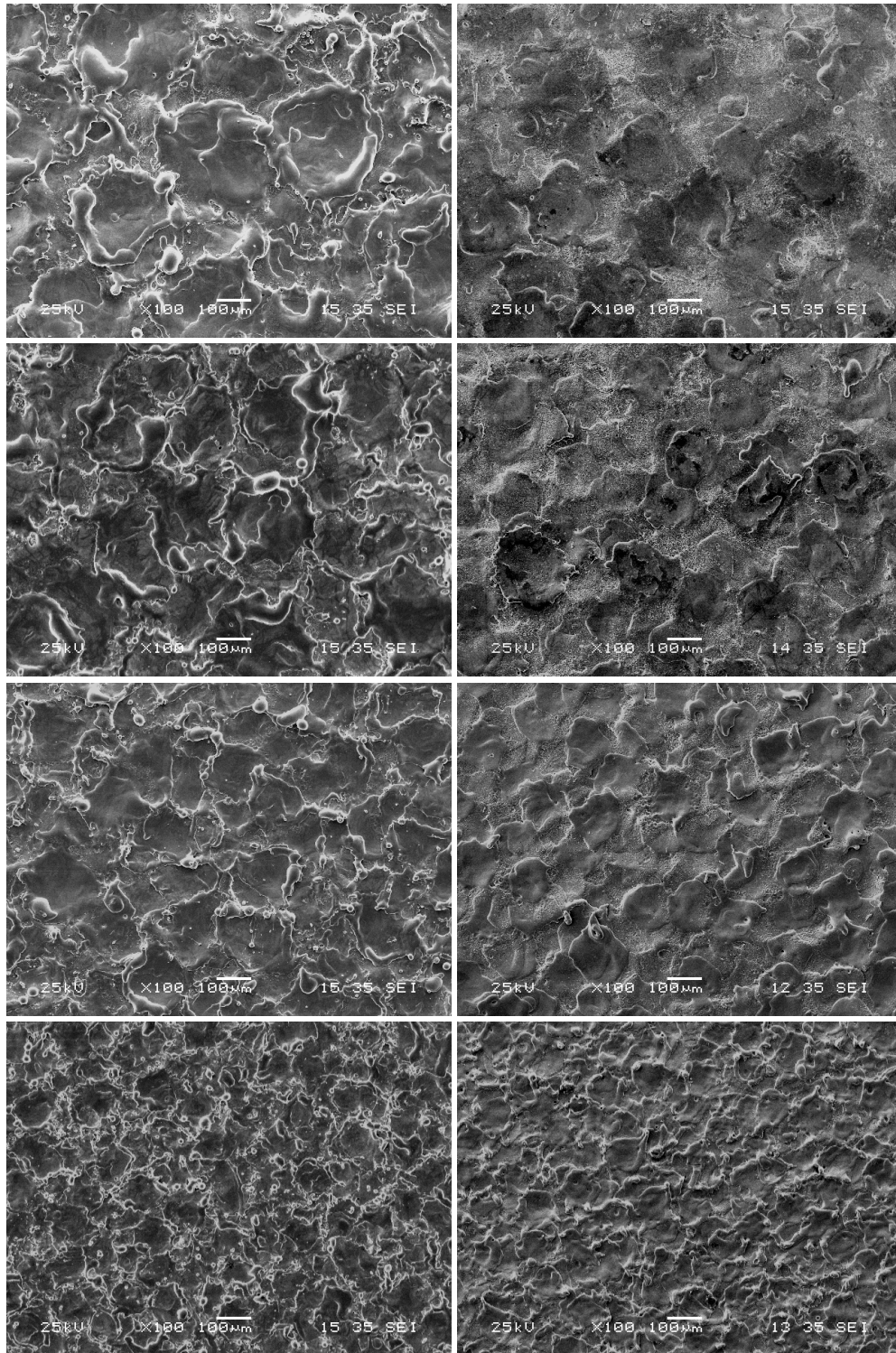


Dielectric Liquid: Kerosene

Dielectric Liquid: De-ionized Water

$t_p=1600,800,400$ and $200 \mu s$ from top to bottom for each row respectively

Figure 6.7 SEM Pictures of EDM'd Surfaces: $I_{av}=8A$, Electrode: Copper, Material: Plastic Mold Steel.



Dielectric Liquid: Kerosene

Dielectric Liquid: De-ionized Water

$t_p=100, 50, 25$ and $8 \mu s$ from top to bottom for each row respectively

Figure 6.8 SEM Pictures of EDM'd Surfaces: $I_{av}=8A$, Electrode: Copper, Material: Plastic Mold Steel.

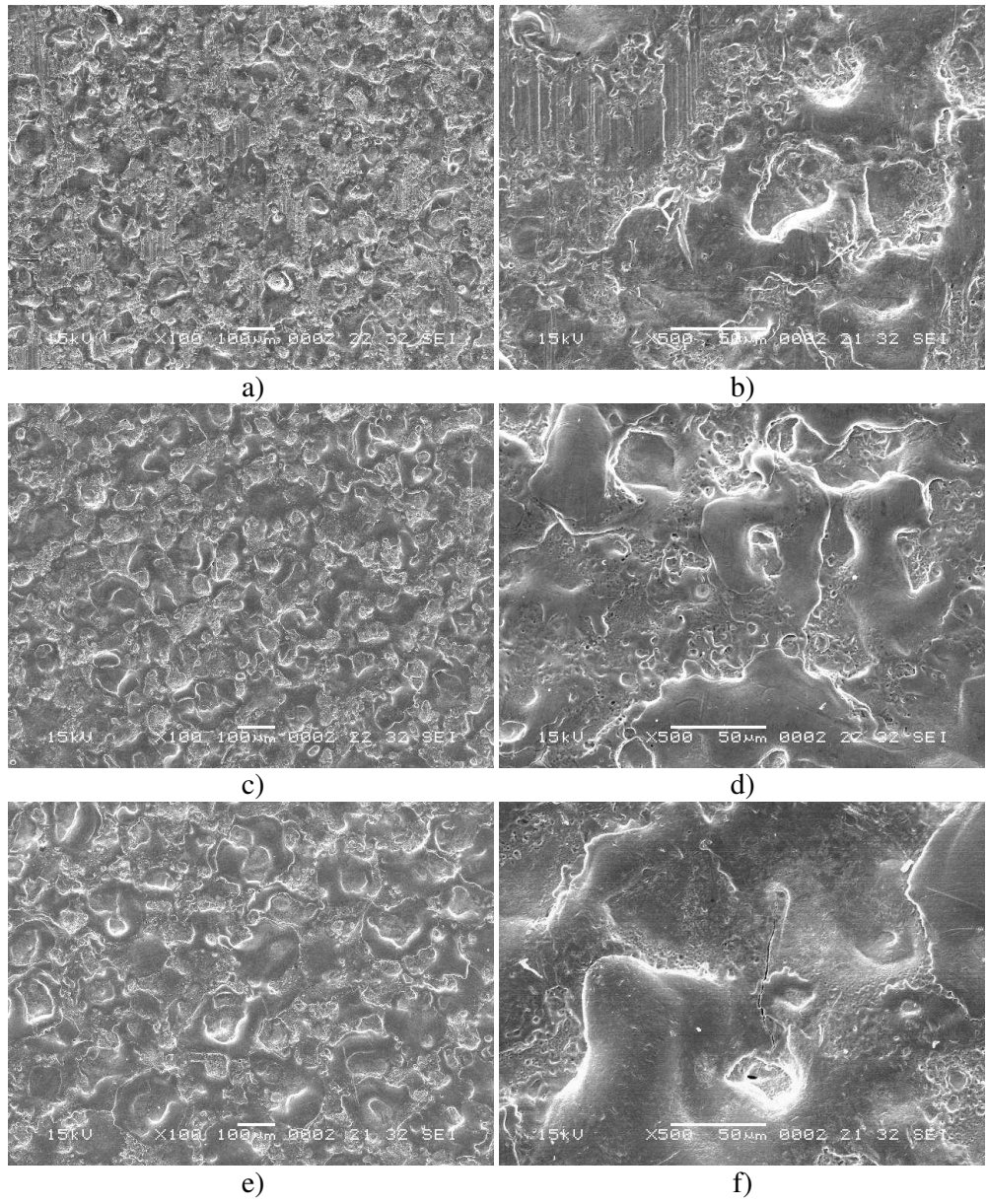
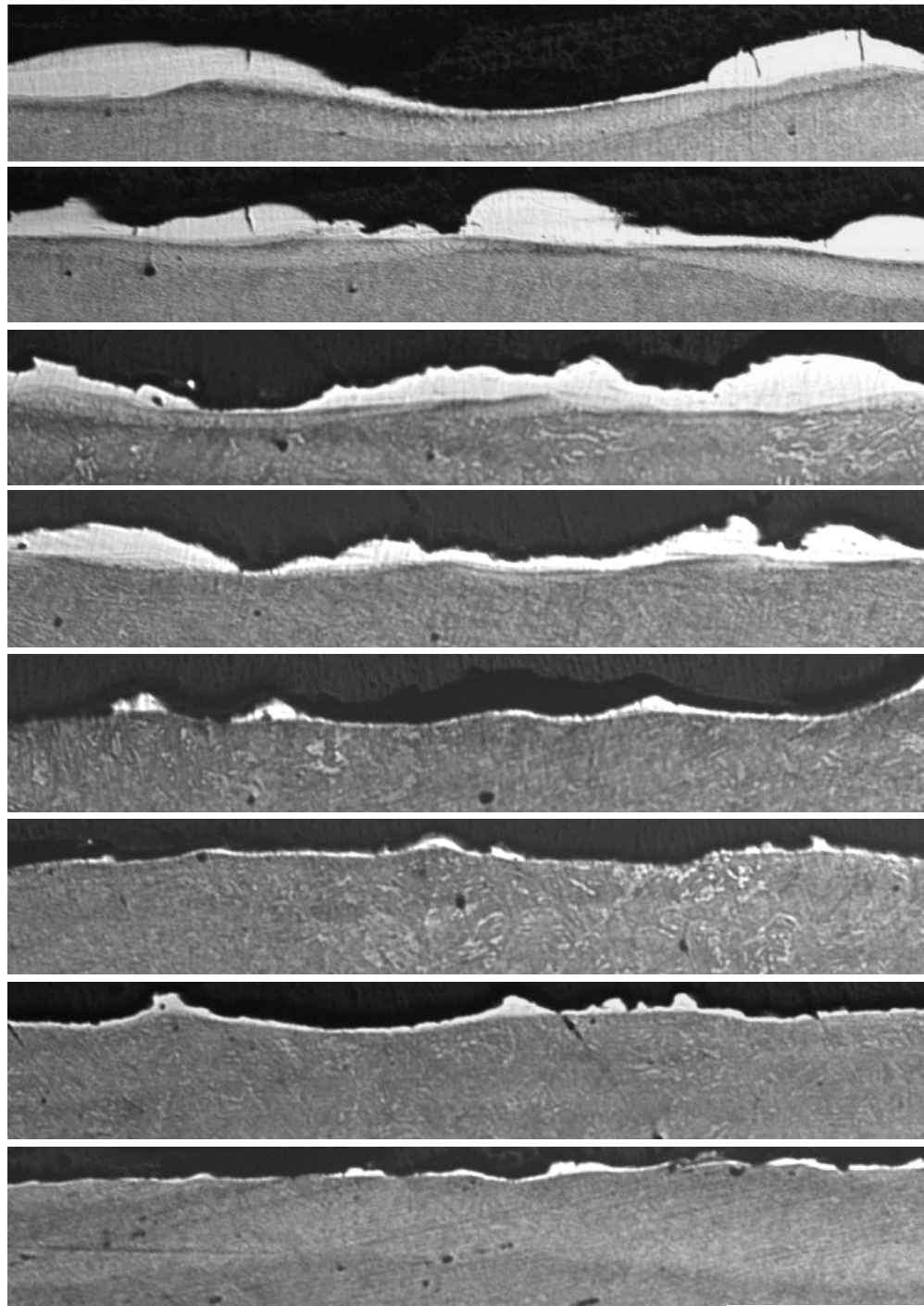


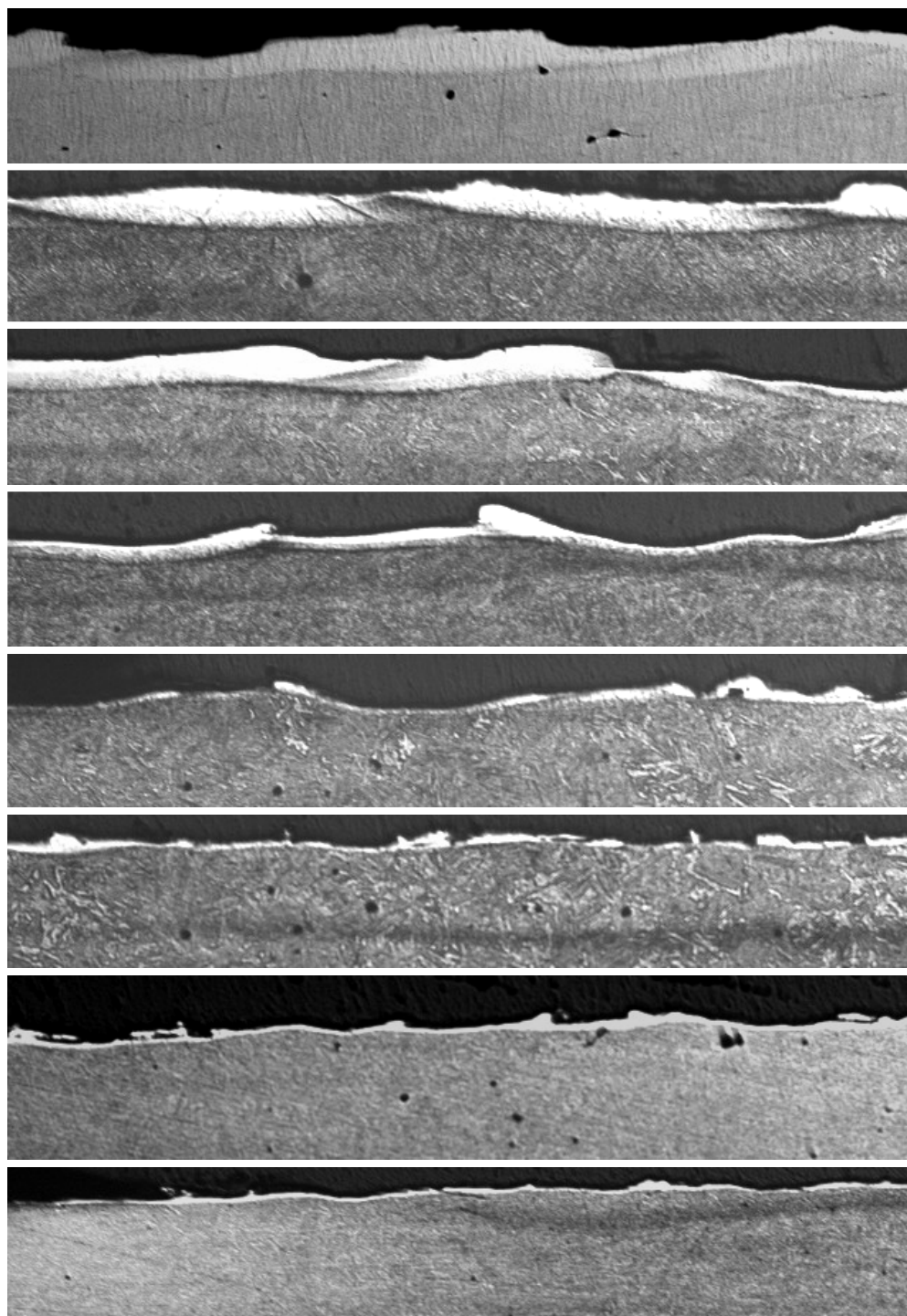
Figure 6.9 EDT'ed Surfaces of Bands A (a, b), B (c, d) and C (e, f).



$t_p=1600, 800, 400, 200, 100, 50, 25$ and $8\mu\text{s}$ from top to bottom respectively

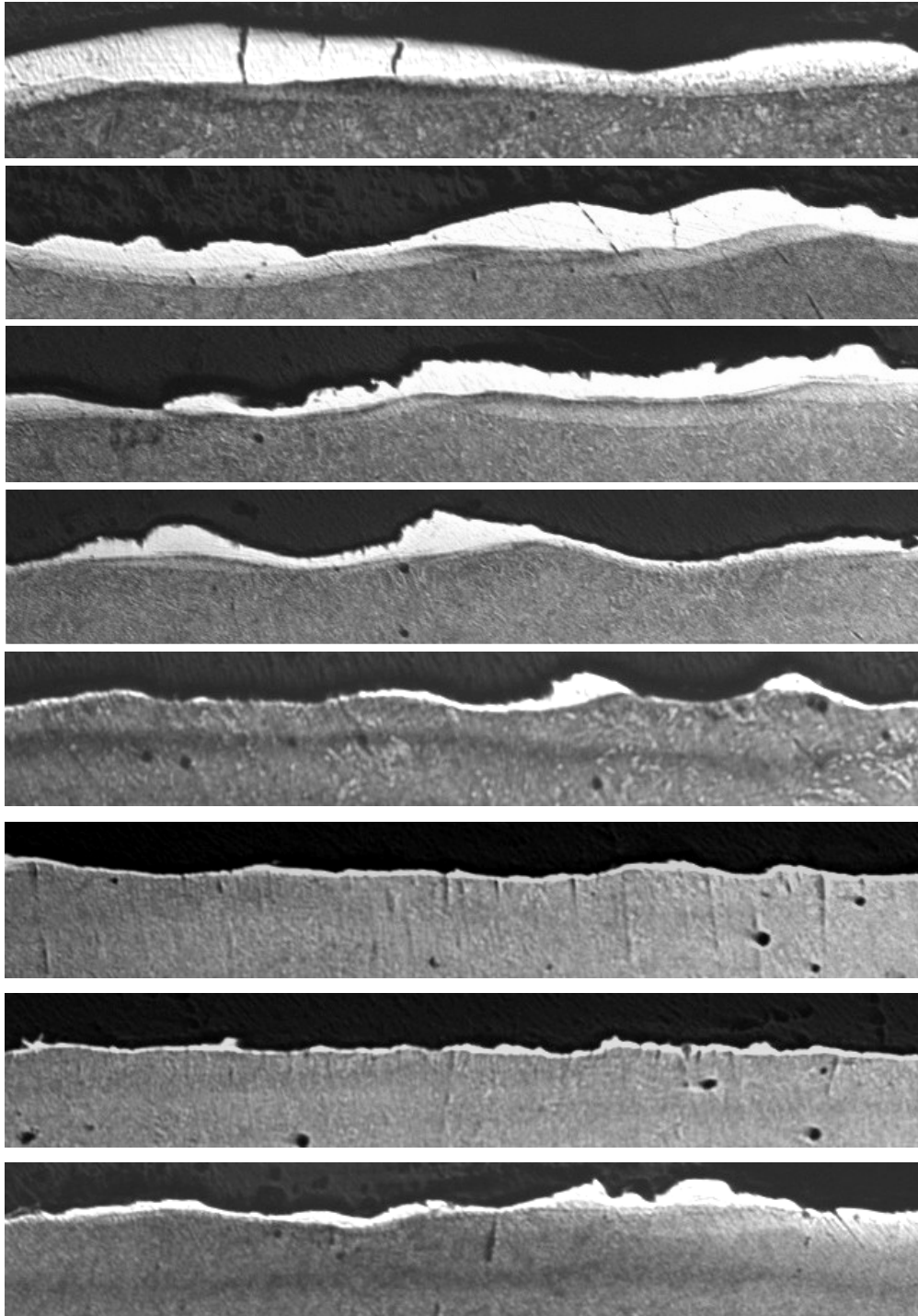
200 μm

Figure 6.10 Cross-Sections EDM'ed Plastic Mold Steel Samples
 $I_{av}=16\text{A}$, Dielectric Liquid: Kerosene, Electrode: Graphite.



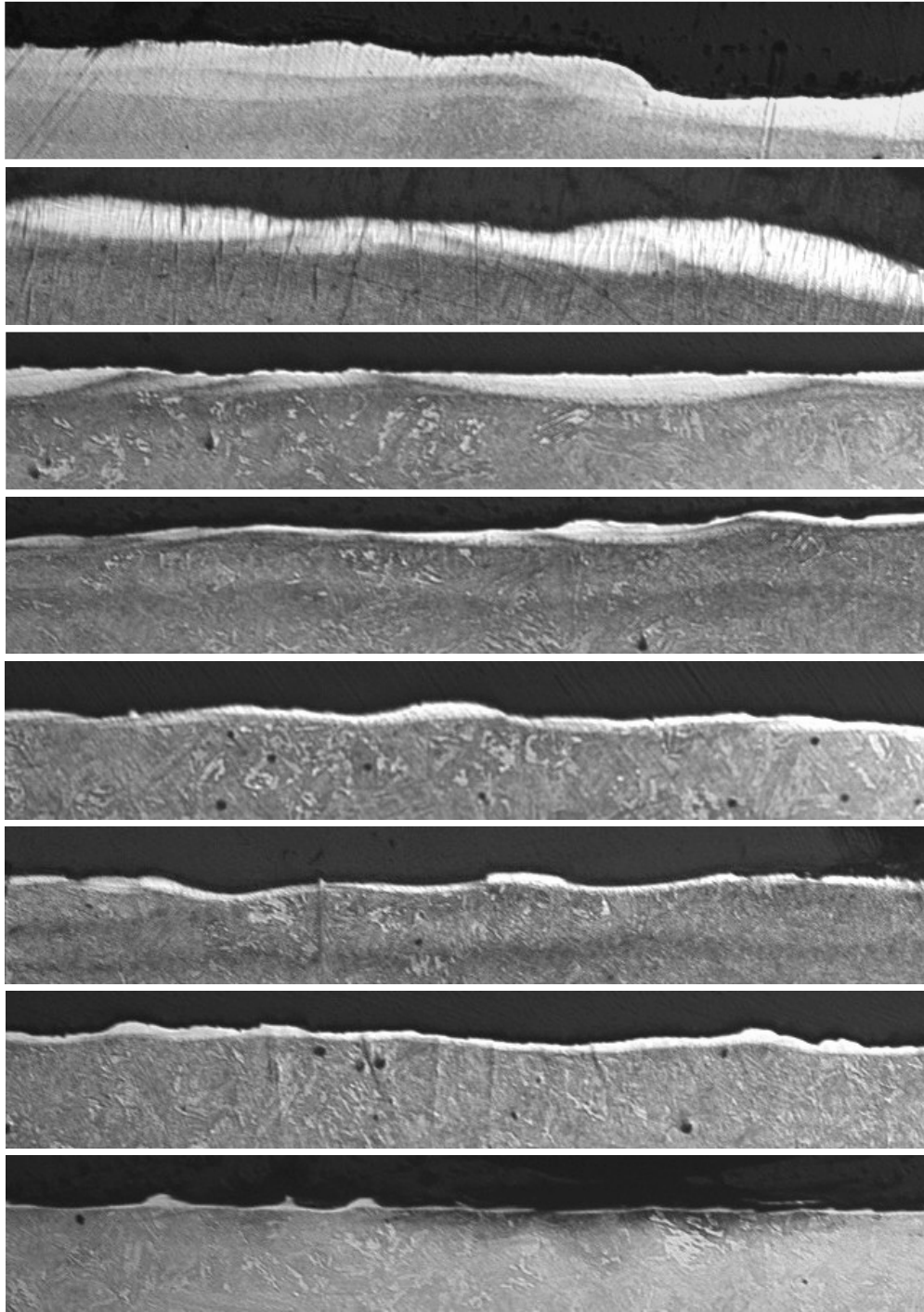
$t_p=1600, 800, 400, 200, 100, 50, 25$ and $8\mu\text{s}$ from top to bottom respectively | 200 μm

Figure 6.11 Cross-Sections EDM'ed Plastic Mold Steel Samples
 $I_{av}=16A$, Dielectric Liquid: De-Ionized Water, Electrode: Graphite.



$t_p=1600, 800, 400, 200, 100, 50, 25$ and $8\mu\text{s}$ from top to bottom respectively | 200 μm

Figure 6.12 Cross-Sections EDM'd Plastic Mold Steel Samples
 $I_{av}=16A$, Dielectric Liquid: Kerosene, Electrode: Copper.



$t_p=1600, 800, 400, 200, 100, 50, 25$ and $8\mu s$ from top to bottom respectively |—————|
200 μm

Figure 6.13 Cross-Sections EDM'd Plastic Mold Steel Samples
 $I_{av}=16A$, Dielectric Liquid: De-Ionized Water, Electrode: Copper.

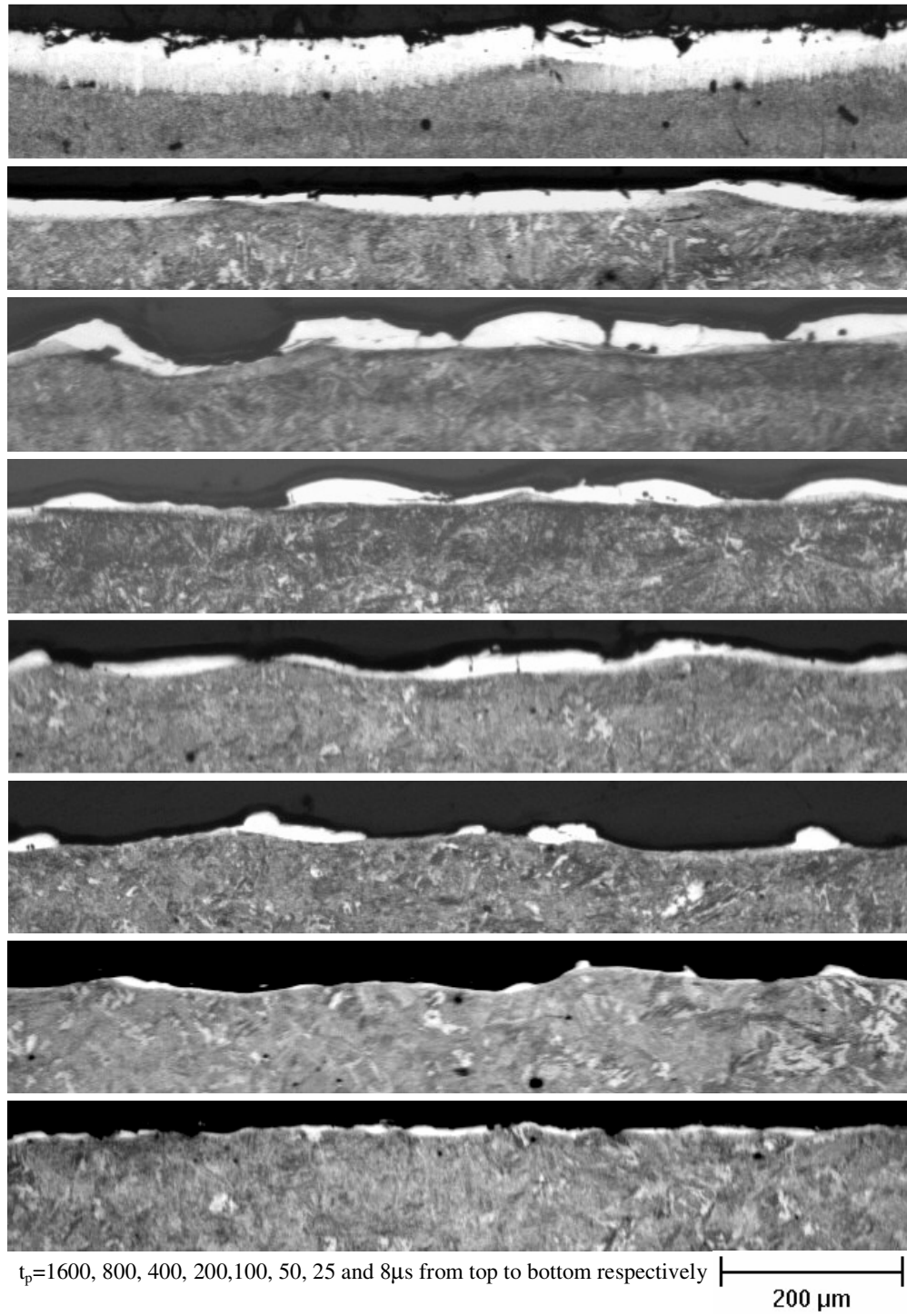
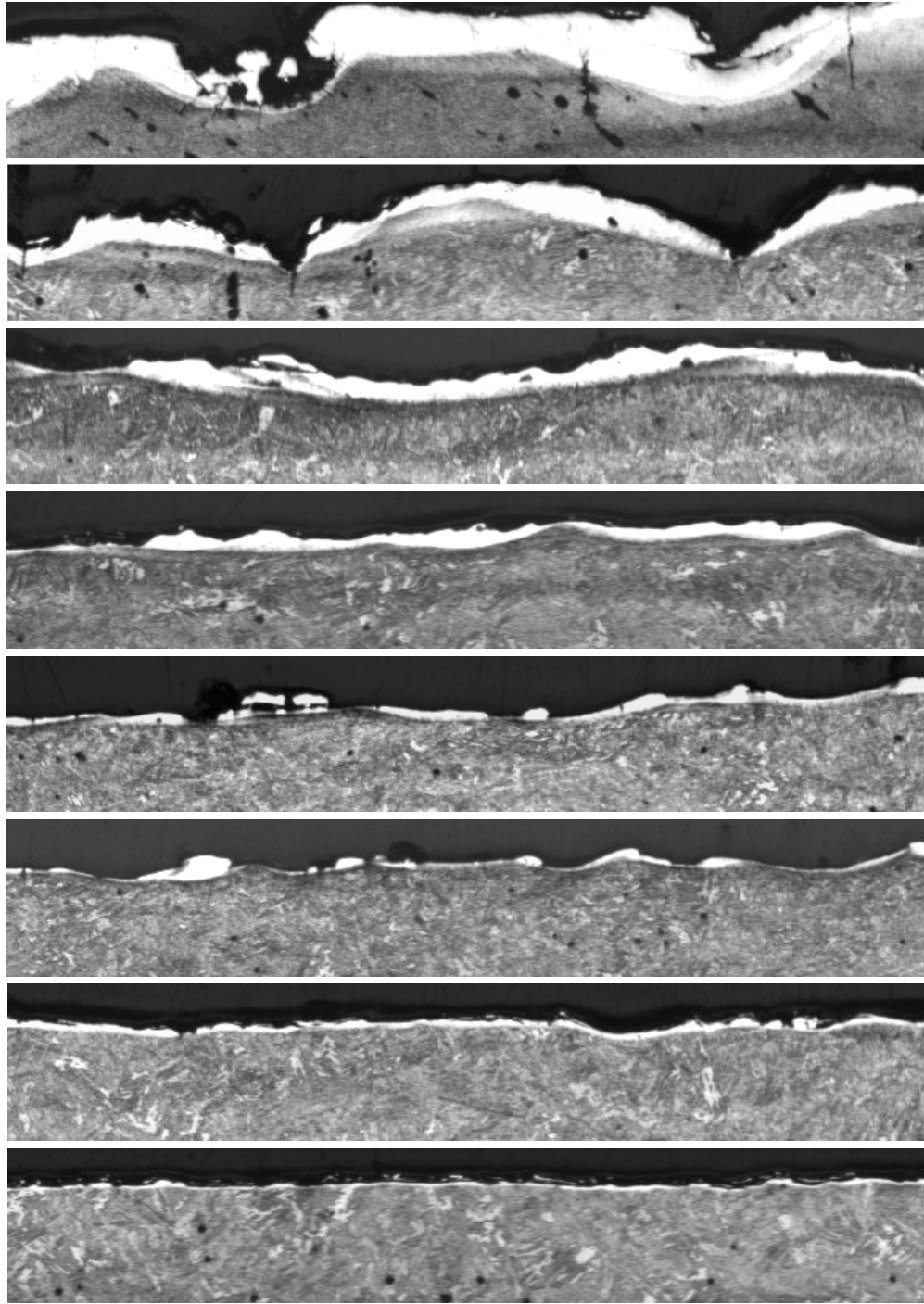
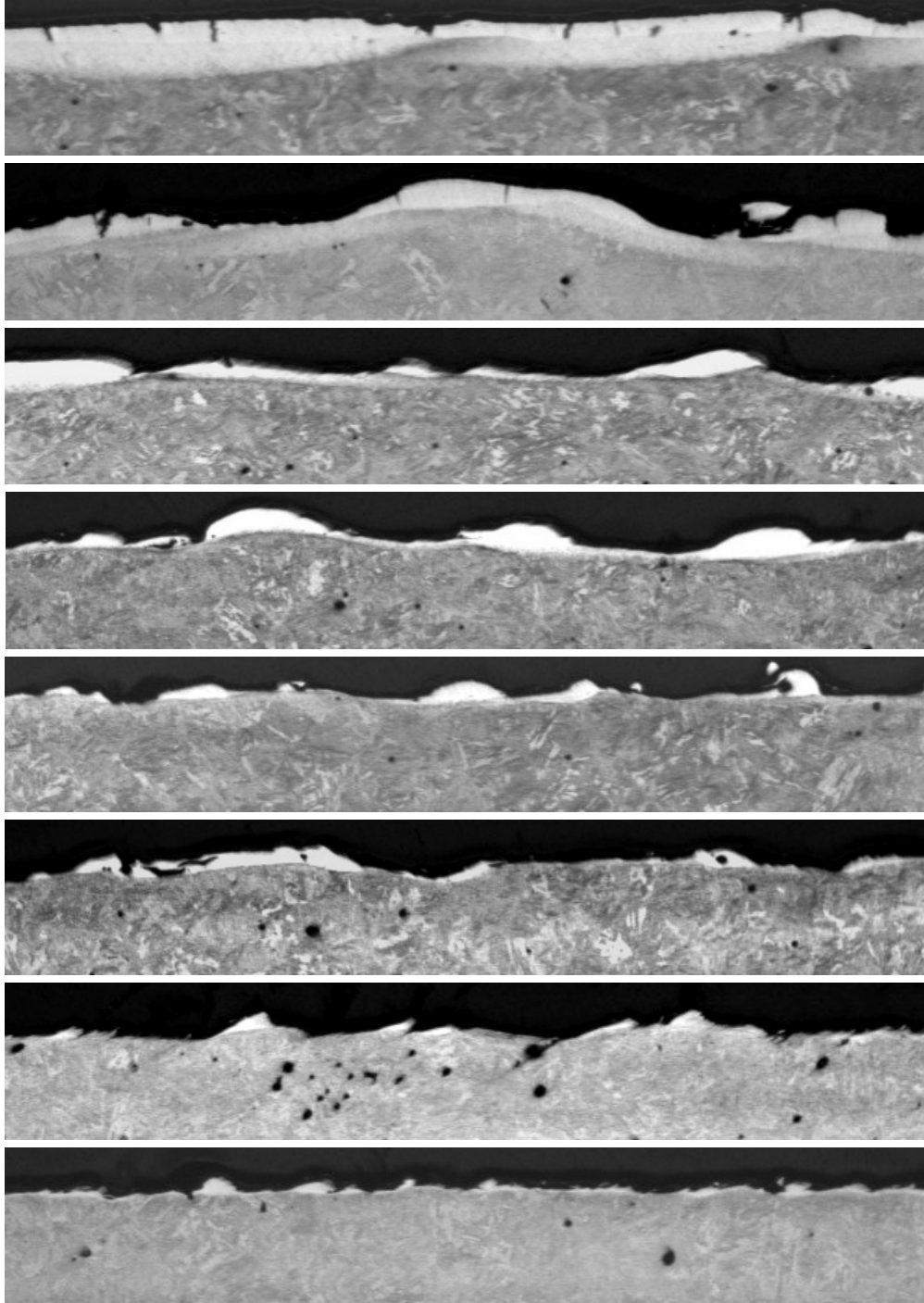


Figure 6.14 Cross-Sections EDM'd Plastic Mold Steel Samples
 $I_{av}=8A$, Dielectric Liquid: Kerosene, Electrode: Graphite.



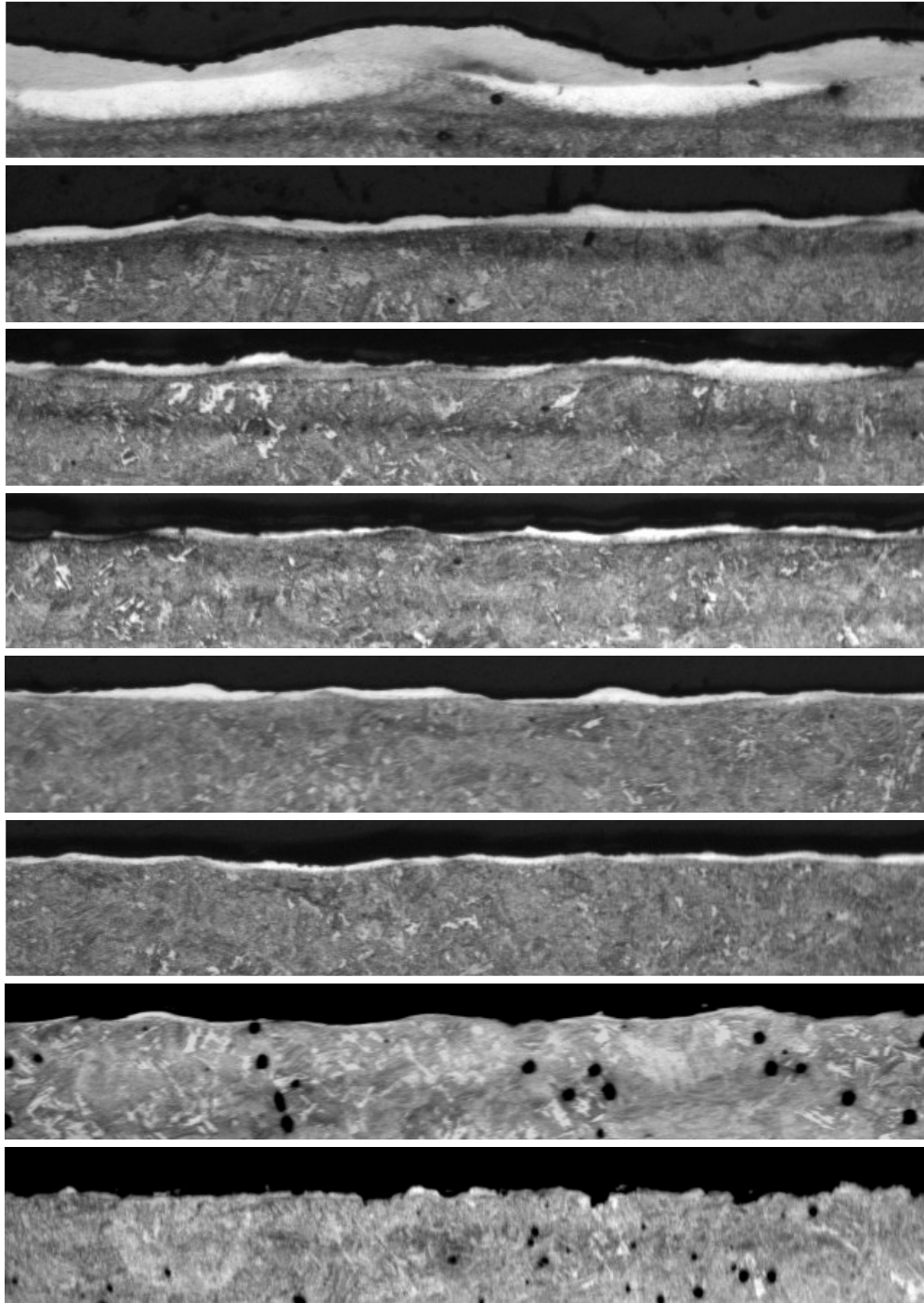
$t_p=1600, 800, 400, 200, 100, 50, 25$ and $8\mu\text{s}$ from top to bottom respectively | 200 μm

Figure 6.15 Cross-Sections EDM'd Plastic Mold Steel Samples
 $I_{av}=8\text{A}$, Dielectric Liquid: De-Ionized Water, Electrode: Graphite.



$t_p=1600, 800, 400, 200, 100, 50, 25$ and $8\mu\text{s}$ from top to bottom respectively |—————|
200 μm

Figure 6.16 Cross-Sections EDM'ed Plastic Mold Steel Samples
 $I_{av}=8\text{A}$, Dielectric Liquid: Kerosene, Electrode: Copper.



$t_p=1600, 800, 400, 200, 100, 50, 25$ and $8\mu\text{s}$ from top to bottom respectively | 200 μm

Figure 6.17 Cross-Sections EDM'd Plastic Mold Steel Samples
 $I_{av}=8\text{A}$, Dielectric Liquid: De-Ionized Water, Electrode: Copper.

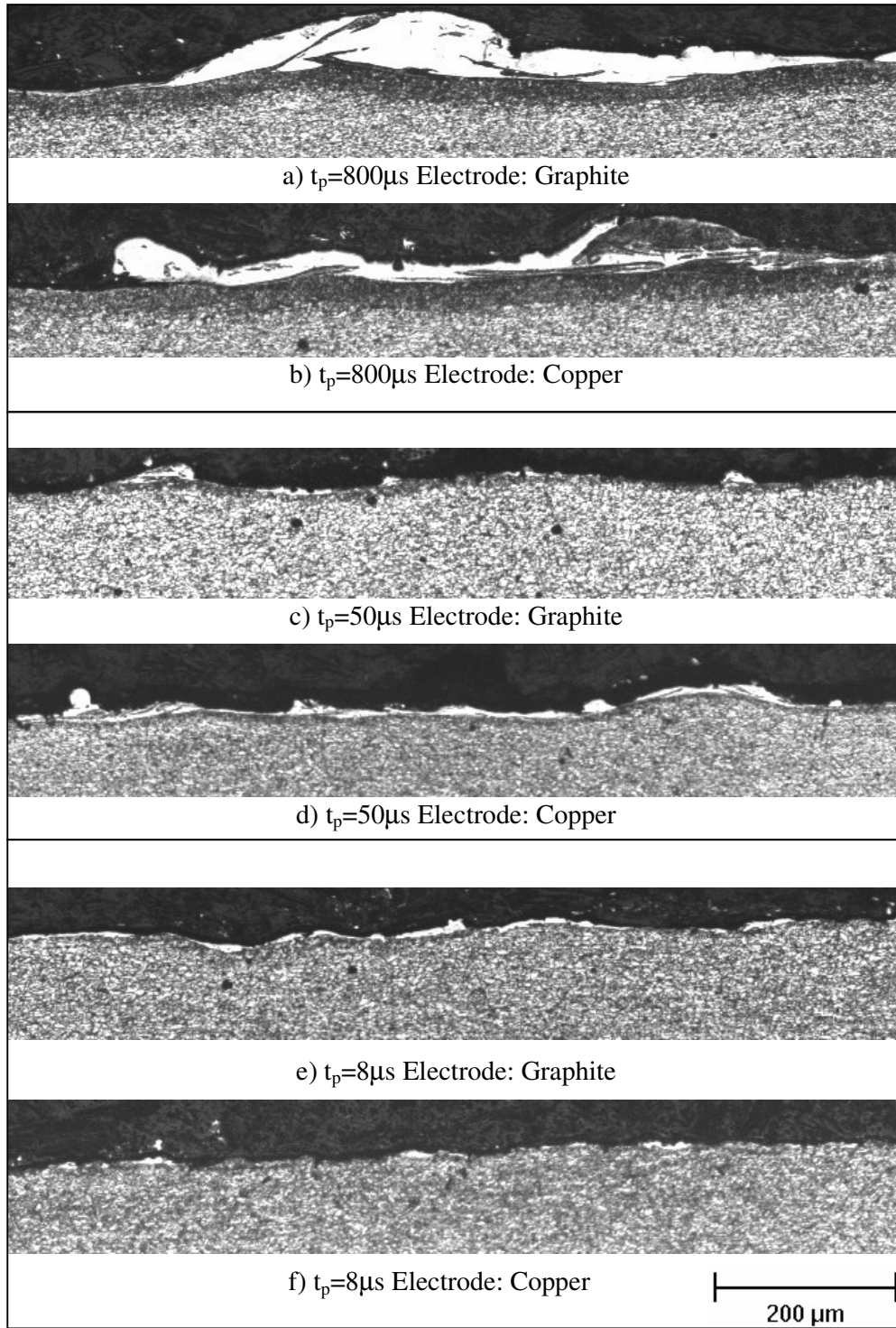


Figure 6.18 Cross-Sections EDM'd Micro Alloy Steel Samples
 $I_{av}=16A$, Dielectric Liquid: Kerosene, Electrode: Copper.

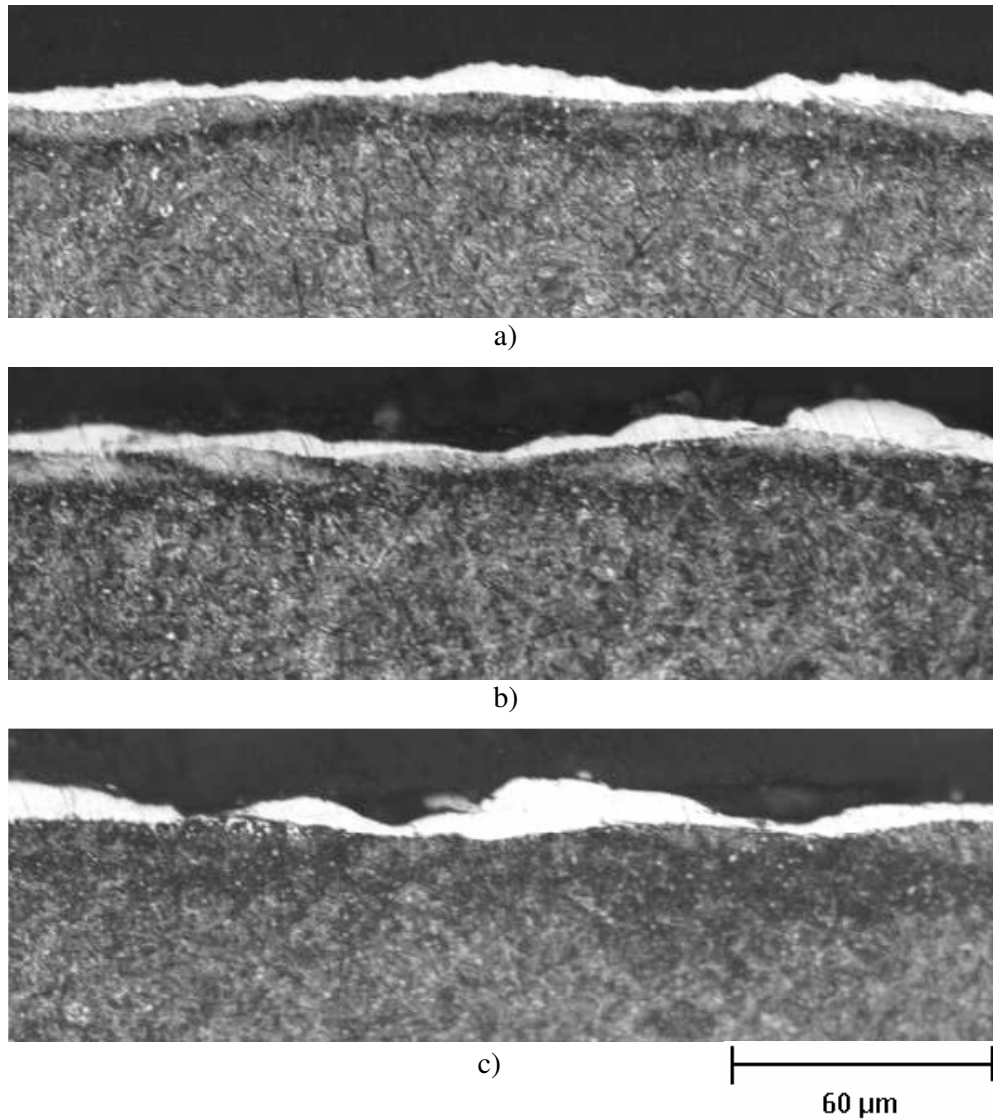


Figure 6.19 Cross-Sections of EDT'ed Bands A (a), B (b) and C (c).

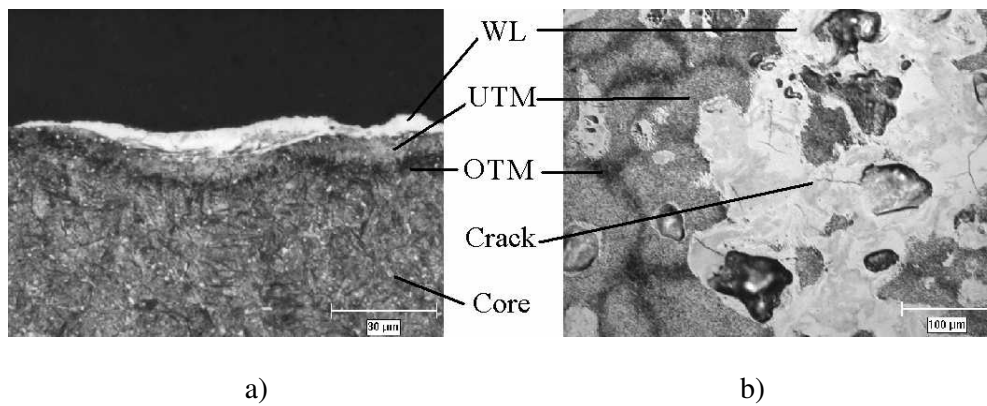


Figure 6.20 Cross (a) and Tangential (b) Sections of EDT'ed Surfaces.

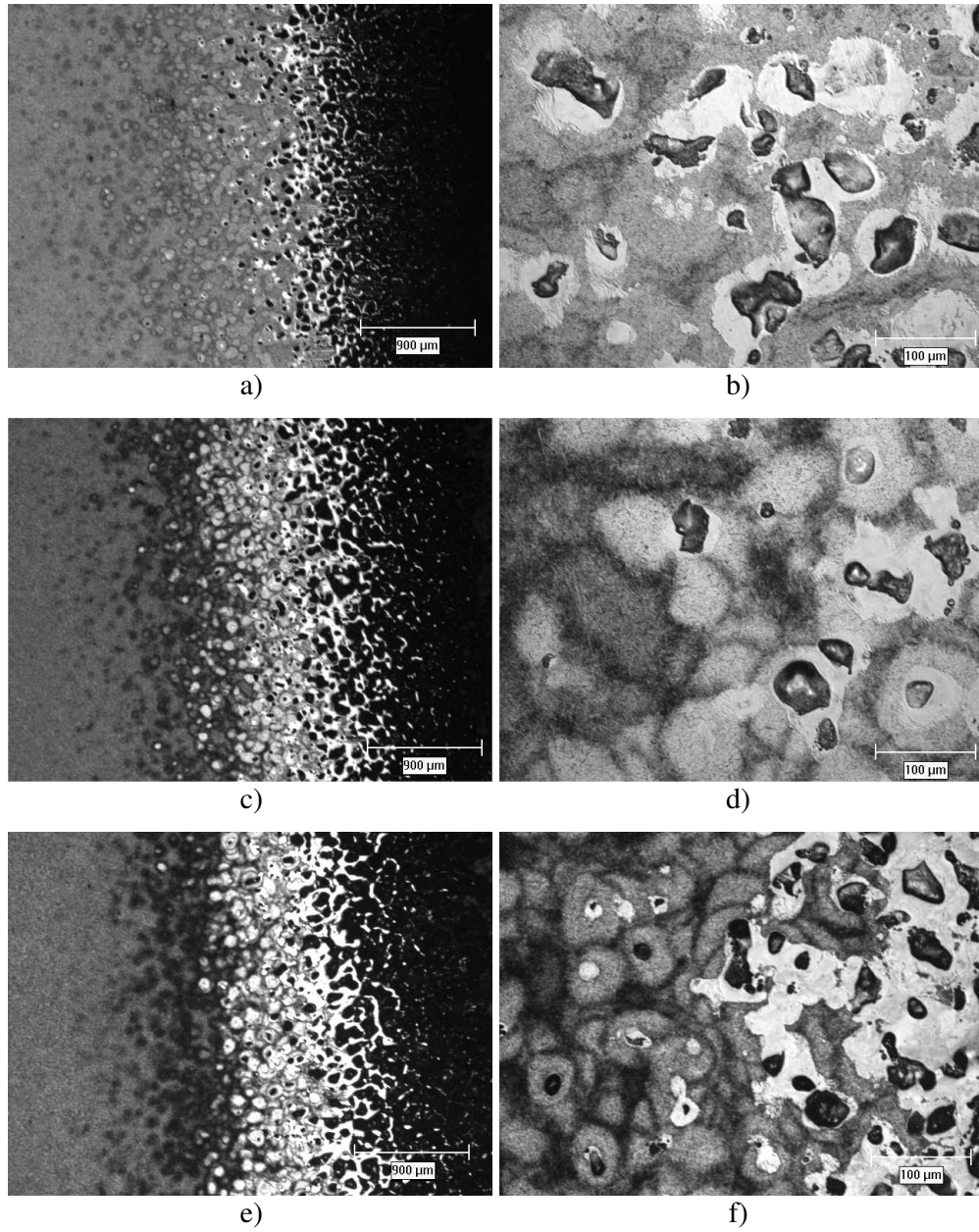


Figure 6.21 Tangential Sections of EDT'ed Bands A (a,b), B (c,d) and C (e,f).

6.5 Hardness Depth

Interfacial zone between the white layer and heat-affected zone is taken as the reference point for hardness measurements due to non-uniformity of the white layer thickness. The Vickers micro hardness readings of plastic mold steel samples indicate high hardness values within white layer and then substantially decrease through the base material (Figure 6.22-6.25). White layer is found much harder than the parent material.

Slightly low values of white layer hardness are observed while using kerosene as dielectric liquid and graphite as tool electrode (Figure 6.22), compared with the other cases. When de-ionized water is used as dielectric liquid and graphite as tool electrode (Figure 6.24), hardness values within the white layer are comparable, but again a shift with respect to pulse duration is evident when copper is used as tool electrode (Figure 6.25). A dramatic decrease is obvious through the heat-affected zone that stays beneath the white layer and then settled to the unaffected material hardness value. Decrease in affected layer thickness can be visualized for all cases. An interesting result is the effect of tool electrode and dielectric liquid on hardness variations within the white layer. Hydrocarbon based dielectric and graphite tool electrode is found to be the reason for fluctuating results in white layer.

Hardness measurements of EDT'ed roll steel (Figure 6.26) resulted in a low hardness just beneath the surface and then reached to its maximum value within the white layer. After that, decreased below the unaffected parent material value and finally settled to its core material hardness value.

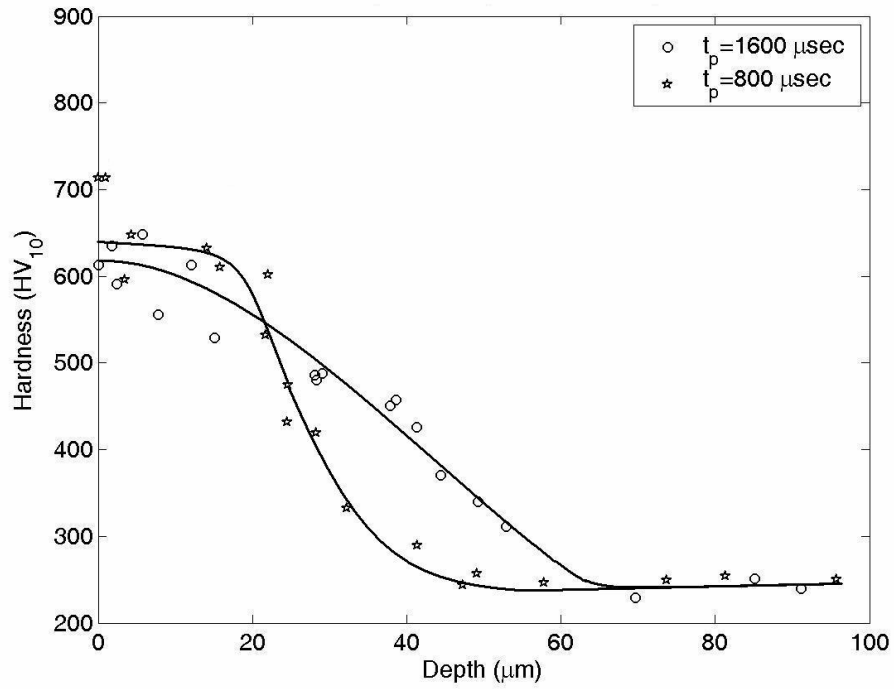


Figure 6.22 Hardness Depth Profile on Cross-Sectioned Surfaces of EDM'ed Plastic Mold Steel. $I_{av}=16A$, Dielectric: Kerosene, Tool Electrode: Graphite.

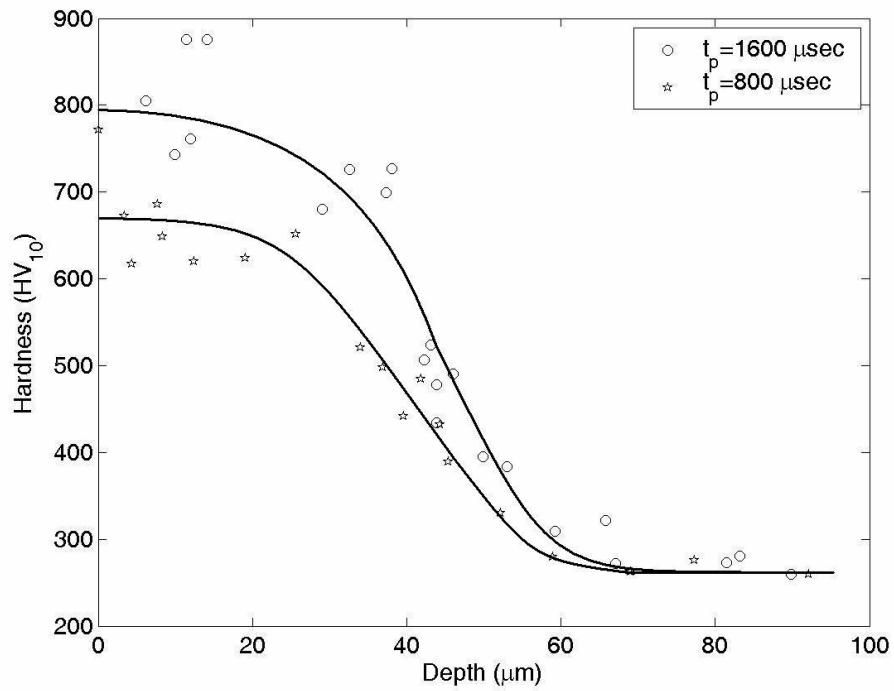


Figure 6.23 Hardness Depth Profile on Cross-Sectioned Surfaces of EDM'ed Plastic Mold Steel. $I_{av}=16A$, Dielectric: Kerosene, Tool Electrode: Copper.

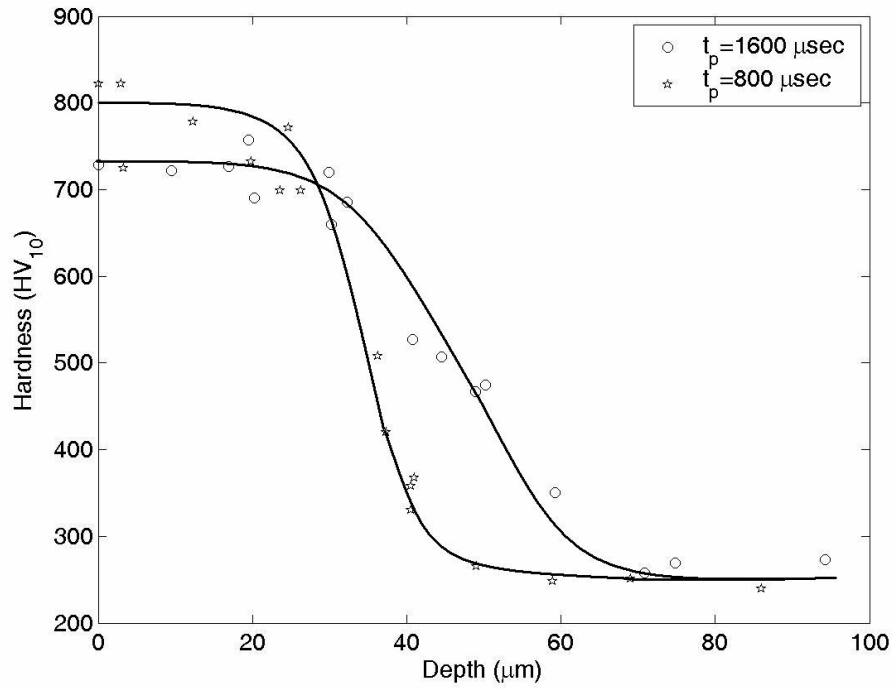


Figure 6.24 Hardness Depth Profile on Cross-Sectioned Surfaces of EDM'ed Plastic Mold Steel. $I_{av}=16A$, Dielectric Liquid: Water, Tool Electrode: Graphite.

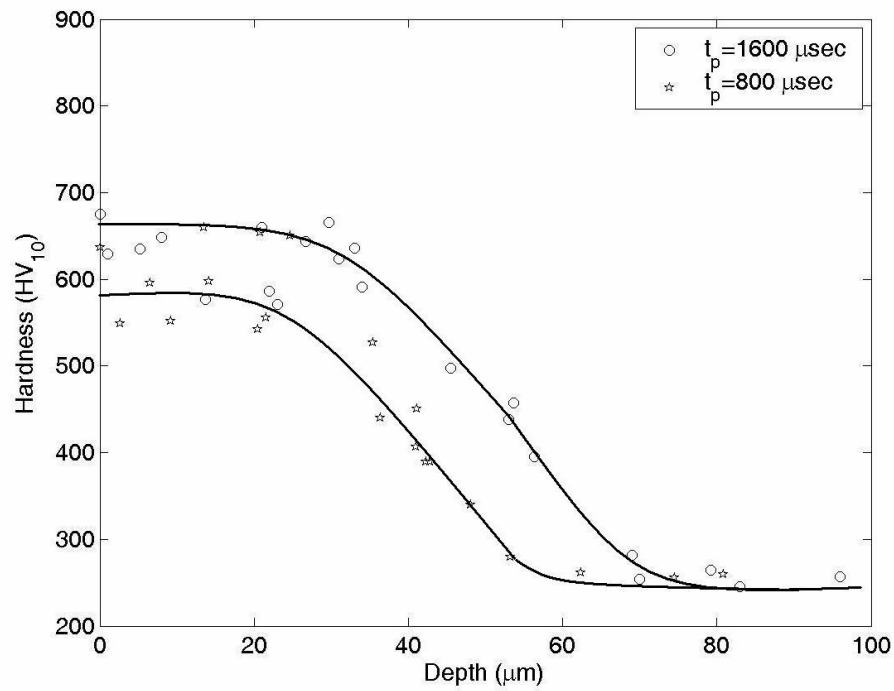


Figure 6.25 Hardness Depth Profile on Cross-Sectioned Surfaces of EDM'ed Plastic Mold Steel. $I_{av}=16A$, Dielectric Liquid: Water, Tool Electrode: Graphite.

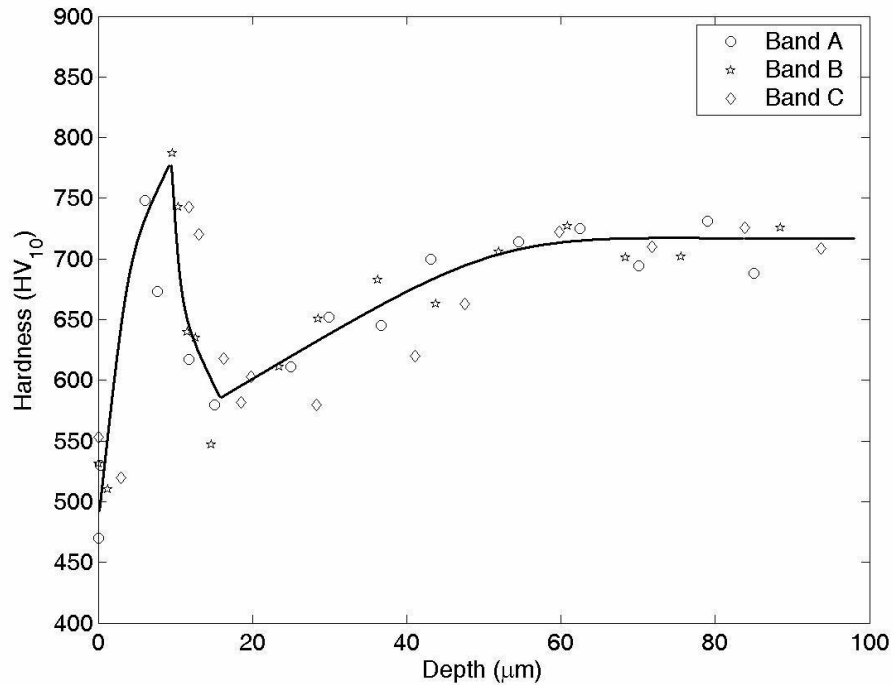


Figure 6.26 Hardness Depth Profile on Cross Sectioned Surfaces of EDT'ed Bands A, B and C.

6.6 X-Ray Diffraction Patterns

X-Ray patterns of analyzed samples are presented in tabular form (Table 6.4). X-Ray diffraction patterns for plastic mold steel samples (Figure 6.27) have shown basically two different trend. When samples are machined in kerosene, iron carbide, Fe_3C , is formed (Table 6.5) regardless of tool electrode type. Austenite is also detected on all samples, but smaller amount is found when water is used as dielectric liquid. Diffraction patterns for EDT'ed samples (Figure 6.28) have shown similar results with EDM'ed samples when kerosene is used as dielectric liquid. Formation of austenite and iron carbide compound (Table 6.4) is pointed out at textured surfaces. The use of copper and graphite electrodes has almost no influence on the structure of the white layer, because only small amounts of electrode material migrate from the electrode to the white layer. JPDS-Diffraction Data for analyzed x-ray patterns are given in Appendix A.



Figure 6.27 X-Ray Diffraction Patterns of Plastic Mold Steel Samples a) Before EDM b), c) Copper and Graphite Electrodes in Kerosene Dielectric d), e) Copper and Graphite Electrodes in De-Ionized Water ($I_{av} = 16A, t_p = 800 \mu s$)

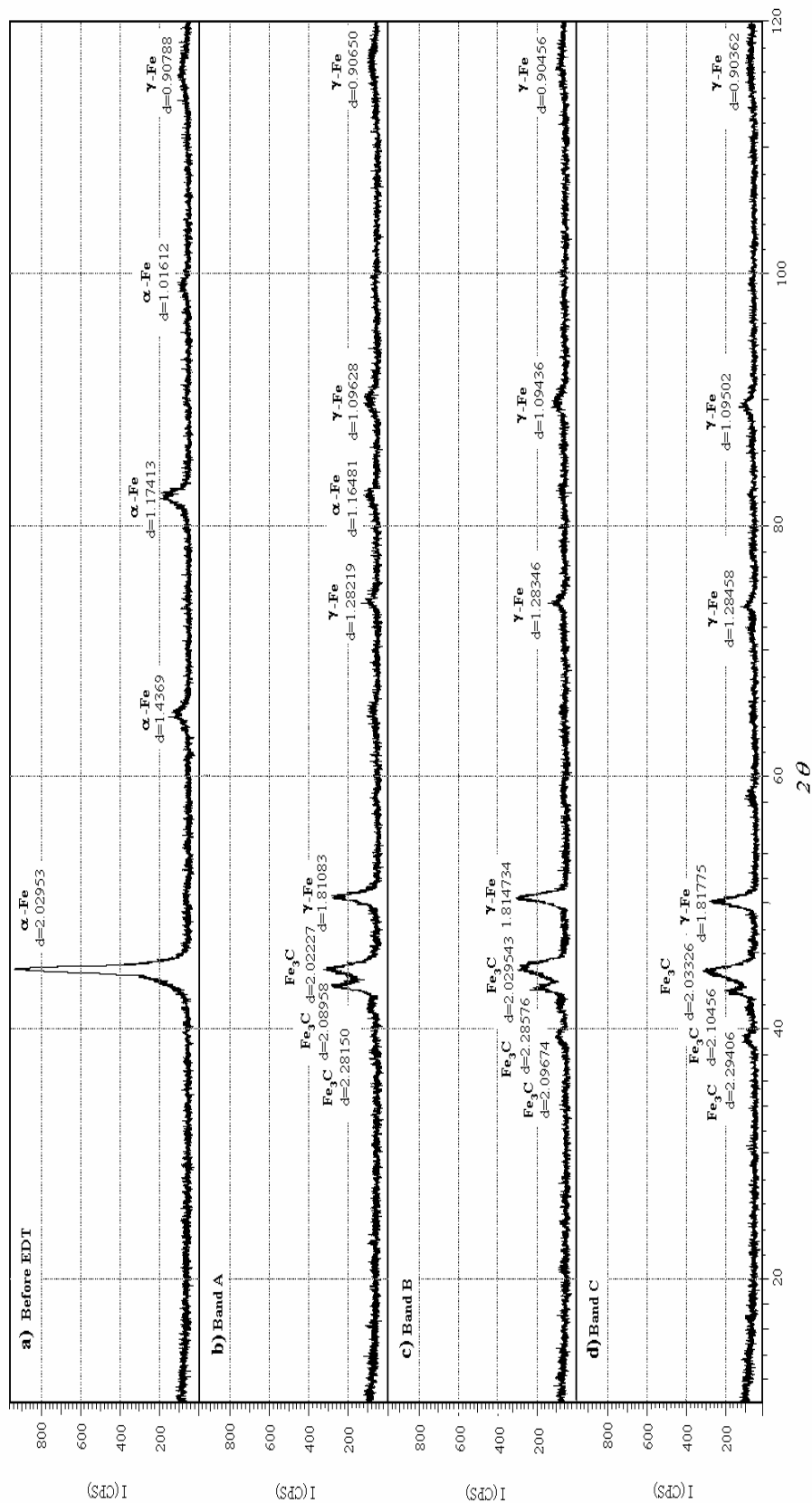


Figure 6.28 X-Ray Diffraction Patterns of EDT Roll Steel Samples a) Before EDT b) Band A c) Band B d) Band C.

Table 6.4 Detected Compounds from X-Ray Patterns.

<i>Before EDM</i>		
Iron, α -Fe	PDF No: 6-696	BCC
<i>Tool Electrode Copper, Dielectric: Kerosene</i>		
Iron, α -Fe	PDF No: 6-696	BCC
Cementite, Fe ₃ C	PDF No: 34-1	Orthorhombic
Austenite (Fe,C)	PDF No: 31-619	FCC
<i>Tool Electrode Graphite, Dielectric: Kerosene</i>		
Iron, α -Fe	PDF No: 6-696	BCC
Cementite, Fe ₃ C	PDF No: 34-1	Orthorhombic
Austenite (Fe,C)	PDF No: 31-619	FCC
<i>Tool Electrode Copper, Dielectric: De-ionized Water</i>		
Iron α -Fe	PDF No: 6-696	BCC
Austenite (Fe,C)	PDF No: 31-619	FCC
<i>Tool Electrode Graphite, Dielectric: De-ionized Water</i>		
Iron α -Fe	PDF No: 6-696	BCC
Austenite (Fe,C)	PDF No: 31-619	FCC
<i>Before EDT</i>		
Iron, α -Fe	PDF No: 6-696	Cubic
<i>Band A</i>		
Iron, α -Fe	PDF No: 6-696	Cubic
Cementite, Fe ₃ C	PDF No: 34-1	Orthorhombic
Austenite (Fe,C)	PDF No: 31-619	Cubic
<i>Band B</i>		
Iron, α -Fe	PDF No: 6-696	Cubic
Cementite, Fe ₃ C	PDF No: 34-1	Orthorhombic
Austenite (Fe,C)	PDF No: 31-619	Cubic
<i>Band C</i>		
Iron α -Fe	PDF No: 6-696	Cubic
Cementite, Fe ₃ C	PDF No: 34-1	Orthorhombic
Austenite (Fe,C)	PDF No: 31-619	Cubic

CHAPTER VII

RESIDUAL STRESS MEASUREMENTS

7.1 Introduction

Layer removal method is used to measure the residual stress profile in function of depth beneath surface caused by die sinking type EDM. In this method, tiny stressed layers are removed from machined samples by electrochemical polishing and corresponding deformations due to stress relaxation are recorded for each removal to determine the stress profile from elasticity theory. Residual stresses due to EDM measured for plastic mold steel samples under similar operating conditions are described in the previous section. Results of these measurements will be presented in this section.

7.2 Measured Data

Theoretically, removing stressed layers from a beam shaped component result in deflection due to construction of a new equilibrium state. Deflection after each removal is expected to form a second order polynomial curve. Measured deflections and corresponding second order polynomials for an EDM'ed sample (Table 7.1) after removal of each layer (Figure 7.1) has shown a good agreement with the expectation. The curvature can be easily found from the following equation.

$$C_i = \frac{1}{\rho_i} \approx \frac{\partial^2 P_i(x)}{\partial^2 x} = 2d_i \quad (7.1)$$

Here, C is the curvature $P(x)$ is the deflection polynomial and d is the coefficient found after curve fitting. The sub indices i represent the number of removed layer. Corresponding thickness (Figure 7.2) can be obtained since measurements are taken with two dial indicators and the sum of the readings would be equal to that if the initial gap between the indicators is zero.

Variation in sample curvature with respect to removed layer thickness, δ_i can be easily found from the previous measured deflection data and corresponding curve fit. Sample thickness is taken as the average values obtained after surface profiling for layer removal (Figure 7.3).

Table 7.1 Machining Parameters for EDM'ed Sample.

t_p (μs)	100
I_{av} (A)	16
Electrode	Graphite
Dielectric	H ₂ O
Polarity	+

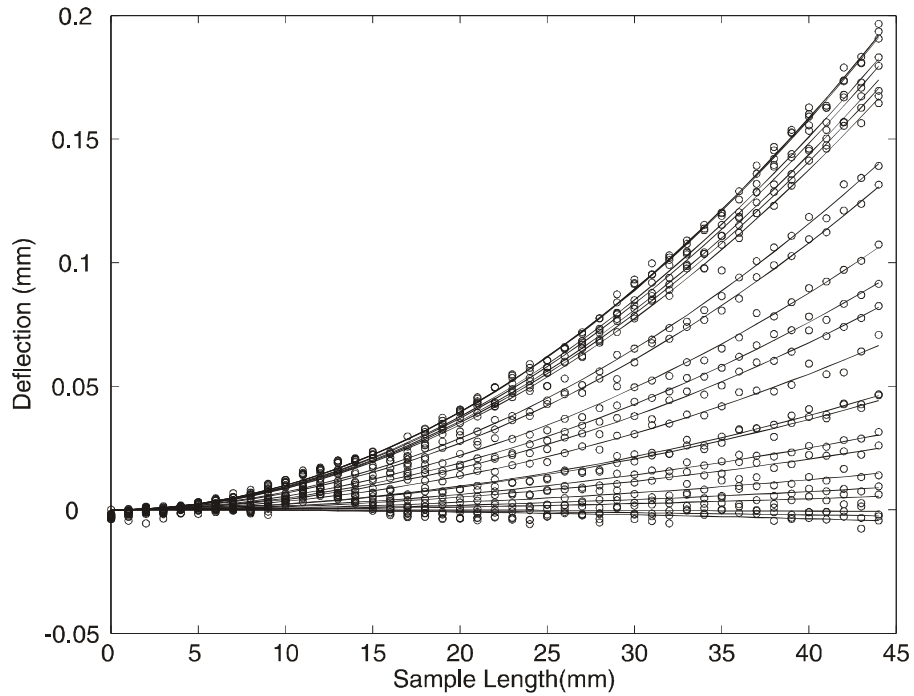


Figure 7.1 Deflection Curves after Removal of Consecutive Layers.

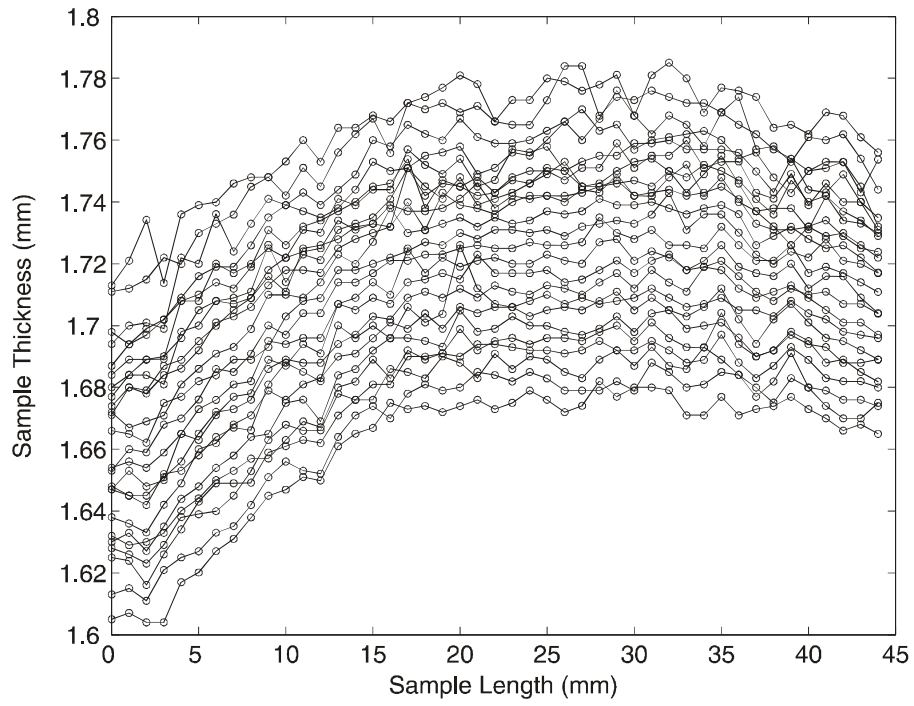


Figure 7.2 Surface Thickness Profiles after Removal of Consecutive Layers.

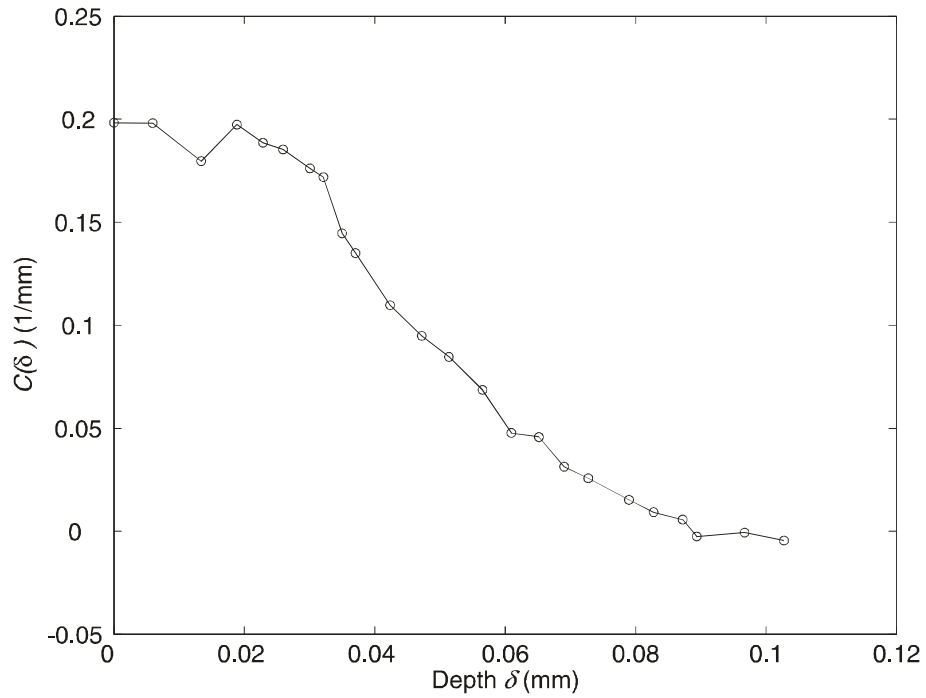


Figure 7.3 Change in Radius of Curvature, $C(\delta)$, with respect to Removed Layer Thickness, δ

7.2.1 Repeatability of the Measurements

The procedure has been applied for 12 different specimens, which were machined under similar machining conditions (Table 7.1). The following dimensionless parameters are defined:

$$\delta^* = \frac{\delta}{H}, \quad C^*(\delta^*) = H \cdot C(\delta) \quad (7.2)$$

Here, H is the initial sample thickness. A well-defined data cloud was obtained (Figure 7.4) and analyzed for possible candidates of fitting functions. The most suitable descriptive function representing the relational dependence of variables is found as a special form of Gauss distribution, which is the sum of two Gaussian peaks, with the same amplitude and pulse width but opposite center location.

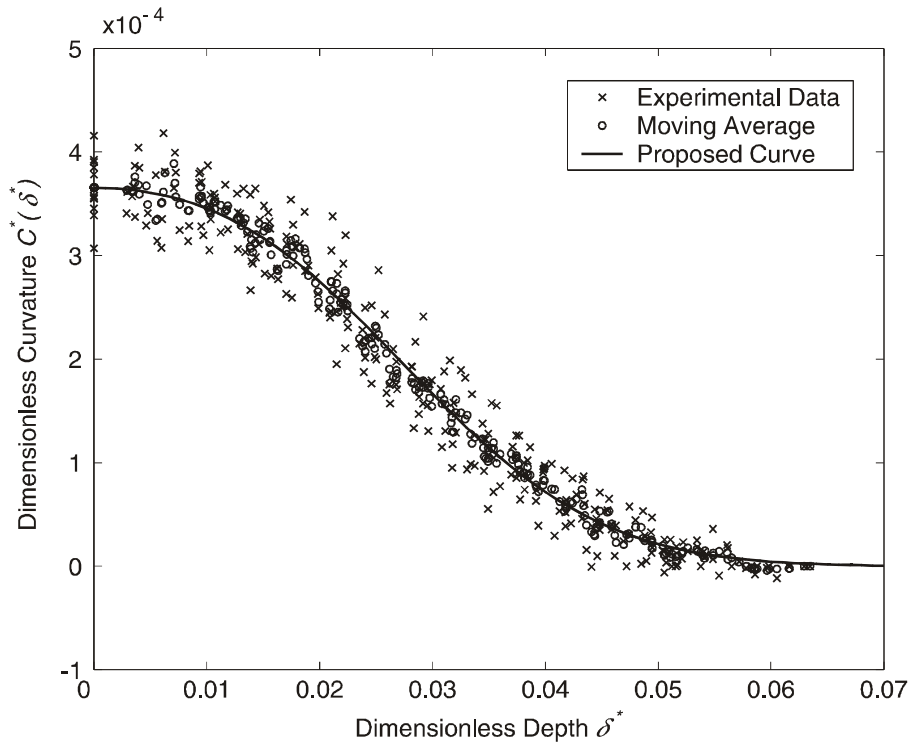


Figure 7.4 Data Cloud and Corresponding Curve Fit.

The fitting equation can be expressed in the following form:

$$C^*(\delta^*) = a_1 \exp(-(a_2 \delta^*)^2) \cosh(a_3 \delta^*) \quad (7.3)$$

Constant coefficients a_1 , a_2 and a_3 can be found by using non-linear least squares method. Calculated values are 0.0003653, 43.89 and 53.33 respectively. The square of the correlation between the response values and the predicted response values, which is also called the square of the multiple correlation coefficients, R^2 , is found as 0.99817 over the moving average.

7.2.2 Analysis of Measured Data

The new balance of internal stresses due to layer removal results in a change in deflection. Consequently, the amount of residual stress can be found by using elastic theory if deflection and removal rate are known. In this case, only the principal stresses parallel to the axis of the test specimen are considered (Figure 7.5). The specimen subjected to a constant bending moment and has a constant curve. The stress will only vary according to a depth and will be identical along the entire length and width of the specimen.

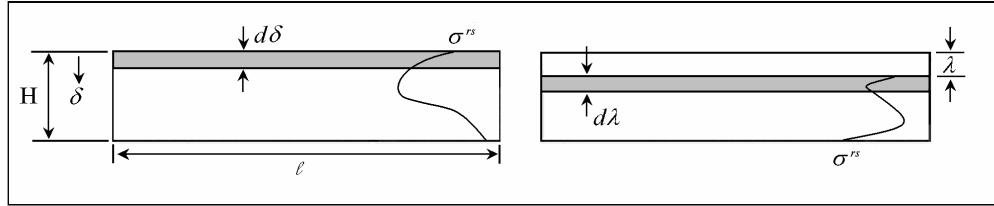


Figure 7.5 Layer Removal.

When a stressed layer is removed, the test specimen will be subjected to the force and moment dF and dM such that:

$$dF = -\sigma^{rl} w d\delta \quad (7.4)$$

$$dM = -\sigma^{rl} \frac{(H - \delta)}{2} w d\delta \quad (7.5)$$

To reestablish the equilibrium, the test specimen will be deformed in such a way that an opposite force and moment act on it. The deflection curve of the test specimen can be obtained by double integration of the following integral;

$$\frac{d^2y}{dx^2} = -\frac{M}{EI} \approx \frac{1}{\rho} = C \quad (7.6)$$

Here E is the elasticity modulus of the material. Putting the moment caused by residual stress into the equation leads to the following equation.

$$\sigma^r = -\frac{(H-\delta)^2}{6} E \frac{1}{l^2} \frac{dy}{d\delta} = -\frac{(H-\delta)^2}{6} E \frac{dC(\delta)}{d\delta} \quad (7.7)$$

This equation gives the value of the stress present in each layer. Subsequent removal of layers will add forces and moments into the test specimen. Therefore, after the first layer is removed, residual stresses cannot be calculated. Stress variation, which results from removal of the layers, should be added.

The force dF and the moment dM produced by removing a layer causes a variation in normal stress at dimension $(H-\xi)$ such that:

$$d\sigma = d\sigma_n + d\sigma_b \quad (7.8)$$

The normal and bending stresses are given by:

$$d\sigma_n = \frac{dF}{w(H-\xi)} = -\frac{1}{6} E(H-\xi) dC(\xi) \quad (7.9)$$

$$d\sigma_b = dM \frac{(H-\delta) - (H-\xi)/2}{w(H-\xi)^3/12} = -E \left\{ (H-\delta) - \frac{1}{2}(H-\xi) \right\} dC(\xi) \quad (7.10)$$

Therefore:

$$d\sigma = \frac{1}{3} E(H-\xi) dC(\xi) - E(H-\delta) dC(\xi) \quad (7.11)$$

The total stress variation at dimension $(H-\lambda)$ due to the removal of the layers above dimension $(H-\lambda)$ is given by the expression:

$$\Delta\sigma = -E(H-\delta)\int_0^{\delta} dC(\xi) + \frac{1}{3}E\int_0^{\delta} (H-\xi)dC(\xi) \quad (7.12)$$

The residual stresses which existed in the test specimen before machining is therefore equal to:

$$\sigma^{rs} = \sigma^{rl} + \Delta\sigma \quad (7.13)$$

Finally, adding the terms given by the Equations (7.11) and (7.12) yields the solution in the following form.

$$\begin{aligned} \sigma^{rs}(\delta) = & -\frac{1}{6}E(H-\delta)^2 \frac{dC(\delta)}{d\delta} + \frac{2}{3}E(H-\delta)C(\delta) + \frac{1}{3}EC(0)(3\delta-2H) \\ & -\frac{1}{3}E\int_0^{\delta} C(\xi)d\xi \end{aligned} \quad (7.14)$$

This equation, derived by Stäblein (1931), describes the relation between the curvature of the sample and the residual stress for a one dimensional stress situation. This equation can be expressed also in dimensionless form by using expressions in Equation (7.2) and the following dimensionless parameters given as

$$\xi^* = \frac{\xi}{H}, \quad \sigma^*(\delta^*) = \frac{\sigma^{rs}(\delta^*)}{S_{HS}} \quad (7.15)$$

Here S_{HS} is a hot strength value of the material such as yield or ultimate tensile strength of the material. Hence,

$$\begin{aligned} \sigma^*(\delta^*) = & -\frac{E}{S_{HS}} \frac{1}{6}(1-\delta^*)^2 \frac{dC^*(\delta^*)}{d\delta^*} + \frac{2}{3} \frac{E}{S_{HS}}(1-\delta^*)C^*(\delta^*) \\ & + \frac{E}{S_{HS}} \frac{1}{3}C^*(0)(3\delta^*-2) - \frac{1}{3} \frac{E}{S_{HS}} \int_0^{\delta^*} C^*(\xi^*)d\xi^* \end{aligned} \quad (7.16)$$

Residual stress can be found by putting Equation (7.3) into Equation (7.16) if variation of curvature with respect to removed depth follows the proposed functional form for a beam specimen.

$$\begin{aligned} \sigma^*(\delta^*) = & \frac{E}{S_{HS}} \frac{(1-\delta^*)^2}{6} a_1 \exp(-(a_2\delta^*)^2) \cosh(a_3\delta^*) \cdot \\ & \left\{ 2a_2^2\delta^* + \frac{4}{(1-\delta^*)} - a_3 \tanh(a_3\delta^*) \right\} + \frac{E}{S_{HS}} \frac{(3\delta^* - 2)}{3} a_1 - \\ & \left. \frac{E}{S_{HS}} \frac{\sqrt{\pi}}{12} \frac{a_1}{a_2} \exp(-(a_3/2a_2)^2) \left\{ \operatorname{erf}\left(\delta^* a_2 - \frac{a_3}{2a_2}\right) + \operatorname{erf}\left(\delta^* a_2 + \frac{a_3}{2a_2}\right) \right\} \right\} \end{aligned} \quad (7.17)$$

7.2.3 Electro-Chemical Polishing in Affected Layers

Variation of voltage, bath and room temperature during layer removal process are also recorded (Figure 7.6). Electrical potential is found to be unchanged during removal of outermost layers on analyzed samples. The steadiness in voltage starts to increase with respect to time after removal of proceeding layers and reaches to its peak value. After that, electrical parameters in electro-chemical polishing exhibit a steady variation (Figure 7.7). This behavior can be related to affected layers during EDM (Table 7.2). It is known that the structure of the white layer is completely different from the base metal and therefore have different electrochemical machining characteristic. Hence, within affected layers, a non-linear variation of material removal rate with respect to time has been observed.

7.3 Parametric Measurements

Measurements on plastic mold steel samples EDM'ed are revealed a dependency on pulse duration without change in pattern for each dielectric and tool electrode combination (Figure 7.8, 7.15, 7.22, 7.29). Decrease in energy level does not alter this trend (Figure 7.9, 7.16, 7.23, 7.29). Therefore, the proposed fitting function (Equation 7.3) for each combination has been applied. The best representing function coefficients a_1 , a_2 , a_3 is found for each particular case by using nonlinear least squares method and a unit amplitude shape function, $a_1=1$, is defined (Table 7.3).

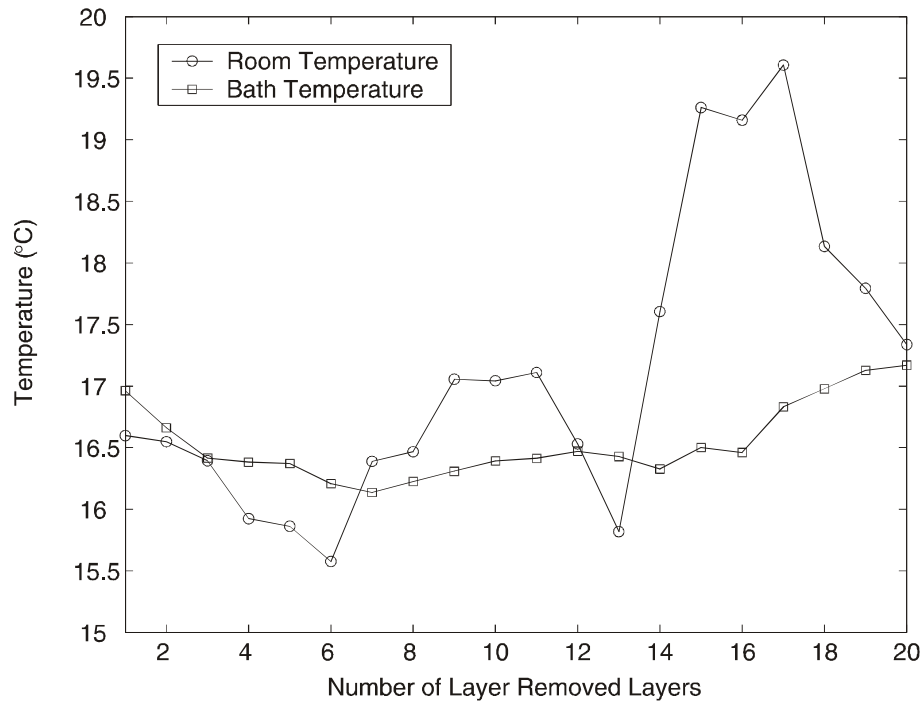


Figure 7.6 Variation of Room and Electrolytic Bath Temperatures.

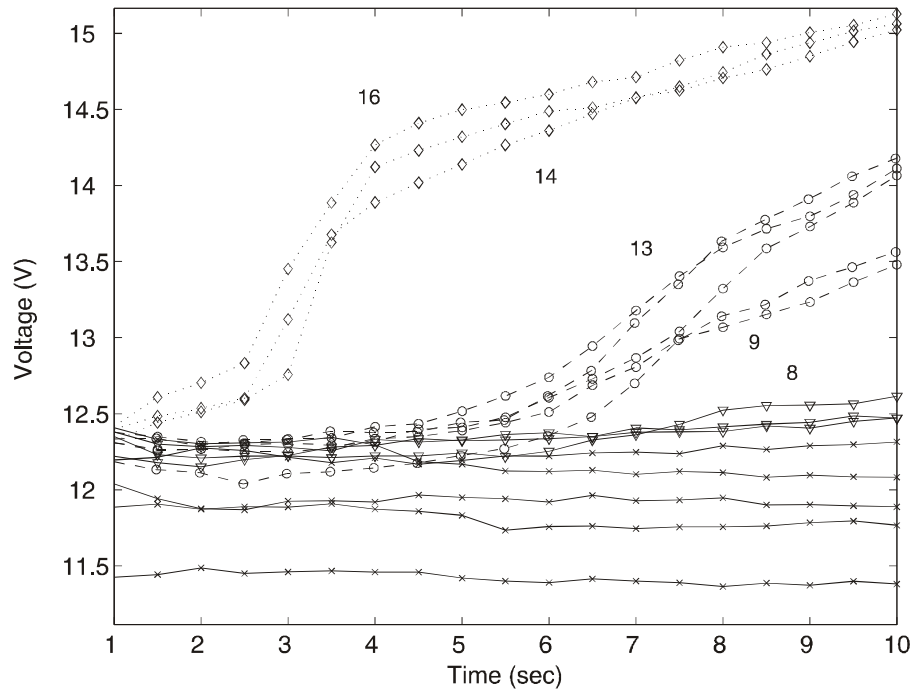


Figure 7.7 Variation in Voltage During Layer Removal.

Table 7.2 Estimation of Affected Layer Thickness with respect to Electro Chemical Machining Parameters.

No	Average Sample Thickness (μm)	Removed Layer Thickness (μm)	Total Removed Layer Thickness (μm)	
0	1737	0.0	0.0	
1	1731	5.9	5.9	
2	1729	1.9	7.8	White Layer
3	1727	2.1	9.9	
4	1722	4.5	14.4	
5	1714	8.5	22.9	
6	1712	2.1	25.0	
7	1706	5.4	30.4	
8	1703	3.4	33.8	
9	1699	3.9	37.7	Heat Affected Zone
10	1696	3.3	41.0	
11	1694	2.2	43.2	
12	1687	6.6	49.8	
13	1685	1.4	51.2	
14	1682	3.4	54.7	Base Metal
15	1677	4.8	59.5	
16	1673	4.6	64.1	

Total energy release due to single spark is given as

$$E_R = I_{av} U_{av} t_p \quad (7.18)$$

Results have shown a dependency with respect to energy release in following functional form (Figure 7.10, 7.17, 7.24, 7.31).

$$g = \gamma E_R^\beta \quad (7.19)$$

Here, γ and β are constant coefficients found after nonlinear curve fitting over experimental data (Table 7.4). This completes the required variables to determine residual stresses (Equation 7.17) in analyzed samples.

Table 7.3 Unit Shape Function Coefficients.

Dielectric	Electrode	a_2	a_3
Water	Graphite	0.0158504	0.0194815
Water	Copper	0.0146037	0.0085726
Kerosene	Graphite	0.0134824	0.0130720
Kerosene	Copper	0.0132371	0.0008234

Table 7.4 Gain Coefficients.

Dielectric	Electrode	$\gamma (\times 10^{-3})$	β
Water	Graphite	0.8854	0.3821
Water	Copper	0.80174	0.335
Kerosene	Graphite	0.86544	0.3718
Kerosene	Copper	0.8968	0.36

The residual stresses have been found to be tensile in nature. It increases from the surface and reaches to its maximum value. Then falls rapidly to relatively low values of compressive residual stresses (Figure 7.11, 7.12, 7.18, 7.19, 7.25, 7.26, 7.32, 7.33). Compressive stresses can be related to sample thickness, since residual stresses within plastically deformed layers are equilibrated with elastic stresses in the core of the material (Figure 7.13, 7.14, 7.20, 7.21, 7.27, 7.28, 7.34, 7.35). Intensity of the stresses does not change considerably with the amount of spark energy. This peak indicates ultimate tensile strength or, alternatively, equivalent hot strength value of the material.

7.3.1 Graphite Tool Electrode and De-Ionized Water as Dielectric Liquid

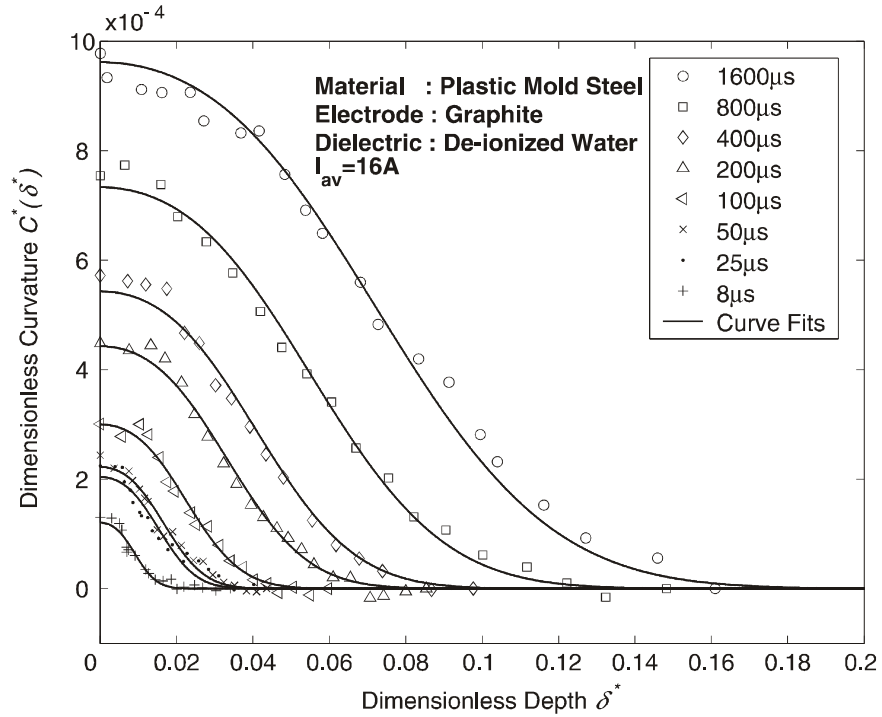


Figure 7.8 Change Curvature with respect to Removed Layer Thickness. (Electrode: Graphite, Dielectric: De-Ionized Water, $I_{av}=16\text{A}$)

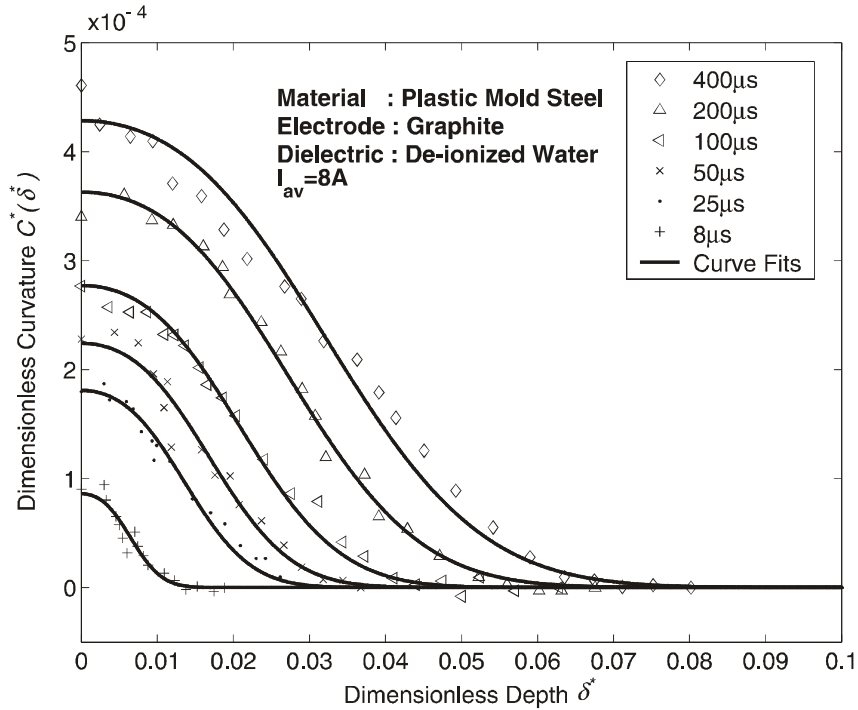


Figure 7.9 Change Curvature with respect to Removed Layer Thickness. (Electrode: Graphite, Dielectric: De-Ionized Water, $I_{av}=8\text{A}$)

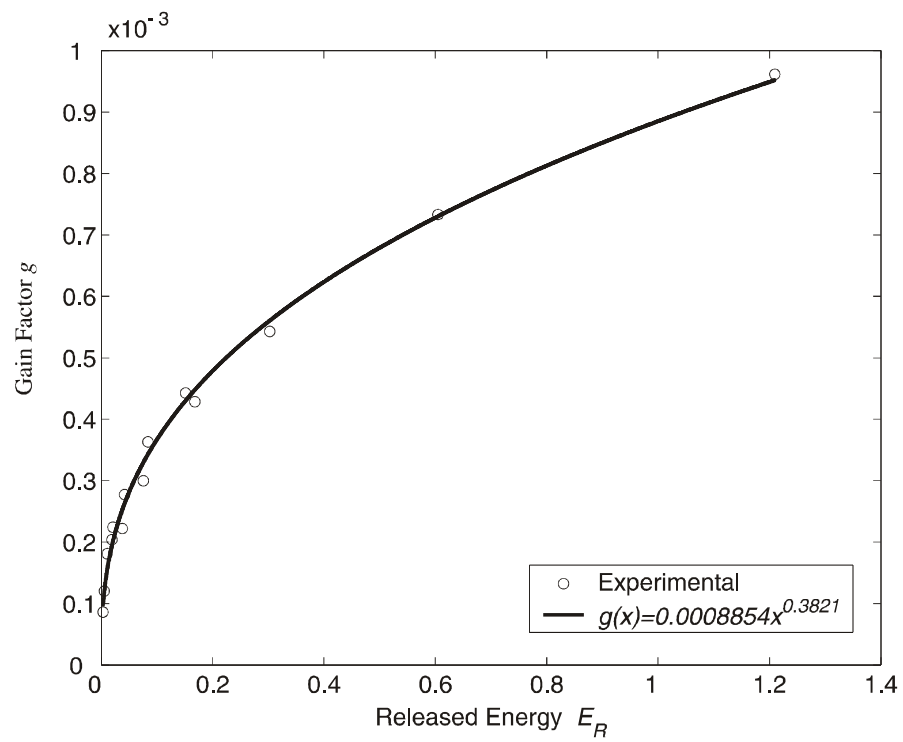


Figure 7.10 Change in Gain with respect to Released Energy.
 (Electrode: Graphite, Dielectric: De-Ionized Water)

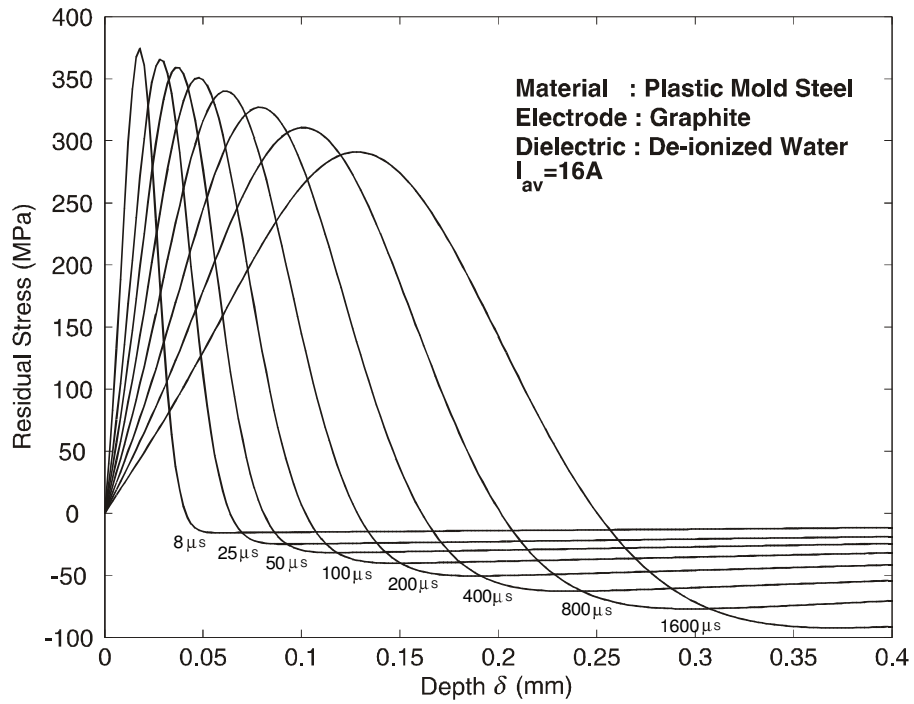


Figure 7.11 Residual Stresses in EDM'ed Surface.
 (Electrode: Graphite, Dielectric: De-Ionized Water, $I_{av}=16A$)

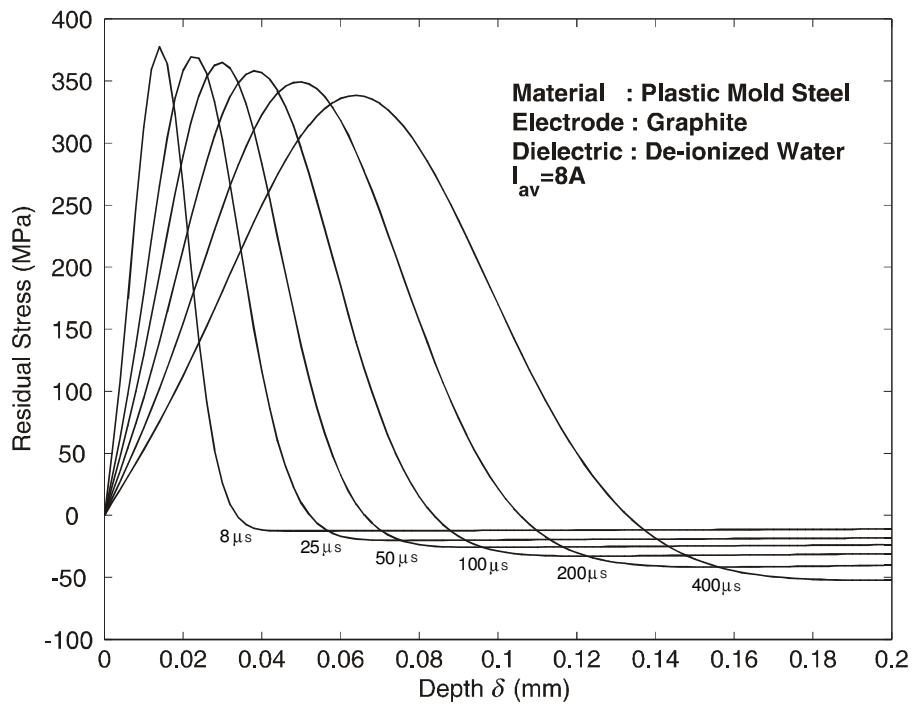


Figure 7.12 Residual Stresses in EDM'ed Surface.
 (Graphite, Dielectric: De-Ionized Water, $I_{av}=8A$)

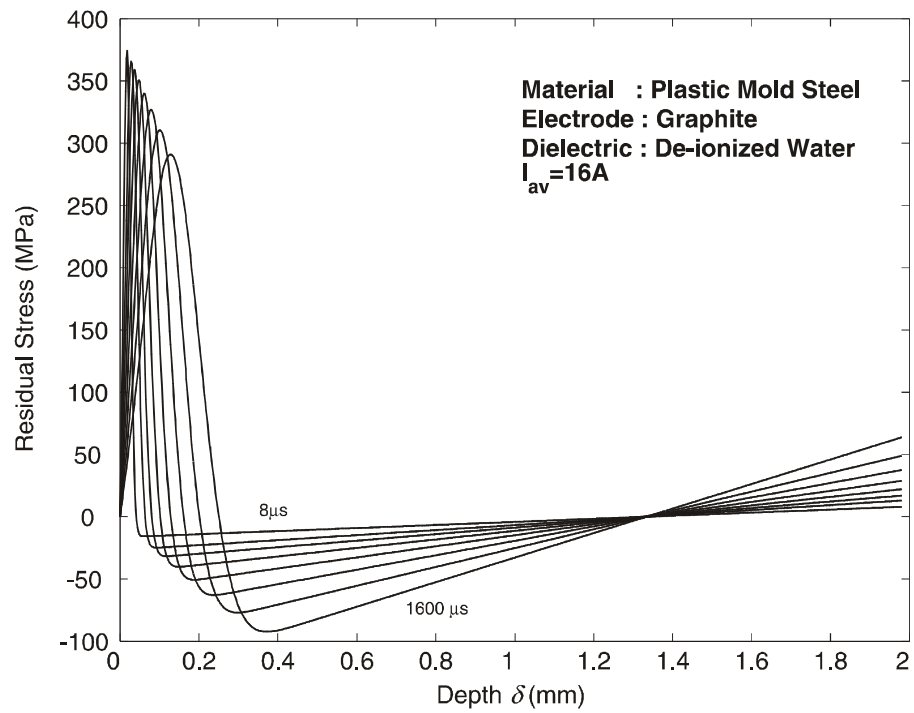


Figure 7.13 Residual Stresses in EDM'ed Surface Through the Thickness.
 (Electrode: Graphite, Dielectric: De-Ionized Water, $I_{av}=16A$)

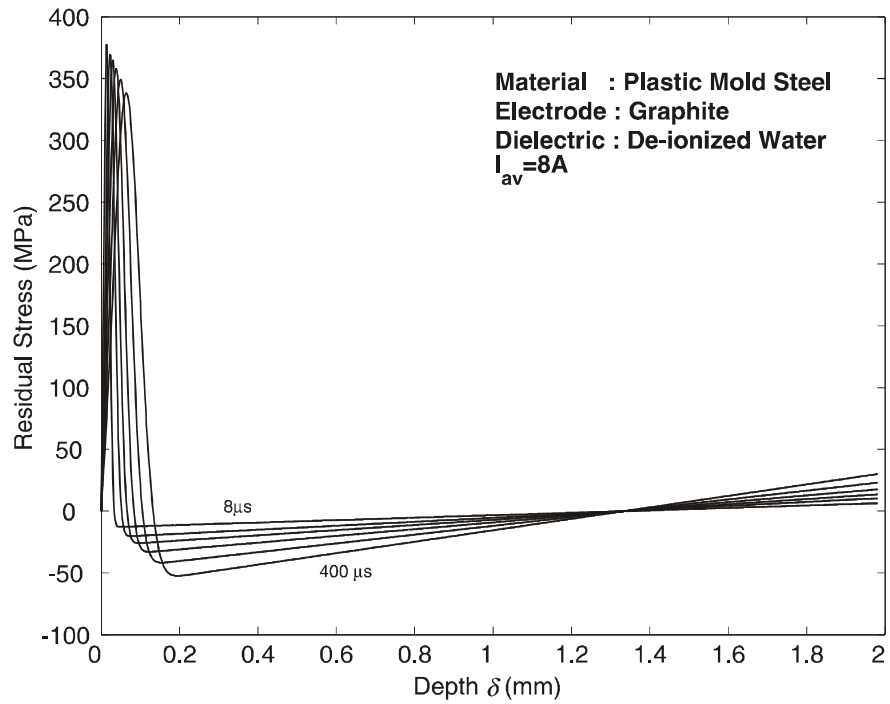


Figure 7.14 Residual Stresses in EDM'ed Surface Through the Thickness.
 (Electrode: Graphite, Dielectric: De-Ionized Water, $I_{av}=8A$)

7.3.2 Copper Tool Electrode and De-Ionized Water as Dielectric Liquid

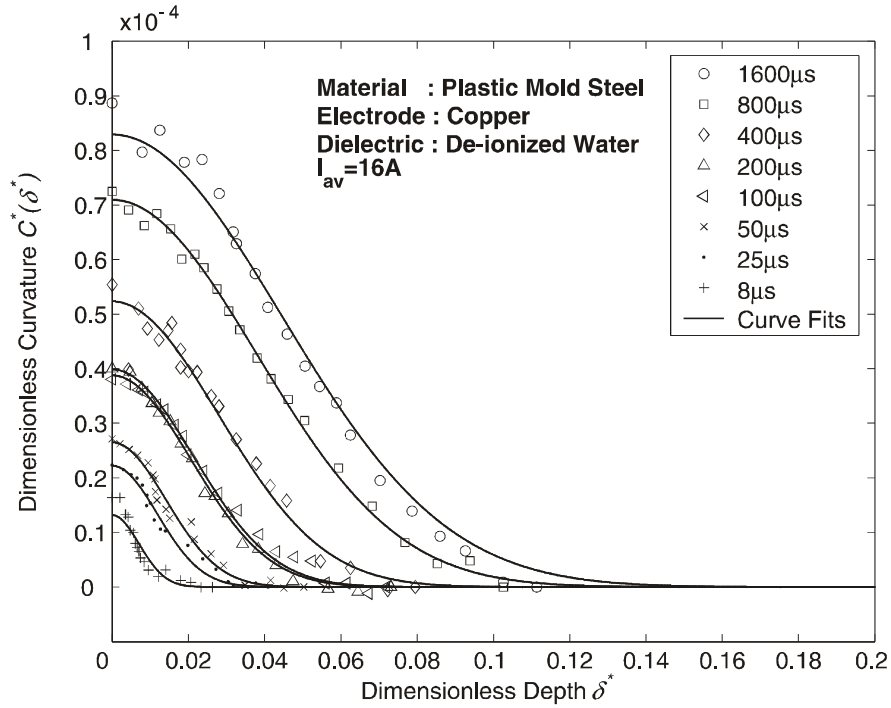


Figure 7.15 Change Curvature with respect to Removed Layer Thickness.
 (Electrode: Copper, Dielectric: De-Ionized Water, $I_{av}=16A$)

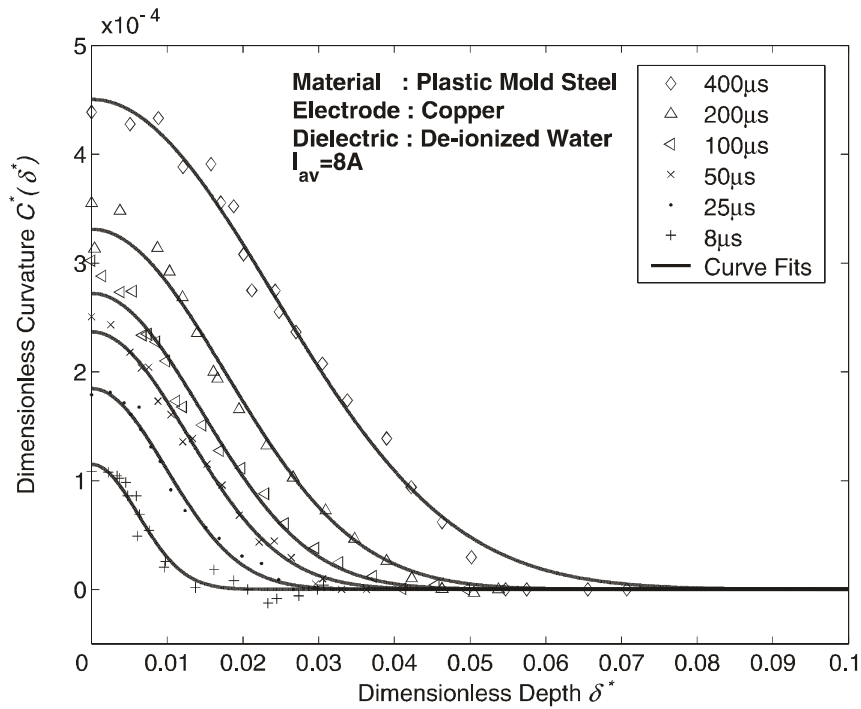


Figure 7.16 Change Curvature with respect to Removed Layer Thickness.
 (Electrode: Copper, Dielectric: De-Ionized Water, Water, $I_{av}=8A$)

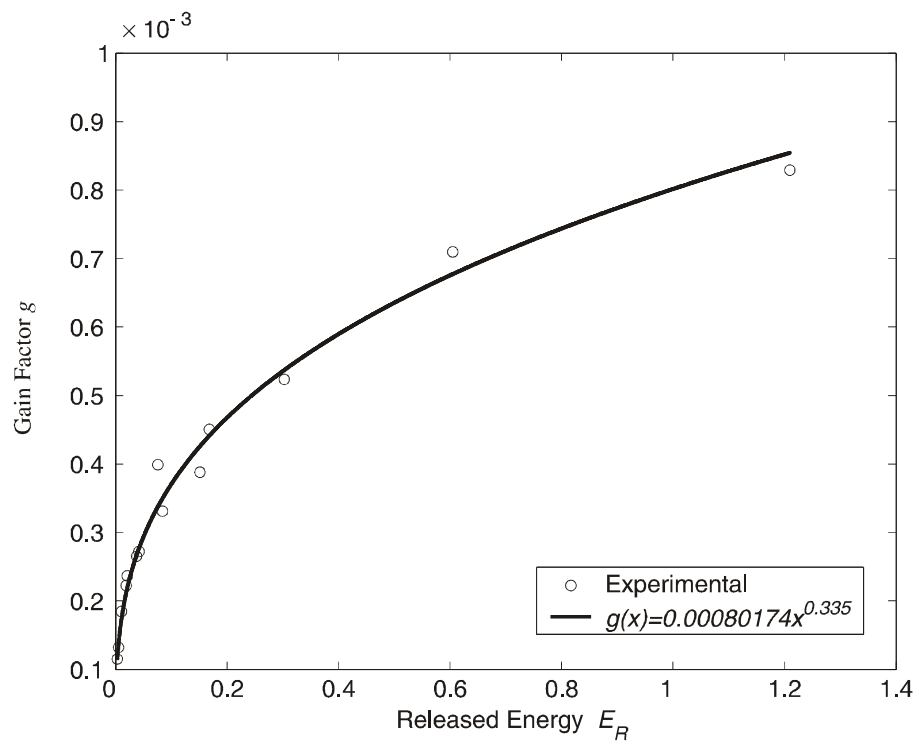


Figure 7.17 Change in Gain with respect to Released Energy.
 (Electrode: Copper, Dielectric: De-Ionized Water)

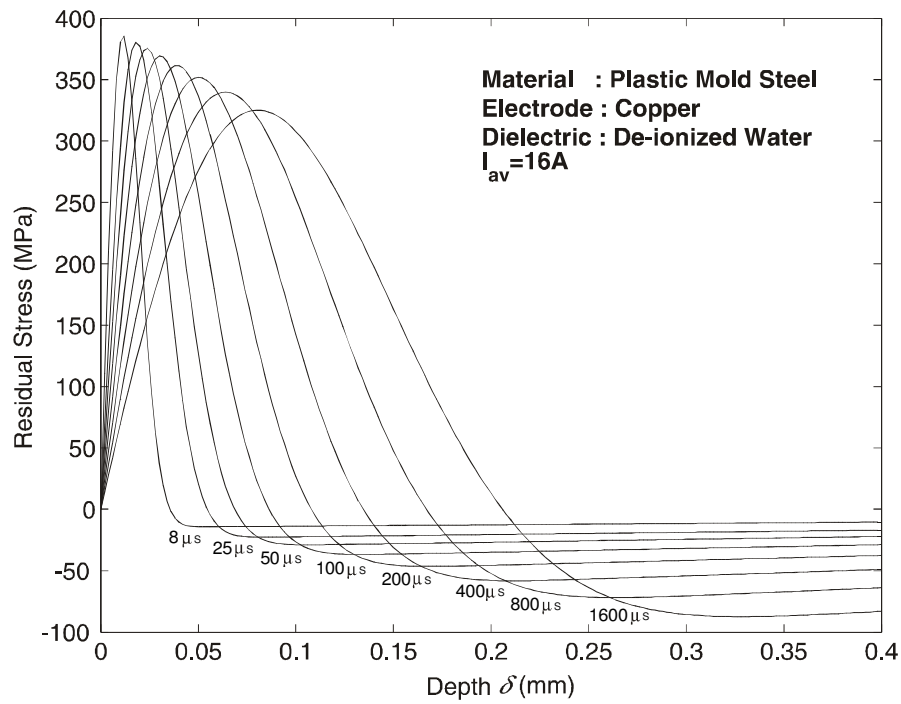


Figure 7.18 Residual Stresses in EDM'ed Surface.
 (Electrode: Copper, Dielectric: De-Ionized Water, $I_{av}=16A$)

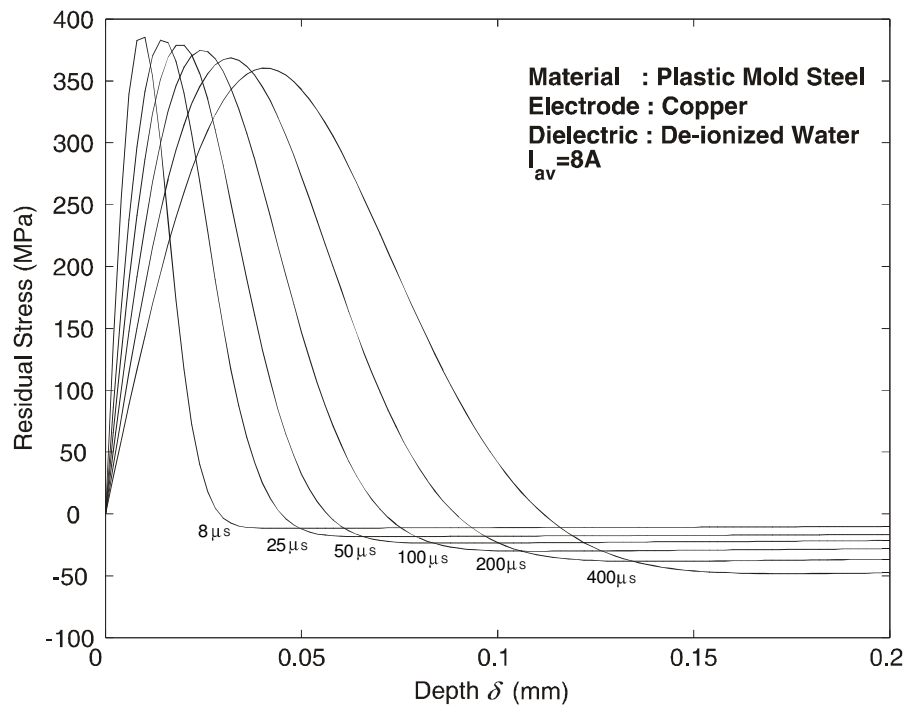


Figure 7.19 Residual Stresses in EDM'ed Surface.
 (Electrode: Copper, Dielectric: De-Ionized Water, $I_{av}=8A$)

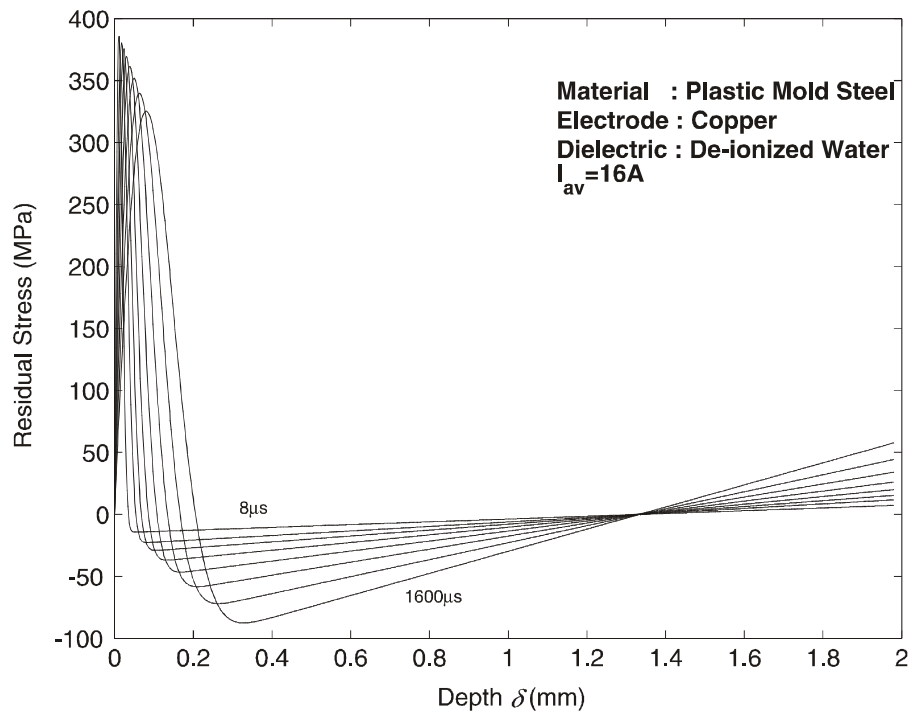


Figure 7.20 Residual Stresses in EDM'ed Surface Through the Thickness.
(Electrode: Copper, Dielectric: De-Ionized Water, $I_{av}=16A$)

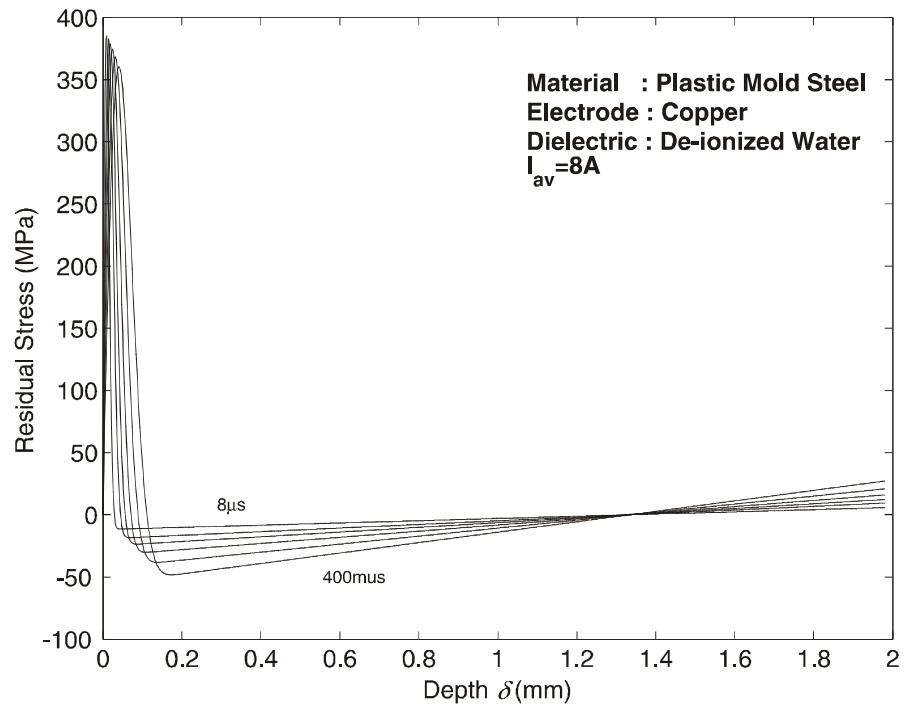


Figure 7.21 Residual Stress in EDM'ed Surface Through the Thickness.
(Electrode: Copper, Dielectric: De-Ionized Water, $I_{av}=8A$)

7.3.3 Graphite Tool Electrode and Kerosene as Dielectric Liquid

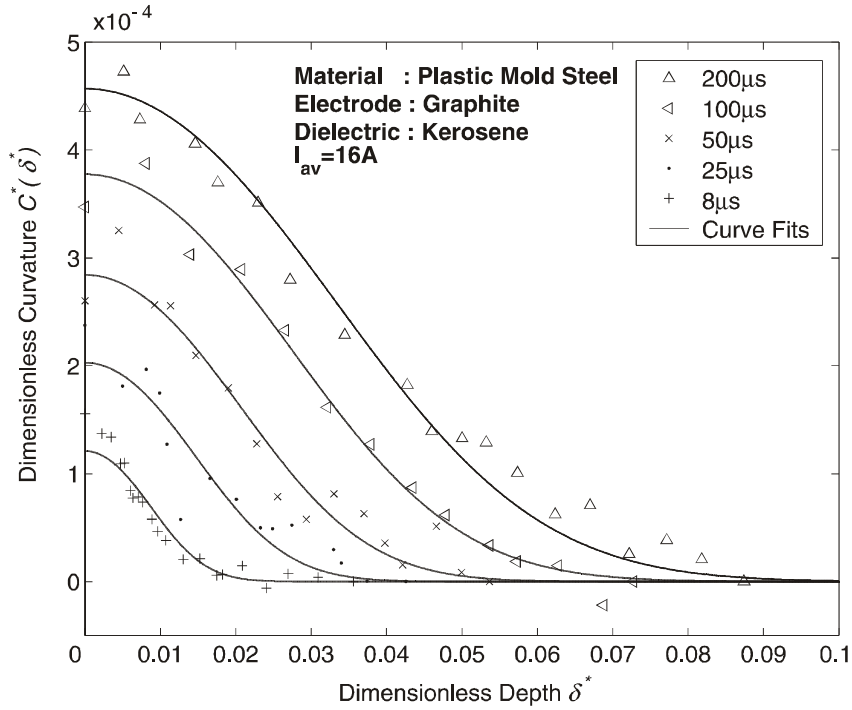


Figure 7.22 Change Curvature with respect to Removed Layer Thickness. (Electrode: Graphite, Dielectric: Kerosene, $I_{av}=16A$)

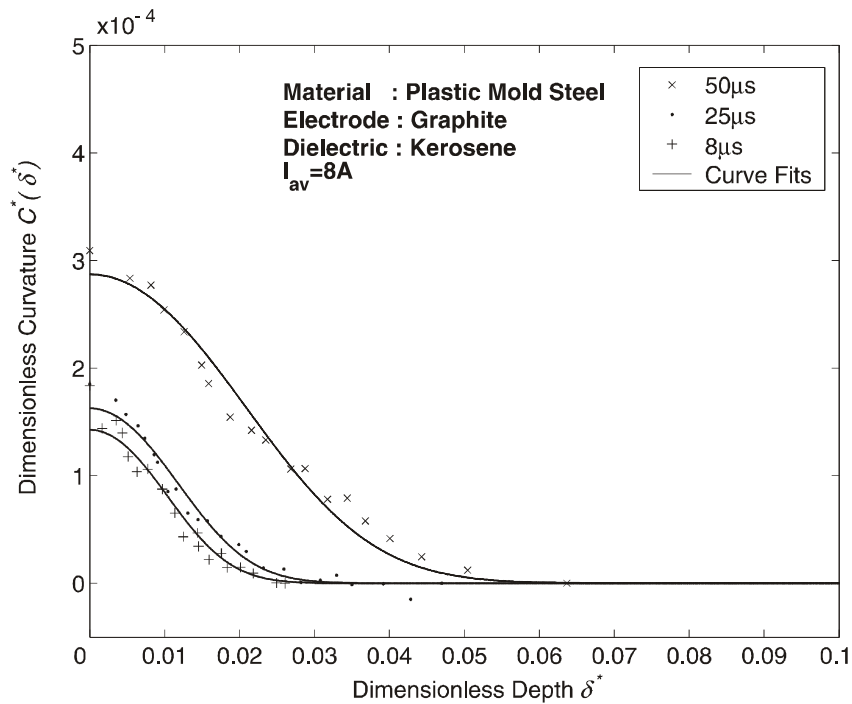


Figure 7.23 Change Curvature with respect to Removed Layer Thickness. (Electrode: Graphite, Dielectric: Kerosene, Water, $I_{av}=8A$)

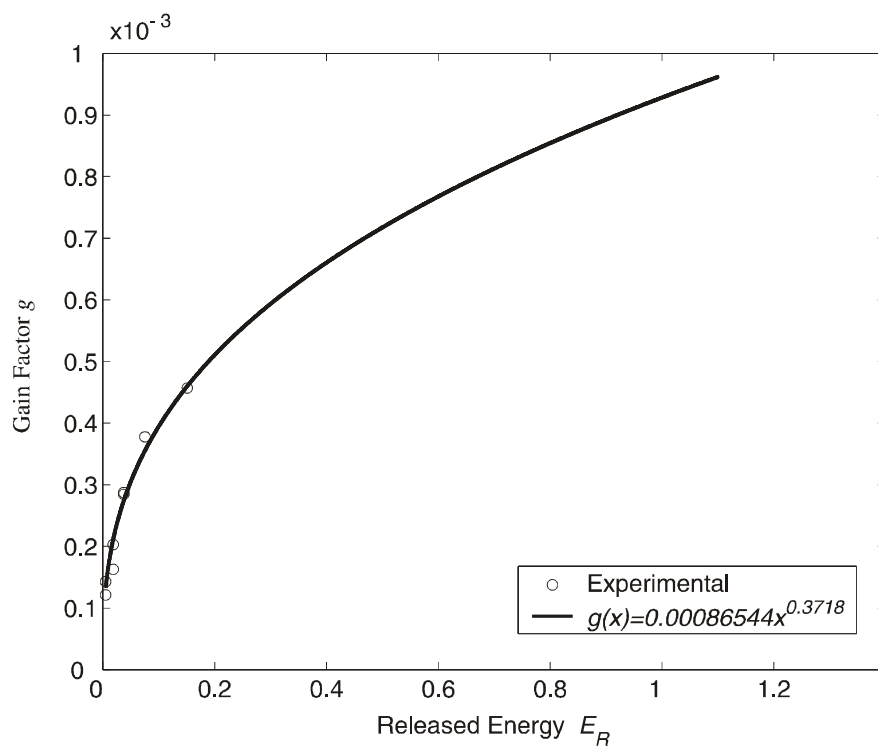


Figure 7.24 Change in Gain with respect to Released Energy.
 (Electrode: Graphite, Dielectric: Kerosene)

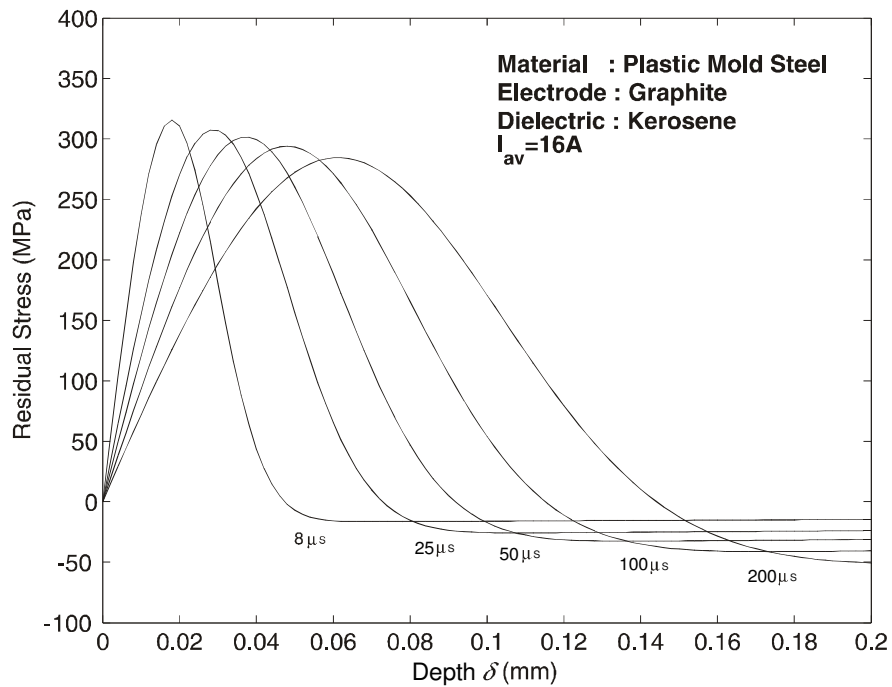


Figure 7.25 Residual Stresses in EDM'ed Surface.
 (Electrode: Graphite, Dielectric: Kerosene, $I_{av}=16A$)

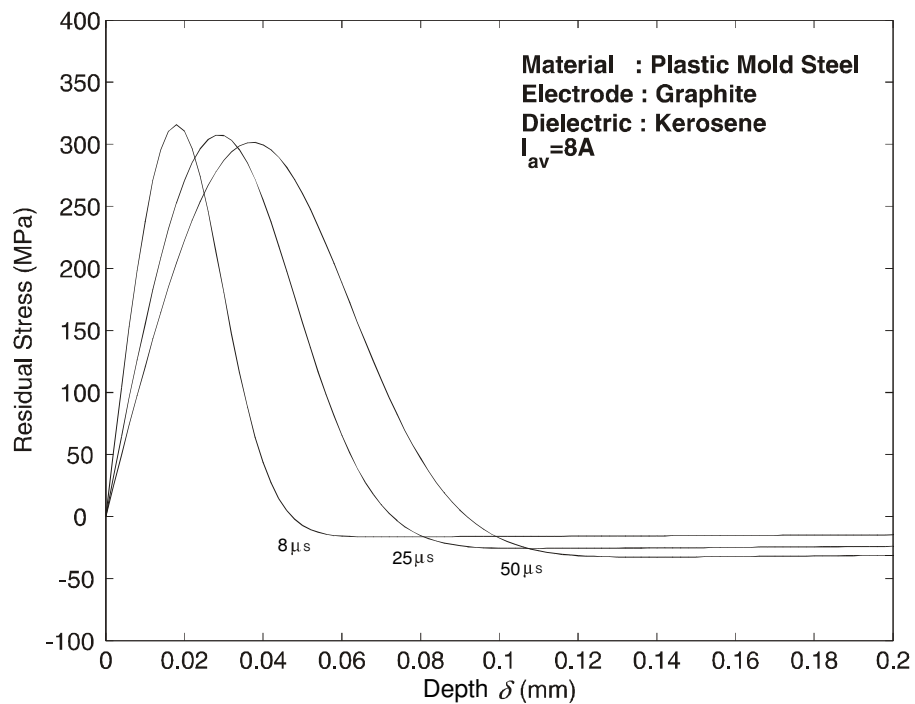


Figure 7.26 Residual Stresses in EDM'ed Surface.
 (Electrode: Graphite, Dielectric: Kerosene, $I_{av}=8A$)

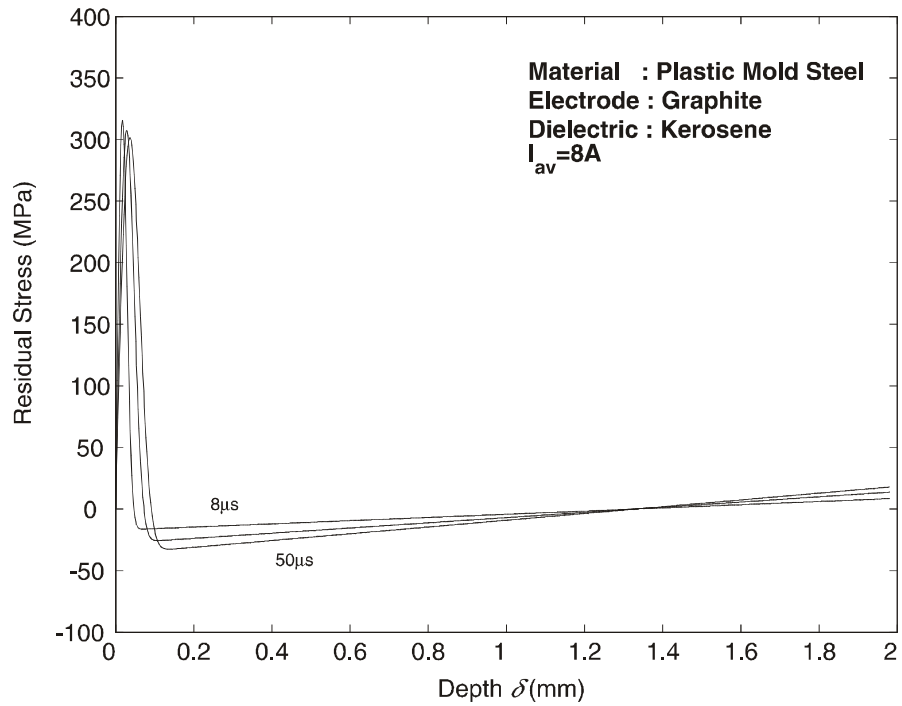


Figure 7.27 Residual Stresses in EDM'ed Surface Through the Thickness.
 (Electrode: Graphite, Dielectric: Kerosene, $I_{av}=16A$)

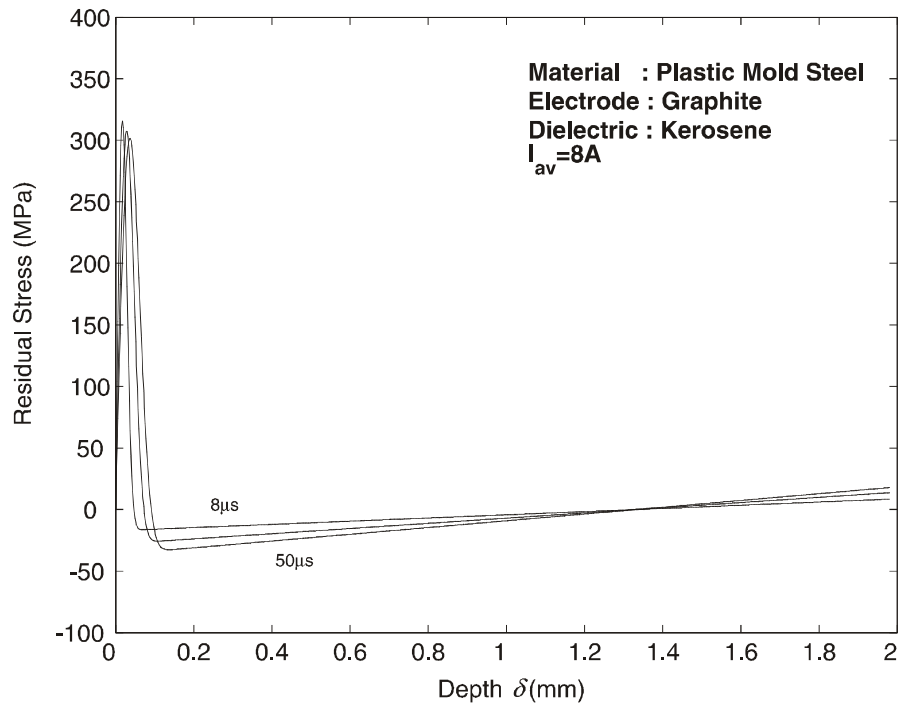


Figure 7.28 Residual Stress in EDM'ed Surface Through the Thickness.
 (Electrode: Graphite, Dielectric: Kerosene, $I_{av}=8A$)

7.3.4 Copper Tool Electrode and Kerosene as Dielectric Liquid

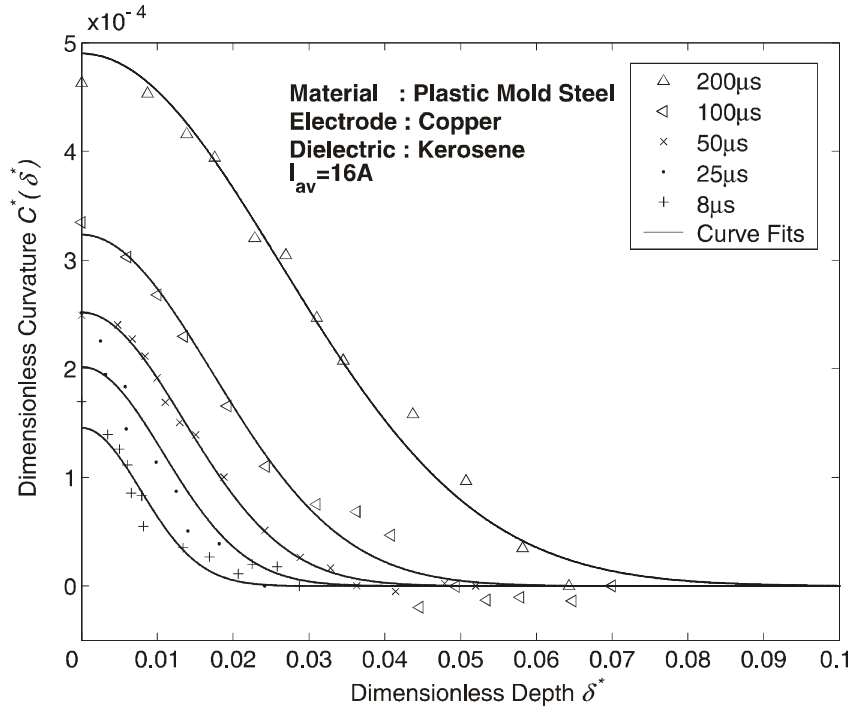


Figure 7.29 Change Curvature with respect to Removed Layer Thickness. (Electrode: Copper, Dielectric: Kerosene, $I_{av}=16A$)

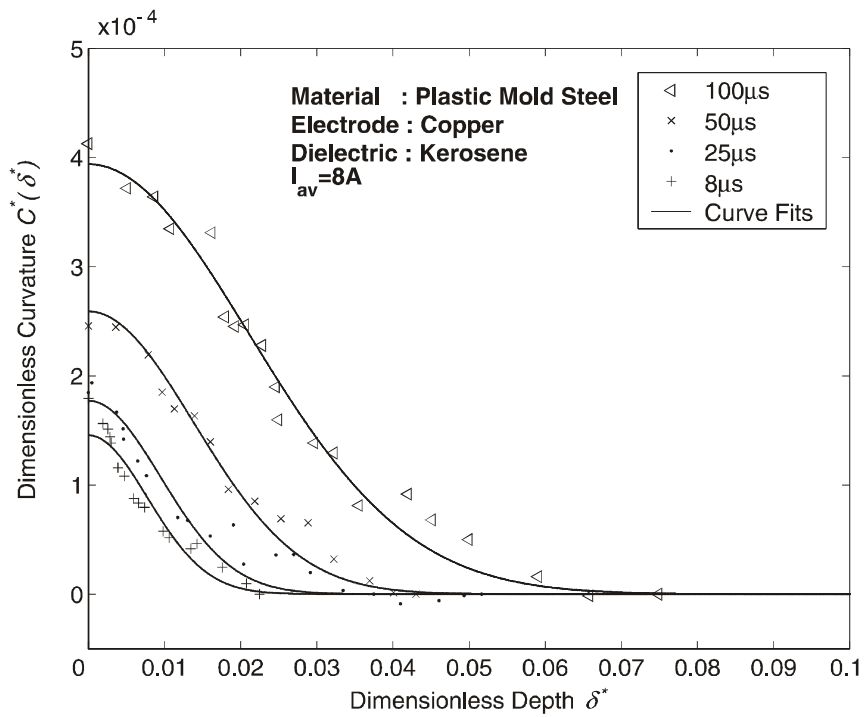


Figure 7.30 Change Curvature with respect to Removed Layer Thickness. (Electrode: Copper, Dielectric: Kerosene, Water, $I_{av}=8A$)

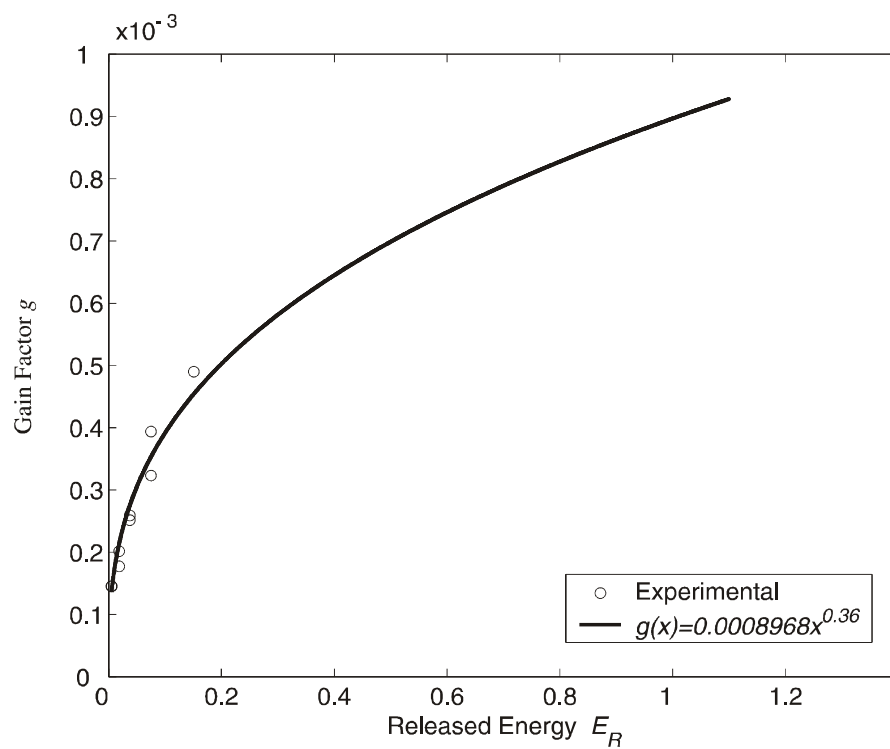


Figure 7.31 Change in Gain with respect to Released Energy.
(Electrode: Copper, Dielectric: Kerosene)

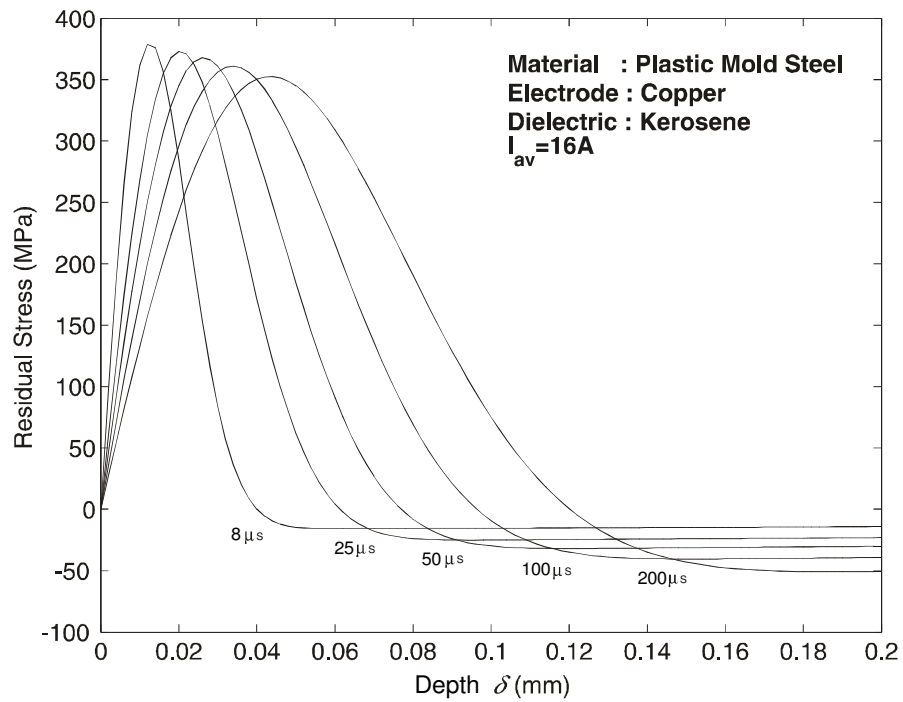


Figure 7.32 Residual Stresses in EDM'ed Surface.
 (Electrode: Copper, Dielectric: Kerosene, $I_{av}=16A$)

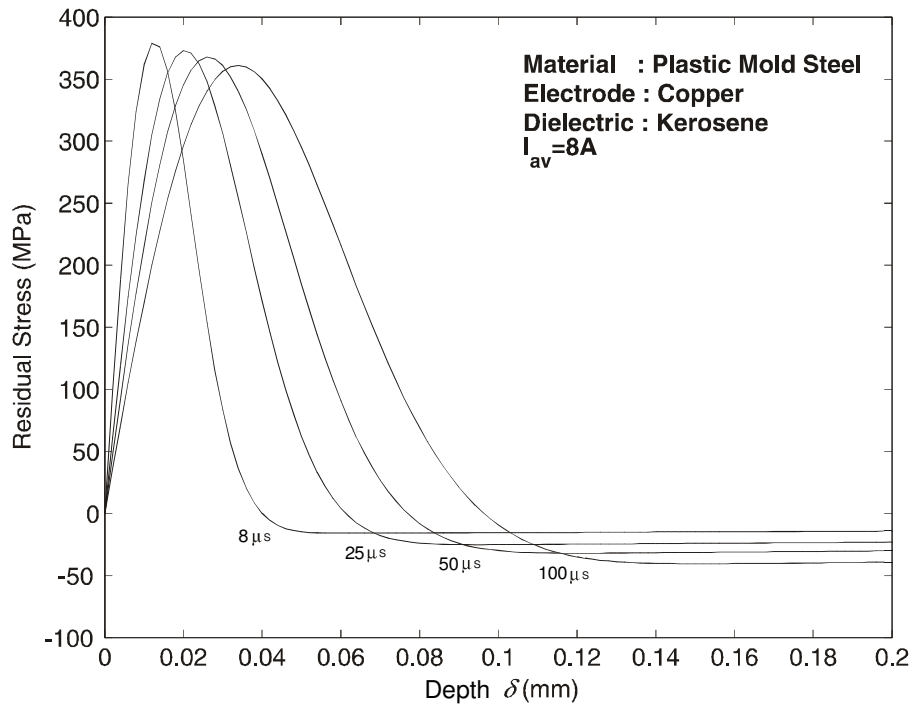


Figure 7.33 Residual Stresses in EDM'ed Surface.
 (Electrode: Copper, Dielectric: Kerosene, $I_{av}=8A$)

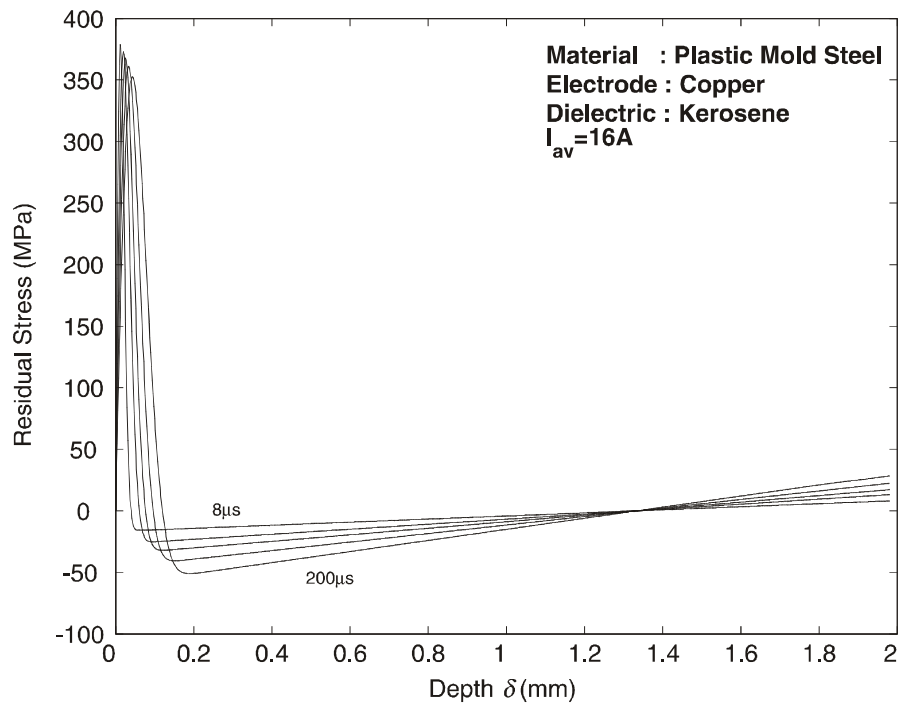


Figure 7.34 Residual Stresses in EDM'ed Surface Through the Thickness.
 (Electrode: Copper, Dielectric: Kerosene, $I_{av} = 16A$)

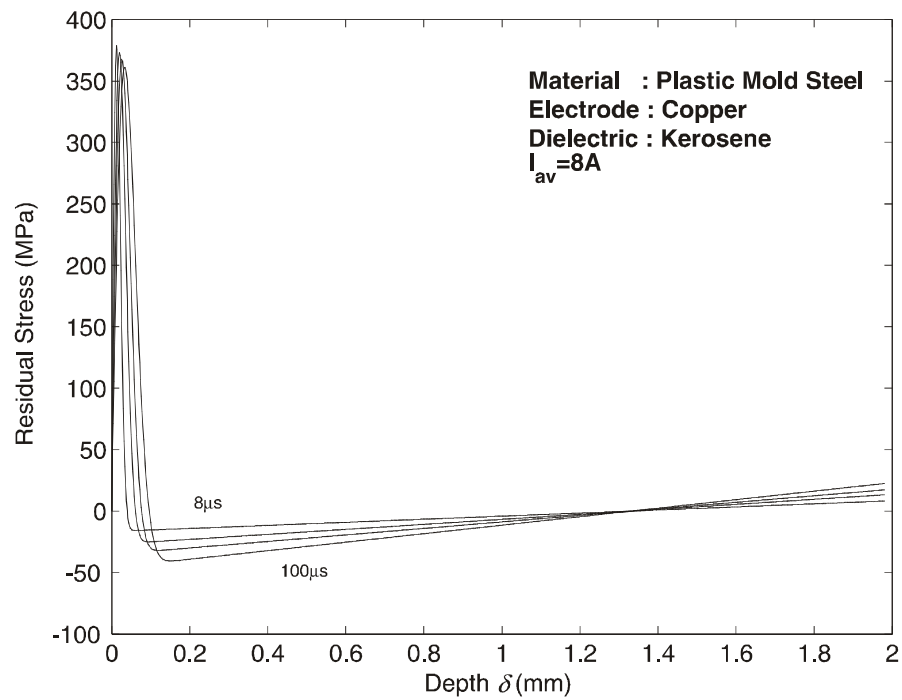


Figure 7.35 Residual Stress in EDM'ed Surface Through the Thickness.
 (Electrode: Copper, Dielectric: Kerosene, $I_{av} = 8A$)

CHAPTER VIII

FINITE ELEMENT ANALYSIS

8.1 Introduction

The high temperature gradients generated at the gap during EDM result in high and localized stresses in a small heat-affected zone. Experimental measurements have confirmed tensile residual stresses and it was found that these stresses could approach to a material hot strength value within thermally affected subsurface layers.

Material removal in this process is through melting and vaporization at the workpiece surface as a result of heat flux that is applied by the plasma discharge. Various theoretical and numerical approaches have been proposed to explain the basic phenomenon of EDM process. Previous published works on such efforts were summarized in Chapter II. This Section is devoted to the modeling efforts and its results.

A finite element based model is developed to estimate the residual stresses distribution due to EDM. A commercial finite element software ANSYS is used for this purpose. The Gaussian heat input model is used to approximate the heat from the plasma. Convective heat transfer boundary conditions are applied on the surface that is exposed to the dielectric. Results are obtained by using thermal-structural coupled field elements and all of the boiled material and a fraction of melted material are removed from the domain at the end of pulse duration.

8.2. Single Spark Solution

Conduction heat transfer within the workpiece is governed by the well-known diffusion equation. Following assumptions are made due to the random and complex nature of EDM.

- i) The domain is axisymmetric.
- ii) The workpiece material is homogenous and isotropic.
- iii) The heat transfer to the workpiece is by conduction.
- iv) The workpiece material is stress-free before EDM.
- v) Gaussian heat flux distribution on spark incident surface of the workpiece material during pulse time period.
- vi) Inertia and body force effects are negligible during stress development.

A small cylindrical portion of the workpiece around the spark is taken as the domain. Energy transferred to the workpiece as heat input and pressure serves the thermal and solid boundary conditions respectively. The heat loss due to dielectric liquid on the non-spark incident surface is modeled using convective boundary conditions. Other boundaries are such distances away from the heat source where there is no heat transfer across them (Figure 8.1).

When $t > 0$, then the boundary condition for the spark incident surface is such as,

$$k \frac{\partial T}{\partial z} = \left\{ \begin{array}{ll} h_c(T - T_\infty) & \text{if } r > R \\ q_s & \text{if } r \leq R \\ h_c(T - T_\infty) & \text{for pause time} \end{array} \right\} \quad (8.1)$$

$$\sigma_z = \left\{ \begin{array}{ll} 0 & \text{if } r > R \\ p_s & \text{if } r \leq R \\ 0 & \text{for pause time} \end{array} \right\} \quad (8.2)$$

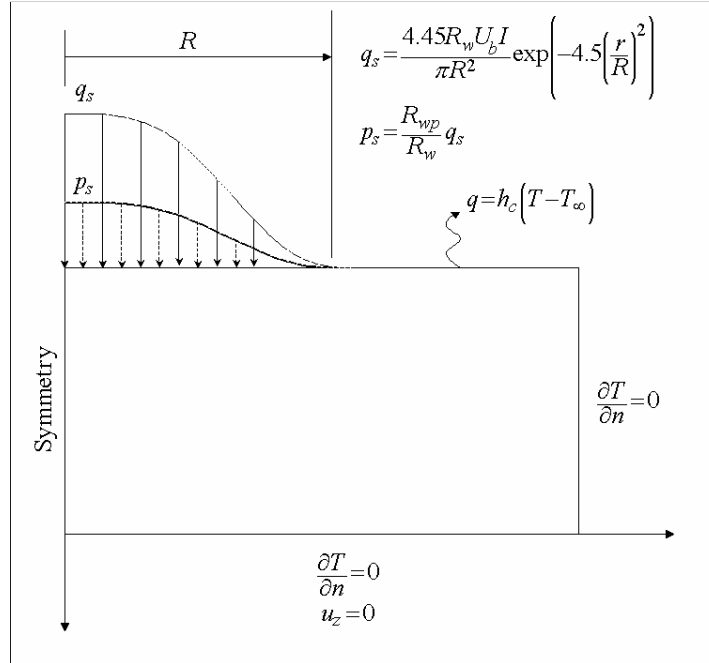


Figure 8.1 Theoretical Model for Single Spark.

Heat transfer coefficient (h_c) and room temperature (T_∞) is taken as 10 kW/m²K and 300 °K respectively.

It is known that the electrode material and dielectric liquid influence the spark radius during machining. Measurement of the spark radius is extremely difficult and no comprehensive information for the evaluation of the spark radius (R) is available in the literature. Hence, this quantity is taken as a constant. However, the effect of change in spark radius is analyzed with parametric simulations around the suggested values (Table 8.1).

The energy partitions (R_w) and (R_{wp}) that are the percentage of heat and pressure input to the workpiece should be known for computational analysis. Most of the researchers have assumed this ratio as a constant fraction of total power transferred to the electrodes. The parameter (R_{wp}) is currently introduced and a parametric study is also performed together with suggested values of (R_w) to estimate the affects on the results (Table 8.1).

Table 8.1 Parametric Simulations

R (μm)	R_w (%)	R_{wp} (%)
95	6	0
110	8	0.1
125	10	0.2
-	-	0.4
-	-	0.8

Temperatures calculated by a transient thermal analysis are used as input to structural analyses for thermal evaluations. Coupling is handled by calculating element matrices or element load vectors that contain all necessary terms. For this purpose, a thermal-stress analysis using the 4 node coupled field element PLANE13 is performed. The Newton-Raphson Method, which is an iterative process for solving the nonlinear equations with line search options, is used for the analyses.

8.2.1 Material Model

High local temperatures are achieved on the point where the plasma struck to the workpiece and result in extreme non-uniformities due to local thermal expansion of the material, which lead to high thermal stresses. The local part is then returned to its initial room temperature in a matter of few microseconds after end of discharge and result in high residual stresses. Consequently, each process cycle leads highly fluctuating temperatures ranging from room to material boiling temperatures. Therefore, temperature dependent material model are vital for modeling the process. Density of the workpiece material is taken as constant due to negligible variations in the working range.

Temperature dependent material properties are very close to common tool steel that is used also in the experimental studies (Table 8.2, 8.3). Temperature dependent bilinear isotropic hardening model is proposed to describe the plastic behavior of the material during EDM (Figure 8.2).

Table 8.2 Temperature Dependent Thermal Conductivity, Specific Heat and Modulus of Elasticity

T ($^{\circ}\text{K}$)	E (GPa)	T ($^{\circ}\text{K}$)	c_p (J/Kg $^{\circ}\text{K}$)	T ($^{\circ}\text{K}$)	k (W/m $^{\circ}\text{K}$)
300	210	343	573.2	300	49
600	193	483	598.7	600	41.7
900	165	1025	611	882	24.88
1200	120	1543	917.9	1476	13.807
				1626	10.863

Table 8.3 Temperature Dependent Thermal Expansion Coefficient

T ($^{\circ}\text{K}$)	α_e ($^{\circ}\text{K}^{-1}$)
293	1.1×10^{-5}
393	1.1×10^{-5}
473	1.25×10^{-5}
573	1.27×10^{-5}
673	1.33×10^{-5}
773	1.4×10^{-5}
873	1.41×10^{-5}

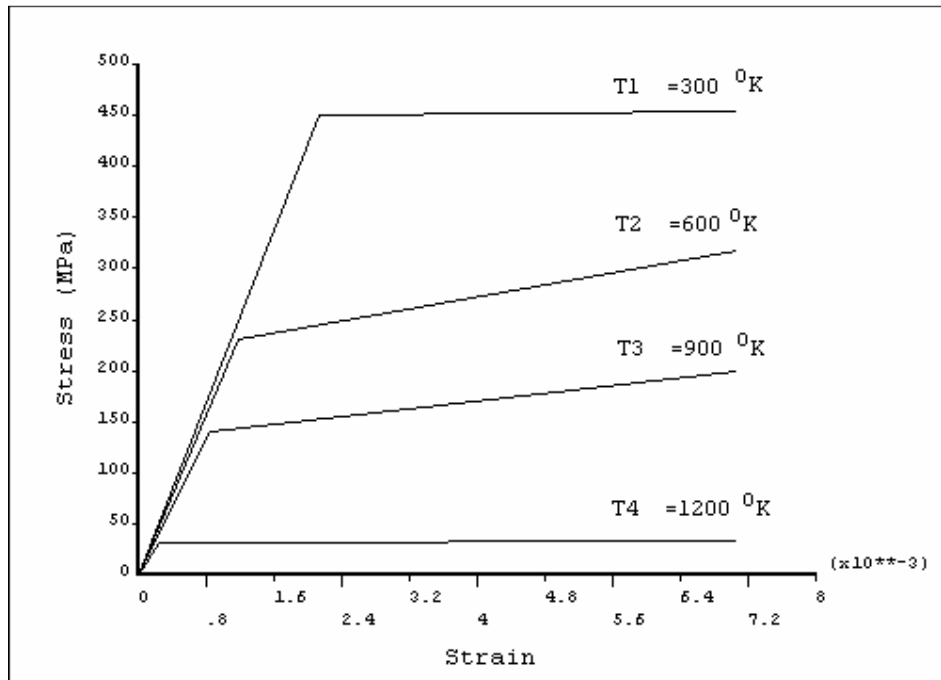


Figure 8.2 Temperature Dependent Bilinear Isotropic Hardening.

8.2.2 Finite Element Mesh

The working domain is defined as a rectangle whose dimension is equal eight times of the final plasma radius (R) (Figure 8.3). Rectangular elements are located in a square whose dimension is equal final plasma radius (R) and placed on the upper left corner of the domain. In this sub domain finer patterned mesh, where element size decreases with respect to edge length with a constant ratio is utilized to capture refined results at the spark incident surface (Figure 8.4). The remained portion of the domain is meshed also in patterned fashion but in a coarser manner due to less variation of temperatures and stresses. Infinite boundary conditions were also checked for larger sizes of the edge and no remarkable changes could be detected within the results. Command listing of the model for ANSYS software is given in Appendix C.

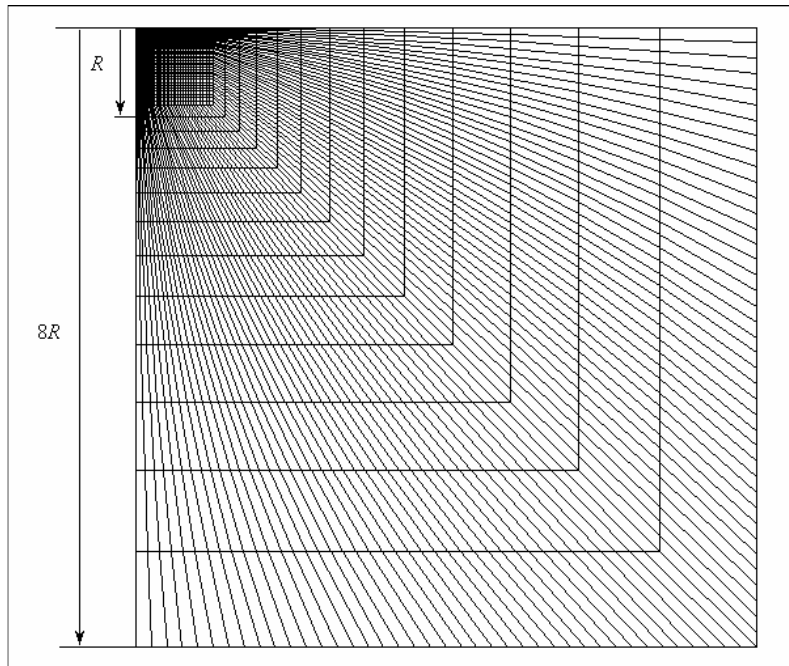


Figure 8.3 Finite Element Mesh in EDM Domain.

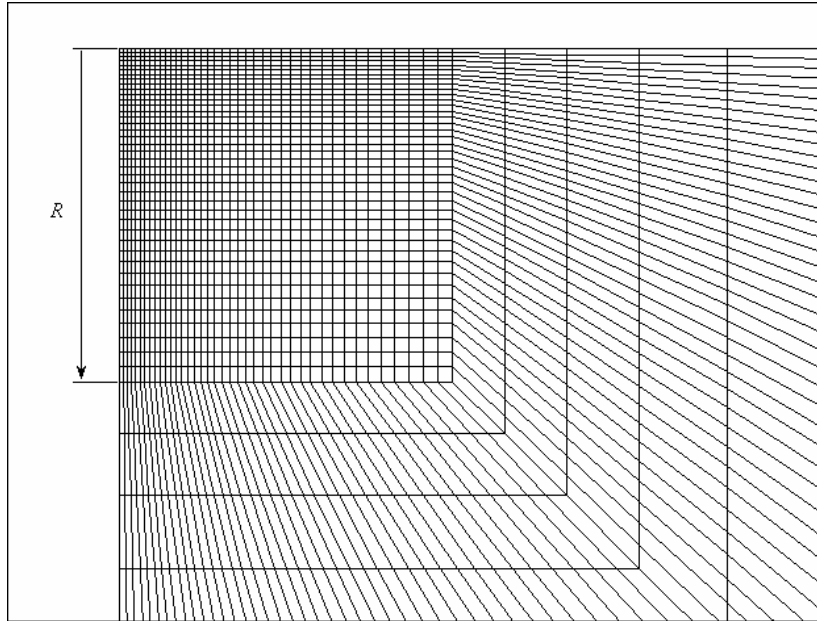


Figure 8.4 Finite Element Mesh in EDM Domain.
(Enlarged on the Spark Incident Surface)

8.2.3 Results

The spark incident surface exposed to convection for the time period, which is required for the workpiece material to return its initial temperature. The total time elapsed for the process is fixed as the 40 times of the pulse period. Time steps are non-uniformly divided such as to ensure convergence of the solution. Time steps during loading and just after unloading kept minimal as 1/40 of the pulse period and then increased to pulse period for decreasing the computational time. All of the boiled material and a fraction of melted material are removed from the model at the end of pulse duration by killing the elements whose temperatures exceeding 2543 °K. Results are categorized as the spark radius, energy partition to the workpiece as heat and pressure. All results are belong to 100 μ s pulse duration, $R=110 \mu\text{m}$, $R_w=0.08$ and $R_{wp}=0$ if otherwise is not specified.

It is known that temperature pattern at the end of pulse duration is a key point to estimate phase transformation of the material. The phase changes from solid to liquid and to gas at regions that have temperatures higher than the melting point.

While the fusion zone experiences solid-liquid transformation, the heat-affected zone experiences solid-solid phase transformation. This transformation is initiated at approximately 1000 °K. Once this temperature is exceeded the parent material transforms to austenite. Subsequently, as the austenite cools several daughter phases, such as ferrite, pearlite or bainite could be created. The cooling rate is an important factor to estimate such changes. In EDM process cooling rate is extremely high and thus expected that most of the heat-affected zone will have transformed to martensite.

In this model, it is possible to predict the extent of the re-solidified molten layer known as 'white layer' and the heat affected zone that mostly contains martensitic material. For this purpose temperature counters at the end of pulse duration was plotted. The region between 2543 and 1812 °K isotherms is assumed as re-solidified molten layer and the region between 1812 and 100 °K as heat-affected zone. Time history of the first analyzed case is also presented to explore the affected sub-layers during machining. Finally, residual stress at the end of cooling cycle also presented for each case.

8.2.3.1 Results at the End of Pulse Time

The crater produced after single spark is shallow shaped with width to depth ratio approximately as 4.4 (Figure 8.5). The depth of heat-affected layer is found about 11 μm whereas the molten zone is approximately 2 μm (Figure 8.6). High compressive stresses are developed on radial direction (Figure 8.7). Tensile stresses can be observed below the crater base. Axial component of stresses in z direction (Figure 8.8) and shear stress component (Figure 8.9) are found small when compared with the radial stresses component at the end of pulse duration. It should be noted that the results are obtained without applying pressure on the sparking surface. The effect of the applied pressure on the surface will be discussed later.

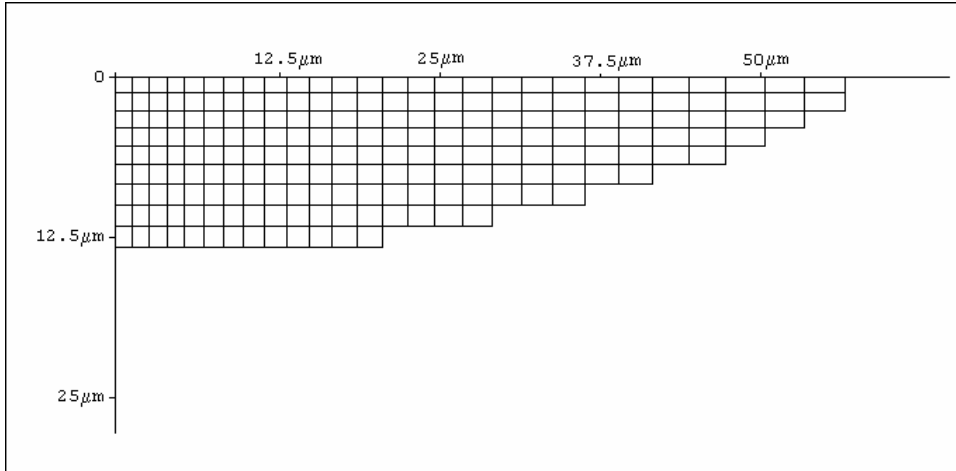


Figure 8.5 Removed Elements from the Spark Domain at the End of Pulse.

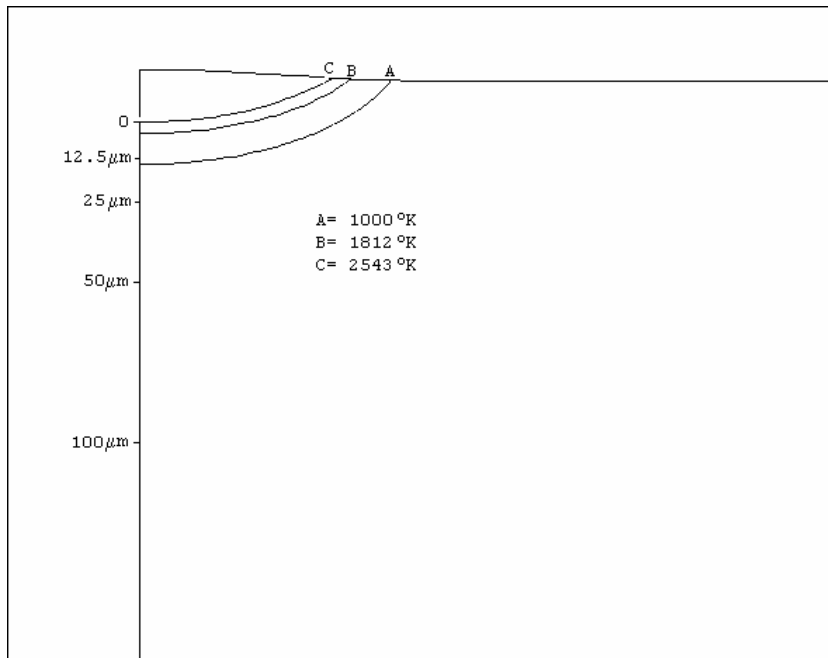


Figure 8.6 Temperature Isotherms at the End of Pulse.

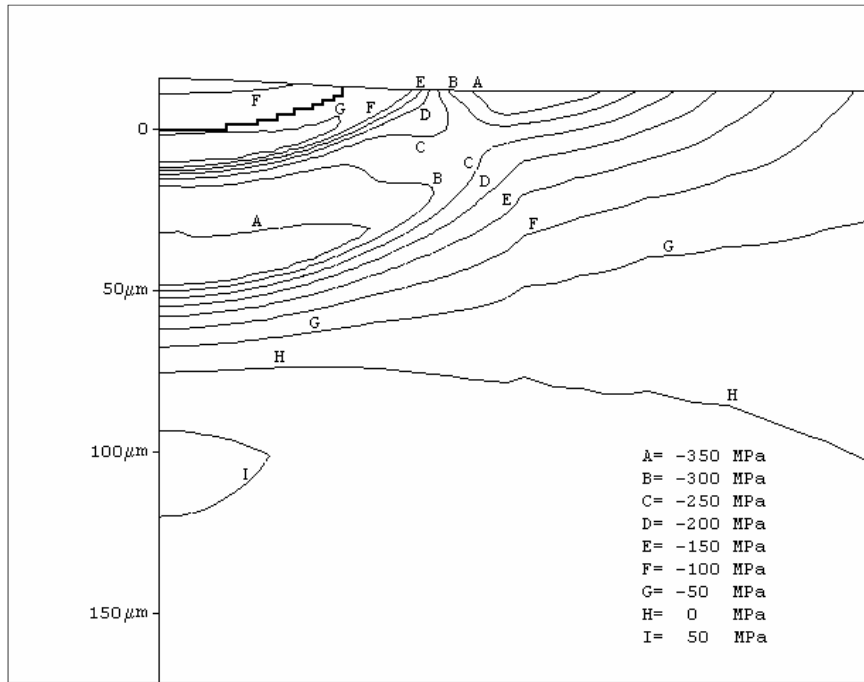


Figure 8.7 Radial Stress Component (σ_r) at the End of Pulse.

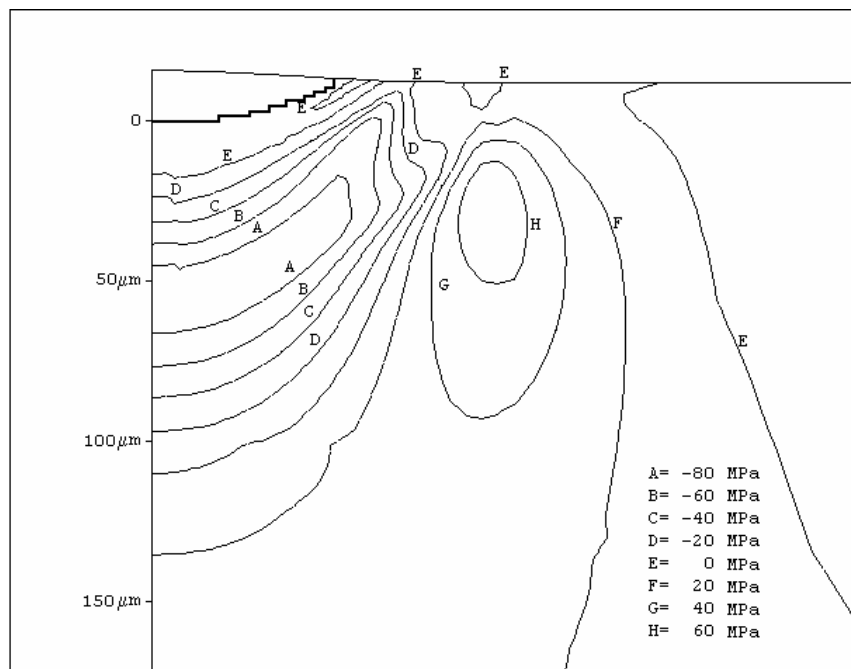


Figure 8.8 Axial Stresses Component in z Direction (σ_z) at the End of Pulse.

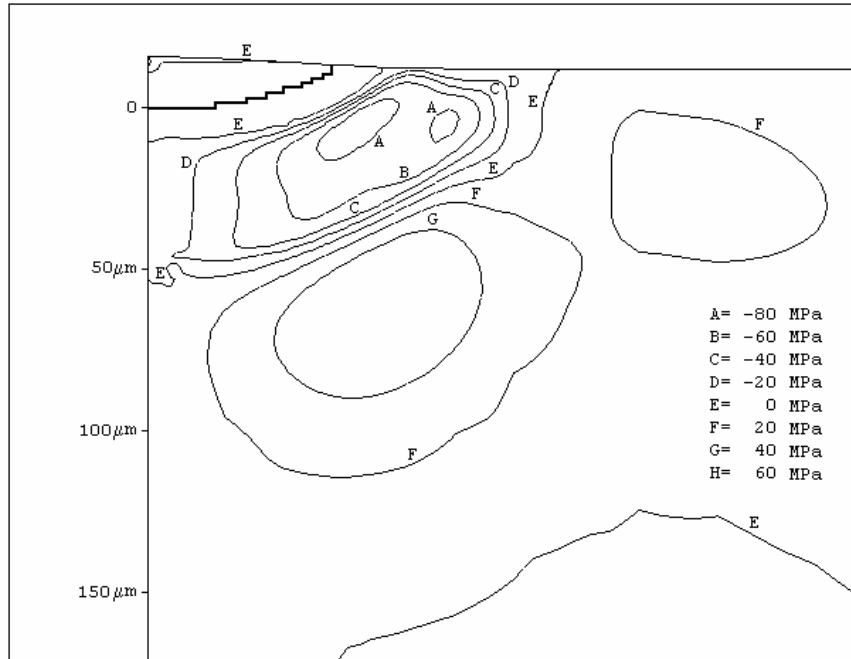


Figure 8.9 Shear Stresses Component (σ_{rz}) at the End of Pulse.

8.2.3.2 Residual Stresses

The results indicate that high radial component of tensional residual stress occurs just beneath the surface (Figure 8.10). These stresses reaches to its peak value within 30 μm below the crater base and then follows with a sharp decrease reaching up to compressive residual stress at the end of cooling cycle. Axial (Figure 8.11) and shear component of residual stresses (Figure 8.12) is also to be found small when compared with the radial component of stresses. For a clear visualization, 3 different paths are defined on working domain (Figure 8.13) and all components of stresses are plotted with respect to path length (Figure 8.14-8.16). Stresses on symmetry and diagonal paths show a small variation of radial stresses within the affected layers and than substantially decrease to compressive residual stresses approaching to remarkable values around 200 MPa. On symmetry path, residual stresses started to increase from the crater base to its maximum value and then decreased without showing compressive residual stresses. For all paths, the maximum tensile residual stress is found to be around 600 MPa.

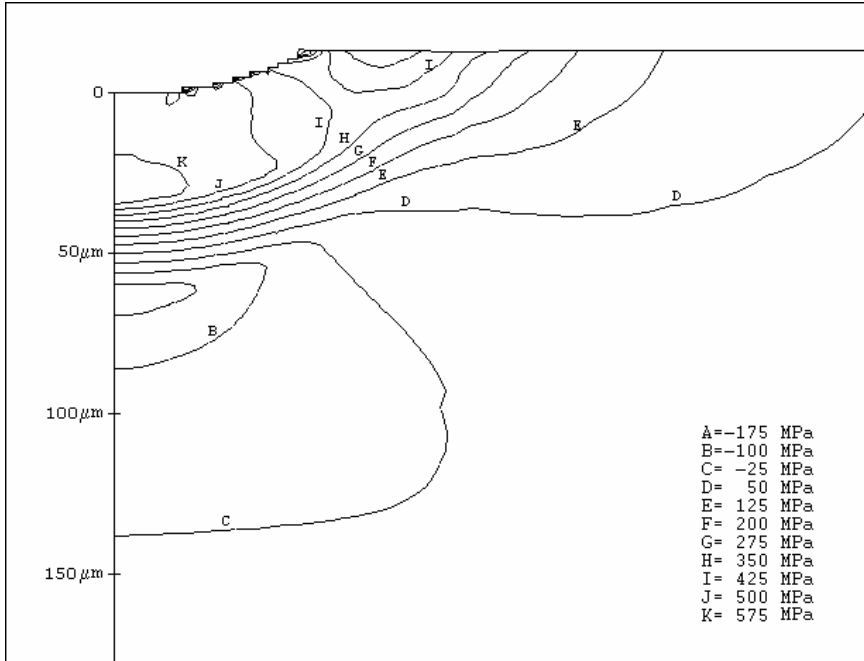


Figure 8.10 Radial Component of Residual Stresses (σ_r).

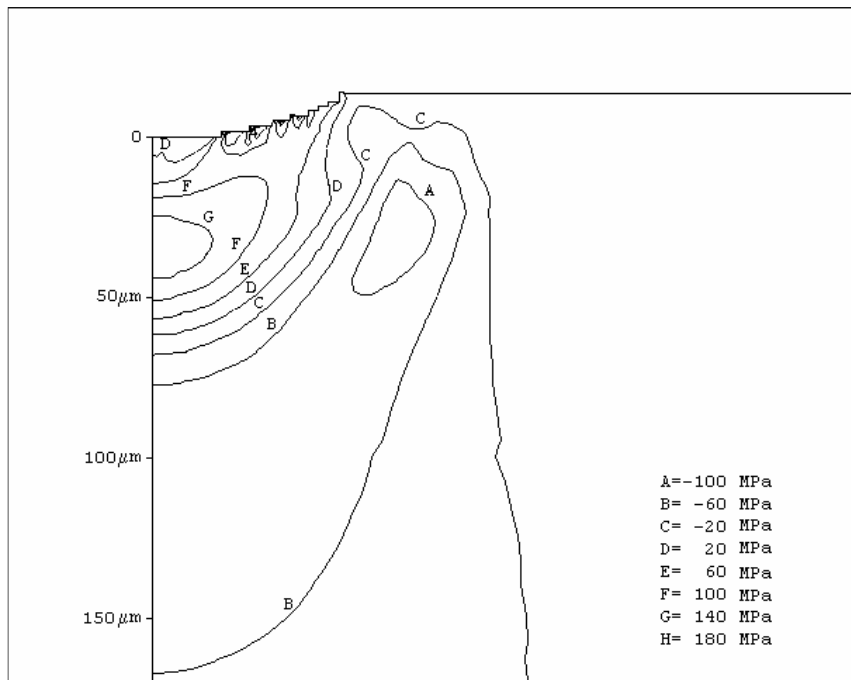


Figure 8.11 Axial Component of Residual Stresses (σ_z).

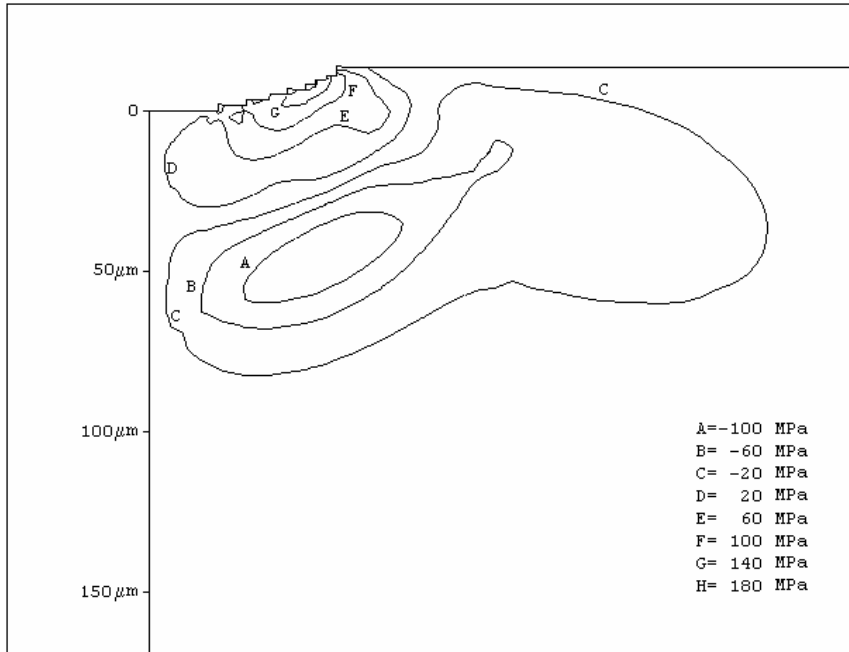


Figure 8.12 Shear Component of Residual Stresses (σ_{rz}).

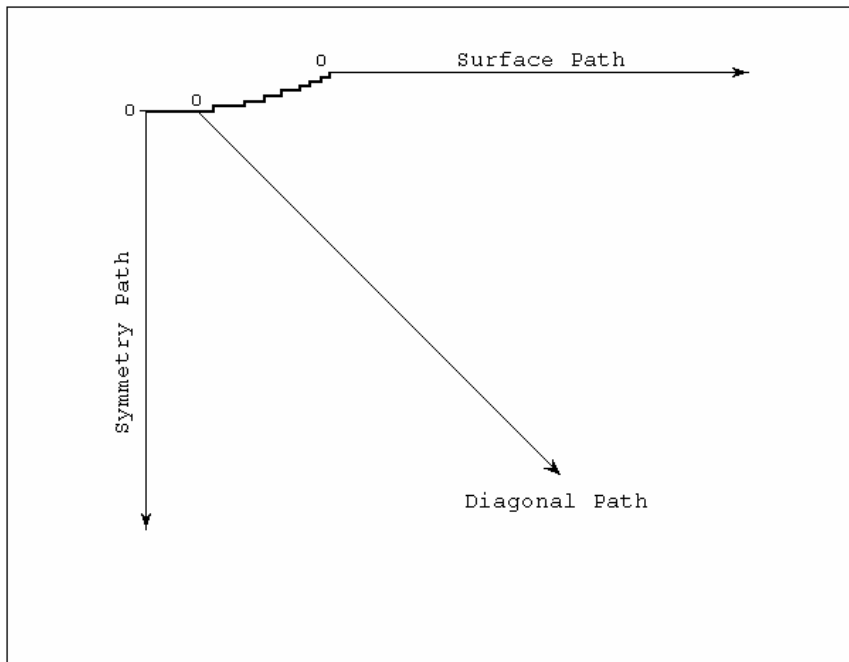


Figure 8.13 Paths on Working Domain.

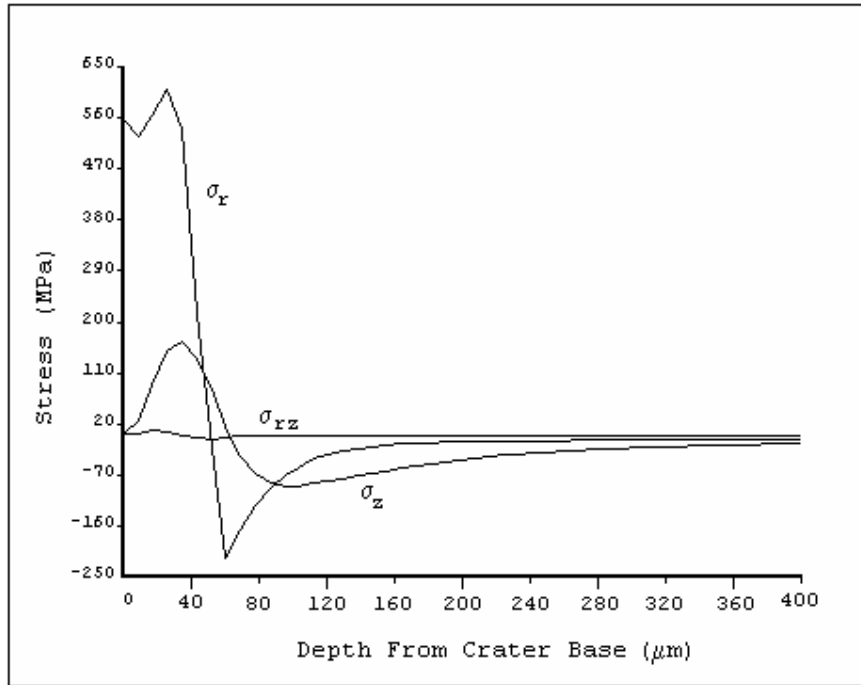


Figure 8.14 Residual Stresses on Symmetry Path.

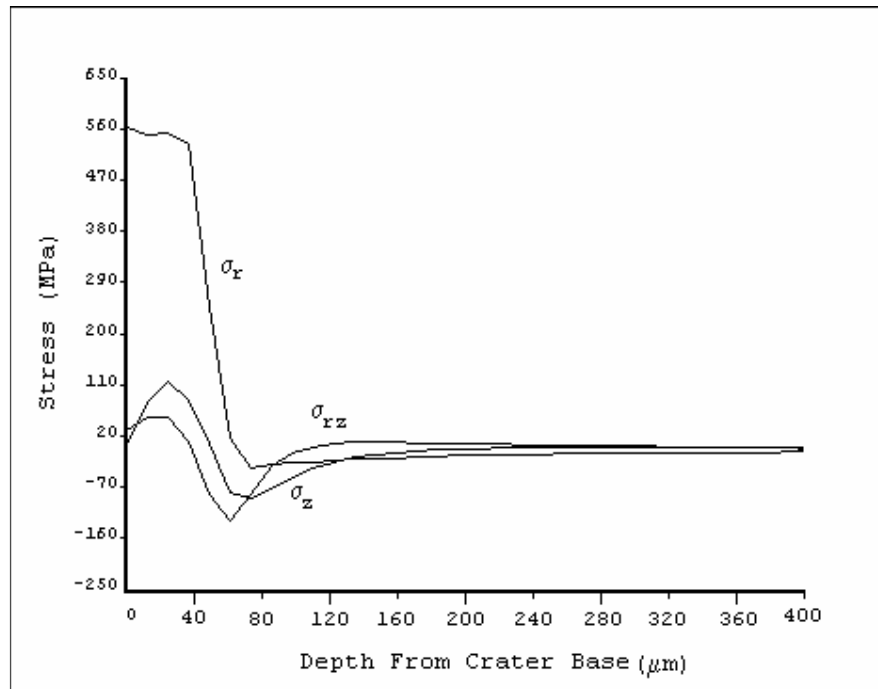


Figure 8.15 Residual Stresses on Diagonal Path.

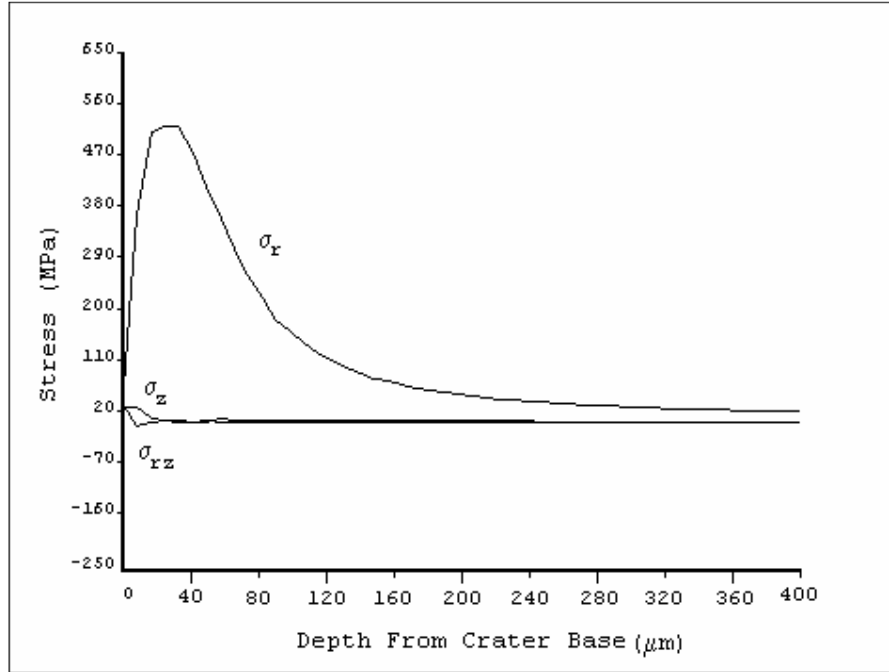


Figure 8.16 Residual Stresses on Surface Path.

8.2.3.3 Time History

The symmetry, diagonal and surface paths are also used in the time history analysis of the working domain. Temperature variation with respect to time on symmetry plane (Figure 8.17) indicates solid-solid phase transformation just after removal pulse within heat-affected zone. Radial stresses exhibit a severe variation just beneath the crater base from compressive to tensile within the pulse duration and continue to increase after removal of pulse to high tensile values and then decreased to its stabilization value (Figure 8.18). The severity of variation decreased with respect to depth (Figure 8.19). It is obvious that solid-solid phase transformation decreases on diagonal path (Figure 8.20) and vanishes on surface path as expected (Figure 8.23). Radial stresses show similar trends on diagonal (Figure 8.21, 8.22) and surface paths (Figure 8.24, 8.25) but decrease in tensile peak values beneath the crater base and increase in stabilized stresses with respect to depth can be remarked.

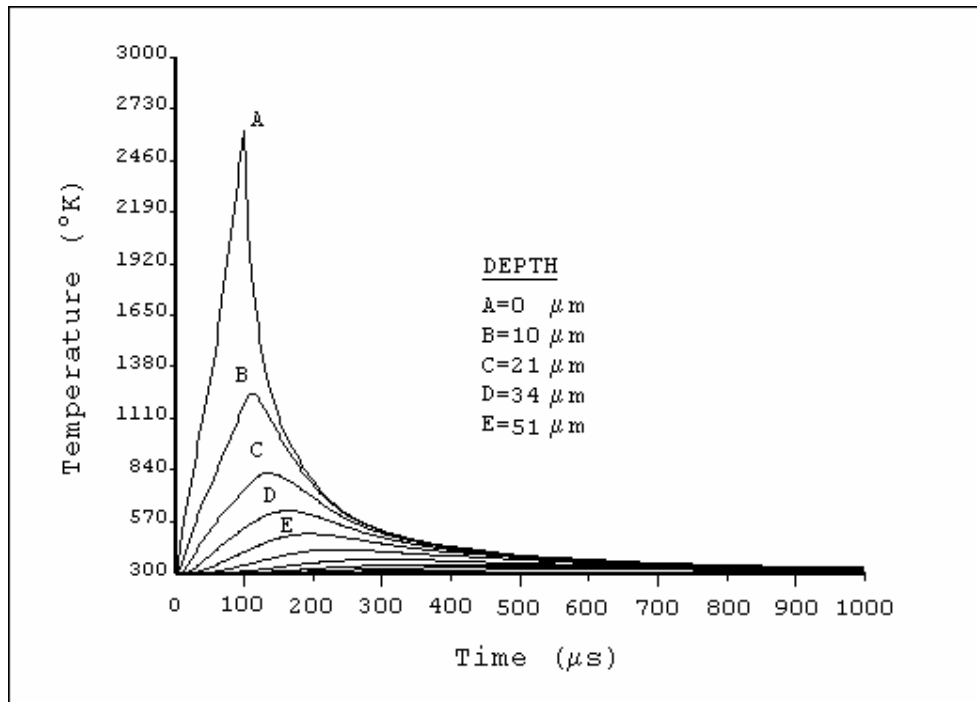


Figure 8.17 Variation of Temperature with respect to Time on Symmetry Path.

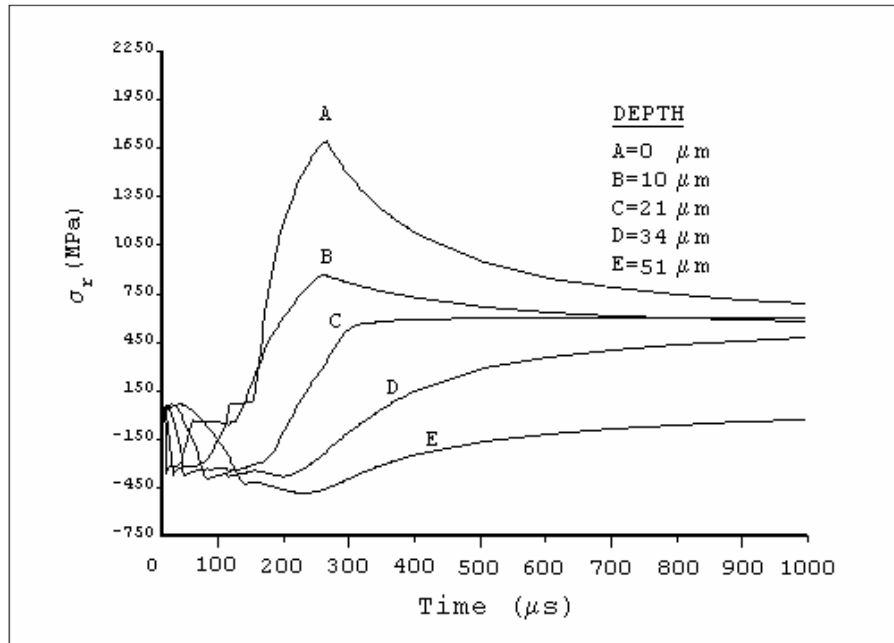


Figure 8.18 Variation of Radial Stresses with respect to Time on Symmetry Path. (Beneath the Crater Base)

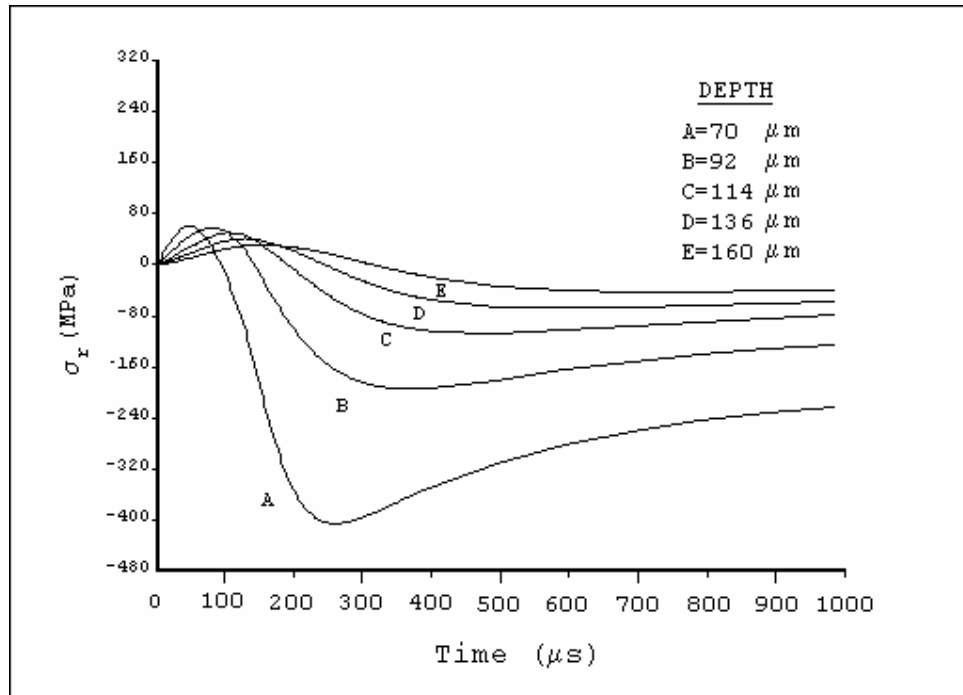


Figure 8.19 Variation of Radial Stresses with respect to Time on Symmetry Path. (Away from the Crater Base)

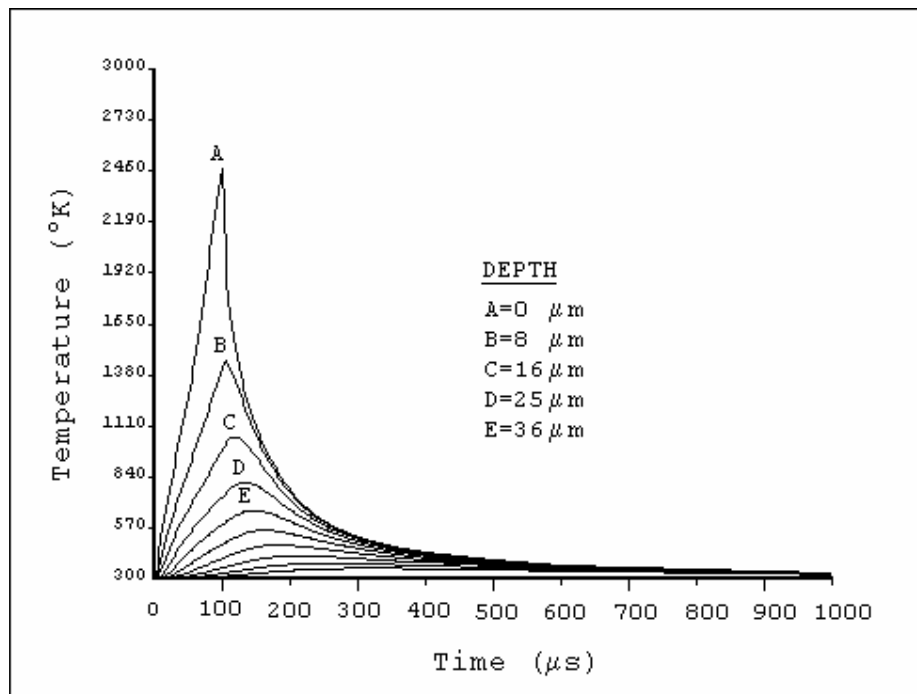


Figure 8.20 Variation of Temperature with respect to Time on Diagonal Path.

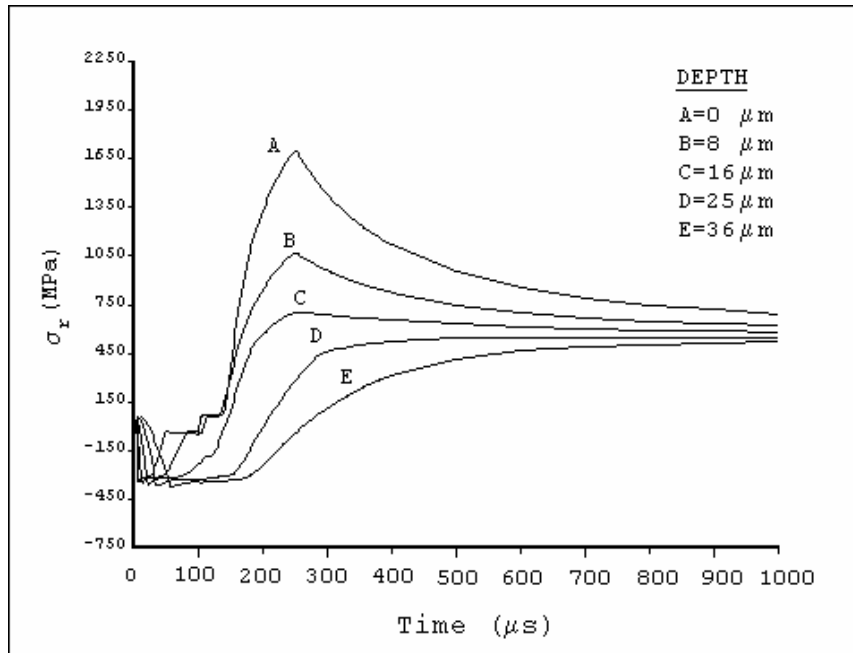


Figure 8.21 Variation of Radial Stresses with respect to Time on Diagonal Path. (Beneath the Crater Base)

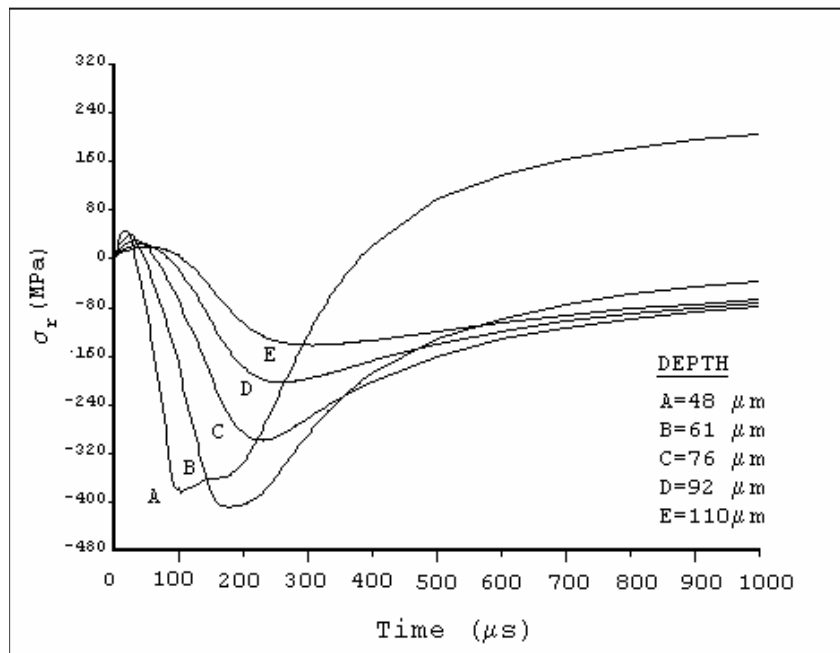


Figure 8.22 Variation of Radial Stresses with respect to Time on Diagonal Path. (Away from the Crater Base)

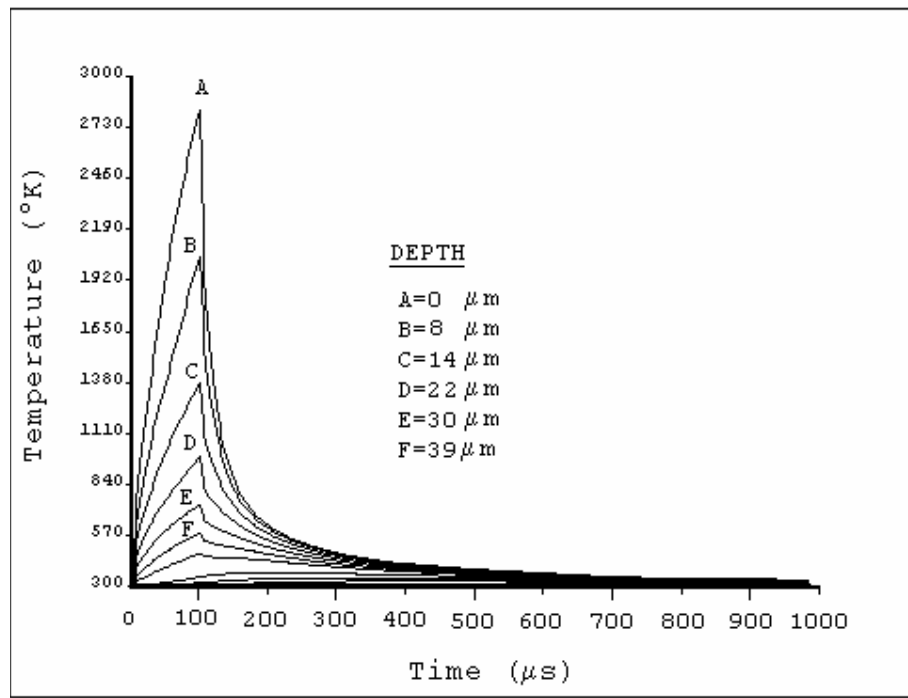


Figure 8.23 Variation of Temperature with respect to Time on Surface Path.

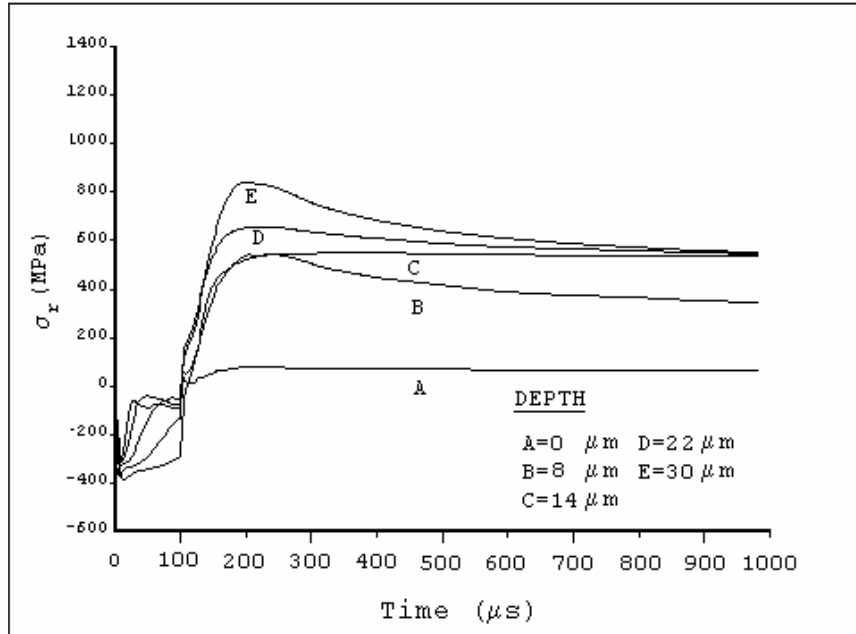


Figure 8.24 Variation of Radial Stresses with respect to Time on Surface Path. (Beneath the Crater Base)

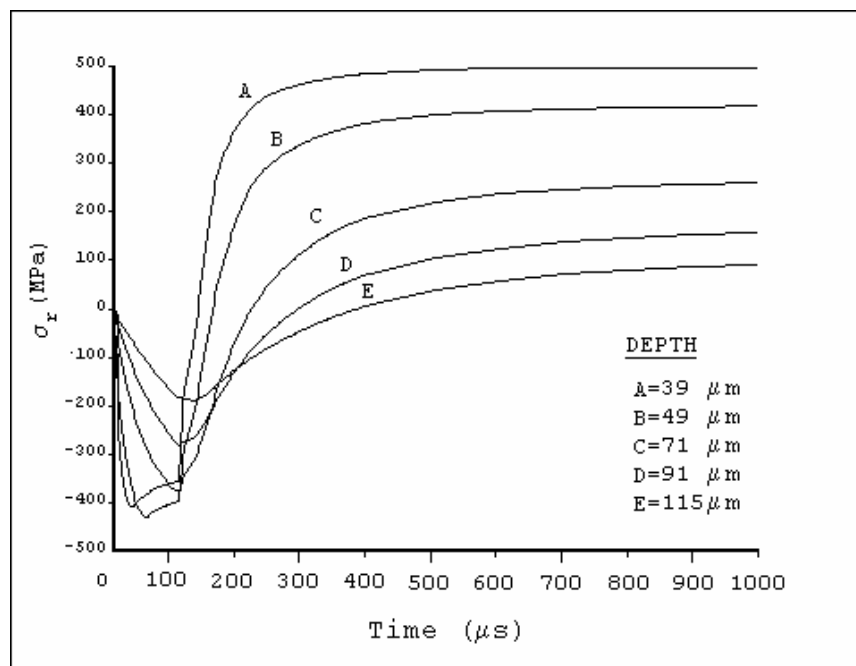


Figure 8.25 Variation of Radial Stresses with respect to Time on Surface Path. (Away from the Crater Base)

8.2.3.4 Parametric Simulations

The effect of energy partition, plasma pressure and plasma radius on the affected layers, and residual stresses are analyzed with parametric simulations. For each case amount of removed material, temperature isotherms, showing the re-melted and heat affected layers at the end of pulse duration and radial component of residual stresses at the end of cooling cycle, are presented (Appendix B).

When the percentage of energy released to the workpiece decreased to 6 % the size of the crater also decreased. In this case (Figure B.1) the depth of the crater is found as 12 μm and width as 50 μm . Although a remarkable change is observed in crater size, thermally affected layer thickness (Figure B.2) found insensitive to energy partition within the analyzed range. Residual stresses have shown similar isostresses (Figure B.3) but the location of peak stresses is found closer to crater base. Increasing the amount of energy released to the material to 10% also increased the size of the crater produced (Figure B.4). Temperature isotherms (Figure B.5) also seem unaffected as in the previous case. The location of peak residual stresses is now away from the crater base (Figure B.6). If pressure is applied during sparking the depth of the crater produced increases although the width remains unchanged (Figure B.7, B.10, B.13, B.16). Temperature isotherms (Figure B.8, B.11, B.14, B.17) also seem unaffected with respect to the applied pressure. Increase in tensile residual stresses around crater base is evident without changing the isostress pattern beneath the heat affected-zone (Figure B.9, B.12, B.15, B.18). Compressive residual stresses are also increased with respect to increase in plasma pressure. Decrease in plasma radius result in deeper craters but in this case, the width of the crater is smaller (Figure B.19). Controversially, shallow craters should be expected in case of larger plasma radius (Figure B.22). Thickness of affected layers, found from temperature isotherms, have also found insensitive to plasma radius change (Figure B.20, B.23). Increase in residual stresses beneath the crater base (Figure B.21) for small plasma radius and analogously, decrease in the stresses beneath the base for higher plasma radius (Figure B.24) can be detected.

8.3. A Triple Spark Approach to Simulate EDM'ed Surface

A triple spark approach is performed to simulate the erosion process. In this approach, sparks are considered to strike on the workpiece surface at different locations. The consequence and locations of the sparks is given in Figure 8.26. Finite element mesh of the working domain is given in Figure 8.27. Removed elements after application of sparks are shown in Figure 8.28. Contour plots of directional residual stresses have shown higher values of residual stresses with respect to single spark solution beneath the surface (Figure 8.29-8.31).

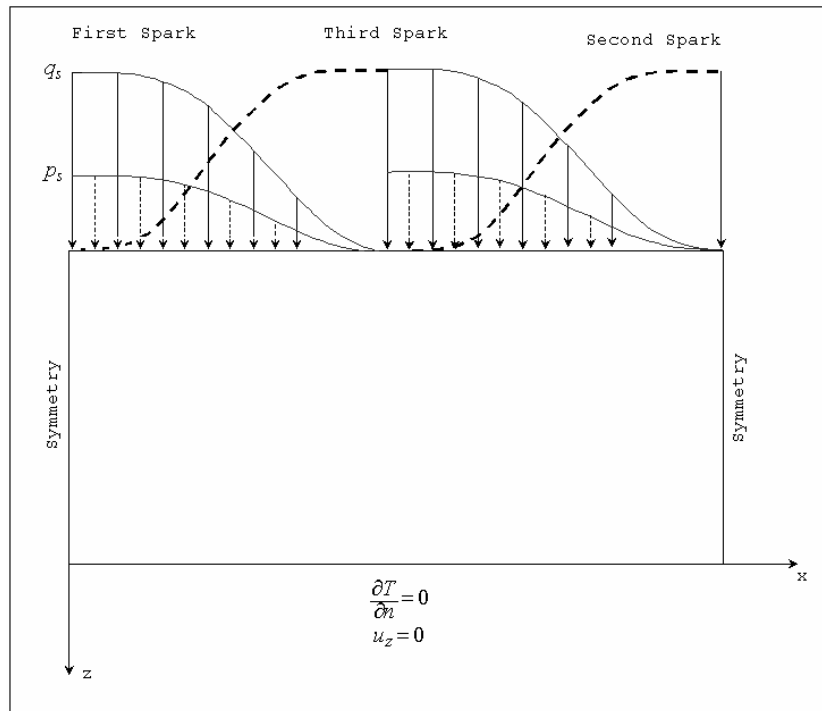


Figure 8.26 Triple Spark Finite Element Model for EDM.

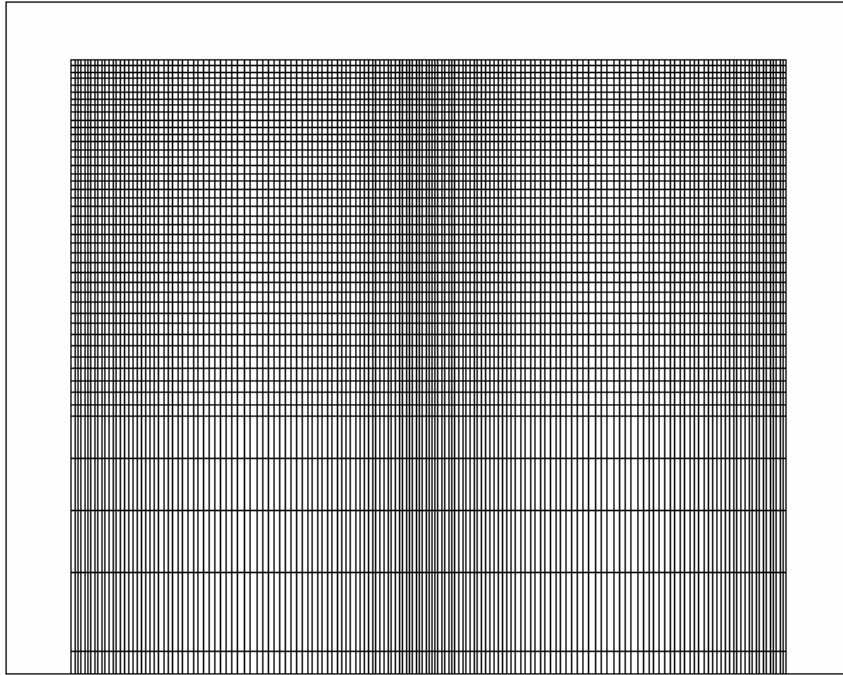


Figure 8.27 Finite Element Mesh for Triple Spark Case (Enlarged).

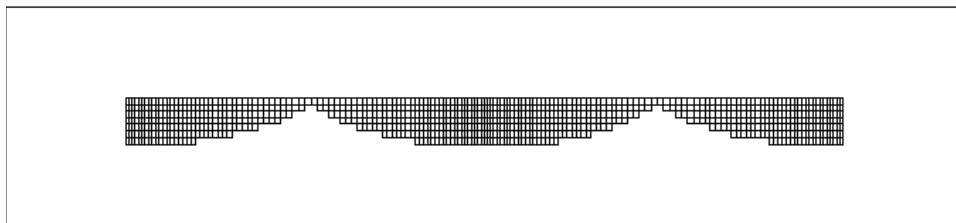


Figure 8.28 Removed Elements at the End of Three Sparks.

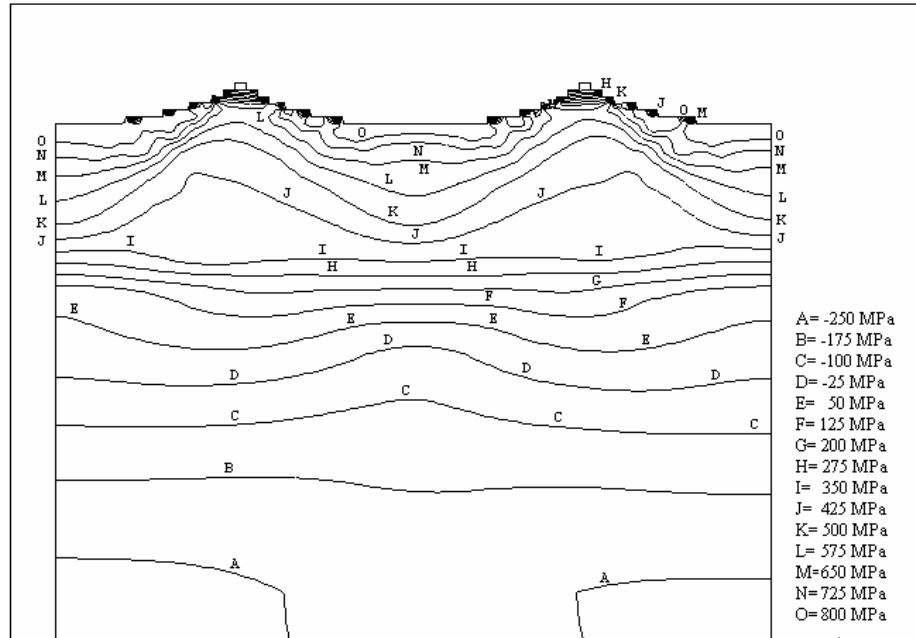


Figure 8.29 Residual Stress Component of x (σ_x) at the End of Three Sparks.

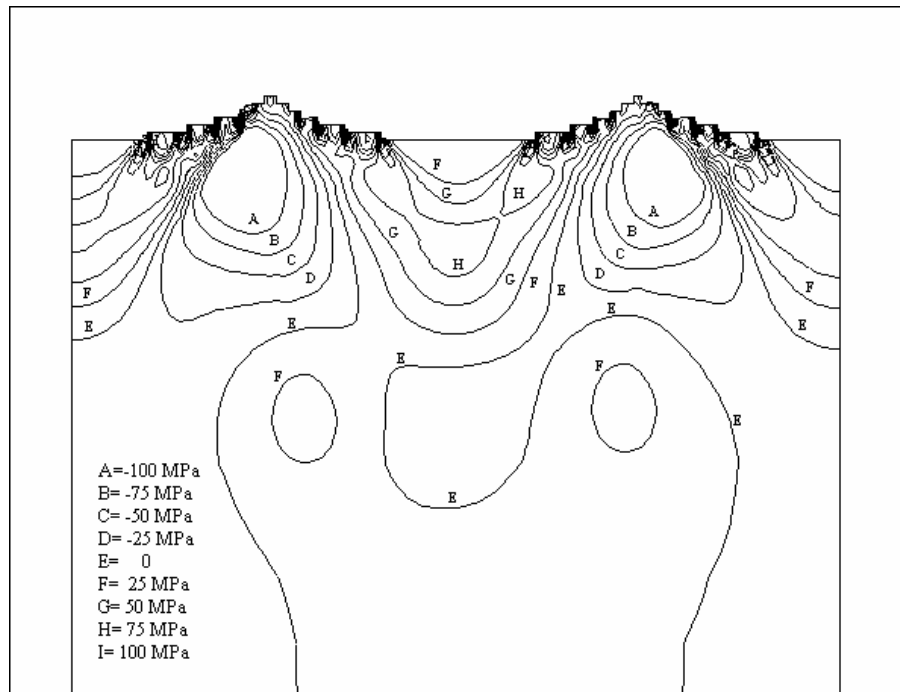


Figure 8.30 Residual Stress Component of z (σ_z) at the End of Three Sparks.

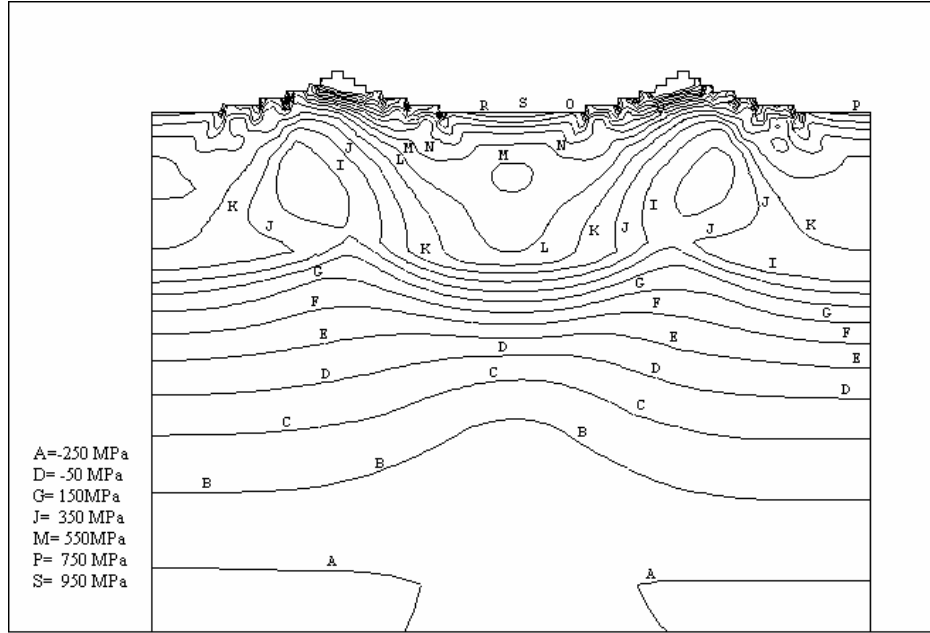


Figure 8.31 Residual Stress Component of y (σ_y) at the End of Three Sparks.

CHAPTER IX

DISCUSSION OF THE RESULTS

9.1 Introduction

This section analyses the basic results presented in chapter VI, VII and VIII. The discussion and analysis presented in this chapter is divided into three topic areas.

First, surface topography, subsurface metallurgy and damage based on metallurgical findings are discussed. Effects of tool electrode, dielectric liquid and pulse energy on affected layers together with cracking are also analyzed. An empirical equation is introduced for scaling residual stresses to pulse energy. Finally, experimental results are compared with the results of finite element analysis for verification.

9.2 Surface Topography, Sub-Surface Metallurgy and Damage

9.2.1 Surface Topography

It is well known that the surface roughness is a function of released energy, which is controlled by power supply settings. High peak current and long pulse duration produce a rough surface. The converse is also true; lower peak current and pulse duration produces a finer surface since each pulse removes a crater shaped quantity of material proportional to the energy of the pulse from the electrode. Most of the researchers (Saito, 1962; Ramaswami and Raj, 1973; Crookall and Khor, 1974; Jeswani, 1978; Rao and Faruqi, 1982; Lee et al., 1988; Chen and

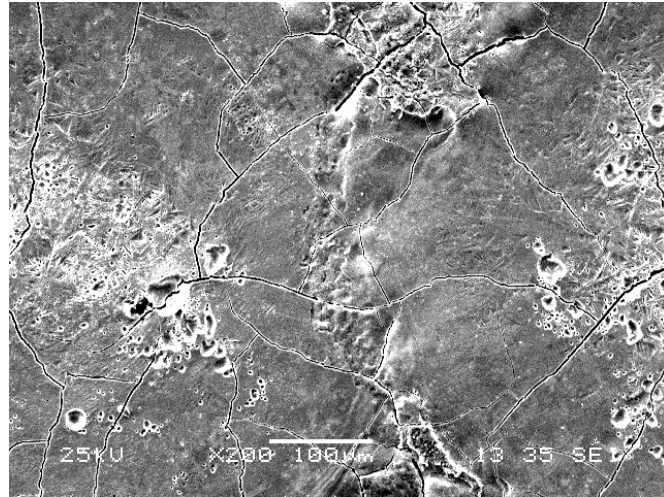
Luo., 1990; Robelo et al., 1998; Chen and Mahdavian, 1999; Chen and Mahdavian, 2000; Tsai and Wang, 2001; Rozenek et al., 2001; Lee and Li, 2001; Halkacı and Erden, 2002; Liu and Huang, 2003; Lee and Tai, 2003; Ghanem et al., 2003; Simao et al., 2003; Guu et al., 2003) have published a logarithmic trend of curves, represent an increase in surface roughness with respect to increased pulse energy. Generally they have used profilometers to measure surface roughness. Scanning Electron Micrographs (Figure 6.1-6.9) show that an EDM'ed surface observed with overlapping craters and also globules of debris and chimneys formed by entrapped gases escaping from the re-deposited material. Cracking is also possible especially at high pulse durations (Figure 6.1, 6.3, 6.5, 6.7). Consequently, surface roughness measurements with a surface profilometer do not describe the surface adequately although a rough estimate is possible. The effect of dielectric liquid and tool electrode on surface topography is not clearly stated in literature. Only a small variation in surface roughness has reported. Tool electrode is found to have a considerable affect on the resultant surface topography. Reduction in number of globules and appendages is observed when copper is used as tool electrode and de-ionized water as dielectric liquid. Changing tool electrode with graphite and/or dielectric liquid with kerosene greatly increased the number of appendages especially at the crater rims. Such appendages have attributed to bulk boiling of the workpiece material at the end of sparking due to high thermal gradients. The micrographs indicate that there is an interaction with dielectric and also with tool electrode. An interesting result is the inhibition of bulk boiling process on the surface during machining if no supply of carbon is available from dielectric or tool electrode. This suggests that carbon assimilated from tool electrode and dielectric liquid triggers the boiling process by producing traps within the melted material.

9.2.2 Cracking

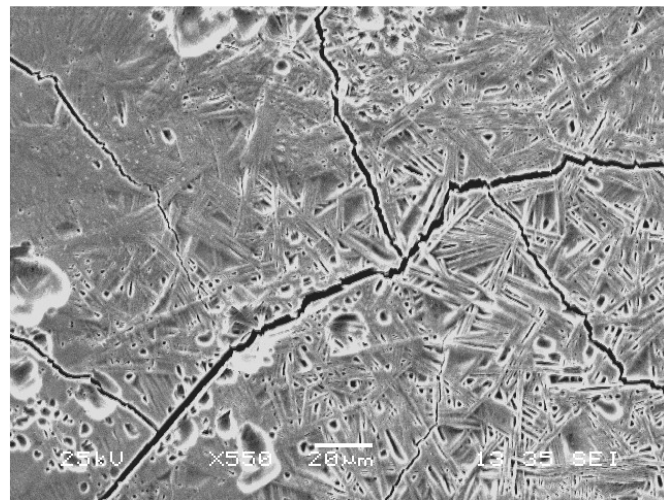
Most of the researchers have reported increase in cracking at increased energy level especially at higher pulse durations (Mamalis et al., 1987; Lee et al., 1988; Lee et al., 1990; Lee et al., 1992). According to them, intensity of the crack

formed during machining should be proportionally increased with respect to pulse energy. However, Lee and Tai (2003) have stated that maximum crack density actually occurs under the minimum pulse current and maximum pulse duration. In this study, results confirm the finding of Lee and Tai (2003). Crack density decreased under high energy levels at same pulse duration (Figure 6.1, 6.3, 6.5, 6.7). If the pulse energy is decreased, a network of cracks following the pitting arrangements with closed loops are observed (Figure 6.5, 6.7). Cracks formed in a crater continue to propagate when another discharge takes place at the neighborhood. It can be noted that intersection points of crack paths usually form perpendicular angles (Figure 9.1-9.4). Lack of appendages and globules can also be distinguished on the samples. Sometimes minor craters presumably due to collapse of bubbles are produced on the machined surface (Figure 9.1, 9.2). Number of cracks decreased when the pulse duration is decreased at same energy level. Radial cracks especially at crater rims are observed (Figure 9.5, 9.6) suggesting that higher thermal radial stress developed during sparking. Change in tool electrode has not altered the surface crack topography. Cracks have found to penetrate up to the white layer and stopped when heat affected portion of the material is reached.

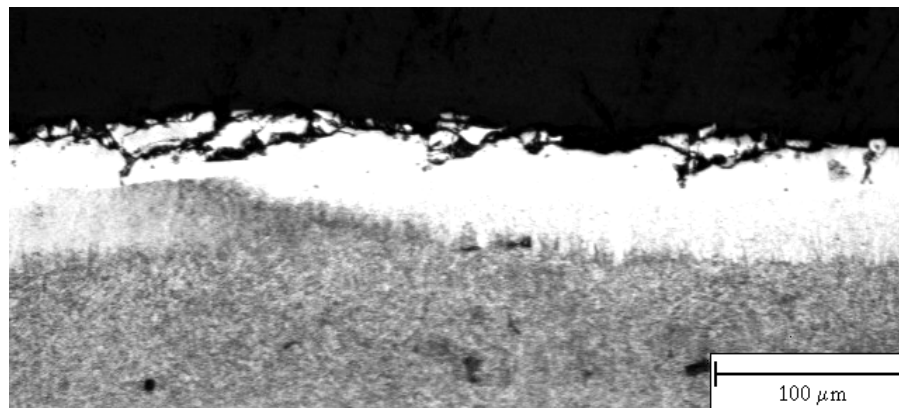
Intensity of cracking greatly decreased when de-ionized water is used as dielectric liquid. Kruth et al. (2001) have also stated that crack density is decreasing when water is used as dielectric liquid. An intense and unusual cracking exceeding the affected layers has been encountered when graphite tool electrode is used as tool electrode and de-ionized water as dielectric liquid at high pulse durations (Figure 9.7, 9.8). Such operational conditions are uncommon for industrial applications and machining is unstable. Shapes of the craters produced are found to be deeper and irregularly shaped when compared with the other cases. Cracks are randomly distributed, usually at crater bases, and extended up to parent material. Occurrence of such defects when using de-ionized water as dielectric liquid is related to the contamination of debris from graphite tool electrode during machining. Increase in contamination decreased the dielectric liquid strength and resulted in arcing during machining.



a)

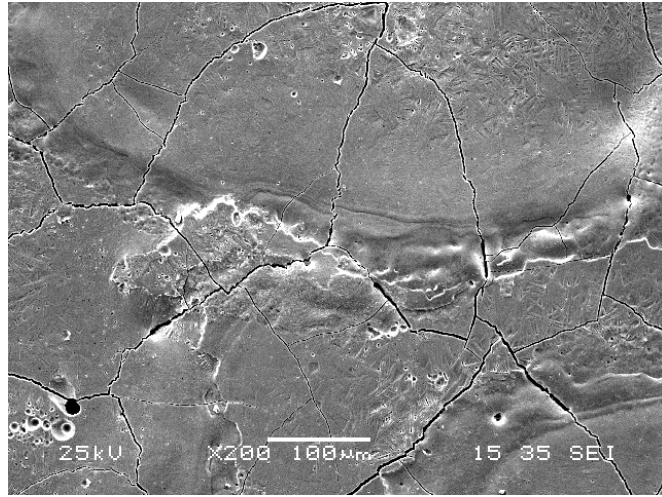


b)

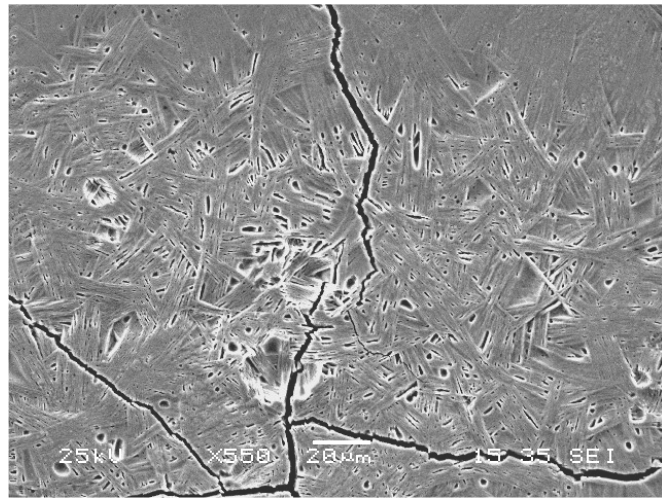


c)

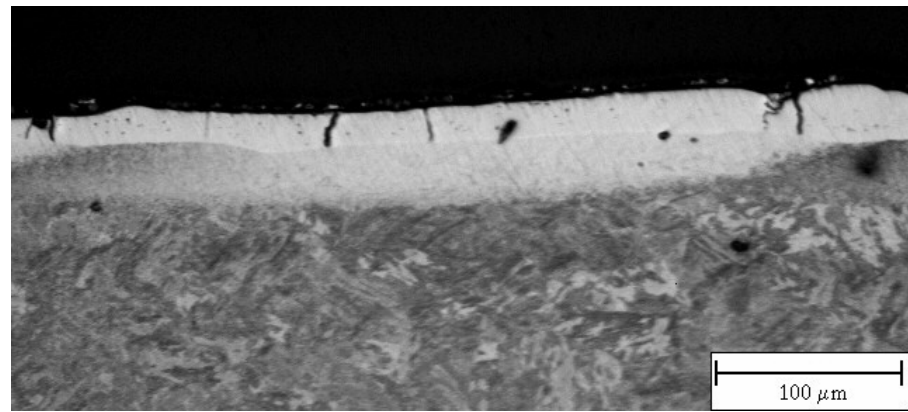
Figure 9.1 Cracking after EDM a)×200 b)×550 SEM c) Cross-Sectional View
Tool Electrode: Graphite, Dielectric: Kerosene; $t_p=1600 \mu s$; $I_{av}= 8A$.



a)

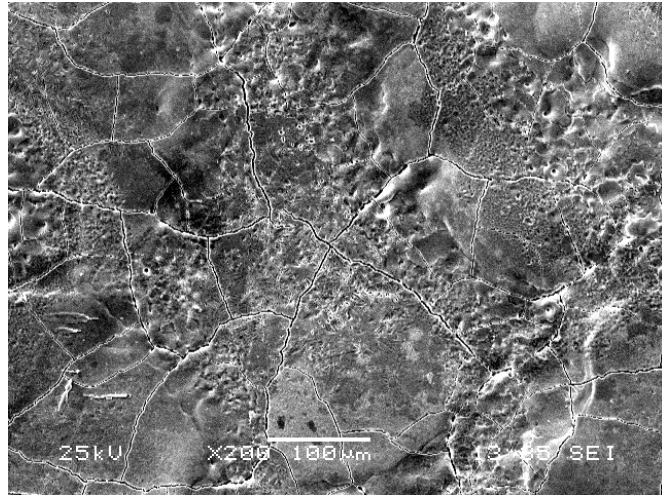


b)

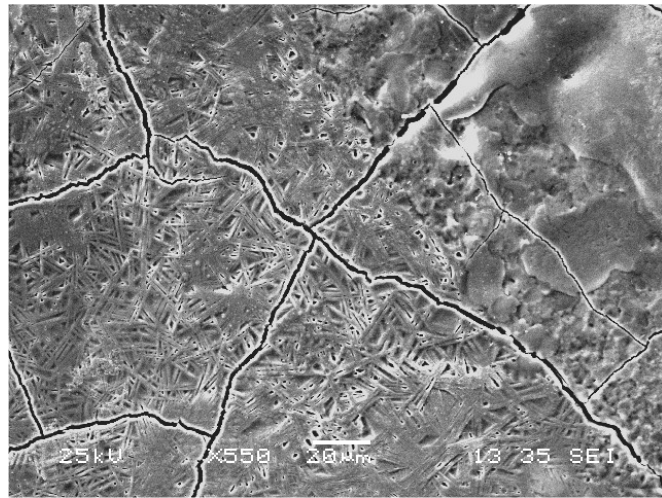


c)

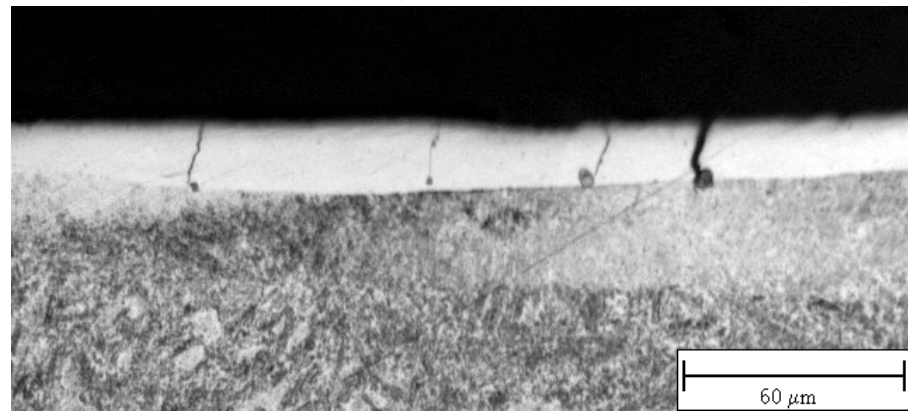
Figure 9.2 Cracking after EDM a)×200 b) ×550 SEM c) Cross-Sectional View
Tool Electrode: Copper, Dielectric: Kerosene; $t_p=1600 \mu s$; $I_{av}= 8A$.



a)

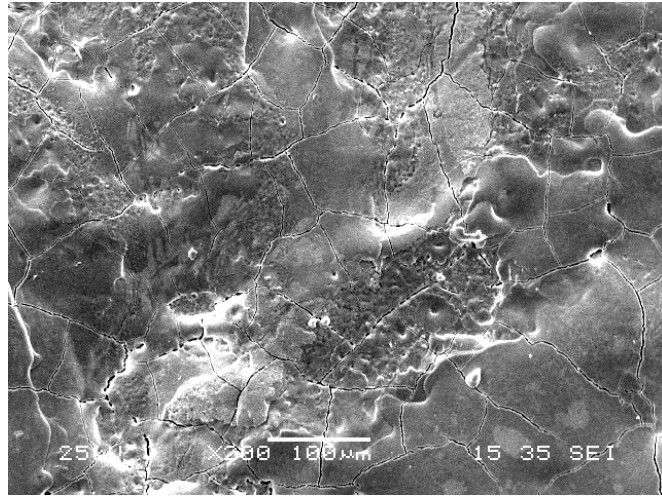


b)

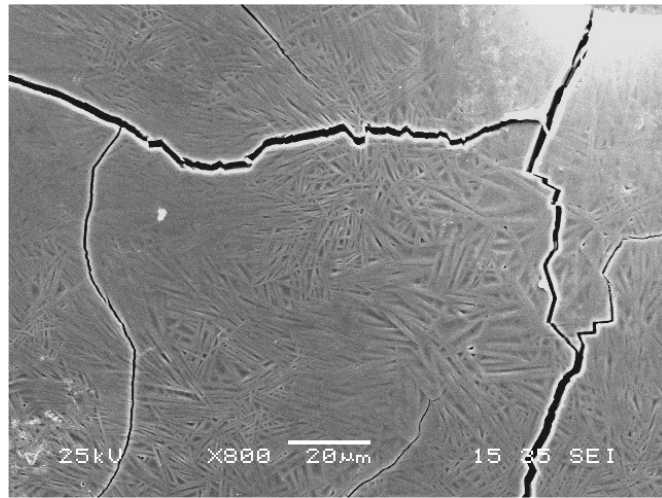


c)

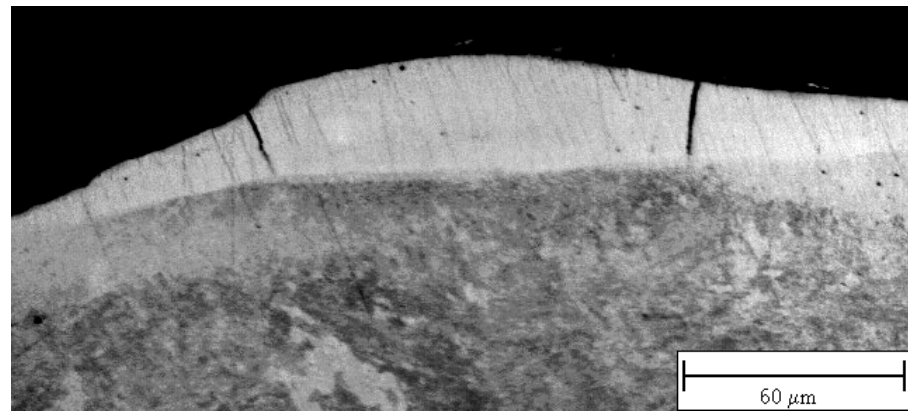
Figure 9.3 Cracking after EDM a)×200 b) ×550 SEM c) Cross-Sectional View
Tool Electrode: Graphite, Dielectric: Kerosene; $t_p=800 \mu s$; $I_{av}= 8A$.



a)

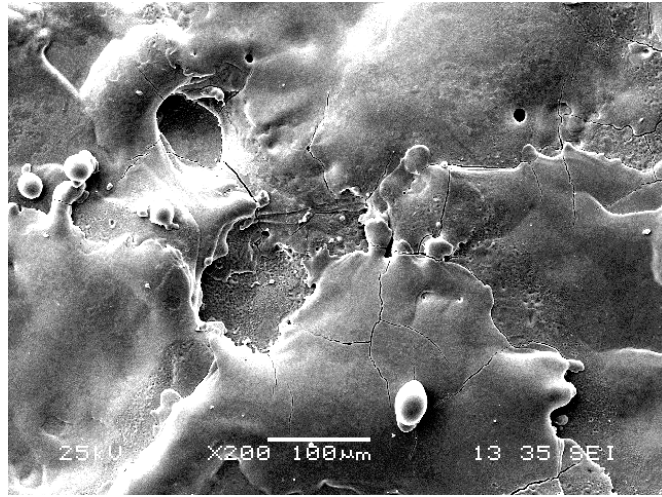


b)

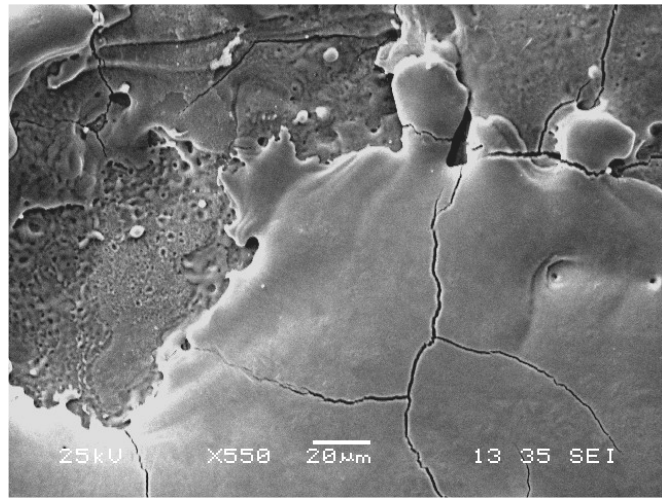


c)

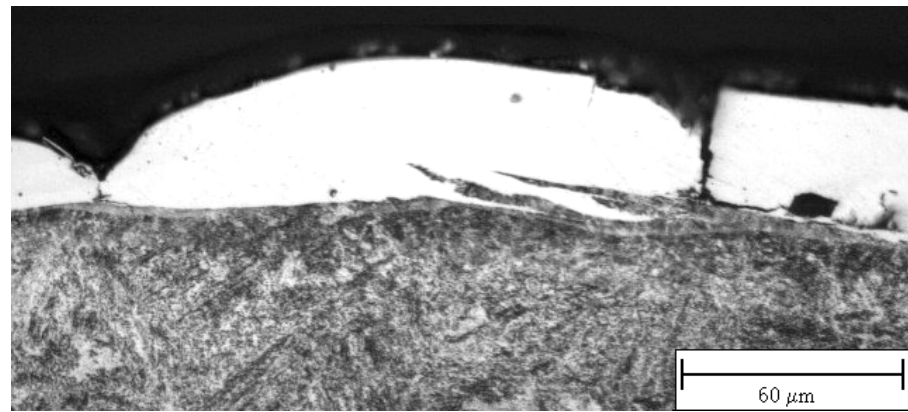
Figure 9.4 Cracking after EDM a)×200 b) ×800 SEM c) Cross-Sectional View
Tool Electrode: Copper, Dielectric: Kerosene; $t_p=800 \mu s$; $I_{av}= 8A$.



a)

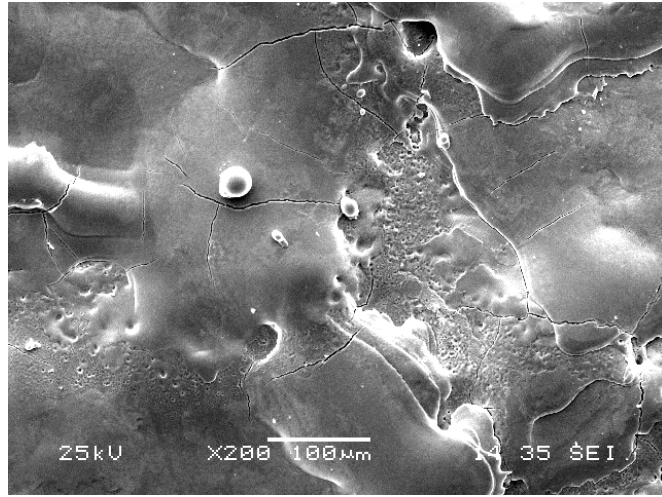


b)

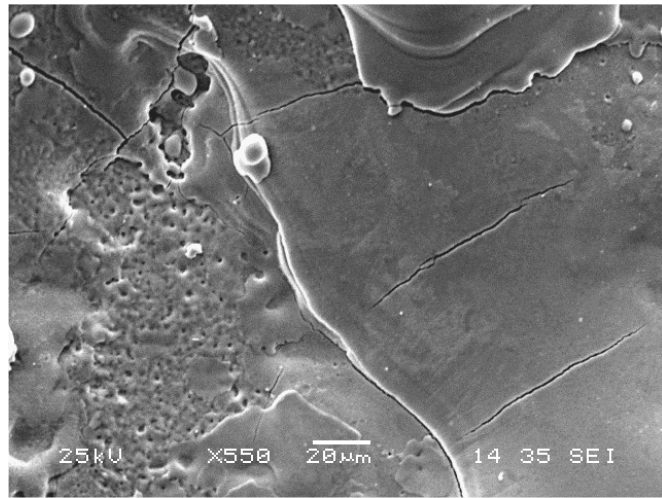


c)

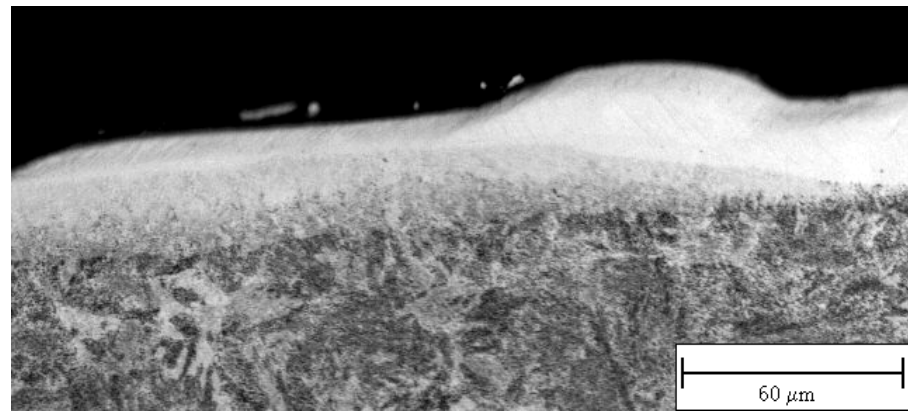
Figure 9.5 Cracking after EDM a)×200 b) ×550 SEM c) Cross-Sectional View
Tool Electrode: Graphite, Dielectric: Kerosene; $t_p=400 \mu s$; $I_{av}= 8A$.



a)

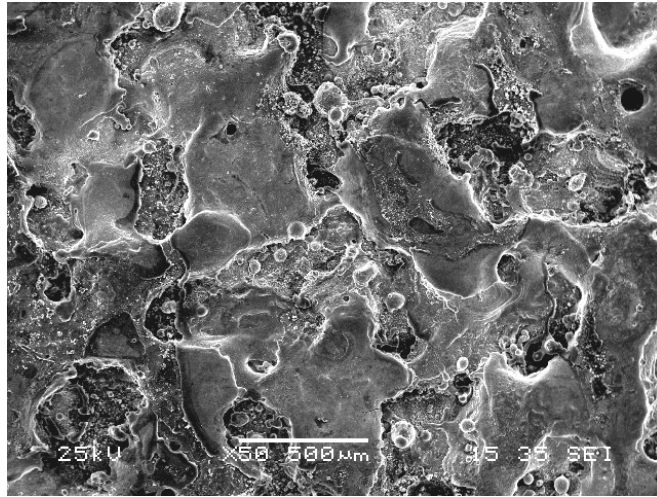


b)

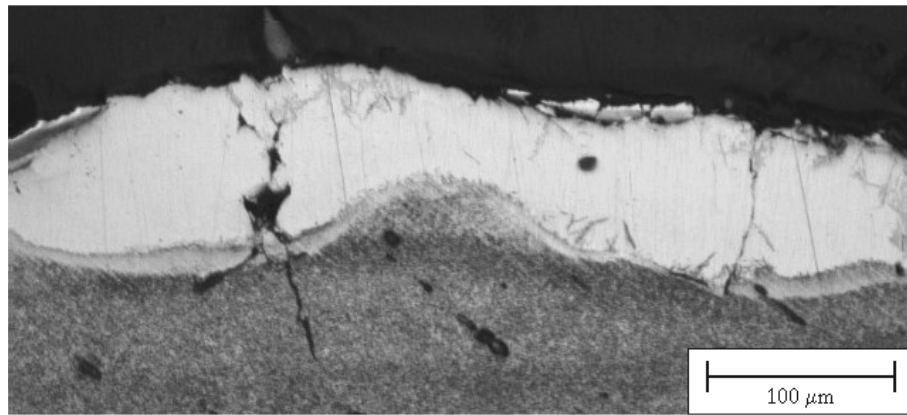


c)

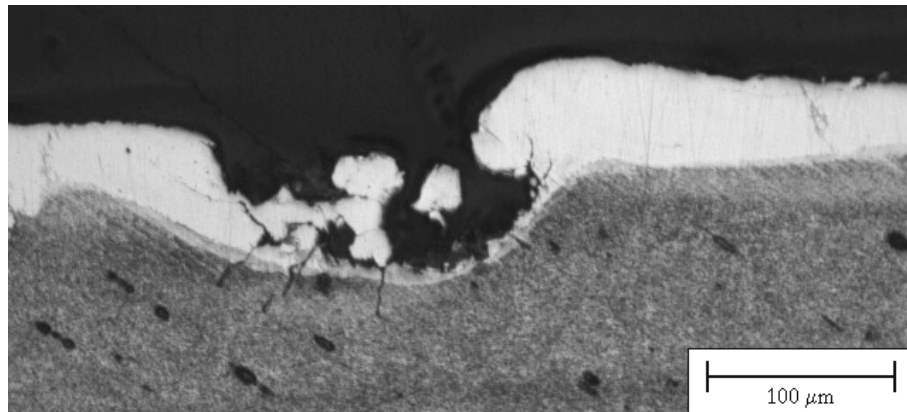
Figure 9.6 Cracking after EDM a)×200 b) ×550 SEM c) Cross-Sectional View
Tool Electrode: Copper, Dielectric: Kerosene; $t_p=400 \mu s$; $I_{av}= 8A$.



a)

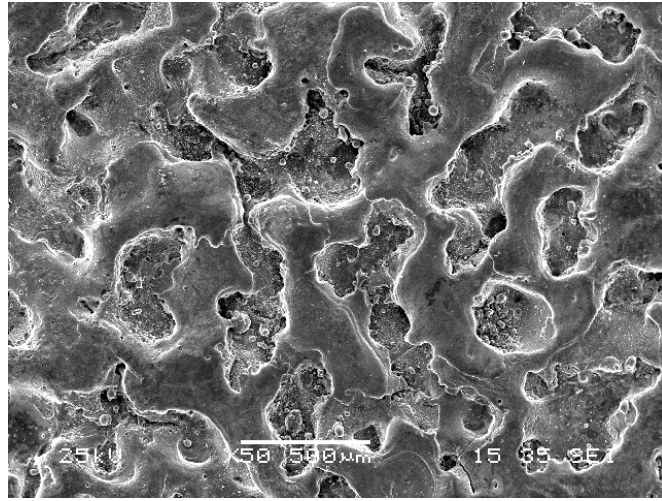


b)

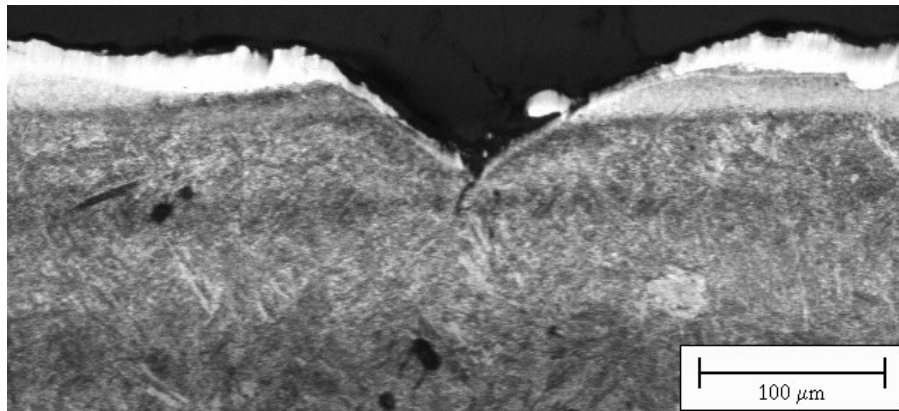


c)

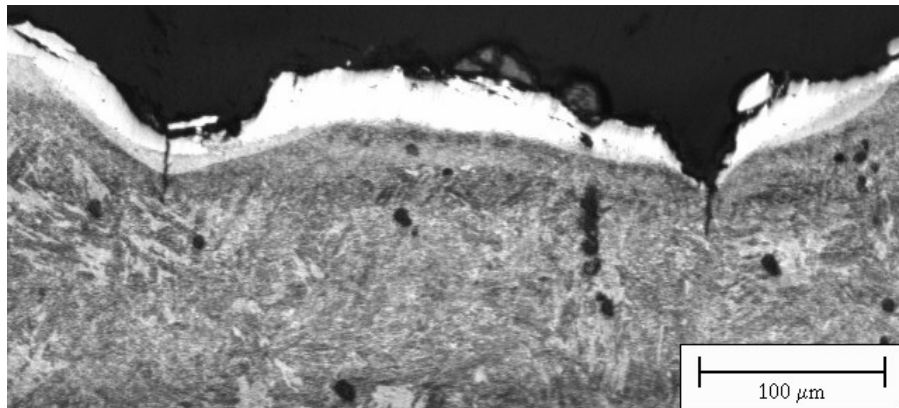
Figure 9.7 Boundary Cracking a) Surface b), c) Cross-Sectional Views
Tool Electrode: Graphite, Dielectric: De-Ionized Water; $t_p=1600 \mu\text{s}$; $I_{av}= 8\text{A}$.



a)



b)



c)

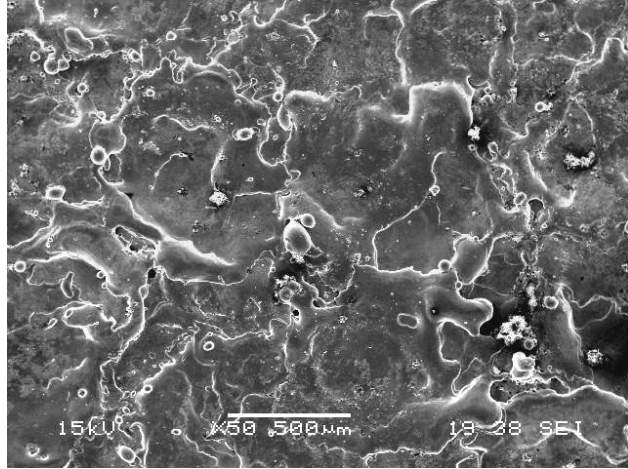
Figure 9.8 Boundary Cracking a) Surface b), c) Cross-Sectional Views
Tool Electrode: Graphite, Dielectric: De-Ionized Water; $t_p=800 \mu\text{s}$; $I_{av}= 8\text{A}$.

Micro alloy steel specimens have shown similar surface cracks (Figure 1.4). Again, intensity of cracks is increased at low energy levels and high pulse durations (Figure 9.9). Cracking could not be observed at average current of 16 A, when it was decreased to 8A, rarely and randomly placed cracks are found on the surface. Decreasing the average current to 4A increased the intensity of cracks and produced a network of cracks as in EDM'ed plastic mold steel samples.

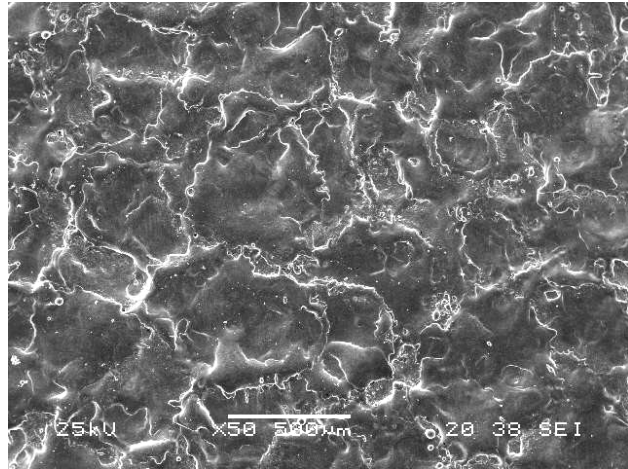
9.2.3 Sub-Surface Metallurgy and Damage

9.2.3.1 Effects of Tool Electrode and Dielectric on White Layer Morphology

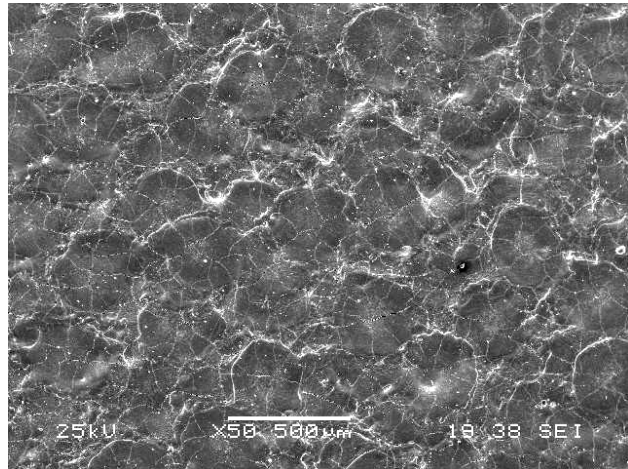
The outermost layer, which is known as the white layer are found under all machining conditions including when de-ionized water is used as dielectric liquid. The thickness of the white layer is found non-uniform over the entire discharged surface. This is due to consecutive application of sparks resulted in overlapped layers. Hence, a multiplayer structure made up of similar microstructures should be expected within the white layer (Figure 9.10). Lim et al. (1991) have also visualized such layered structure under rough machining conditions by using effective reagents and etching conditions. The thickness of the white layer is found to vary from a few micrometers across thin sections to about 80 μ m or more across thick sections. The thickness of the white layer at these thicker sections is build up due to molten metal, which was expelled onto an existing white layer and subsequently solidified. The microstructure of the underlying layer is found to be somewhat modified due to thermal effect imposed by the top layer. Decreasing pulse duration and a current also decreased the thickness of the white layer, but multi layer structure could be visible at thicker sections (Figure 9.11). Single layer structure is observed at thinner sections especially at crater bases (Figure 9.12a). The microstructure is largely columnar and dendritic in nature. It is likely that this single layer type may have retained the solidification microstructure of the molten metal in an undistorted form.



a)

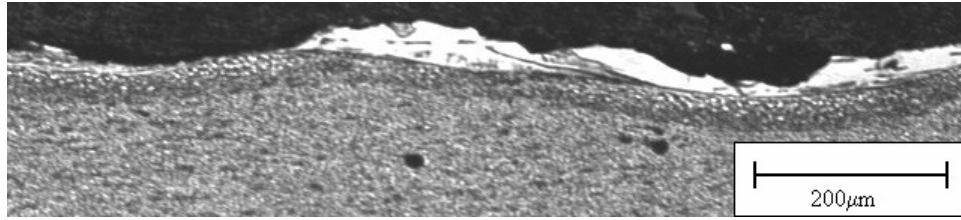


b)

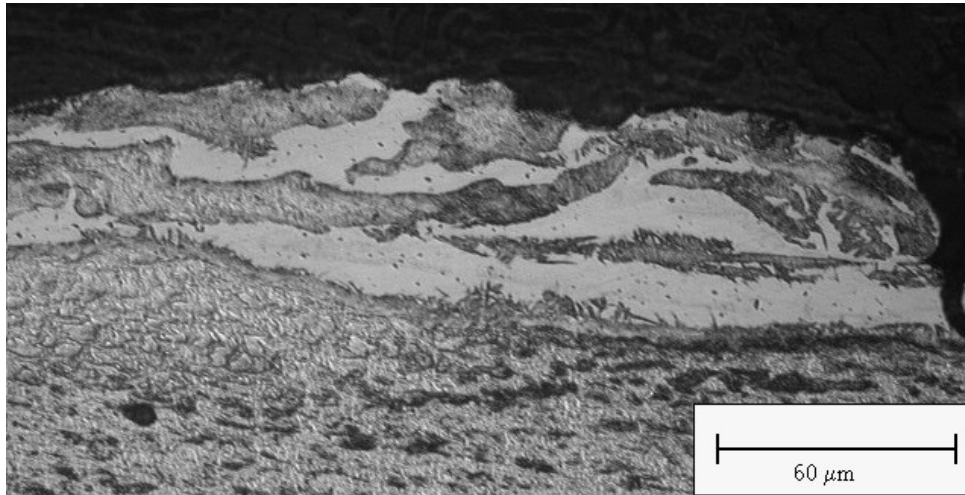


c)

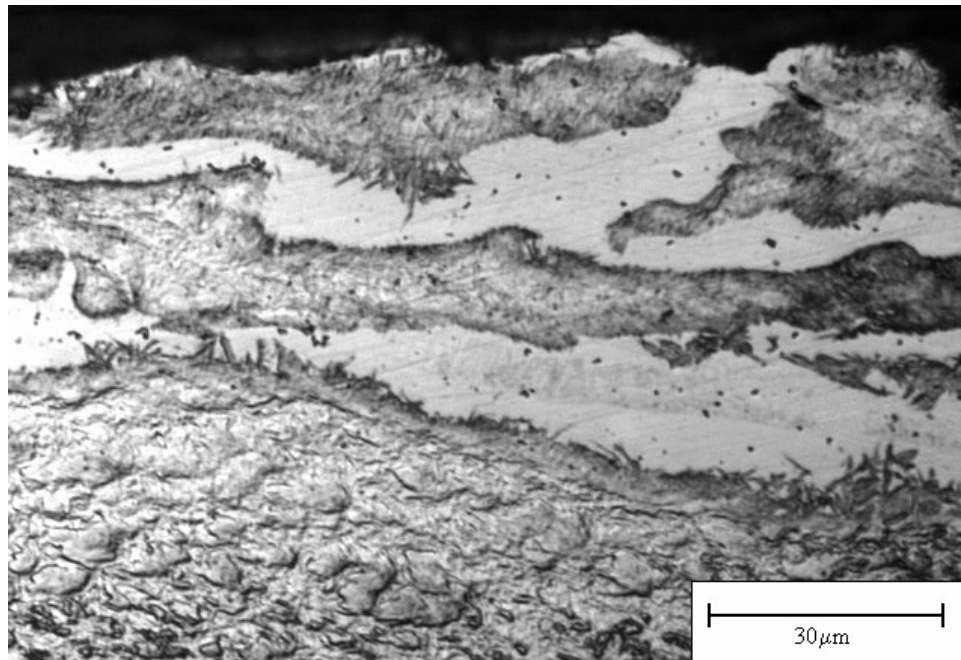
Figure 9.9 EDM'd Surfaces of Micro Alloy Steel a) $I_{av}= 16$ b) $I_{av}= 8$ c) $I_{av}= 4$ A.
Tool Electrode: Copper, Dielectric: Kerosene; $t_p=800 \mu s$.



a)

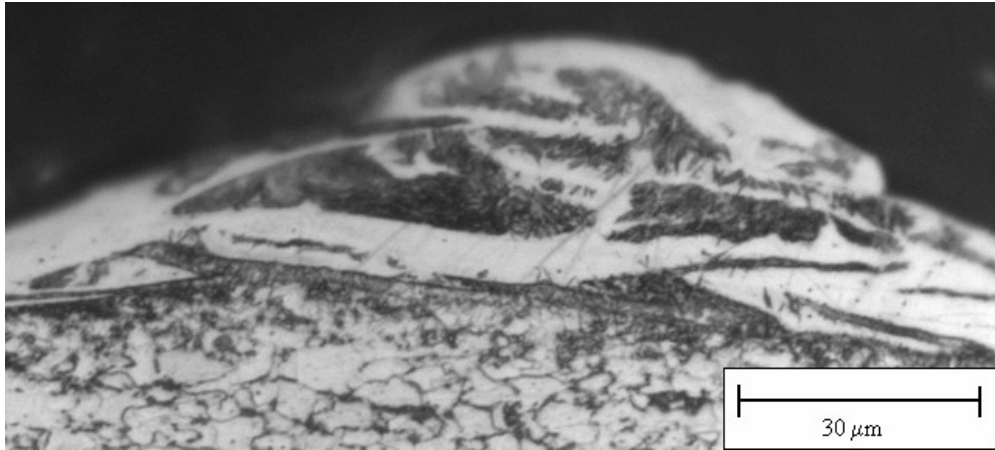


b)

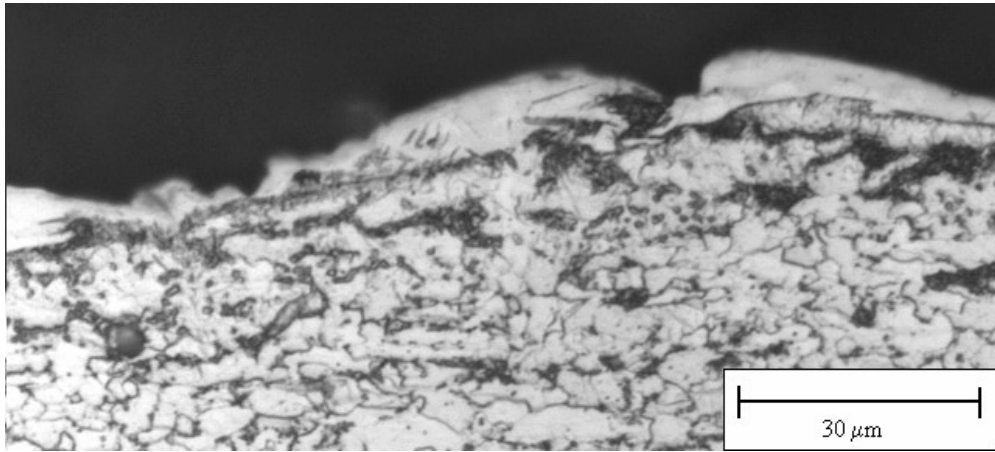


c)

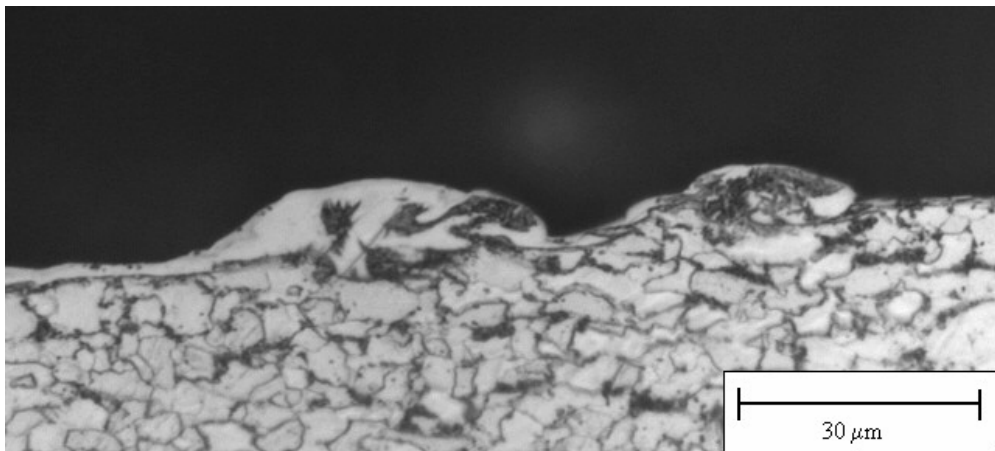
Figure 9.10 Cross-Sectional View of Micro Alloy Steel a) $\times 100$ b) $\times 200$ c) $\times 800$
Tool Electrode: Graphite, Dielectric: Kerosene; $t_p=800 \mu\text{s}$; $I_{av}=16\text{A}$.



a)



b)

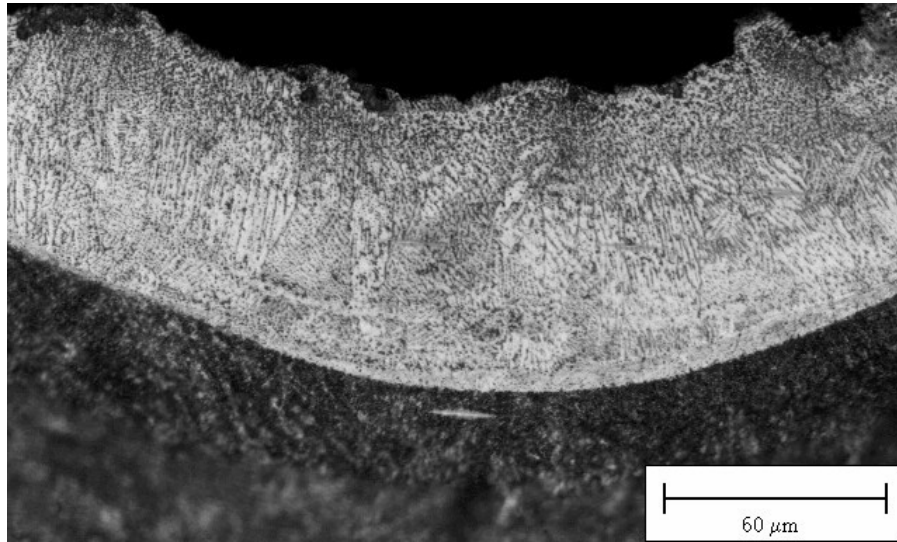


c)

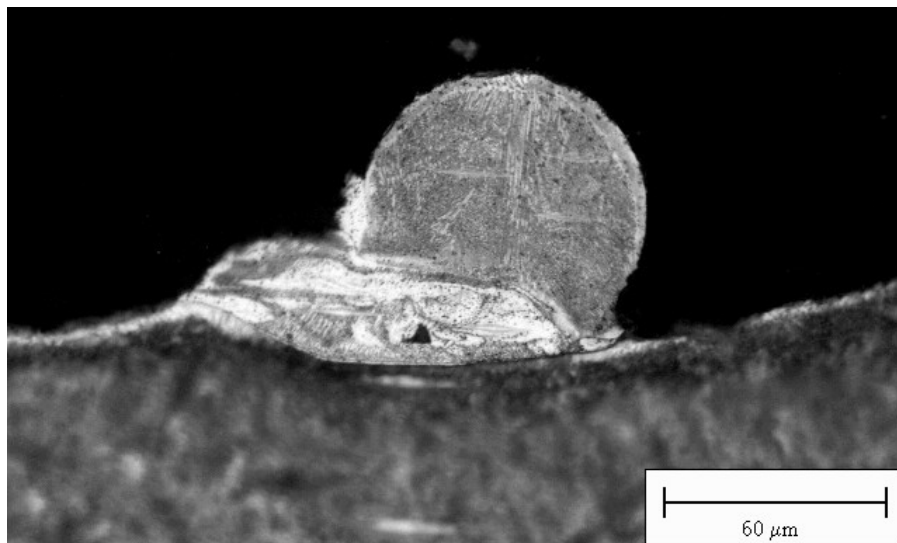
Figure 9.11 Cross-Sectional Views of Micro Alloy Steel a) $I_{av}=16A$; $t_p=50 \mu s$ b) $I_{av}=16A$; $t_p=8\mu s$ c) $I_{av}=4A$; $t_p=8 \mu s$; Electrode: Graphite; Dielectric: Kerosene.

Globule appendages are formed by molten metal droplets, which are expelled randomly during the discharge and later resolidified on the workpiece surface. Such appendages can generally be divided in two groups. The first group of globules is only weakly bonded to the white layer. They are small, spherical in shape and bonded to the substrate either at one or two contact points. Chemical etching can easily dislodge this group of globules. Careful examinations have revealed that, in several instances, no clear evidence of fusion is detectable at the locations where these globules are dislodged (Lim et al., 1991). The second group of globules is fused firmly on to the recast layer and has large contact areas with the substrate (Figure 9.12b). A spherical globule attached to multi-layer substrate during machining. Microstructure of the appendage reveal single layer microstructure and remained as an integral part of the recast layer.

Most of the investigators have reported a severe increase in carbon content when carbonaceous dielectric liquid is used and increase in carbon content in the surface and sub-surface layers has been attributed by most workers to the pyrolysis of the dielectric (Optiz, 1960; Lloyd and Warren, 1965; Crookall and Khor, 1975; Bucklow and Cole, 1975; Massarelli and Marchionni, 1977; Wallbank, 1982; Thomson, 1989; Rebelo et al., 1998; Ghanem et al., 2003). Some investigators have described the white layer as being different if they are machined by graphite or copper electrodes (Optiz, 1960; Lloyd and Warren, 1965; Thomson, 1989); dendritic austenite and a cementite-austenite eutectic (ledeburite), or a fully austenitic surface followed by an austenite-cementite matrix, respectively. Others (Barash and Sri Ram, 1963; Massarelli and Marchionni, 1977) have reported a similar structure of carbides in an austenite matrix, but stated that different electrodes do not change the morphology of the white layer: Only the ratio of the carbide and the austenite phases varies. Kruth et al. (1995) have stated that dielectric liquid caused decarbonization in the white layer when water is used as dielectric liquid and observed a correlation between carbon content and micro hardness. Consequently, they concluded that the hardness of the white layer is caused by the presence of carbides.



a)



b)

Figure 9.12 Cross-Sectional Views of Plastic Mold Steel a) White Layer b) Globule Section Tool Electrode: Graphite, Dielectric: Kerosene; $t_p=100 \mu\text{s}$; $I_{av}=16\text{A}$.

The present study has shown that the white layer is also formed when copper electrode is used as tool electrode and de-ionized water as dielectric liquid. X-Ray diffraction patterns for plastic mold steel samples (Figure 6.25) have shown Fe₃C formation on machined surfaces when kerosene is used as dielectric liquid. Martensite formation at crater bases can be visualized in Figure (9.1b-9.3b) Consequently; the white layer consists of carbides and martensite, distributed within an austenite matrix due to pyrolysis products of the cracked hydrocarbon dielectric during the discharge. Changing the electrode material does not alter the result. Presumably, only the amount phases may vary.

However, samples machined in de-ionized water also show formation of white layer, but differences with the samples obtained when using commercial kerosene can be found out. Formation of iron carbides is not possible. Amount of retained austenite phase and intensity of micro cracks are much less than when hydrocarbon based dielectric liquid is used. Micro hardness measurements have shown hardness increase within the white layer for all cases (Figure 6.22-6.25) in contrast to finding of Kruth et al. (1995). These results have shown that the hardness of the white layer is caused only by martensite.

EDT samples revealed a peak hardness value within the white layer. Measurements on the outermost sections have shown lower values than the parent material, which is increased rapidly to its peak value then again decreased to lower values before settling to unaffected material value (Figure 6.26). This confirms that the retained austenite (Fe- γ) is formed due to extreme cooling rates during sparking. The occurrence of this phase is also proved by sub-zero treatment (Figure 9.13) that the hardness values of the affected layers are increased due to the transformation of retained austenite to martensite.

From the results, it become clear that when using hydrocarbon based dielectric liquid, there is a enrichment in carbon content in the white layer with respect to base material. FEM results (Figure 8.20) indicates that heating workpiece material from room temperature during sparking and cooling the material to 300 °C take

place within three pulse period. Cooling time is much more faster than the traditional quenching. Thus, formation of martensite in the white layer is expectable.

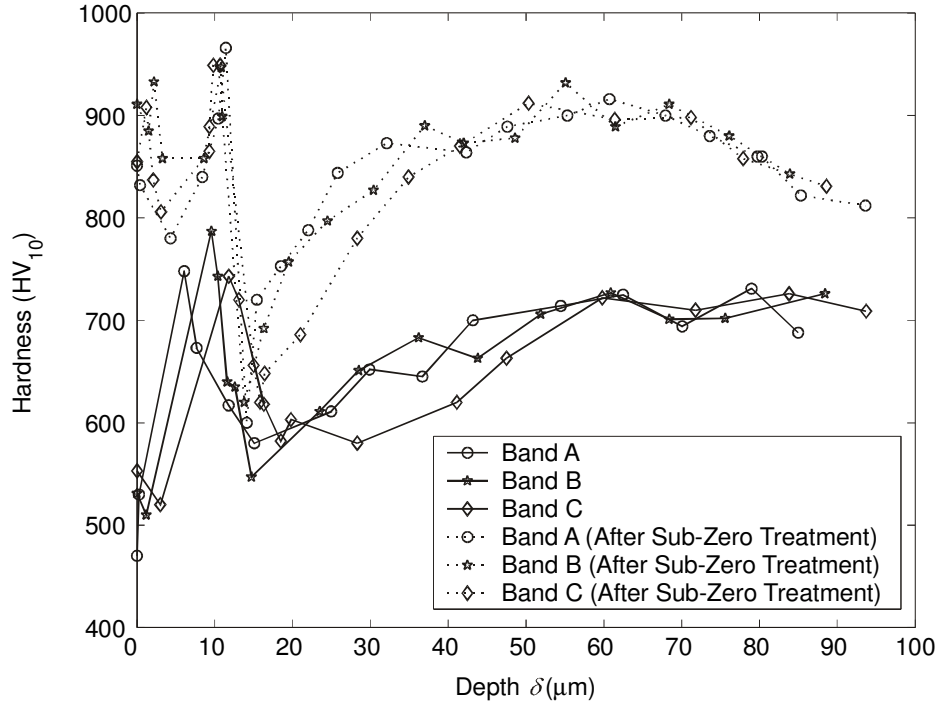


Figure 9.13 Hardness Depth Profile after and before Sub-Zero Treatment on Cross-Sectioned Surface of EDT'ed Bands A, B and C.

9.2.3.2 Thermally Affected Layers

In all cases, thermally affected layers are found beneath the white layer. Different appearances have encountered for different materials under optical microscope. This zone could be barely distinguished from the white layer for EDM'ed plastic mold steels and temper millwork roll steel. This layer has a little darker appearance than the white layer. (Figure 9.1c-9.6c). This layer is considered to be composed of a hard untempered martensite (UTM). However, micro alloy steel samples have shown darker appearance of thermally affected zone with finer grain structure (Figure 1.5). Hardness value of the intermediate layer (UTM) is found to be as high as the white layer hardness value at outermost regions, and then gradually decrease to parent material hardness at inner sections.

An intermediate layer between the white layer and the tempered layer have been observed on micro alloy steel samples at high energy levels. The thickness of this layer is found to be around 2 μm . Most of the researchers (Llyod and Warren, 1965; Bucklow and Cole, 1969; Crookall and Khor, 1975; Massarelli and Marchionni, 1977) have claimed that this layer has carbon gradient and contamination of materials from the tool electrode and includes part of the melted layer plus a region beyond which diffusion has occurred in solid state.

A careful examination has also revealed a dark innermost layer, which can be clearly visualized from tangential sections of EDT'ed samples (Figure 6.21) and defined as overtempered martensite (OTM). The hardness value of this layer is found comparable to or lower than the hardness of the parent material. In general, the thickness of the various surface layers described above and the depth of surface damage increase with increasing discharge energy.

9.3 Residual Stress Measurement

9.3.1 Layer Removal Method

Stressed layer of EDM'ed surfaces is removed by electrochemical polishing. During removal process a non-linear polishing rate is encountered during removal of outermost layers. It is well known that the affected layer properties are different than the parent material. Especially the white layer exhibits a completely different structural behavior. Hence, it is natural to have different electrochemical polishing rates at these affected layers.

Measurements have shown three distinct electrical characteristics of layer removal process (Figure 7.7), during removal of the first layer no variation in voltage is observed. This steadiness has continued up to the removal of the fifth layer. Then a slight increase in voltage is detected for the proceeding three layers. After that, increase in voltage with respect to time could be clearly visualized. Finally, the

voltage pattern settled to its final form for the proceeding layers. Such characteristics are observed for all analyzed samples. Thus, each form could be related to different types of affected layers produced during EDM (Figure 7.1). The steady pattern is showing the removal process performed within the white layer. Proceeding forms are related to transitional zone, heat affected zone and the parent material, respectively. The results showed well agreement with the affected layer thickness.

In spite of the non-linear nature of the material removal rate on EDM'ed surfaces during electrochemical polishing, some of the researchers (Crookall and Khor, 1975; Kruth et al., 2000) have assumed a linear variation of material removal rate with respect to time and only measured sample deflections in a continuous manner. It is shown that such an assumption would lead to erroneous results especially within the white layer and heat-affected zone since the actual removed layer thickness would not be equal to the predicted value based on the assumption of linear material removal rate. In addition, most of the stresses are actually developed within these layers during EDM. Thus, discrete measurements of deflections during layer removal should be preferred to ensure the current thickness of the analyzed sample during electrochemical polishing.

9.3.2 Residual Stresses

The residual stresses are found as tensile in nature. It increases from the surface and reaches to its maximum value. Then falls rapidly to relatively low values of compressive residual stresses (Figure 7.11, 7.12, 7.18, 7.19, 7.25, 7.26, 7.32, 7.33). The depth from surface at which, residual stress reaches its maximum value, depend on the spark energy. Compressive stresses can be related to sample thickness, since residual stresses within plastically deformed layers are equilibrated with elastic stresses in the core of the material (Figure 7.13, 7.14, 7.20, 7.21, 7.27, 7.28, 7.34, 7.35). Intensity of the stresses does not change considerably with the amount of spark energy. This peak indicates ultimate tensile strength or, alternatively, equivalent hot strength value of the material.

Parametric measurement results at different pulse durations and energy levels are analyzed with introducing a new parameter g on the proposed functional equation and setting coefficients a_1 , a_2 and a_3 as known constants found previously. The results showed a good agreement on the proposed form and thus, accepted as generality over the working range for EDM process.

The residual stress pattern has found to be unchanged with respect to the machining parameters. Location of tensile peak stress is directly related to the energy released during sparking. Thus, for each dielectric and tool electrode combination a unit shape form is defined and corresponding dependency with respect to released energy is proposed in power functional form. Consequently, the residual stress state of the EDM'ed plastic mold steel surfaces is defined.

It was found that tool electrode and dielectric liquid affected the residual stress pattern in a similar way. Using graphite tool electrode in de-ionized water dielectric has shifted the location of the peak stress deeper and widened the peak width compared with the use of copper electrode. The similar trend has been also observed when kerosene was used as dielectric liquid. This could be traced from the last coefficients (a_3) of the unit shape function for each particular case. These coefficients control the peak width of the proposed forms and high values are responsible for peak widening. It should be noted that at high pulse duration and low energy levels, residual stress measurement method has failed. These are the cases where dense cracking has observed on the test specimens. Measurement efforts have proven that (Figure 9.14) cracked portion of the material (usually the white layer) could not be homogeneously removed from the sample during electrochemical polishing. This is presumably due to partial flaking off the white layer, which is also proved the weakness of the intermediate layer between the white and thermally affected layers if cracking is occurred.

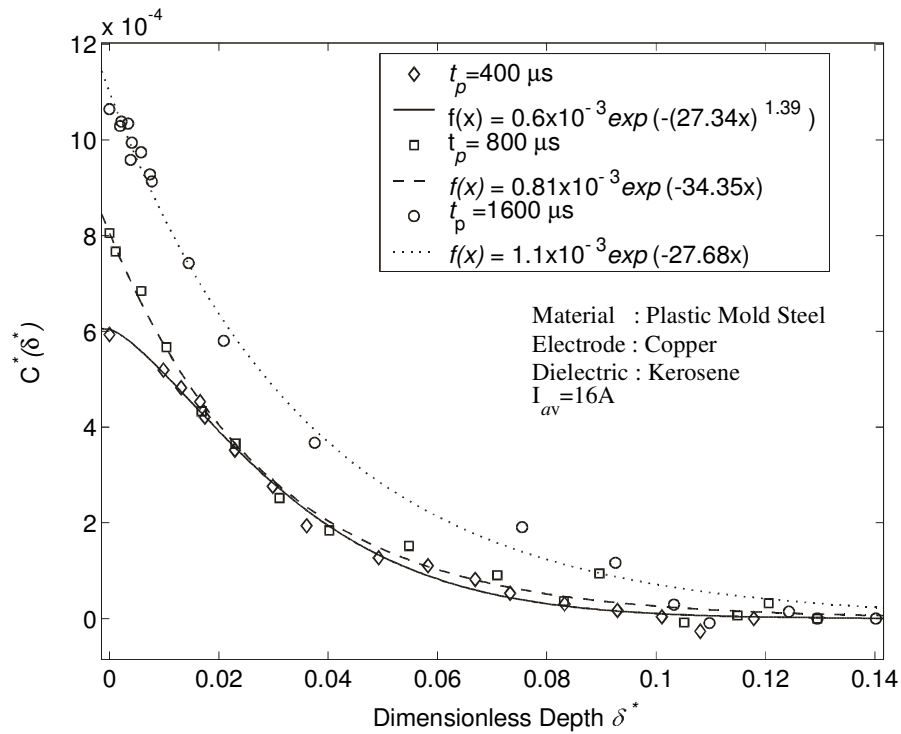


Figure 9.14 Change in Curvature on Cracked Samples.

9.3.3 A Semi Empirical Approach to Estimate Residual Stresses

Thermal material properties can be related with the total energy received to construct a dimensionless group:

$$E_R = \Phi(k, \rho, \alpha, c) \quad (9.1)$$

Here, k , is the thermal conductivity; ρ , is the density; α , is the thermal expansion coefficient and c , is the specific heat of the material. Defining dimensionless energy as:

$$E_R^* = \left[\frac{\rho^5 c^9}{k^8 \alpha} \right]^{1/3} E_R \quad (9.2)$$

It is more realistic to use the total amount of energy received by the workpiece rather than using released energy during machining. Most of the researchers have assumed that a constant fraction of total power is transferred to the electrodes (R_w)

and assumed this value as 0.08 in their work (Dijck and Snoeys, 1974; DiBitonto et al., 1989; Patel et al., 1989; Eubank et al., 1993; Madhu et al., 1991; Bhattacharya et al., 1996; Shankar et al., 1997; Yadav et al., 2002; Das et al., 2003). No comprehensive method has so far proposed to calculate the value of R_w during EDM process (Madhu et al., 1991; Bhattacharya et al., 1996; Shankar et al., 1997; Yadav et al., 2002). The suggested fraction is used for the present work to keep the completeness. The total energy received by the workpiece due to single discharge can be written in the following form:

$$E_w = R_w I_{av} U_{av} t_p \quad (9.3)$$

Thus:

$$E_w^* = \left[\frac{\rho^5 c^9}{k^8 \alpha} \right]^{1/3} R_w E_R \quad (9.4)$$

The newly introduced scaling factor g can be written in dimensionless form representing a relation in terms of received energy as:

$$g^* = (50.22 \times 10^9)^\beta g = \gamma E_w^{*\beta} \quad (9.5)$$

It is found that EDM'ed samples have shown a variation in curvature with respect to removed layer thickness in the following manner.

$$C^*(\delta^*) = A_1 \exp\left(-\left(A_2 \delta^*\right)^2\right) \cosh\left(A_3 \delta^*\right) \quad (9.6)$$

Where the constant coefficients A_1, A_2, A_3 are now equal:

$$\begin{aligned} A_1 &= (19.91 \times 10^{-12})^\beta \gamma E_w^{*\beta} \\ A_2 &= (50.22 \times 10^9)^\beta \frac{a_2}{\gamma E_w^{*\beta}} \\ A_3 &= (50.22 \times 10^9)^\beta \frac{a_3}{\gamma E_w^{*\beta}} \end{aligned} \quad (9.7)$$

If the proposed empirical relation is inserted into the dimensionless form of Stäblein equation:

$$\begin{aligned}
\sigma^* (\delta^*) \frac{S_{HS}}{E} &= \frac{(1-\delta^*)^2}{6(50.22 \times 10^9)^\beta} \exp\left(-\left(\frac{(50.22 \times 10^9)^\beta a_2 \delta^*}{\gamma E_w^{*\beta}}\right)^2\right) \cosh\left(\frac{(50.22 \times 10^9)^\beta a_2 \delta^*}{\gamma E_w^{*\beta}}\right) \\
&\left\{ \frac{2(50.22 \times 10^9)^{2\beta} a_2^2 \delta^*}{\gamma^2 E_w^{*2\beta}} + \frac{4}{(1-\delta^*)} - \frac{(50.22 \times 10^9)^\beta a_3}{\gamma E_w^{*\beta}} \tanh\left(\frac{(50.22 \times 10^9)^\beta a_3 \delta^*}{\gamma E_w^{*\beta}}\right) \right\} \gamma E_w^{*\beta} \\
&+ \frac{(3\delta^* - 2)}{3(50.22 \times 10^9)^\beta} \gamma E_w^{*\beta} - \frac{(396.5 \times 10^{-24})^\beta \sqrt{\pi}}{12a_2} \exp\left(-\left(\frac{a_3}{2a_2}\right)^2\right) \\
&\left\{ \operatorname{erf}\left(\frac{(50.22 \times 10^9)^\beta a_2 \delta^*}{\gamma E_w^{*\beta}} - \frac{a_3}{2a_2}\right) + \operatorname{erf}\left(\frac{(50.22 \times 10^9)^\beta a_2 \delta^*}{\gamma E_w^{*\beta}} + \frac{a_3}{2a_2}\right) \right\} \gamma^2 E_w^{*2\beta}
\end{aligned} \tag{9.8}$$

The last term is negligibly small when compared to the others. Hence, the result can be written in a more compact form by dropping it.

$$\begin{aligned}
\sigma^* (\delta^*) \frac{S_{HS}}{E} &= \frac{(1-\delta^*)^2}{6(50.22 \times 10^9)^\beta} \exp\left(-\left(\frac{(50.22 \times 10^9)^\beta a_2 \delta^*}{\gamma E_w^{*\beta}}\right)^2\right) \cosh\left(\frac{(50.22 \times 10^9)^\beta a_2 \delta^*}{\gamma E_w^{*\beta}}\right) \\
&\left\{ \frac{2(50.22 \times 10^9)^{2\beta} a_2^2 \delta^*}{\gamma^2 E_w^{*2\beta}} + \frac{4}{(1-\delta^*)} - \frac{(50.22 \times 10^9)^\beta a_3}{\gamma E_w^{*\beta}} \tanh\left(\frac{(50.22 \times 10^9)^\beta a_3 \delta^*}{\gamma E_w^{*\beta}}\right) \right\} \gamma E_w^{*\beta} \\
&+ \frac{(3\delta^* - 2)}{3(50.22 \times 10^9)^\beta} \gamma E_w^{*\beta}
\end{aligned} \tag{9.9}$$

The result is the residual stress induced by EDM on machined surfaces. Constants γ and β are found experimentally for different tool electrode and dielectric liquid combinations (Table 7.2, 7.3). It is considered that this equation may be used to estimate residual stresses induced during EDM in most of the tool steels.

9.4 Finite Element Analysis of EDM

Single spark solution has shown depressed craters from the middle with edges that rose above the surface. Such crater shape is quite well known to researchers. From parametric simulations, it is proved that raise of the crater edge is due to plasma

pressure induced during sparking. Thickness of thermally affected layers is found insensitive to change in plasma pressure, energy partition and plasma radius although a remarkable change in crater shape can be observed. Estimated white layer thickness is usually thinner than the actual thickness. It is shown that white layer usually overlapped with the previous formed layer during machining which lead to non-homogeneous and thicker distribution on the machined surface. On the other hand the thickness of heat-affected layer is well predicted. The thickness of the layer is found as $9.5\mu\text{m}$ from the micrographs that is very close to estimated thickness of $10\ \mu\text{m}$.

Lim et al. (1991) have also stated that after cessation of fast successive discharges, the molten metal is subjected to two rapid quenching actions: flushes of dielectric on the top and the cold underlying metal below. It is therefore most probable that solidification of the molten metal would take place both downwards from the interface with the dielectric and upwards from the interface with the underlying metal, leading to the formation of the topmost and the innermost sublayers. Time history of temperature found from finite element analysis supports this conclusion. Peak temperatures shifted with an increased time delay with respect to depth after the end of pulse duration (Figure 8.17, 8.20, 8.23).

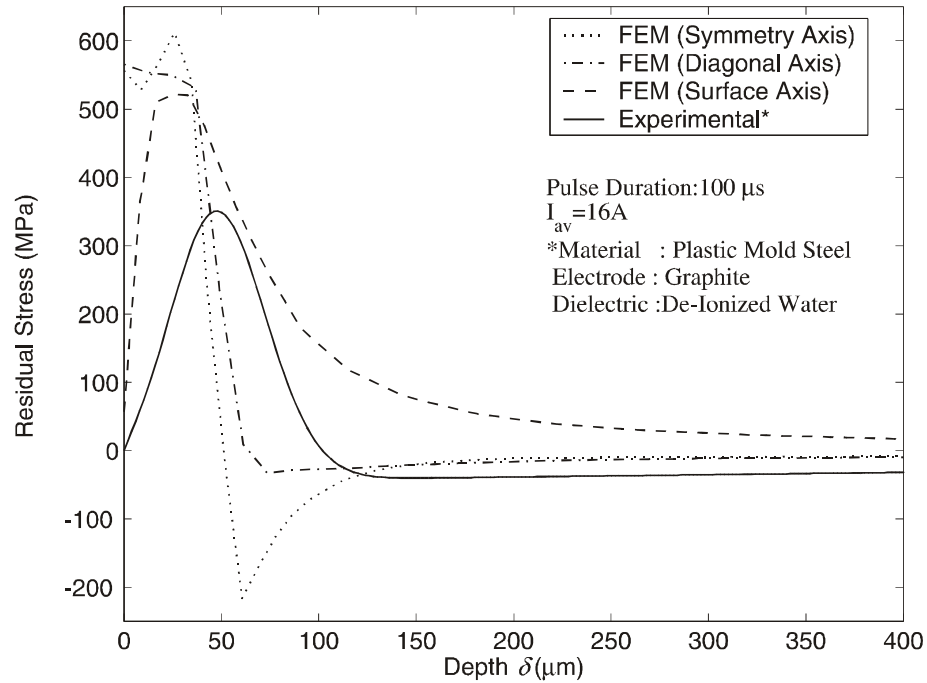
It is not easy to validate residual stress data, especially for a single spark, with experimentally obtained multi-spark results. Experimental results show residual stress pattern that is equilibrated with elastic bending stresses. For that reason, surface, diagonal and symmetry paths are defined to obtain comparable results in FEM analysis. It should be noted that compressive equilibrating stresses on these paths are different from the bending equilibrating stresses obtained from the experimental results since analyzed sample geometries are different between experiments and FEM.

Finite element analysis of EDM machining has revealed that the radial component of residual stresses is dominant. This component of stresses has shown a good agreement with the experimental results in single spark case (Figure 9.15, 9.16).

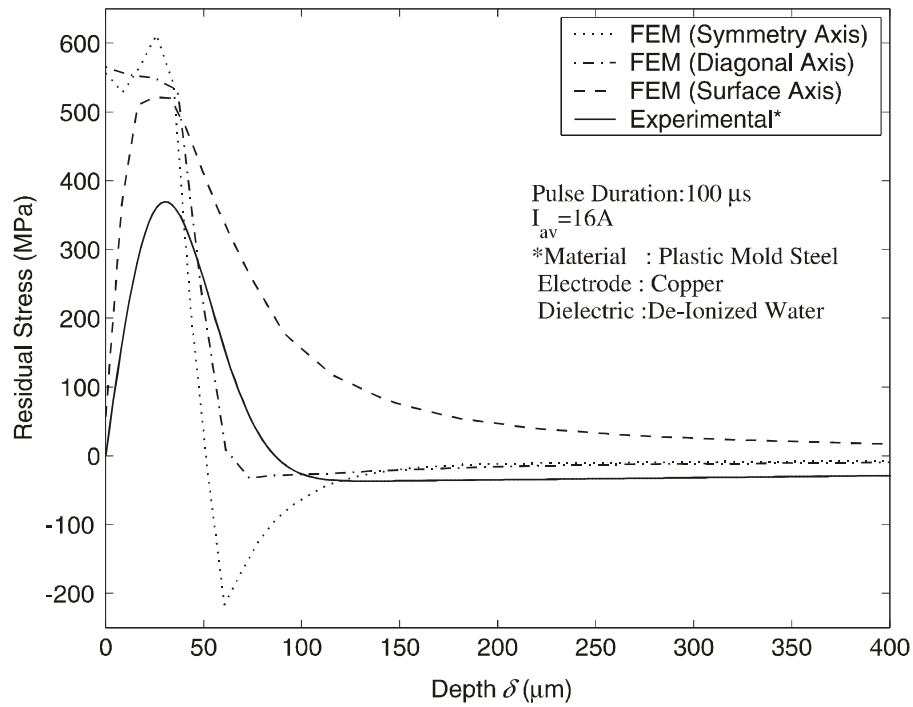
In these figures radial residual stress component on symmetry, diagonal and surface paths found from finite element analysis are compared with the measured residual stresses for different electrode and dielectric liquid combinations. The results indicate that the stress levels reach very high values close to the surface but decrease very quickly in the sub-surface region, which is analogous with the experimental results. Although the exact values of stresses do not match especially at near surface region, the order of magnitude and the general trend of the data match very well. This is a clear sign that estimation of residual stresses within the recast layer fails since this portion of the material actually liquefy and hence relief its stresses during sparking that is not take into consideration in FEM analysis. In addition, cracks also work as a stress relieving mechanism. Once crack occur, they reduce the stress level of residual stresses in the surrounding area. Hence, the actual stress level of recast portion of the material lesser in value. The best agreement is achieved when copper electrode is used as tool electrode and de-ionized water as dielectric liquid. This situation could be described as the lack of carbon source during machining, which prevents carbon diffusion to the machined surface.

Parametric simulations for different pulse durations (Figure 9.17-9.27) have also shown a good agreement with experimental results although plasma radius kept constant. These results indicate that residual stresses induced on machined surfaces due to EDM is directly related with the energy released during sparking with a constant power factor depending on tool electrode material, dielectric liquid.

An attempt has been done to simulate the erosion process for triple spark, which struck to the workpiece surface at different locations. Such a model is failed since extremely high stresses are developed just beneath the surface, which lead to high compressive residual stress in the access of the material. This is presumably due to the plane strain assumption, which is not the actual case. Thus a three dimensional model should be tested to simulate the erosion process for multi sparks.

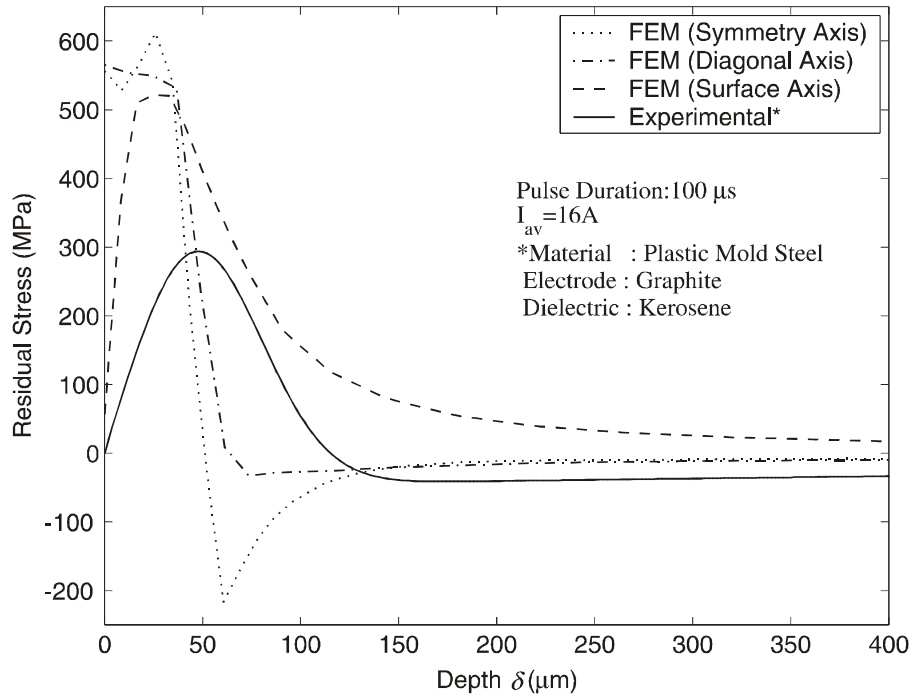


a)

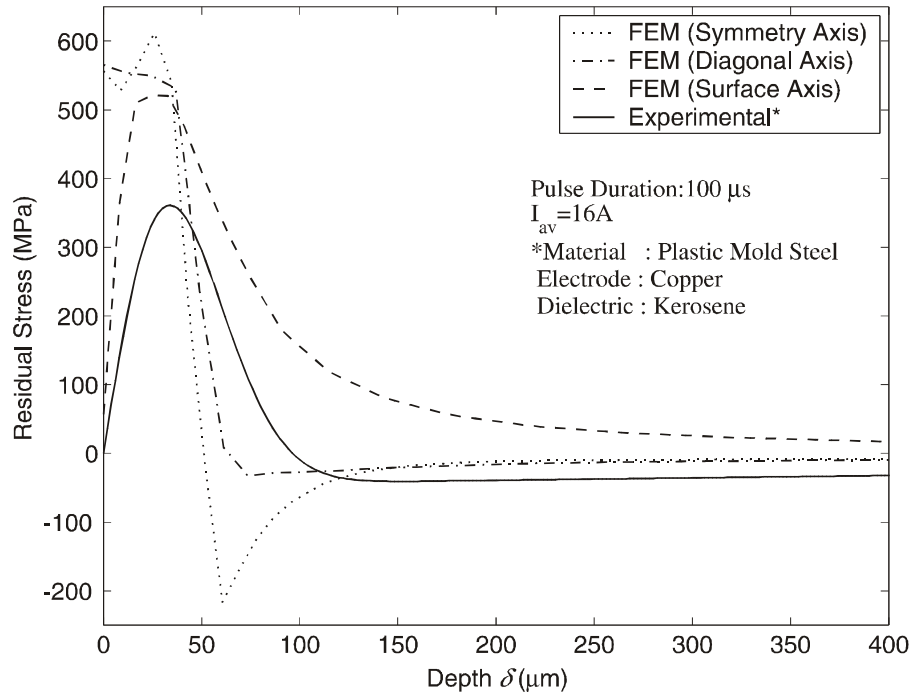


b)

Figure 9.15 Comparison of Finite Element Analysis Results with Measured Residual Stresses ($I_{av}=16A$, $t_p=100\mu s$). a) Graphite b) Copper Electrode in De-Ionized Water Dielectric Liquid.



a)



b)

Figure 9.16 Comparison of Finite Element Analysis Results with Measured Residual Stresses ($I_{av}=16\text{A}$, $t_p=100\mu\text{s}$). a) Graphite b) Copper Electrode in Kerosene Dielectric Liquid.

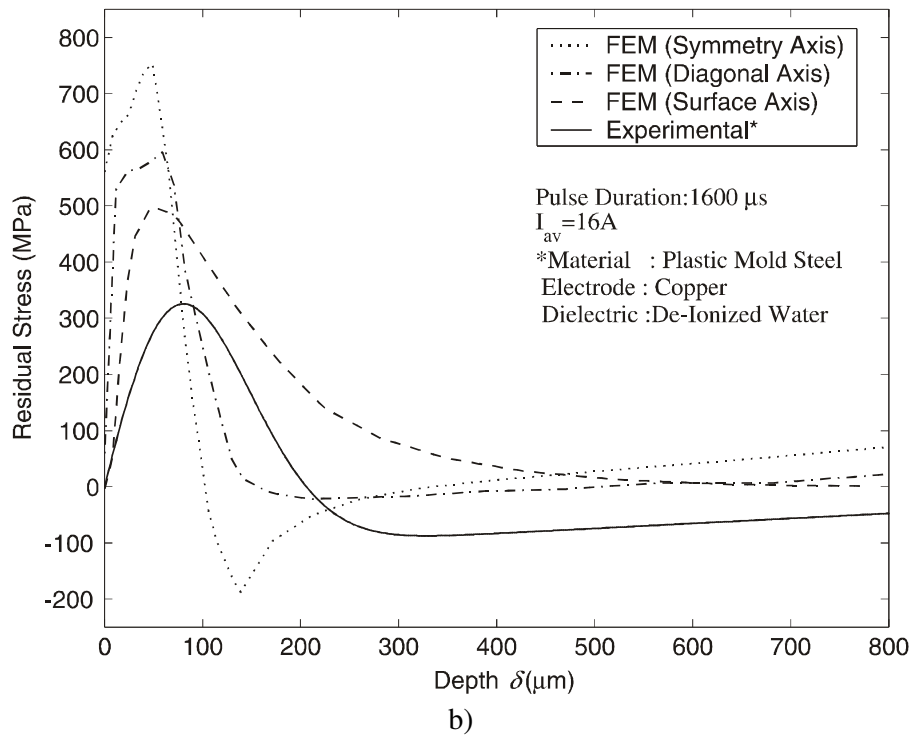
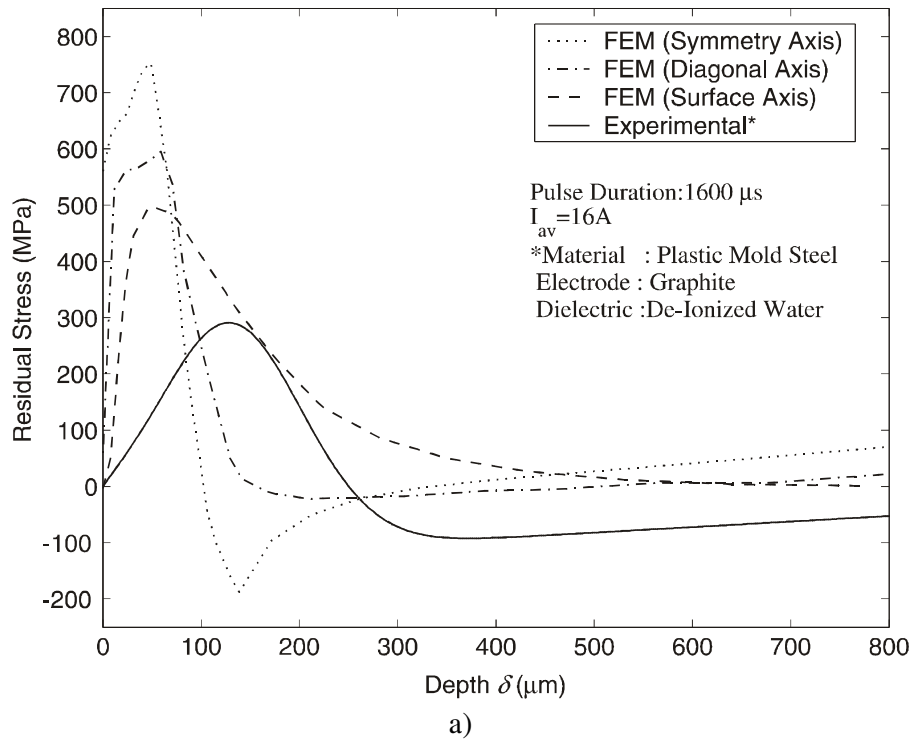
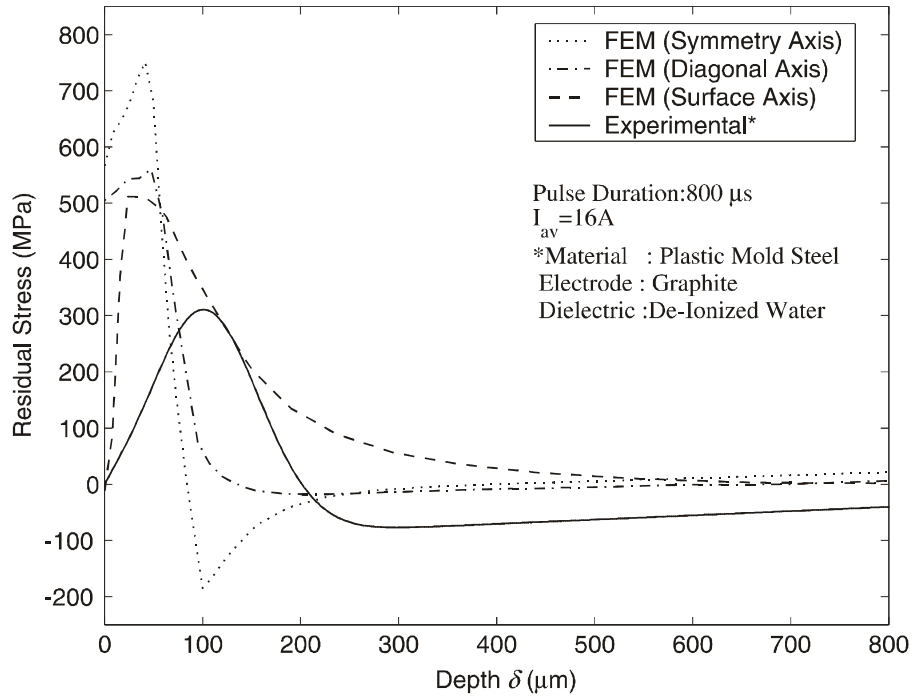
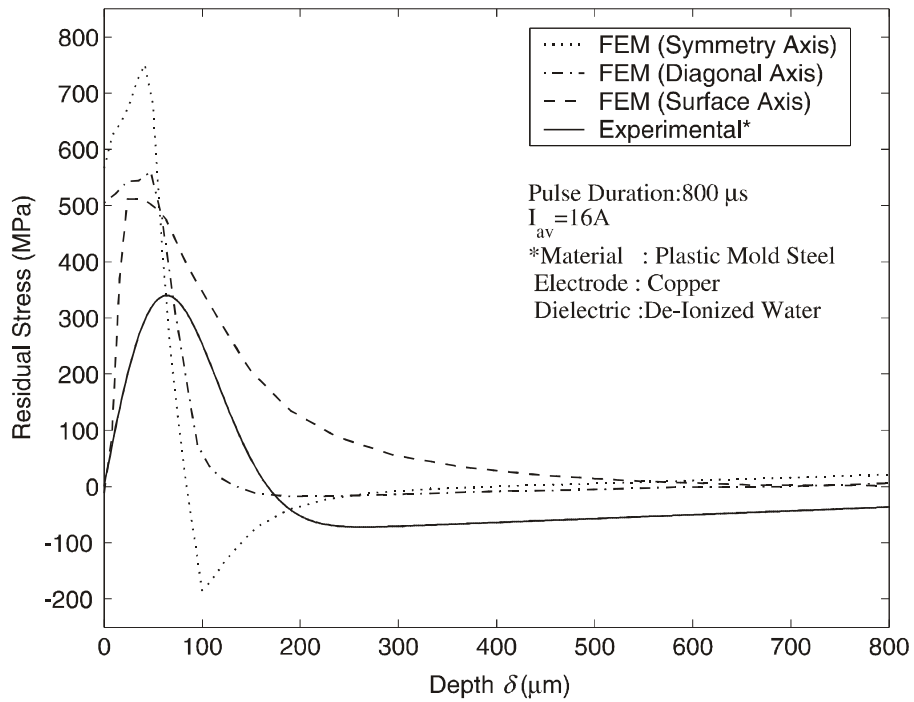


Figure 9.17 Comparison of Finite Element Analysis Results with Measured Residual Stresses ($I_{av}=16\text{A}$, $t_p=1600\mu\text{s}$). a) Graphite b) Copper Electrode in De-Ionized Water Dielectric Liquid.

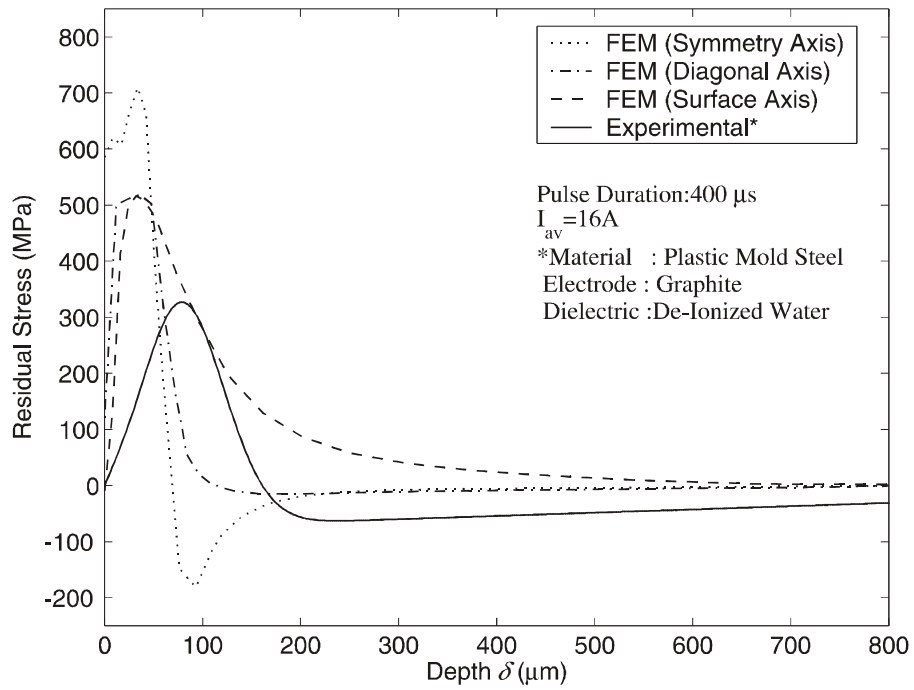


a)

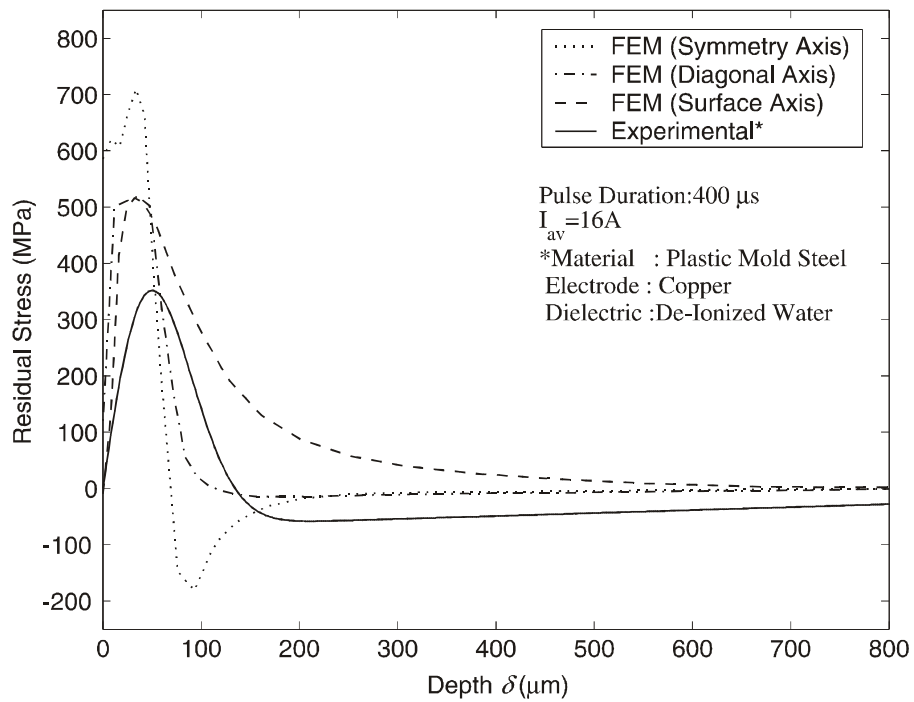


b)

Figure 9.18 Comparison of Finite Element Analysis Results with Measured Residual Stresses ($I_{av}=16\text{A}$, $t_p=800\mu\text{s}$). a) Graphite b) Copper Electrode in De-Ionized Water Dielectric Liquid.

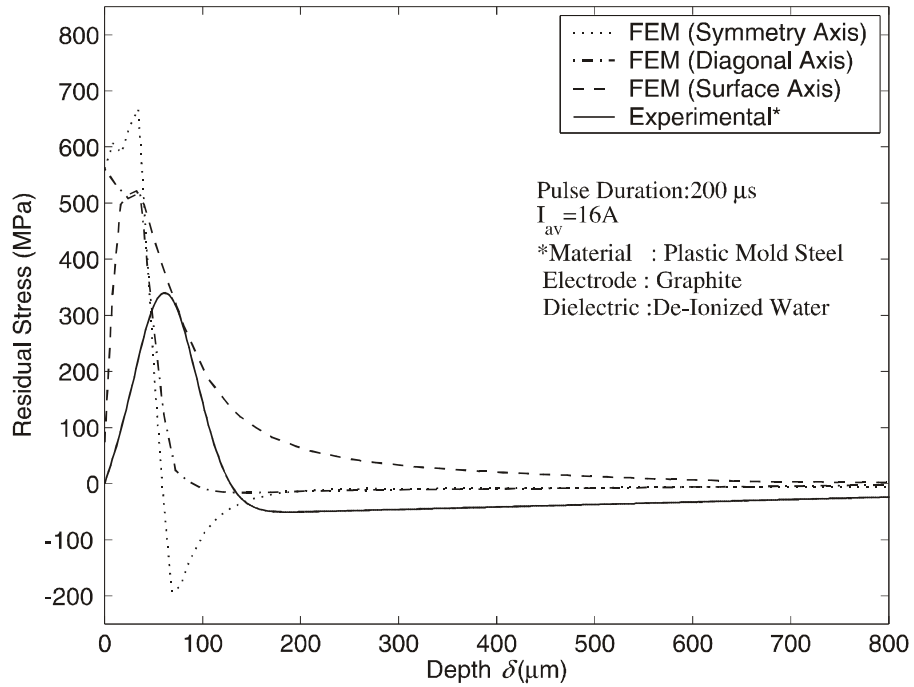


a)

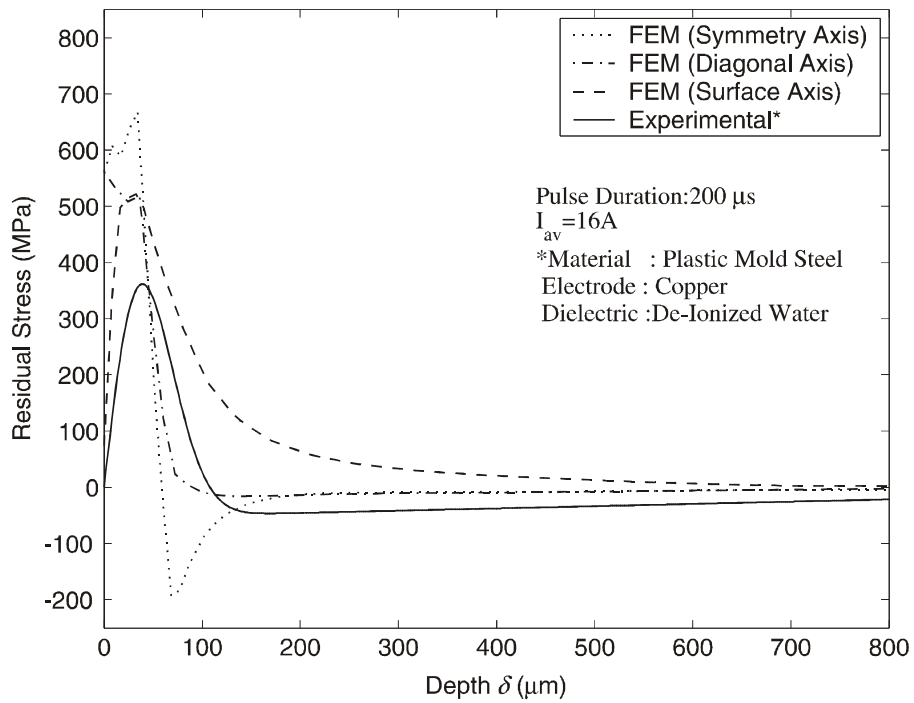


b)

Figure 9.19 Comparison of Finite Element Analysis Results with Measured Residual Stresses ($I_{av}=16\text{A}$, $t_p=400\mu\text{s}$). a) Graphite b) Copper Electrode in De-Ionized Water Dielectric Liquid.



a)



b)

Figure 9.20 Comparison of Finite Element Analysis Results with Measured Residual Stresses ($I_{av}=16\text{A}$, $t_p=200\mu\text{s}$). a) Graphite b) Copper Electrode in De-Ionized Water Dielectric Liquid.

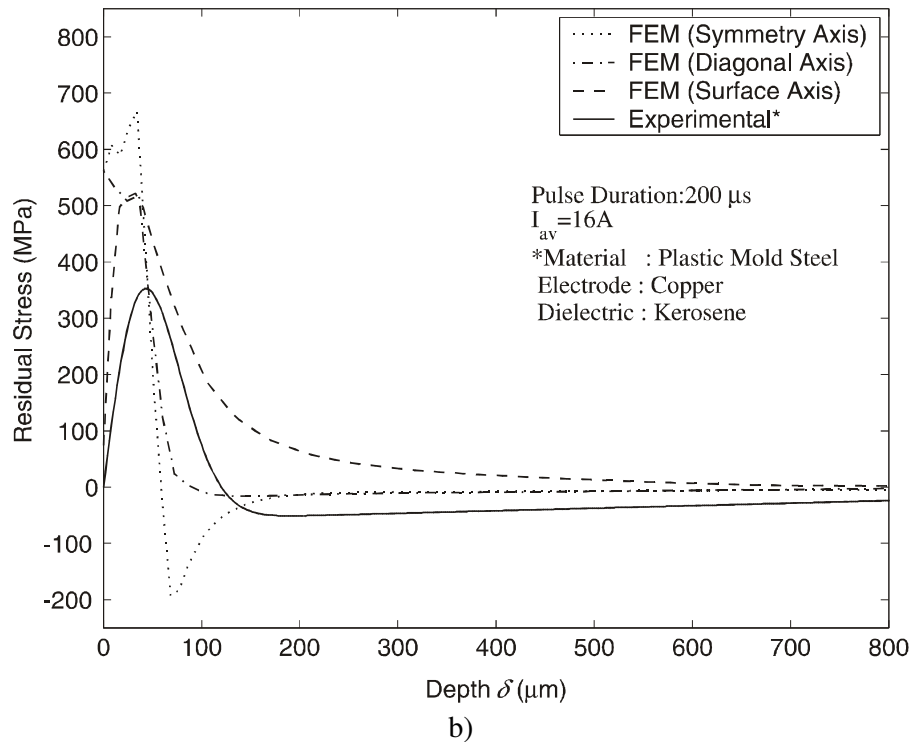
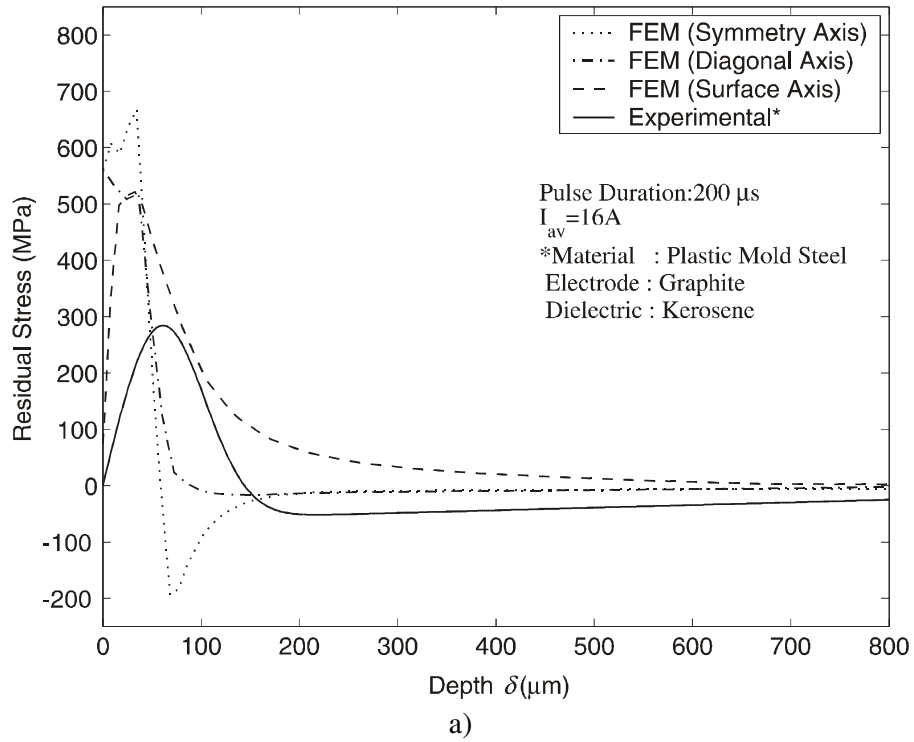
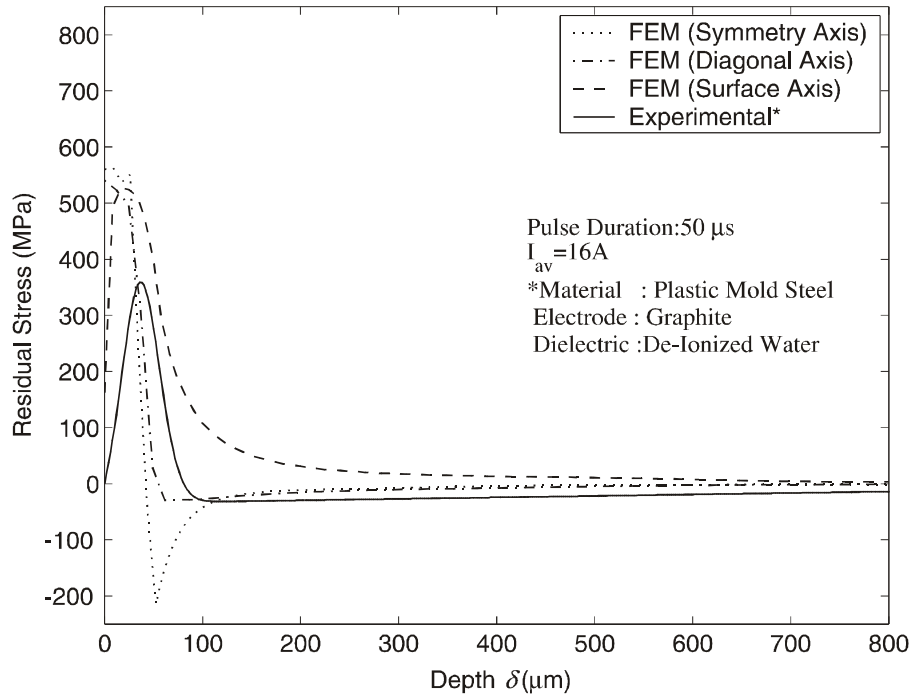
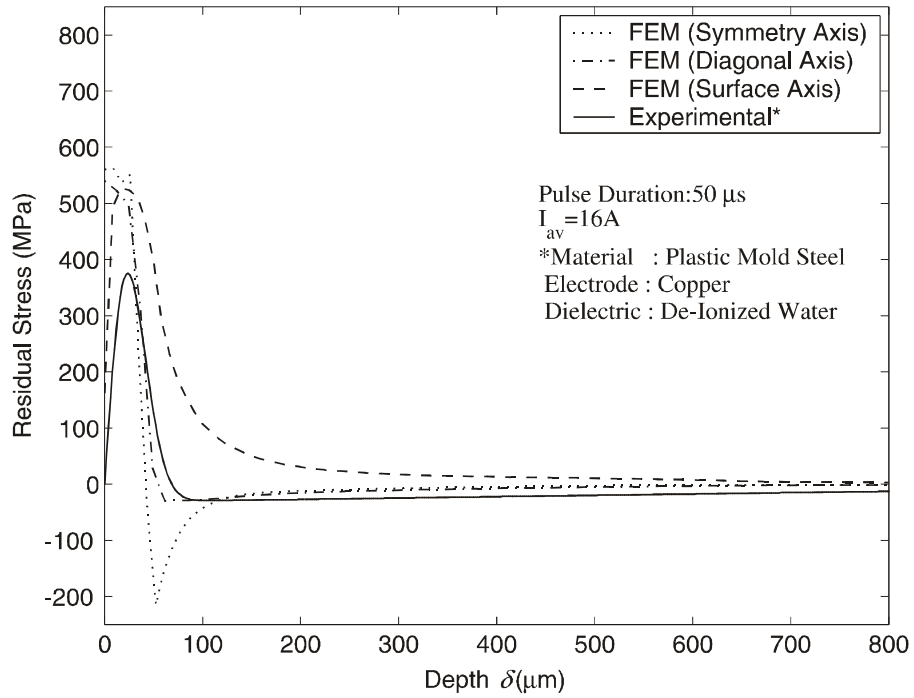


Figure 9.21 Comparison of Finite Element Analysis Results with Measured Residual Stresses ($I_{av}=16\text{A}$, $t_p=200\mu\text{s}$). a) Graphite b) Copper Electrode in Kerosene Dielectric Liquid.



a)



b)

Figure 9.22 Comparison of Finite Element Analysis Results with Measured Residual Stresses ($I_{av}=16\text{A}$, $t_p=50\mu\text{s}$). a) Graphite b) Copper Electrode in De-Ionized Water Dielectric Liquid.

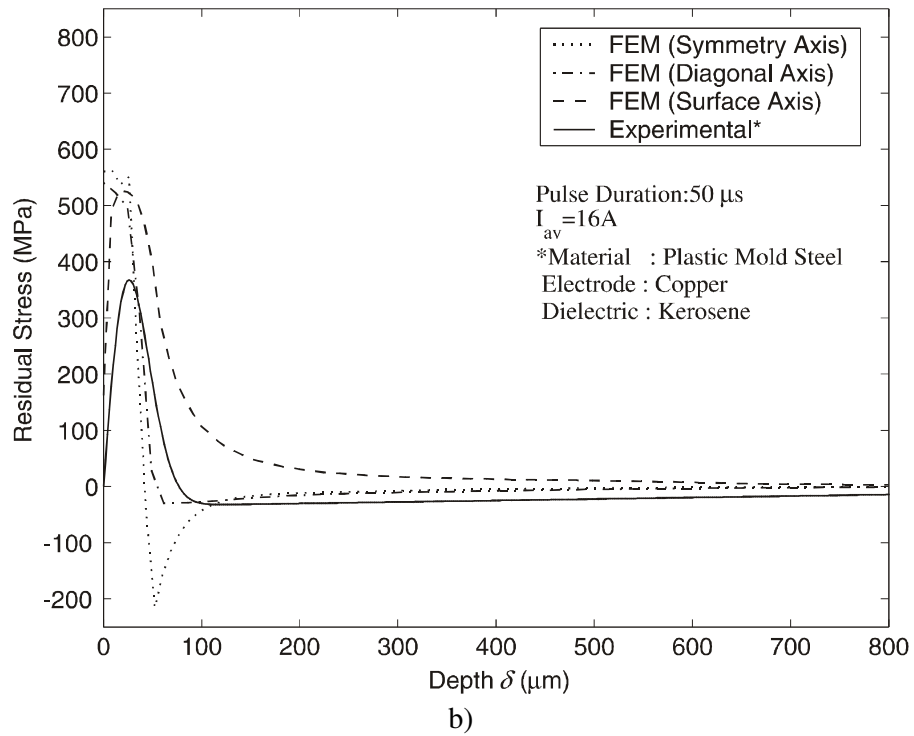
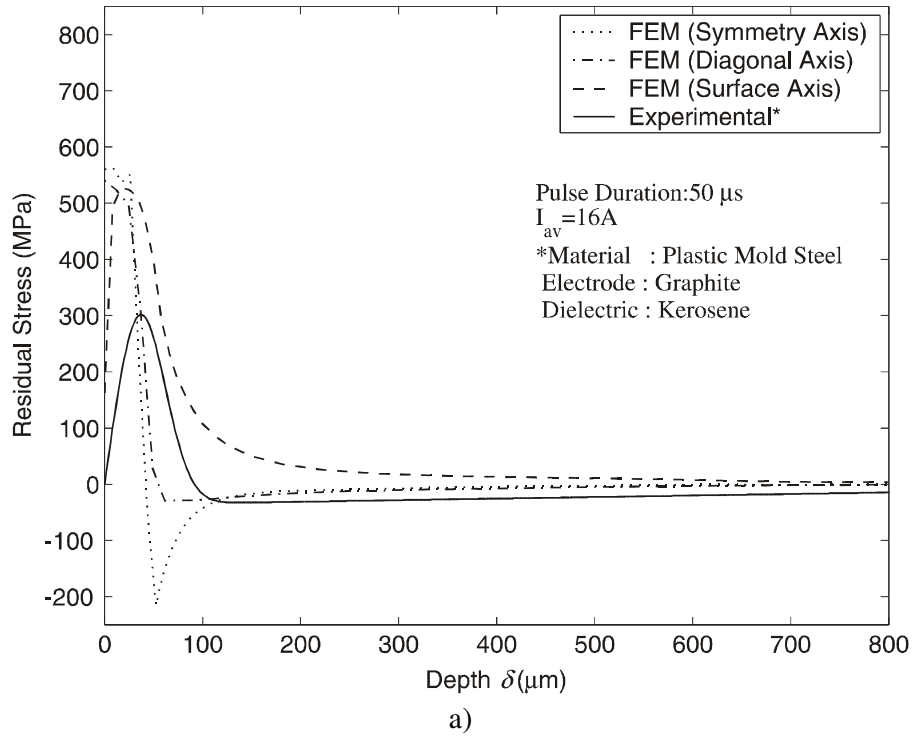


Figure 9.23 Comparison of Finite Element Analysis Results with Measured Residual Stresses ($I_{av}=16\text{A}$, $t_p=50\mu\text{s}$). a) Graphite b) Copper Electrode in Kerosene Dielectric Liquid.

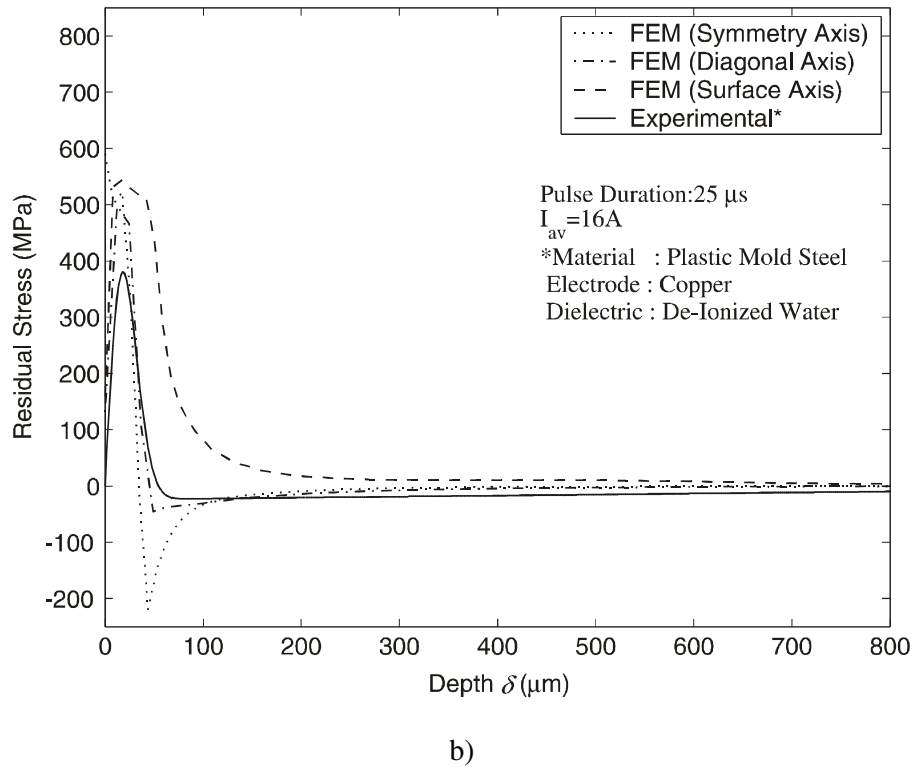
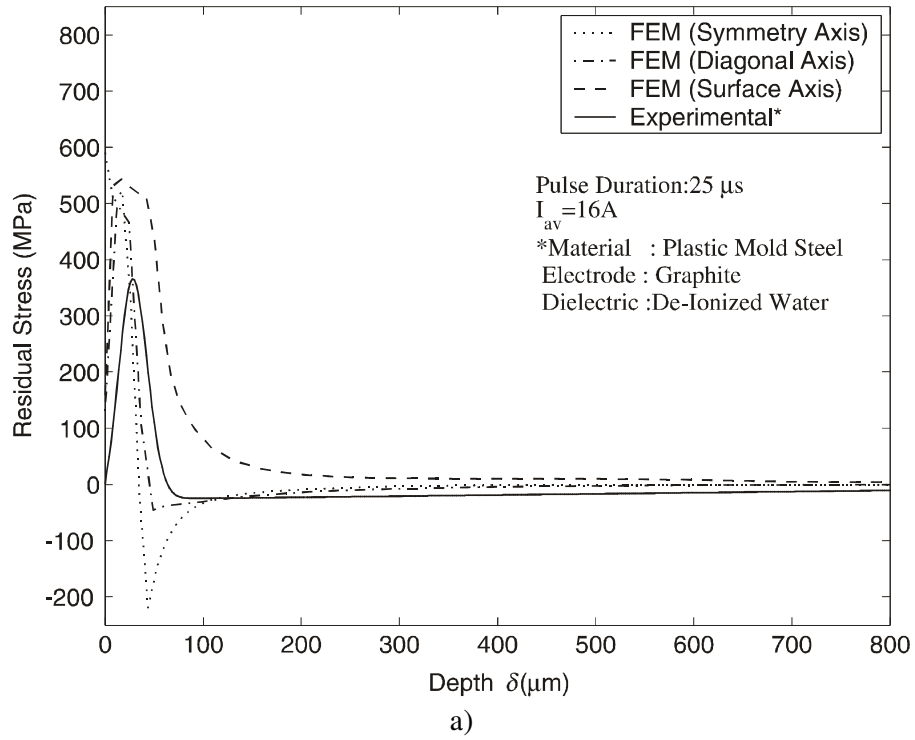
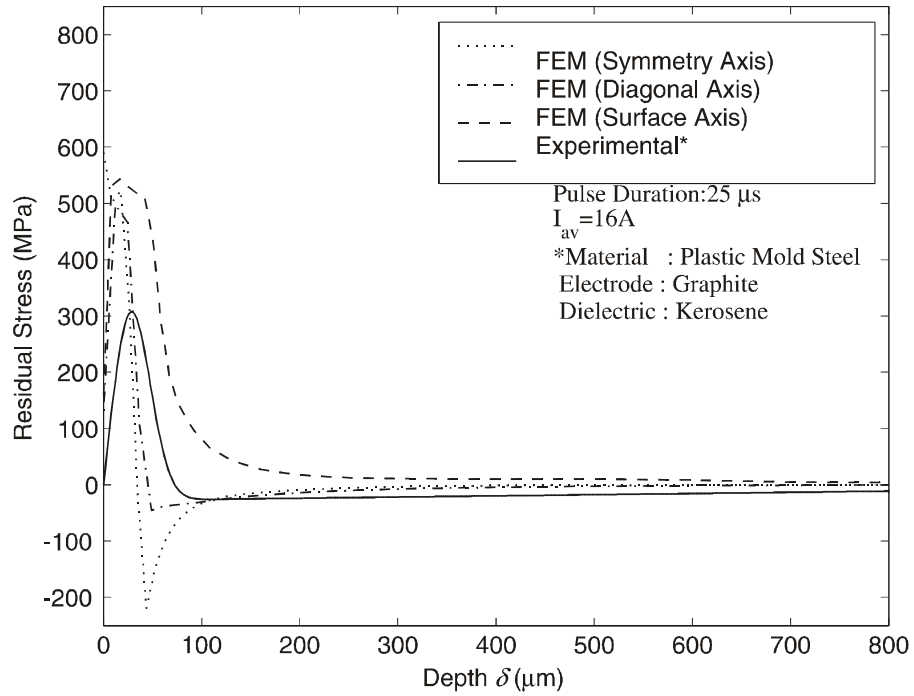
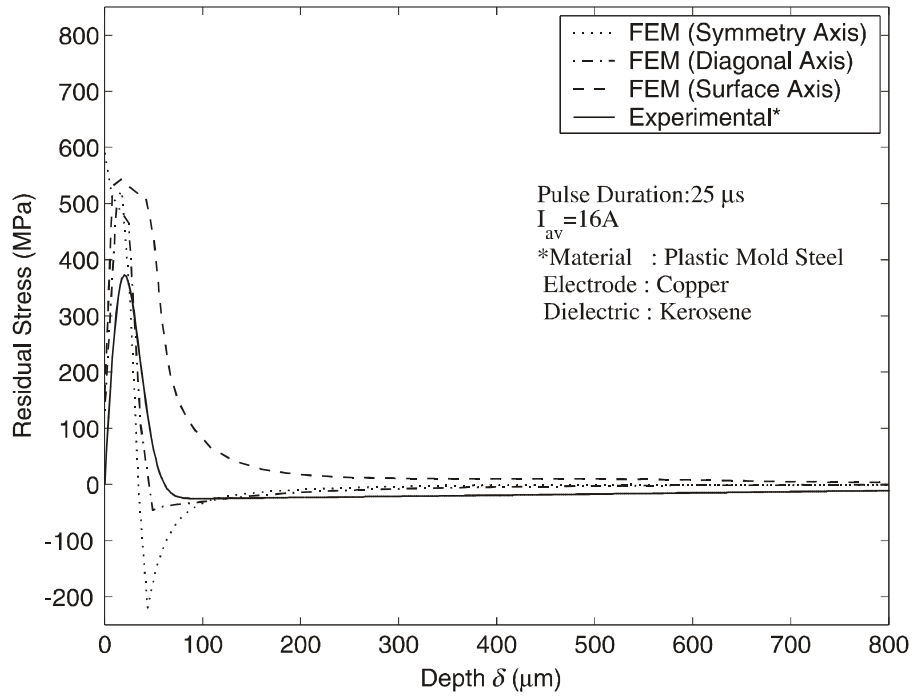


Figure 9.24 Comparison of Finite Element Analysis Results with Measured Residual Stresses ($I_{av}=16\text{A}$, $t_p=25\mu\text{s}$). a) Graphite b) Copper Electrode in De-Ionized Water Dielectric Liquid.



a)



b)

Figure 9.25 Comparison of Finite Element Analysis Results with Measured Residual Stresses ($I_{av}=16\text{A}$, $t_p=25\mu\text{s}$). a) Graphite b) Copper Electrode in Kerosene Dielectric Liquid.

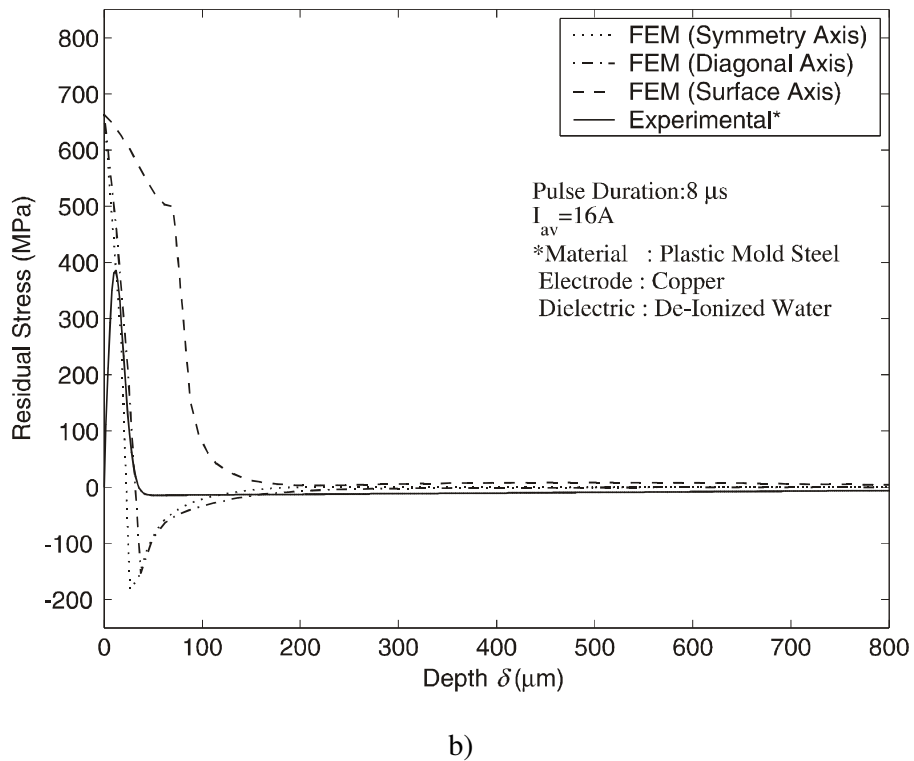
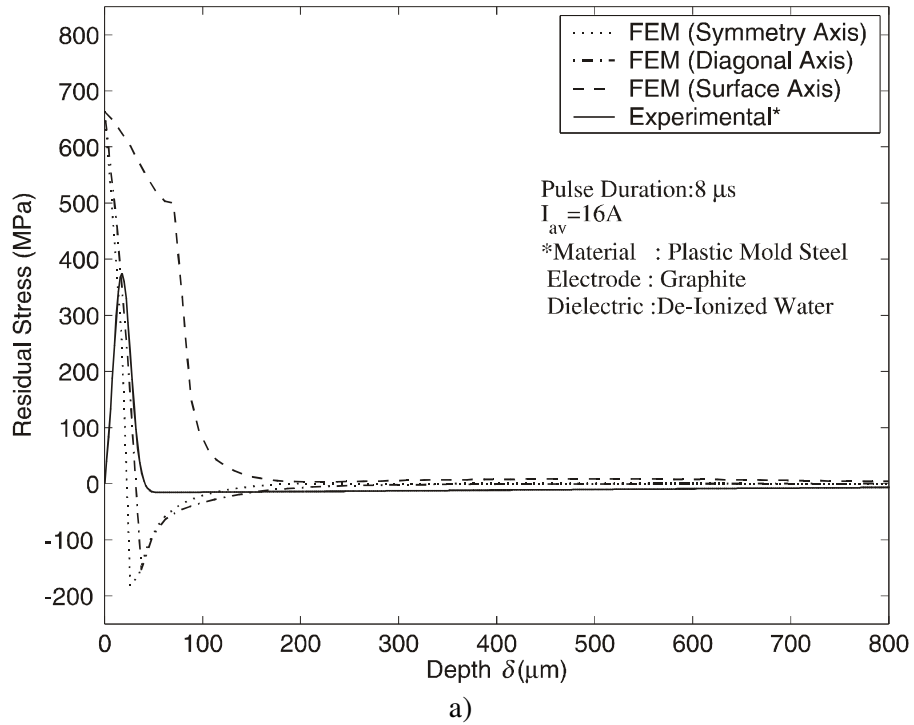
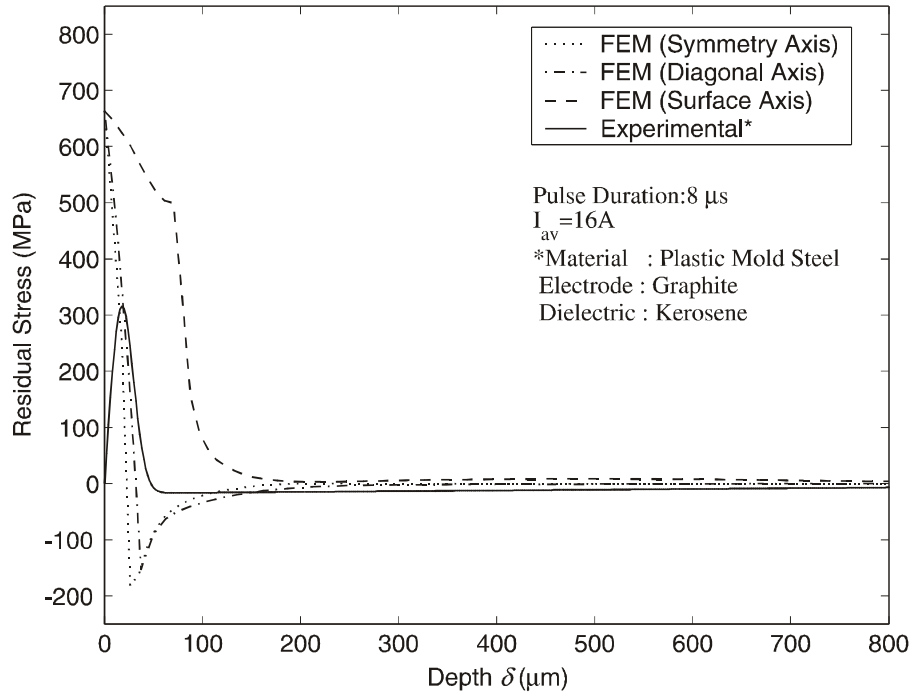
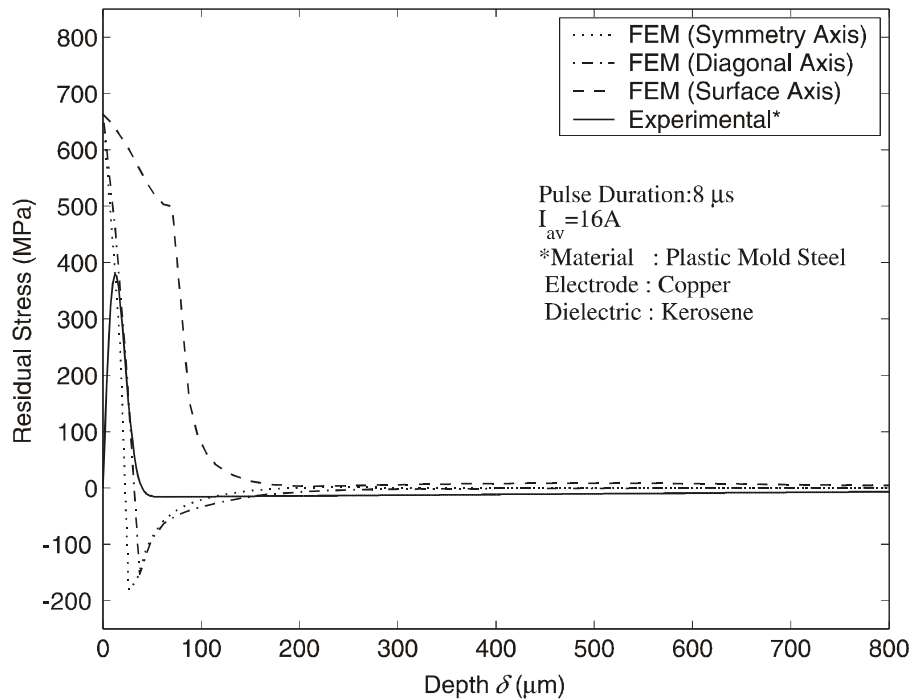


Figure 9.26 Comparison of Finite Element Analysis Results with Measured Residual Stresses ($I_{av}=16\text{A}$, $t_p=8\mu\text{s}$). a) Graphite b) Copper Electrode in De-Ionized Water Dielectric Liquid.



a)



b)

Figure 9.27 Comparison of Finite Element Analysis Results with Measured Residual Stresses ($I_{\text{av}}=16\text{A}$, $t_p=8\mu\text{s}$). a) Graphite b) Copper Electrode in Kerosene Dielectric Liquid.

CHAPTER X

SUMMARY AND CONCLUSIONS

This research study is concerned with describing surface integrity phenomena with an emphasis on residual stresses in EDM'ed surfaces. Surface topography and sub-surface metallurgy are investigated by scanning electron and optical microscopy respectively. Metallurgical phases on machined surfaces are analyzed by using x-ray diffraction patterns. Hardness of affected layers is measured with a microhardness tester. Residual stresses are obtained by discrete measurements of deflections after removal of each layer from machined surfaces using electro chemical polishing. Finally, a finite element based model is developed to estimate the residual stress distribution beneath the EDM'ed surfaces.

The outermost layer, which is known as the white layer is found under all machining conditions including when de-ionized water is used as dielectric liquid. A multilayer structure made up of similar microstructures is found within white layer under rough machining conditions when carbon based dielectric is used. In this case, columnar and dendritic microstructures are overlapped with featureless layers. The hardness increase of the white layer is caused by both the presence of carbides and martensite. Although a relatively small amount of austenite is detected on EDM samples, EDT produced a considerable amount of retained austenite within white layer. It is found that excessive amount of austenite soften the white layer. Consequently, carbide formation attributed to the pyrolysis of the dielectric liquid. Tool electrode is less effective on carbide formation. Small amount of retained austenite and martensite, which increase white layer hardness, is formed when de-ionized water is used as dielectric liquid.

In all cases, thermally affected layers are found beneath the white layer. Different appearances are obtained for different materials. This layer is considered as composed of a hard-untempered martensite on the top and overtempered martensite below. An intermediate layer, between the white layer and the tempered zone, is observed on micro alloy steel samples at rough machining conditions.

It is found that tool electrode and dielectric liquid alter the resultant surface topography. Number of globules and chimneys formed on machined surfaces decreased when non-carboneous tool electrode and dielectric liquid are used. Controversially, amount of these features decreased if carbon based dielectric liquid is used.

Cracks formed on the machined surface are found to follow the pitting arrangements with closed loops and crossing perpendicularly with radial cracks. Cracks formed in a crater are continued to propagate when another discharge takes place at the neighborhood. Intensity of cracking is increased at high pulse durations and low pulse current when carbon based dielectric liquid is used during machining. Such cracking pattern is not observed when de-ionized water is used as dielectric liquid. This was suggesting formation of a brittle structure just beneath the EDM'ed surfaces due to carbon absorption from the dielectric liquid.

The residual stresses are found to be tensile in nature. They increase from the surface and reach their maximum value. Then falls rapidly to relatively low values of compressive residual stresses. Compressive stresses are related to sample thickness since residual stresses within plastically deformed layers are balanced with elastic stresses in the core of the material. The residual stress pattern is found to be unchanged with respect to machining parameters. Thus, a unit amplitude shape function representing change in curvature with respect to removal depth is proposed. The proposed form is found as a special form of Gauss Distribution, which is the sum of two Gaussian peaks, with the same amplitude and pulse width

but opposite center location that is represented by three constant coefficients. In each case, a well agreement with the proposed form is established with the experimental results. Results have shown that these coefficients have a power functional dependency with respect to released energy.

Finite element analysis of EDM has revealed that the radial component of residual stresses is dominant. This component of stresses has shown a good agreement with the experimental results in single spark case. These results have proved that residual stresses induced on the machined surfaces due to EDM is directly related with the energy released during sparking with a constant power factor depending on tool electrode and dielectric liquid.

The effect of operating parameters on surface cracking, residual stresses and heat affected layer thickness are summarized in Table (10.1).

Table 10.1 Affects of Operating Parameters on Cracking, Residual Stresses and Affected Layer Thickness.

	Cracking	Residual Stress and Affected Layer Thickness
Pulse Time	Possible at high pulse durations.	Increase in energy level increases thickness of affected layers and residual stress profile.
Average Pulse Current	Possible at low current settings.	
Dielectric Liquid	Increases when hydrocarboneous based dielectric liquid is used.	Increase in thickness of affected layer and residual stress profile when hydrocarboneous based dielectric liquid is used.
Tool Electrode	Have a minor effect.	Have a minor effect.

The above paragraphs contain a summary of the results found in the present research study. Several important conclusions can be reached from this information.

Conclusion 1: The white layer is produced on EDM surfaces regardless of the dielectric liquid and tool electrode material.

Conclusion 2: The white layer of samples machined in hydrocarbonaceous dielectric liquid contains more carbon than the base material due to pyrolysis products of the cracked hydrocarbon dielectric during the discharge. Consequently, the white layer consists of iron carbides and martensite distributed in austenite matrix, forming dendritic structures due to rapid solidification of the molten metal.

Conclusion 3: Amount of retained austenite phase and intensity of micro cracks are much less in the white layer of samples machined in de-ionized water dielectric liquid. The hardness increase of the white layer with respect to parent material is caused only by martensite.

Conclusion 4: There is no conclusive evidence of carbon enrichment from the graphite electrode. Thus, carbon is absorbed from the dielectric liquid rather than from the electrode.

Conclusion 5: Cracks on EDM surfaces follow the pitting arrangements with closed loops and crossing perpendicularly with radial cracks and continues to propagate when another discharge takes place at the neighborhood. Intensity of cracking is increased at high pulse durations and low pulse currents.

Conclusion 6: Material removal rate during electrochemical polishing on EDM'ed surfaces is non-linear due to different electrochemical polishing behavior of affected layers. Therefore, discrete measurements of deflections during layer removal should be preferred to ensure thickness of the analyzed sample during electrochemical polishing.

Conclusion 7: Residual stresses mainly as a result of the thermal contraction of the resolidified metal, which was not expelled from the craters, onto the relatively unaffected parent metal, inducing plastic deformation and biaxial tensile stress.

Conclusion 8: High tensile residual stresses are generated by EDM. It increases from the surface and reaches to its maximum value. This maximum value is around the ultimate tensile strength of the material. Then falls rapidly to relatively low values of compressive residual stresses. Compressive stresses are related to sample thickness since residual stresses within plastically deformed layers are balanced with elastic stresses in the core of the material.

Conclusion 9: Thickness of affected layers and location of tensile peak stress is directly related with the energy released during sparking. Thus, a semi empirical model is proposed to estimate these stresses.

This research study is described the surface integrity phenomena with an emphasis on residual stresses in EDM'ed surfaces in detail. Proposed models can now be used to investigate the effects of different process parameters on different kinds of materials that are used in EDM. It is expected these models and experimental data in this work to become a powerful tool and data in the hands of EDM researchers to not only extend the understanding of the process but also for better process and product design.

REFERENCES

- Aleksandrov, V.P.: "Residual Stresses and the Long Term and Fatigue Strengths of Heat-Resistant Materials After Electro-Spark Machining", in book: Lazarenko (Ed.) *Electrospark Machining of Metals*, Vol. 3, pp. 98-102, 1965.
- Aleksandrov, V.P. and Zolotykh, B.N.: "On the Selection of the optimum conditions in machining Nickel-Based Heat-Resistant Alloys by the Electrospark Method", *Izv. Akad. Nauk SSSR*, Vol. 6, 1958.
- Aspinwall, D.K.; Wise, M.L.H.; Stout, K.J.; Goh, T.H.A.; Zhao, F.L. and Menshawy, M.F.: "Electric Discharge Texturing", *Int. J. Mach. Tools Manufact.* Vol. 32, No. 1/2, pp. 183-193, 1992.
- Barash, M. and Sri-Ram, M.G.: "Some Properties of Spark Machined Heat Treated Steel", In Proc. 3rd Int. MTDR Conf., Birmingham, pp. 85-91, 1962.
- Barash, M.: "Effect of EDM on the Surface Properties of Tool and Die Steels", *Metals Eng. Quart.*, pp. 48-51, Nov. 1965.
- Beck, J.V.: "Transient Temperatures in a Semi-Infinite Cylinder Heated By a Disc Heat Source", *Int. J. Heat and Mass Transfer*, Vol. 24, No. 10, pp. 1631, 1981.
- Beck, J.V.: "Large Time Solutions for Temperatures in a Semi-Infinite Body with a Disc Heat Source", *Int. J. Heat and Mass Transfer*, Vol. 24, pp. 155, 1981.
- Beck, G. and Ericsson, T.: "Prediction of Residual Stresses due to Heat Treatment" In Proc. of Int. Conf. on Residual Stresses, Residual Stresses in Science and Technology, Garmisch-Partenkirchen, 1987.
- Bhattacharya, R.; Jain, V.K. and Ghoshdastidar, P.S.: "Numerical Simulation of Thermal Erosion in EDM Process", *IE(I) Journal-PR*, Vol. 77, pp. 13-19, 1996.
- Brinksmeier, E.; Koning, W.; Leskover, P. and Tonshoff, H. K.: "Residual Stress Measurement and Causes in Machining Process", *Ann. of CIRP*, Vol. 31, No. 2, pp. 491-510, 1982.
- Bucklow, I.A. and Cole, M.: "Spark Machining", *Metall. Rev.*, Review No. 135, Vol. 3, No. 6, pp. 103-118, 1969.
- Cabanillas, E.D.; Desimoni, J.; Punte, G. and Mercader, R.C.: "Formation of Carbides by Electro-Discharge Machining of Alpha Iron" *Mater. Sci. Eng.*, Vol. A276, pp. 133-140, 2000.

Carlsaw, M.S. and Jeager, J.C.: "Conduction of Heat in Solids" Oxford Press, Oxford, 1959.

Chen, Y. and Mahdivan, S.M.: "Analysis of Electro-Discharge Machining Process and its Comparison with Experiments" J. Mater. Process. Technol., Vol. 104, pp. 150-157, 2000.

Chen, Y. and Mahdivan, S.M.: "Parametric Study into Erosion Wear in a Computer Numerical Controlled Electro-Discharge Machining Process" Wear, Vol. 236, pp. 350-354, 1999.

Chen, S.L.; Yan, B.H. and Huang, F.Y.: "Influence of Kerosene and Distilled Water as Dielectrics on the Electric Discharge Machining Characteristics of Ti-6Al-4V" J. Mater. Process. Technol., Vol. 87, pp. 107-111, 1999.

Chow, H.M.; Yan, B. H.; Huang, F.Y. and Hung, J.C.: "Study of Added Powder in Kerosene for the Micro-Slit Machining of Titanium Alloy using Electro-Discharge Machining", J. Mater. Process. Technol., Vol. 101, pp. 95-103, 2000.

Cogun, C. and Savsar M.: "Statistical Modeling of Discharge Pulses in Electric Discharge Machining", Int. J. Mach. Tools Manufact., Vol. 30, No. 3, pp. 467-474, 1990.

Crookall, J.R. and Khor, B.C.: "Residual Stresses and Surface Effects in Electro Discharge Machining", In Proc. of 13th MTDR Conf., Birmingham, pp. 331-338, 1972.

Crookall, J.R. and Khor, B.C.: "Electro-Discharge Machined Surfaces", In Proc. of 15th MTDR Conf., Macmillan, pp.1-12, 1972.

Crookall, J.R. and Heuvelman, C.J.: "Electro Discharge Machining-the State of Art", Annals. CRIP, Vol. 20, No.2, pp. 113-120, 1971.

Dallas, D.B.: "EDM: A Standard Technology for Special Machines" Manufacturing Engineering, Vol. 82, No. 3, pp. 62-66, 1979.

Das, S.; Klotz, M. and Klocke, F.: "EDM Simulation: Finite Element-based Calculation of Deformation, Microstructure and Residual Stresses", J. Mater. Process. Technol., Vol. 142, No. 2, pp. 434-451, 2003.

DeVries, M.F.; Field, M. and Kahles, J.F.: "Relationship of Surface Roughness and Surface Integrity to Functional Properties", Ann. of CIRP, Vol. 25, No. 2, pp. 569-573, 1976.

DiBitonto, D.D.; Eubank, P.T.; Patel, M.R. and Barrufet, M.A.: "Theoretical Models of the Electrical Discharge Machining Process. I. A Simple Cathode Erosion Model", J. Appl. Phys., Vol. 66, No. 9, pp. 4095-4103, 1989.

Dijck, F.V. and Snoeys, R.: "Metal Removal and Surface Layer in Electro- Discharge Machining", In Proc. of Int. Conf. on Prod. Eng., Tokyo- Japan, pp. 46-50, 1974.

Drabkina, S. I.: "The Theory of Development of the Channel in the Spark Discharge", Zurl. Ekspper. Thor. Fiz., Vol. 21, No. 4, pp. 473-483, 1954.

Erden, A. and Bilgin, S.: "Role of Impurities in Electric Discharge Machining", In Proc. of 21st Int. MTDR Conf., Swansea, pp. 345-350, 1980.

Erden, A. and Kaftanoglu, B.: "Heat Transfer Modeling of Electric Discharge Machining" In Proc. of 21st Int. MTDR Conf., Swansea, pp. 351-357, 1980.

Erden, A. and Kaftanoglu, B.: "Investigations on Breakdown Phase of Sparks in Electric Discharge Machining", METU Journal of Pure and Applied Sciences, Vol. 13, No. 1, pp. 45-73, 1980.

Erden, A. and Temel, T.: "Investigation on the Use of Water As a Dielectric Liquid in EDM", In Proc. of 22nd Int. MTDR. Conf., Manchester, pp. 437-440, 1981.

Erden, A. and Kaftanoglu, B.: "Thermo-Mathematical Modeling and Optimization of Energy Pulse Forms in Electric Discharge Machining (EDM)", Int. J. Mach. Tool Des. Res., Vol. 21, No. 1, pp. 11-22, 1981.

Erden, A.: "Role of Dielectric Flushing on Electric Discharge Machining Performance", In Proc. of 23rd Int. MTDR Conf., Swansea, pp. 283-289, 1982.

Erden, A.: "Effect of Materials on the Mechanism of Electric Discharge Machining (E.D.M.)", Trans. ASME, Journal of Engineering Materials and Technology, Vol. 105, pp. 132-138, 1983.

Erden, A.: "Investigations on the Discharge Channel in Electric Discharge Machining", Modeling Measurement and Control, AM SE Press, Vol. 49, No. 3, 39-51, 1993.

Erden, A.; Arınc, F. and Kogmen, M.: "Comparison of Mathematical Models for Electric Discharge Machining", Journal Mater. Process. Manuf. Sci., Vol. 4, pp.163-175, 1995.

Eubank, P.; Patel, R.M.; Barrufel, A. M. and Bozkurt, B.: "Theoretical Models of the Electrical Discharge Machining Process. III. The Variable Mass, Cylindrical Plasma Model", J. Appl. Phys., Vol. 73, No. 11, pp. 7900-7909, 1993.

Field, M. and Kahles, F.: "Review of Surface Integrity of Machined Components" Ann. of CIRP, Vol. 20, No. 1, pp. 107-108, 1971.

Furutani, K.; Saneto, A.; Takezawa, H.; Mohri, N. and Miyake, H.: "Accretion of Titanium Carbide by Electrical Discharge Machining with Powder Suspended in Working Fluid" Journal of the International Society for Precision Engineering and Nano Technology, Vol. 25, pp. 138-144, 2001.

Ghabrial, S.R.: "The Significance of the Hardness Depth and the Effect of Notches on the Fatigue Strength of a Tool Steel for Various Rates of Spark Erosion", *Int. J. Mach. Tool Des. Res.*, Vol. 12, pp. 297-309, 1972.

Ghanem, F.; Braham C. and Sidhom, H.: "Influence of Steel Type on Electrical Discharge Machined Surface Integrity", *J. Mater. Process. Technol.*, Vol. 142, No. 1, pp. 163-173, 2003.

Greene, J.E. and Guerrero-Alvarez, J.L.: "Electro Erosion of Metal Surfaces", *Metallurgical Trans.*, Vol. 5, pp. 695-706, 1974.

Gough, P.J.: "Advances in E.D.M. Technology", *Metallurgia*, Vol. 46, pp. 315-321, 1979.

Guu, Y.H.; Hocheng, H.; Chou, C.Y. and Deng, C.S.: "Effect of Electrical Discharge Machining on Surface Characteristics and Machining Damage of AISI D2 Tool Steel", *Mater. Sci. Technol.*, Vol. 358, pp. 37-43, 2003.

Halkacı, S.H. and Erden, A.: "Experimental Investigation of Surface Roughness in Electric Discharge Machining (EDM)" In *Proc. of 6th Biennial Conference on Engineering Systems Design and Analysis (ESDA)*, Istanbul, Turkey, 2002.

Haron, C.H.; Deros, B.; Ginting, A. and Fauziah, M.: "Investigation on the Influence of Machining Parameters when Machining Tool Steel using EDM", *J. Mater. Process. Technol.*, Vol. 116, pp. 84-87, 2001.

Hauk, V.; Holler, P. and Macherauch, E.: "Measuring Techniques of Residual Stresses-Present Situations and Future Aims" In *Proc. of Int. Conf. on Residual Stresses, Residual Stresses in Science and Technology*, Garmisch-Partenkirchen, 1987.

Heuvelman, C.J.: "Some Aspects of the Research on Electro-Erosion Machining", *Ann. of CIRP*, Vol. 17, No. 1, pp. 195-199, 1969.

Ho, K.H. and Newman, S.T.: "State of the Art Electrical Discharge Machining (EDM)", *Int. J. Mach. Tools Manufact.*, Vol. 43, pp. 1287-1300, 2003.

Hung, N.P.; Yang, L.J. and Leong, K.W.: "Electrical Discharge Machining of Cast Metal Matrix Composites", *J. Mater. Process. Technol.*, Vol. 44, pp. 229-236, 1994.

Jeswani, M.L.: "Roughness and Wear Characteristic of Spark-Eroded Surfaces", *Wear*, Vol. 51, pp. 227-236, 1978.

Jeswani, M.L. and Basu, S.: "Electron Microscope Study of the Deposition and Diffusion of Tool Material in Electrical Discharge Machining", *Int. J. Prod. Res.*, Vol. 17, No. 1, 1979.

Koning, W.; Wertheim, R.; Zvirin, Y. and Toren, M.: "Material Removal and Energy Distribution in Electrical Discharge Machining", *Ann. of CIRP*, Vol. 24, No. 1, pp. 95-100, 1975.

Kruth, J.P.; Stevens, L.; Froyen, L. and Lauwers, B.: "Study of the White Layer of a Surface machined by Die-Sinking Electro-Discharge Machining", *Ann. of CIRP*, Vol. 44, No. 1, pp. 169-172, 1995.

Kruth, J.P.; Lauwers, B.; Schacht, B.; Bleys, P. and Stucki, M.: "Comparison Between Oil and Water Dielectric in Wire EDM of Tool Steel", In *Proc. of 13th Int. Symp. for Electro-Machining*, 463-472, Bilbao, 2001.

Kruth, J.P. and Bleys, P.: "Measuring Residual Stress Caused by Wire EDM of Tool Steel", *Int. J. Electrical Mach.*, Vol. 5, No. 1, pp. 23-28, 2000.

Larsson, C.N.: "A Large Increase in Cutting Rate by Using a Dielectric Under Static Pressure", In *Proc. of 17th Int. MTDR Conf.*, pp. 277-282, 1976.

Lee, L.C.; Lim, L.C.; Narayanan, V. and Venkatesh, V.C.: "Quantification of Surface Damage of Tool Steels After EDM", *Int. J. Mach. Tools Manufact.*, Vol. 28, No. 4, pp. 359-372, 1988.

Lee, L.C.; Lim, L.C. and Wong, Y.S.: "Towards a Better Understanding of the Surface Features of Electro-Discharge machined Tool Steels", *J. Mater. Process. Technol.*, Vol. 24, pp. 513-523, 1990.

Lee, L.C.; Lim, L.C. and Wong, Y.S.: "Toward Crack Minimization of EDMed Surfaces", *J. Mater. Process. Technol.*, Vol. 32, pp. 45-54, 1992.

Lee, L.C.; Lim, L.C. and Wong, Y.S.: "Crack Susceptibility of Electro-Discharge Machined Surfaces" *J. Mater. Process. Technol.*, Vol. 29, pp. 213-221, 1992.

Lee, H.T. and Tai, T.Y.: "Relationship Between EDM Parameters and Surface Crack formation", *J. Mater. Process. Technol.*, Vol. 142, No. 3, pp. 676-683, 2003.

Lee, S.H. and Li, X.P.: "Study of the Effect of Machining Parameters on the Machining Characteristic in Electrical Discharge Machining of Tungsten Carbide", *J. Mater. Process. Technol.*, Vol. 115, pp. 344-358, 2001.

Lee, S.H. and Li, X.: "Study of the Surface Integrity of the Machined Workpiece in the EDM of Tungsten Carbide", *J. Mater. Process. Technol.*, Vol. 139, pp. 315-321, 2003.

Lenz, E.; Katz, E.; Koning, W. and Wertneim, R.: "Cracking Behavior of Sintered Carbides During EDM", *Ann. of CIRP*, Vol. 24, No. 1, pp. 109-114, 1975.

Lim, L.C.; Lee, L.C.; Wong, Y.S. and Lu, H.H.: "Solidification Microstructure of Electrodischarge Machined Surfaces of Tool Steels" *Mater. Sci. Technol.*, Vol. 7, pp. 239-248, 1991.

Liu, C.C. and Huang, J.L.: "Effect of the Electrical Discharge Machining on Strength and Reliability of TiN/Si₃N₄ Composites", *Ceramics International*, Vol. 29, pp. 679-687, 2003.

Lloyd, H.K. and Warren, R.H.: "Metallurgy of Spark-Machined Surfaces", *J. of Iron and Steel Ins.*, Vol. 203, No. 3, pp. 238-247, 1965.

Lowke, J.J. and Ludwing, H.C.: "A Simple Model for High Current Arcs Stabilized by Forced Convection", *Journal of Applied Physics*, Vol. 46, No. 8, pp. 3252-3260, 1975.

Luikov, A.V.: "Analytical Heat Diffusion Theory", Academic Press Inc., London, 1968.

Luo, Y.F.; Zhang, Z.Y. and Yu, C.Y.: "Mirror Surface EDM by Electric Field Partially Induced", *Ann. of CIRP*, Vol. 37, No. 1, pp. 179-181, 1988.

Luo, Y.F. and Chen, C.G.: "Effect of a pulsed Electromagnetic Field on the Surface Roughness in Superfinishing EDM", *Precision Engineering*, Vol. 12, No. 2, pp. 97-100, 1990.

Macherauch, E.: "Introduction to Residual Stress, Advances in Surface Treatments: 4. Residual Stresses", Pergamon Oxford, 1-35, (1987).

Macherauch, E. and Kloos K.H.: "Origin, Measurement and Evaluation of Residual Stresses", In *Proc. of Int. Conf. on Residual Stresses, Residual Stresses in Science and Technology*, Garmisch-Partenkirchen, 1987.

Madhu, P.; Jain, V.K. and Sundararajan, T.: "Finite Element Analysis of EDM Process" *Processing of Advanced Materials*, Vol. 1, pp. 161-173, 1991.

Mamalis, A.G.; Vosniakos, N.M.; Vacevanidis, N.M. and Junzhe, X.: "Residual Stress Distribution and Structural Phenomena of High-Strength Steel Surfaces Due to EDM and Ball-Drop Forming", *Ann. CIRP*, Vol. 37, No. 1, pp. 531-535, 1988.

Marty, C.C. and Laracine, M.: "Accuracy of the Physico-Mathematical Analysis in E.D.M. Process-Correlation with Electrode Tool Wear", *Ann. of CIRP*, Vol. 25, No. 1, pp. 65-69, 1977.

Marty, C.C.: "Investigation of Surface Temperature in Electro-Discharge Machining", *Trans. of ASME, Journal of Engineering for Industry*, pp. 1-3, 1977.

Massarelli, L. and Marchionni, M.: "Morphology of spark-affected surface layers produced on pure iron and steels by electro discharge machining", *Met. Technol.*, Vol. 4, No. 2, pp. 100-105, 1977.

McGeough, J.A. and Rasmussen, H.: "A Macroscopic Model of Electro-Discharge Machining", *Int. J. Mach. Tool Des. Res.*, Vol. 22, No. 4, pp. 333-339, 1982.

- Mohri, N.; Saito, N.; Takawashi, T. and Kobayashi, K.: "Mirror Like Finishing by EDM (Multi Divided Electrode Method)", In Proc. of 26th MTDR Conf., pp. 329-336, 1985.
- Opitz, H.: "Metallurgical Aspects and Surface Characteristics", In Proc of Spark Machining Symposium, Birmingham, pp. 237-251, 1960.
- Özışık, N.: "Boundary Value Problems of Heat Conduction", International Textbook Co., Scranton, Pennsylvania, 1968.
- Pandey, P.C. and Jilani, S.T.: "Plasma Channel Growth and the Resolidified Layer in EDM", Precision Eng., Vol. 8, No. 2, pp. 104-110, 1986.
- Pandit, S.M. and Rajurkar, K.P.: "Data Dependent System Approach To EDM Process Modeling from Surface Roughness Profiles" Ann. of CIRP, Vol. 29, No. 1, pp. 107-112, 1980.
- Pandit, S.M. and Rajurkar, K.P.: "Crater Geometry and Volume From Electro-Discharge Machined Surface Profiles by Data Dependent Systems", Trans. ASME, Journal of Engineering for Industry, Vol. 102, pp. 289-295, 1980.
- Pandit, S.M. and Rajurkar, K.P.: "A Stochastic Approach to Thermal Modeling Applied to Electro-Discharge Machining", Trans. ASME, J. Heat Trans., Vol. 105, pp. 555-562, 1983.
- Patel, M.R.; Barrufet, M.A.; Eubank, P.T. and DiBitonto, D.D.: "Theoretical Models of the Electrical Discharge Machining Process. II. The Anode Erosion Model", J. Appl. Phys., Vol. 66, No. 9, pp. 4104-4111, 1989.
- Powley, C.: "EDM: Controversy Stimulates Progress", Machinery and Production Engineering, pp. 18-22, May 1982.
- Qin, G.W.; Oikawa, K.; Smith, G.D.W. and Hao, S.M.: "Wire Electric Discharge Machining Induced Titanium Hydride in Ti-46Al-2Cr Alloy" Intermetallics, Vol. 11, No. 9, pp. 907-910, 2003.
- Qu, J.; Riester, L.; Shih, A.J.; Scattergood, R.O.; Curzio, E.L. and Watkins, T.R.: "Nanoindentation Characterization of Surface Layers of Electrical Discharge Machined WC-Co", Mater. Sci. Eng., Vol. A344, pp. 125-131, 2003.
- Radhakrishnan, V. and Achyutha, B.T.: "Study of the Surface Formed in EDM Using Relocation Technique" IE(I) Journal-ME, Vol. 60, pp. 217-222, 1980.
- Rajurkar, K.P. and Pandit, S.M.: "Quantitative Expressions for Some Aspects of Surface Integrity of Electro Discharge Machined Components" Trans. ASME, Journal of Engineering for Industry, Vol. 106, pp. 171-177, 1984.

Rama Rao, P.V. and Faruqi, M.A.: "Characteristics of the Surfaces obtained in Electro-Discharge Machining", Precision Engineering, Vol. 4, No. 2, pp. 111-113, 1982.

Rama Rao, P.V. and Faruqi, M.A.: "Time Series Modeling of the Surface Profile Produced by EDM", In Proc. of the 10th All India Mach. Tool Design Conf., Durgapur, pp. 344-350, 1982.

Ramaswami, R. and Louis R.S.: "A Study of Wear and Surface Finish During Spark Erosion Machining of High Speed Tool Steel", Wear, Vol. 24, pp. 153-160, 1973.

Ramulu, M. and Garbini, J.L.: "EDM Machined Surface Characterization of a Ceramic Composite, TiB₂/SiC", J. Eng. Mater. Technol., Vol. 113, No. 4, pp. 437-442, 1991.

Rebelo, J.C.; Diaz, A.M.; Kremer, D. and Lebrun, J.L.: "Influence of Pulse Energy on the Surface Integrity of Martensitic Steels" J. Mater. Process. Technol., Vol. 84, pp. 90-96, 1998.

Report of AGIE: "Controlling EDM Surface Integrity", American Machinist and Automated Manufacturing, Vol. 9, No. 6, pp. 80-83, 1987.

Rozenek, M.; Kozak, J.; Dabrowski, L. and Lubkowski, K.: "Electrical Discharge Machining Characteristics of Metal Matrix Composites" J. Mater. Process. Technol., Vol. 109, pp. 367-370, 2001.

Saito, N.: "The Mechanism of Surface Roughness on Electrical Discharge Machining", Mitsubishi Denki Laboratory Reports, pp. 375-390, 1962.

Saito, N.: "Mechanism of Electric Discharge Machining", Bull. of The Japan Soc. of Process. Eng., Vol. 1, No. 2, pp. 95-101, 1964.

Schachrai, A. and Lenz, E.: "LBM and EDM –A Comparison on the Cracks Behavior", Ann. of CIRP, Vol. 25, No. 1, pp. 121-123, 1976.

Simao, J.; Aspinwall, D.; El-Menshawy, F. and Meadows, K.: "Surface Alloying using PM Composite Electrode Materials When Electrical Discharge Texturing Hardened AISI D2" J. Mater. Process. Tech., Vol. 127, pp. 211-216, 2002.

Simao, J.; Lee, H.G.; Aspinwall, D.K.; Dewes, R.C. and Aspinwall, E.M.: "Workpiece surface Modification Using Electrical Discharge Machining", Int. J. Machine Tools Manufact., Vol. 43, pp. 121-128, 2003.

Singh, A. and Ghosh, A.: "A Thermo-Electric Model of Material Removal During Electric Discharge Machining", Int. J. Mach. Tools and Manufact., Vol. 39, pp. 669-682, 1999.

Shankar, P.; Jain, V.K. and Sundararajan, T.: "Analysis of Spark Profiles During EDM Process" Mach. Sci. Technol., Vol. 1, No. 2, pp. 196-217, 1997.

Snoeys, R. and Dijck, F.V.: "Plasma Channel Diameter Growth Affects Stock Removal in EDM", *Ann. of CIRP*, Vol. 21, No. 1, pp. 39-40, 1972.

Stablein, F.: "Spannungsmessungen in eiseiting abgeloschten Knüppeln" *Kruppsche Monatshefte*, 12 Jahrgang, pp. 93-99, 1931.

Tabrett, C.P.: "The Electro-Discharge Machining Surface of High Chromium White Irons", *J. Mater. Sci. Letters*, Vol. 15, pp. 1792-1794, 1996.

Thomson, P.H.: "Surface Damage in Electrodischarge Machining" *Mater. Sci. Technol.*, Vol. 5, pp. 1153-1157, 1989.

Toren, M.; Zvirin, Y. and Winograd, Y.: "Melting and Evaporation Phenomena During Electrical Erosion" *Trans. ASME, Journal of Heat Transfer*, pp. 576-581, 1975.

Timoshenko, S.P.; Goodier, N.J.: "Theory of Elasticity", Third Edition, McGraw-Hill, N.Y., 1970.

Tosun, N.; Coğun, C. and İnan, A.: "The Effect of Cutting Parameters on Workpiece Surface Roughness in Wire EDM", *Mach. Sci. Technol.*, Vol. 7, No. 2, pp. 209-219, 2003.

Tsai, K.M. and Wang, P.J.: "Semi-Empirical Model of Surface Finish on Electrical Discharge Machining" *Int. J. Mach. Tools Manuf.*, Vol. 41, pp. 1455-1477, 2001.

Tsai, H.C.; Yan, B.H. and Huang, F.Y.: "EDM performance of Cr/Cu-Based Composite Electrodes" *Int. J. Mach. Tools Manuf.*, Vol. 43, pp. 245-252, 2002.

Uno, Y.; Okada, A. and Cetin, S.: "Surface Modification of EDMed Surface with Powder Mixed Fluid" In *Proc. of 2nd Int. Conf. on Design and Production of Dies and Molds*, 2001.

Wallbank, J.: "Effect of EDM on Material Properties of Die Steels", *Metallurgia*, Vol. 47, No. 1, pp. 356-362, 1980.

Wong, Y.S.; Rahman, M.; Lim, H.S.; Han, H. and Ravi, N.: "Investigation of Micro-EDM Material Removal Characteristics using Single RC-Pulse Discharges", *J. Mater. Process. Technol.*, Vol. 140, No. 1, pp. 303-307, 2003.

Wong, Y.S.; Lim, L.C.; Rahuman, I. and Tee, W.M.: "Near-Mirror-Finish Phenomenon in EDM using Powder-Mixed Dielectric" *J. Mater. Process. Technol.*, Vol. 79, pp. 30-40, 1998.

Yadav, V.; Jain, V.K. and Dixit, P.M.: "Thermal Stresses due to Electrical Discharge Machining" *Int. J. Mach. Tools Manuf.*, Vol. 42, pp. 877-888, 2002.

Yadav, V.; Jain, V.K. and Dixit, P.M.: "Temperature Distribution During Electro-Discharge Abrasive Grinding", *Mach. Sci. Technol.*, Vol. 6, No. 1, pp. 97-127, 2002.

Zeid, O.A.: "The Role of Voltage Pulse Off-Time in the Electrodischarge Machined AISI T1 High-Speed Steel", *J. Mater. Process. Technol.*, Vol. 61, pp. 287-291, 1996.

Zeid, O.A.: "On the Effect of Electrodischarge Machining Parameters on the Fatigue Life of AISI D6 Tool Steel", *J. Mater. Process. Technol.*, Vol. 68, pp. 27-32, 1997.

Zingerman, A.S.: "Regarding the Problem of the Volume of Molten Metal During Electrical Erosion", *Soviet Physics-Solid*, Vol. 1, pp. 255-259, 1959.

Zolotykh, B.N. and Trofimova, B.: "Liquid Breakdown During Electric-Spark Treatment", *Elektronnaya Obrabotka Materialov*, Vol. 4, No. 28, pp. 33-37, 1969.

Zolotykh, B.N.: "The Mechanism of Electrical Erosion of Metals in Liquid Dielectric Media", *Soviet Physics-Technical Physics*. Vol. 4, No. 1, pp. 1370-1373, 1960.

Zolotykh, B.N.: "Theorie zum Phanomen der Funkenerosiven Bearbeitung" *Fertigung* 2, 1971.

Zvirin, Y. and Toren, M.: "Simultaneous Melting and Evaporation due to an Area Heat Source", *Warme-und Stoffubertragung*, Vol. 11, pp. 29-36, 1978.

APPENDIX A

JPDS-DIFFRACTION DATA FOR ANALYZED X-RAY PATTERNS

Table A.1. JCPDS-International Center for Diffraction Data, PDF No: 31-0619

31-0619		Wavelength= 1.54056								O
(Fe,C)	2 θ	Int	h	k	l	d Å	Int	h	k	l
Iron	43.472100	1	1	1		2.0800	100	1	1	1
	50.673	80	2	0	0	1.80000	80	2	0	0
	74.677	50	2	2	0	1.27000	50	2	2	0
	90.673	80	3	1	1	1.08300	80	3	1	1
	95.940	50	2	2	2	1.03700	50	2	2	2
	117.711	30	4	0	0	.900000	30	4	0	0
Rad.: CoK α λ : 1.7902		Filter:		d-sp:						
Cut off:		Int.: Estimation		I/Teor.:						
Ref: Goldschmidt, Metallurgia, 40, 103 (1949)										
Sys.: Cubic			S.G.: Fm3m (225)							
a: 3.60	b:	c:	A:	C:						
α :	β :	γ :	Z: 0.386 mp:							
Ref: Ibid.										
Dx: 7.730	Dm:		SS/FOM \bar{c} =6(.181, 6)							
Density 8.0 was calculated for 0.75 wt.% C. Material: 13/12 type of stainless steel. The lattice-dimension allows for variations observed. Approximately correct for austenite in most stainless steels. Cu type. Also called: austenite.PSC: cF4. To replace 23-298. Mwt: 562.67. Volume[CD]: 46.66.										

©1996 JCPDS-International Centre for Diffraction Data. All rights reserved.

Table A.2. JCPDS-International Center for Diffraction Data, PDF No: 06-0696

06-0696		Wavelength= 1.54056 *											
Fe	2 θ	Int	h	k	l	d Å	Int	h	k	l			
Iron	44.673	100	1	1	0	2.0268	100	1	1	0			
	65.021	20	2	0	0	1.43320	20	2	0	0			
	82.333	30	2	1	1	1.17020	30	2	1	1			
Iron, syn	98.945	10	2	2	0	1.01340	10	2	2	0			
Rad.: CuK α l:	1.5405	Filter: Ni Beta	M		d-sp:	116.385	12	3	1	0			
Cut off:	Int.: Diffract.	I/Corr.:		137.136	6	2	2	2	.827500	6	2	2	2
Ref: Swanson et al., Natl. Bur. Stand. (U.S.), Circ. 539, IV, 3 (1955)													
Sys.: Cubic		S.G.: Im3m (229)											
a: 2.8664	b:	c:	A:	C:									
α :	β :	γ :	Z: 2	mp:									
Ref: Ibid.													
Dx: 7.875	Dm:	SS/FOM \bar{c} =225(.0044, 6)											
Color: Gray, light gray metallic													
Pattern taken at 25 C. CAS #: 7439-89-6. The iron used was an exceptionally pure rolled sheet prepared at the NBS, Gaithersburg, MD, USA., [Moore, G., J. Met., 5 1443 (1953)]. It was annealed in an H ₂ atmosphere for 3 days at 1100 C and slowly cooled in a He atmosphere. Total impurities of sample <0.0013% each metals and non-met-Fe (fcc)=(1390 C) δ -Fe (bcc). Opaque mineral optical data on specimen from Meteorite: RR2Re= 57.7, Disp.=16, VHN=158 (mean at 100, 200, 300), Color values=.311, .316, 57.9, Ref: IMA Commission on Ore Microscopy QDF. W type. Iron group, iron subgroup. Also called: ferrite.PSC: cI2. Mwt: 55.85. Volume[CD]: 23.55.													

©1996 JCPDS-International Centre for Diffraction Data. All rights reserved.

Table A.3. JCPDS-International Center for Diffraction Data, PDF No: 34-0001

34-0001		Wavelength= 1.54056 *										
Fe3C	2 θ	Int	h	k	l	d Å	Int	h	k	l		
Iron Carbide	35.207*	2	2	0	0	2.54700	2	2	0	0		
	37.652	25	1	2	1	2.38700	25	1	2	1		
	37.751	35	2	1	0	2.38100	35	2	1	0		
Cohenite, syn	39.782	40	0	0	2	2.26400	40	0	0	2		
Rad.: CuK α l:	1.5406	Filter: Mono	M		d-sp: Guinier	40.624	35	2	0	1		
Cut off:	Int.: Film	I/Corr.:		42.865	80	2	1	1	2.10800	80	2	1
Ref: Visser, J., Technisch Physische Dienst, Delft, The Netherlands, ICDD Grant-in-Aid, (1977)	43.737	100	1	0	2	2.0680	100	1	0	2		
	44.553	45	2	2	0	2.03200	45	2	2	0		
	44.973	45	0	3	1	2.01400	45	0	3	1		
	45.850	65	1	1	2	1.97750	65	1	1	2		
	48.567	20	1	3	1	1.87300	20	1	3	1		
	49.098	45	2	2	1	1.85400	45	2	2	1		
	51.799	14	1	2	2	1.76350	14	1	2	2		
	54.398	12	0	4	0	1.68520	12	0	4	0		
	54.398	12	2	3	0	1.68520	12	2	3	0		
	55.968	10	2	1	2	1.64160	10	2	1	2		
Ref: Ibid.	57.969	25	3	0	1	1.58960	25	3	0	1		
	59.708*	8	3	1	1	1.54740	8	3	1	1		
	61.258	10	2	2	2	1.51190	10	2	2	2		
	70.789	10	3	1	2	1.32990	10	3	1	2		
	70.789	10	1	2	3	1.32990	10	1	2	3		
	77.878	14	4	0	1	1.22560	14	4	0	1		
	78.549*	8	1	3	3	1.21680	8	1	3	3		
	79.454*	4	4	1	1	1.20520	4	4	1	1		
Dx: 7.671 Dm: 7.200 SS/FOM \bar{c} =26(.0158, 53)												
Compound was electrochemically extracted from steel, which contained: C 0.82%, P 0.002%, S 0.01%, Si 0.03%, Al 0.09%, Cr 0.01%, Ni 0.01%, Sn 0.03%, V 0.01%, N 0.0025%. The steel was annealed at 800 C during 1 hour in argon. See also 35-772. Cell parameters were also determined by Van Mourik, P., Technical Univ., Delft, The Netherlands. This determination (Debye-Scherrer method with Nelson-Riley extrapolation) has the following cell parameter values: a=5.0901, b=6.7398, c=4.5269. C Fe3 type. Also called: cementite.Silicon used as an internal stand. PSC: oP16. Mwt: 179.55. Volume[CD]: 155.48.												

©1996 JCPDS-International Centre for Diffraction Data. All rights reserved.

APPENDIX B

RESULT OF PARAMETRIC SIMULATIONS

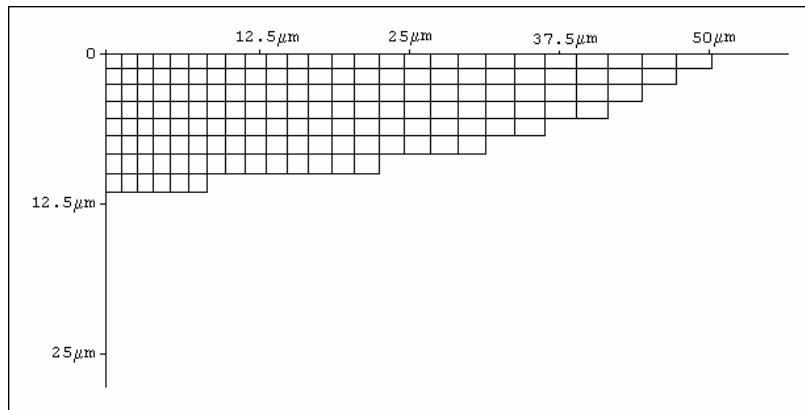


Figure B.1. Removed Elements from the Spark Domain at the End of Pulse.
($t_p = 100 \mu\text{s}$, $I_{av} = 16\text{A}$, $R = 110 \mu\text{m}$, $R_w = 0.06$, $R_{wp} = 0$)

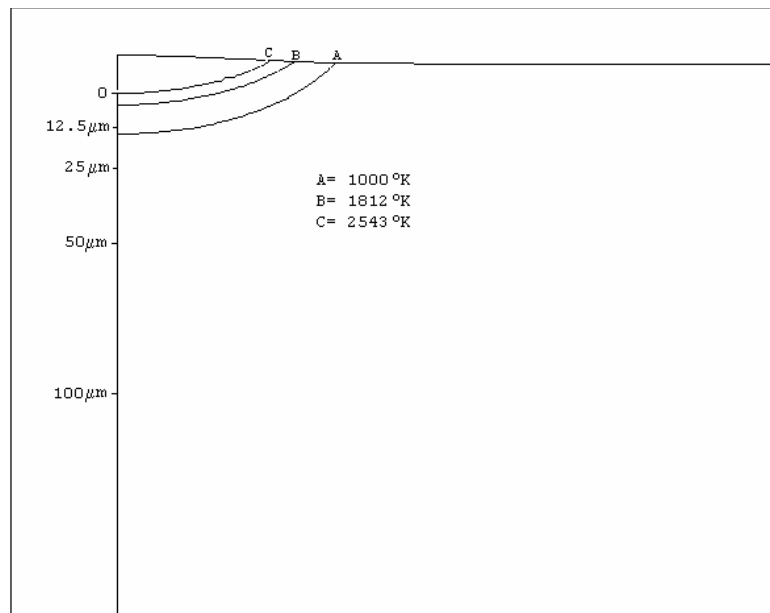


Figure B.2. Temperature at the End of Pulse.
($t_p = 100 \mu\text{s}$, $I_{av} = 16\text{A}$, $R = 110 \mu\text{m}$, $R_w = 0.06$, $R_{wp} = 0$)

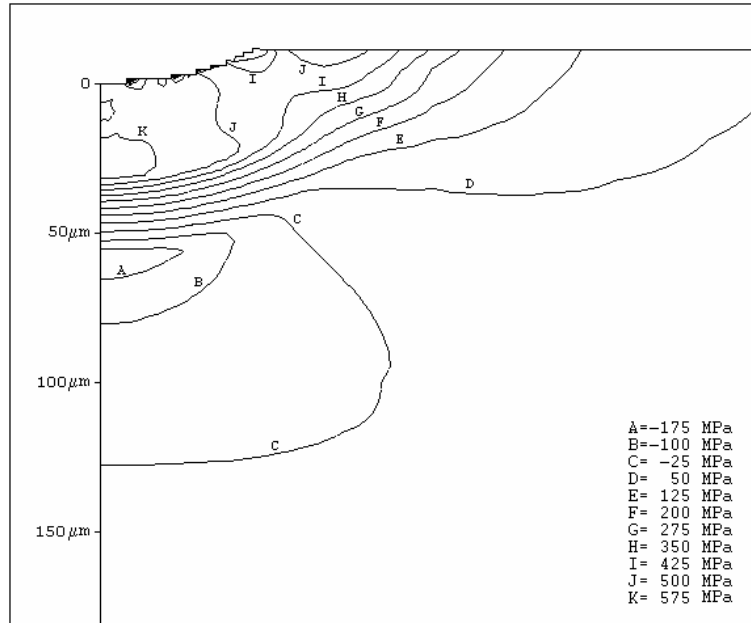


Figure B.3. Radial Component of Residual Stresses (σ_{rr}).
 ($t_p = 100 \mu s$, $I_{av} = 16A$, $R = 110 \mu m$, $R_w = 0.06$, $R_{wp} = 0$)

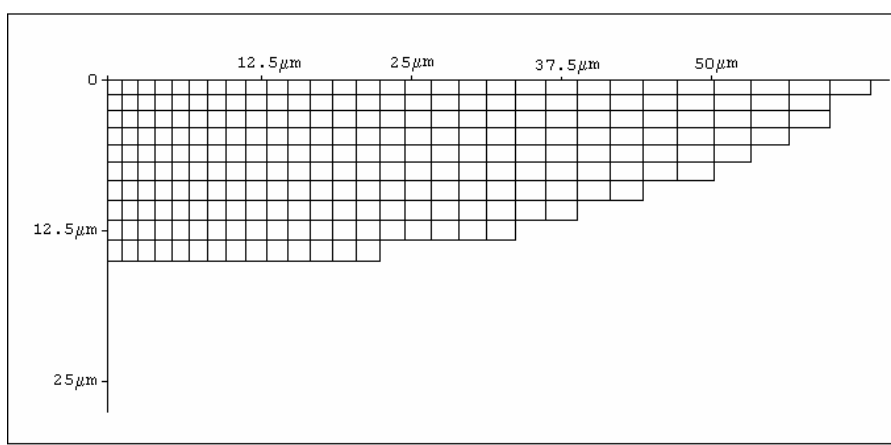


Figure B.4. Removed Elements from the Spark Domain at the End of Pulse.
 ($t_p = 100 \mu s$, $I_{av} = 16A$, $R = 110 \mu m$, $R_w = 0.1$, $R_{wp} = 0$)

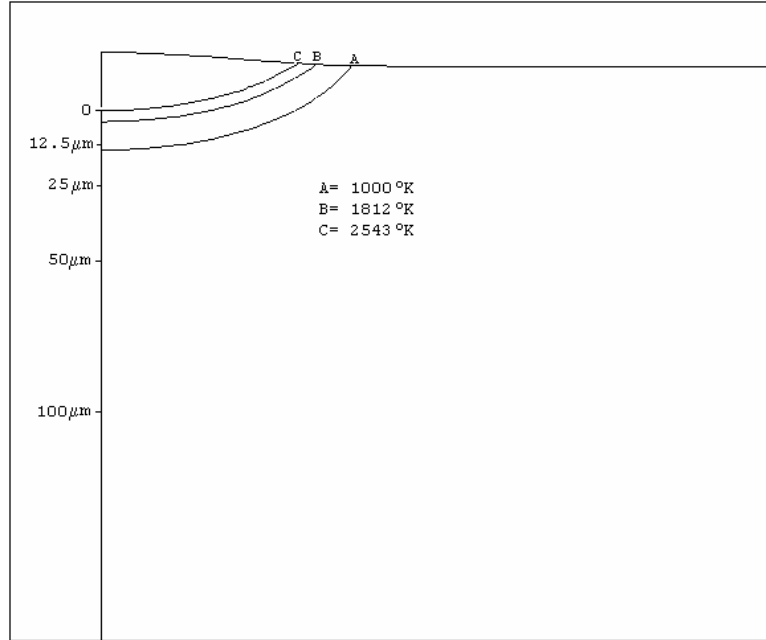


Figure B.5. Temperature at the End of Pulse.
 ($t_p = 100 \mu s$, $I_{av} = 16A$, $R = 110 \mu m$, $R_w = 0.1$, $R_{wp} = 0$)

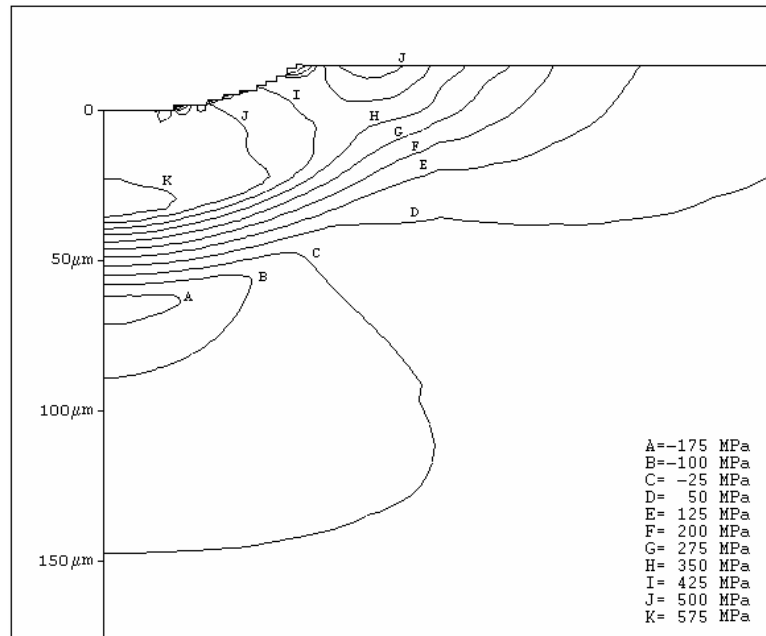


Figure B.6. Radial Component of Residual Stresses (σ_r).
 ($t_p = 100 \mu s$, $I_{av} = 16A$, $R = 110 \mu m$, $R_w = 0.1$, $R_{wp} = 0$)

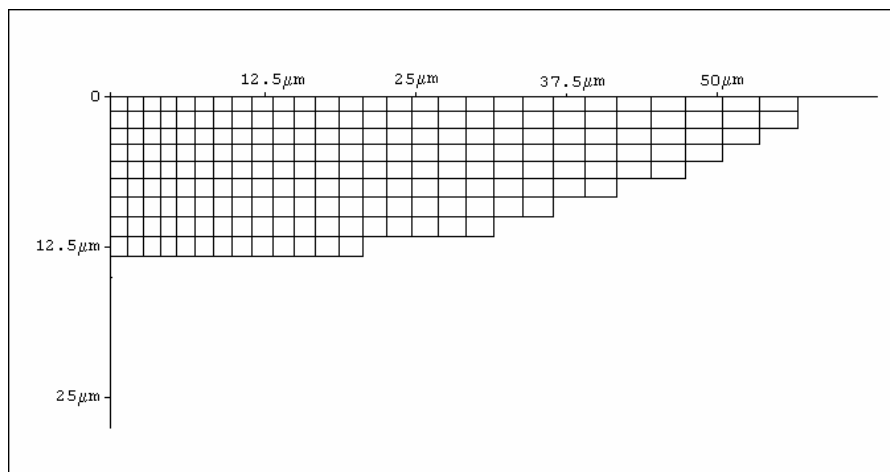


Figure B.7. Removed Elements from the Spark Domain at the End of Pulse.
 ($t_p = 100 \mu\text{s}$, $I_{av} = 16\text{A}$, $R = 110 \mu\text{m}$, $R_w = 0.08$, $R_{wp} = 0.001$)

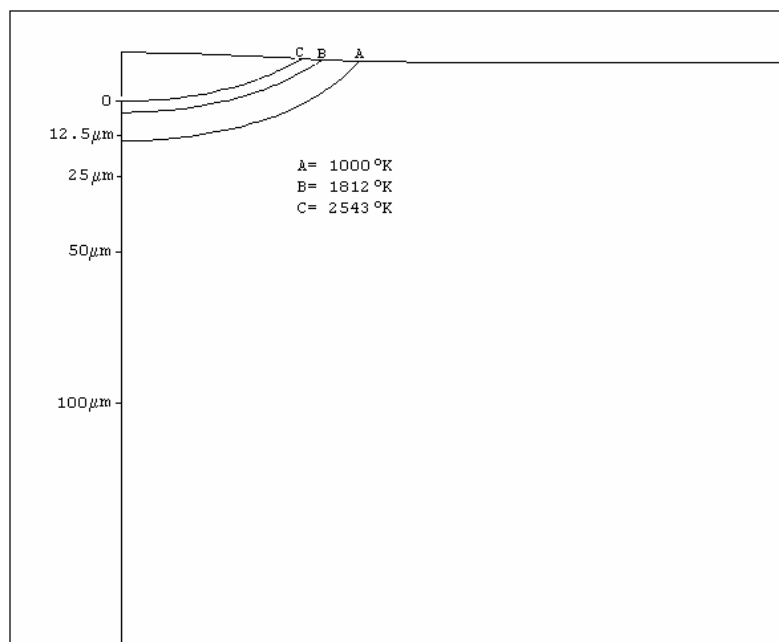


Figure B.8. Temperature at the End of Pulse.
 ($t_p = 100 \mu\text{s}$, $I_{av} = 16\text{A}$, $R = 110 \mu\text{m}$, $R_w = 0.08$, $R_{wp} = 0.001$)

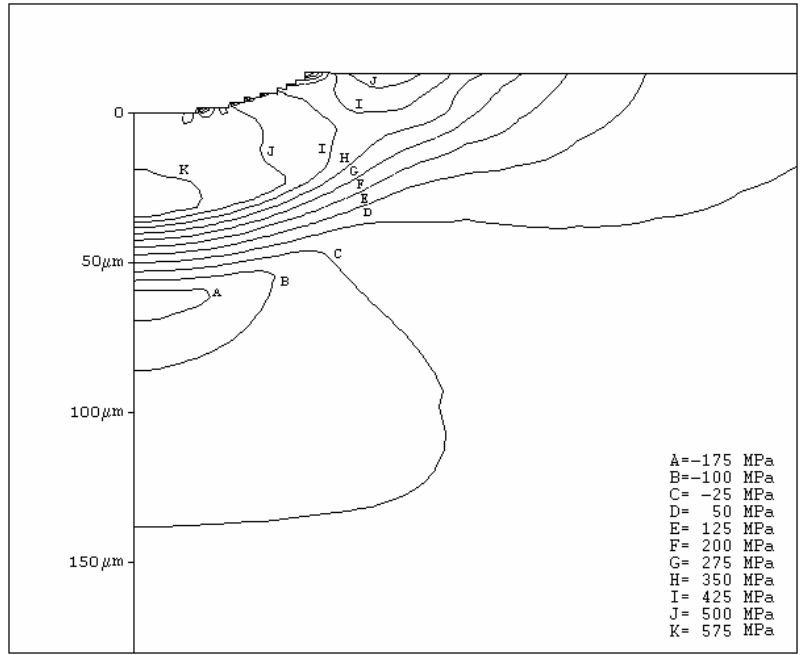


Figure B.9. Radial Component of Residual Stresses (σ_r).
 ($t_p = 100 \mu\text{s}$, $I_{av} = 16\text{A}$, $R = 110 \mu\text{m}$, $R_w = 0.08$, $R_{wp} = 0.001$)

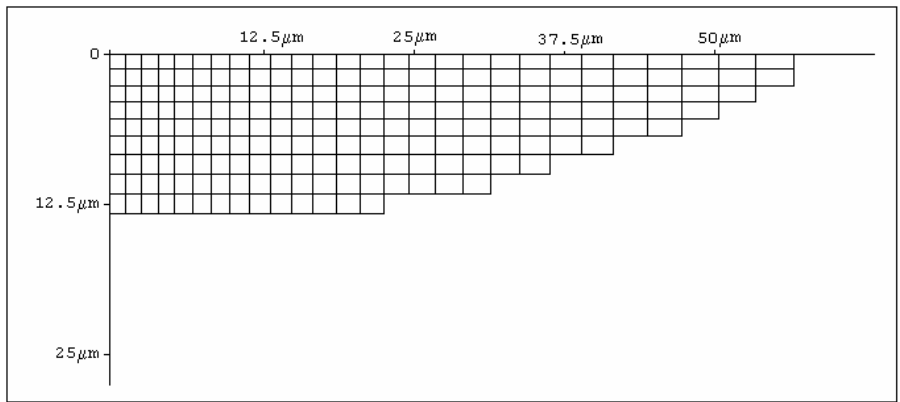


Figure B.10. Removed Elements from the Spark Domain at the End of Pulse.
 ($t_p = 100 \mu\text{s}$, $I_{av} = 16\text{A}$, $R = 110 \mu\text{m}$, $R_w = 0.08$, $R_{wp} = 0.002$)

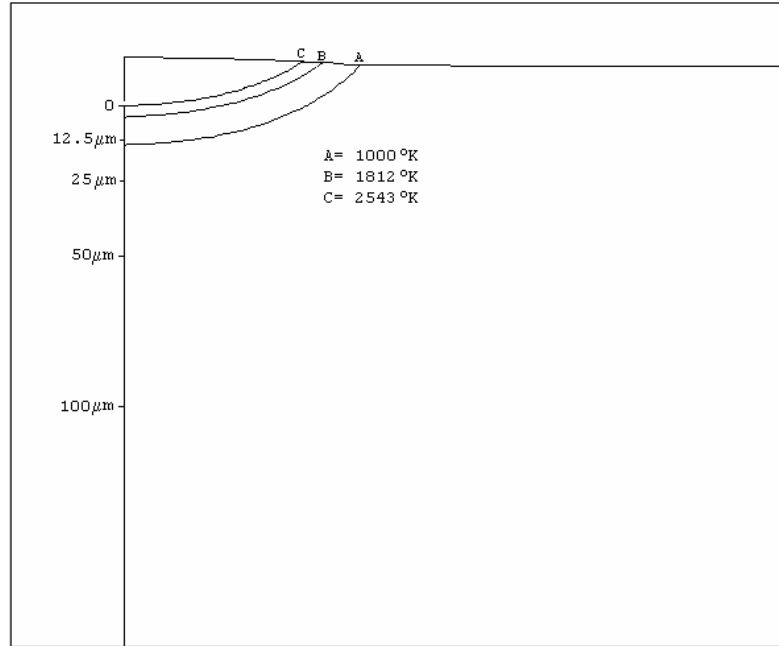


Figure B.11. Temperature at the End of Pulse.
 ($t_p = 100 \mu\text{s}$, $I_{av} = 16\text{A}$, $R = 110 \mu\text{m}$, $R_w = 0.08$, $R_{wp} = 0.002$)

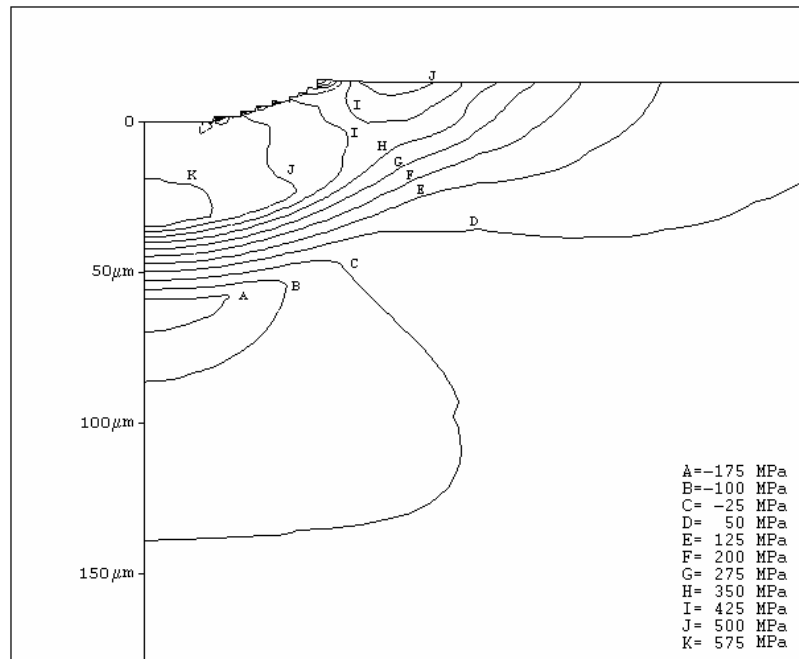


Figure B.12. Radial Component of Residual Stresses (σ_r).
 ($t_p = 100 \mu\text{s}$, $I_{av} = 16\text{A}$, $R = 110 \mu\text{m}$, $R_w = 0.08$, $R_{wp} = 0.002$)

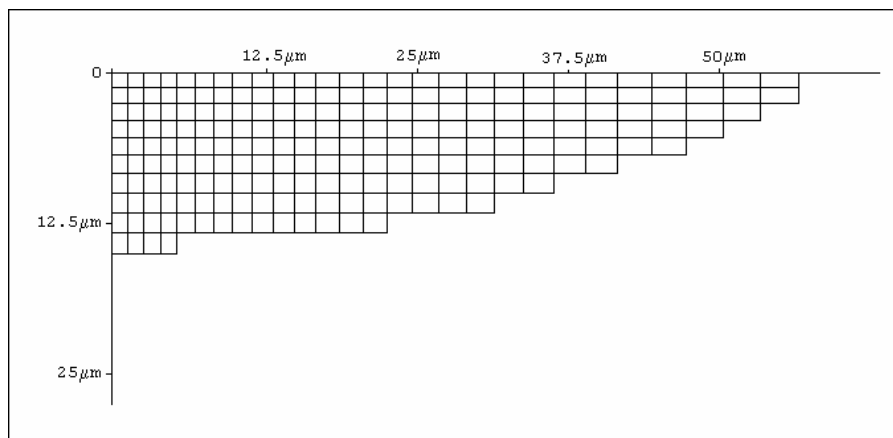


Figure B.13. Removed Elements from the Spark Domain at the End of Pulse.
 ($t_p = 100 \mu\text{s}$, $I_{av} = 16\text{A}$, $R = 110 \mu\text{m}$, $R_w = 0.08$, $R_{wp} = 0.004$)

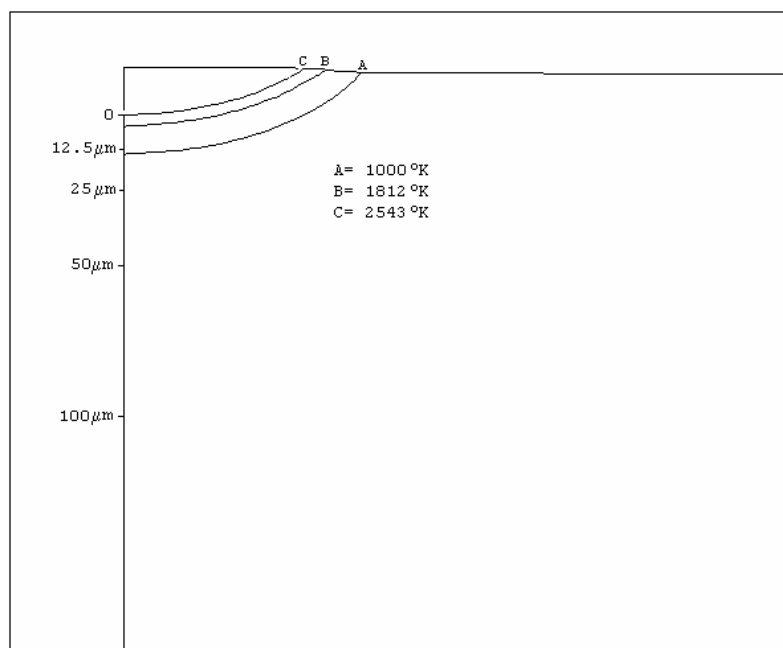


Figure B.14. Temperature at the End of Pulse.
 ($t_p = 100 \mu\text{s}$, $I_{av} = 16\text{A}$, $R = 110 \mu\text{m}$, $R_w = 0.08$, $R_{wp} = 0.004$)

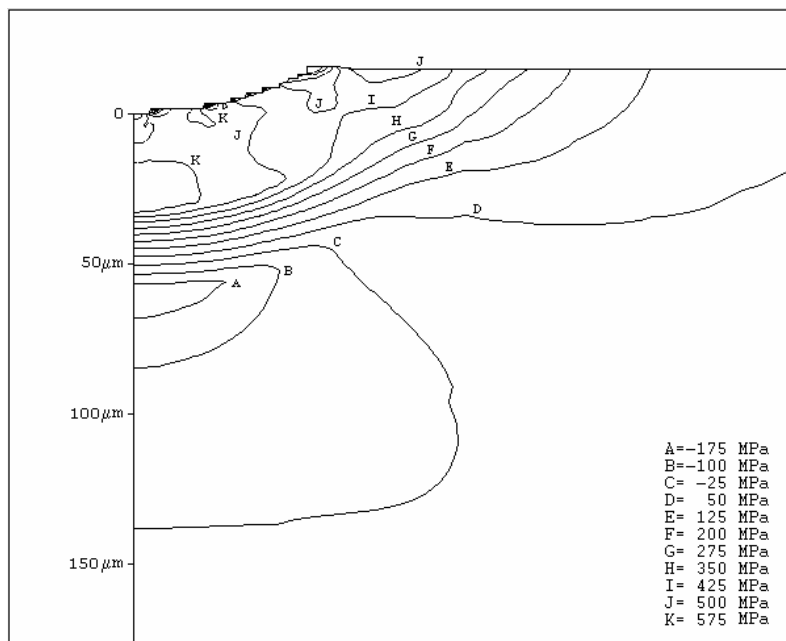


Figure B.15. Radial Component of Residual Stresses (σ_r).
 ($t_p=100 \mu s$, $I_{av}=16A$, $R=110 \mu m$, $R_w=0.08$, $R_{wp}=0.004$)

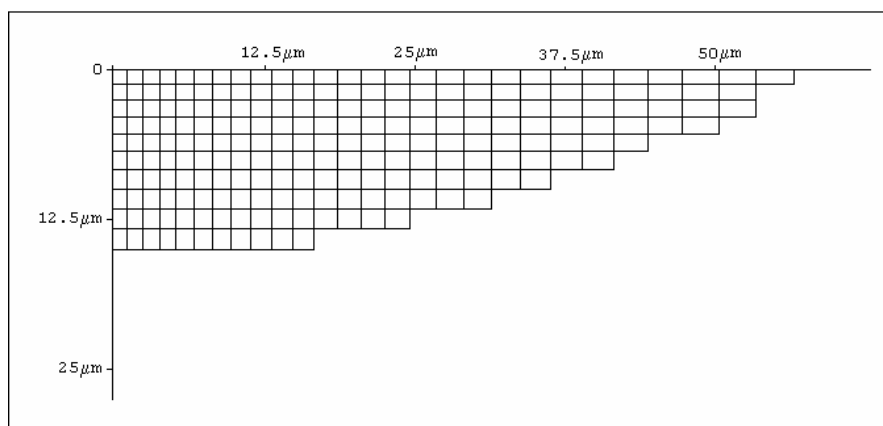


Figure B.16. Removed Elements From the Spark Domain at the End of Pulse.
 ($t_p=100 \mu s$, $I_{av}=16A$, $R=110 \mu m$, $R_w=0.08$, $R_{wp}=0.008$)

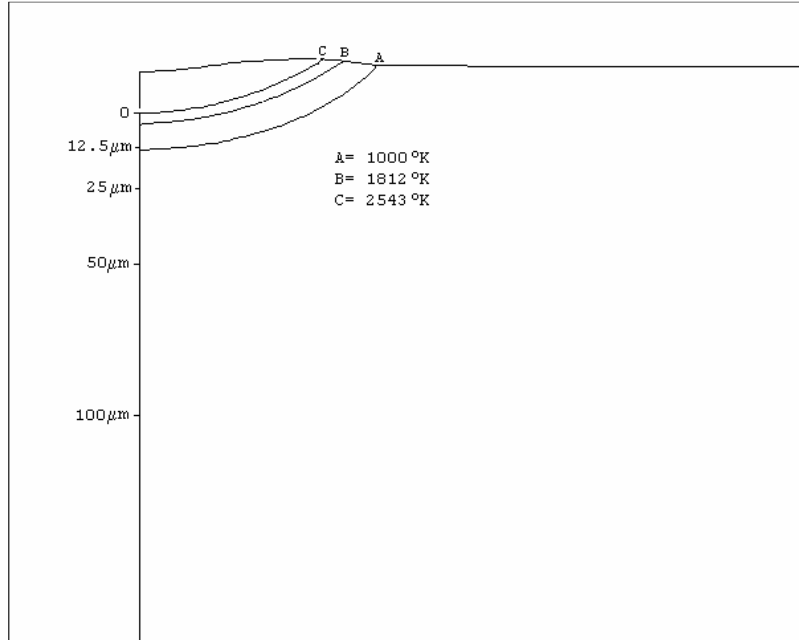


Figure B.17. Temperature at the End of Pulse.
 ($t_p = 100 \mu s$, $I_{av} = 16A$, $R = 110 \mu m$, $R_w = 0.08$, $R_{wp} = 0.008$)

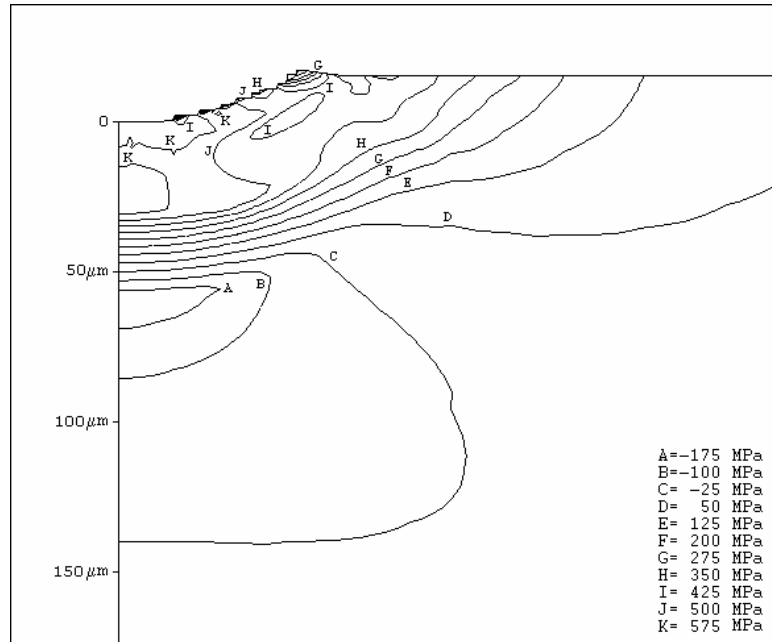


Figure B.18. Radial Component of Residual Stresses (σ_{rr}).
 ($t_p = 100 \mu s$, $I_{av} = 16A$, $R = 110 \mu m$, $R_w = 0.08$, $R_{wp} = 0.008$)

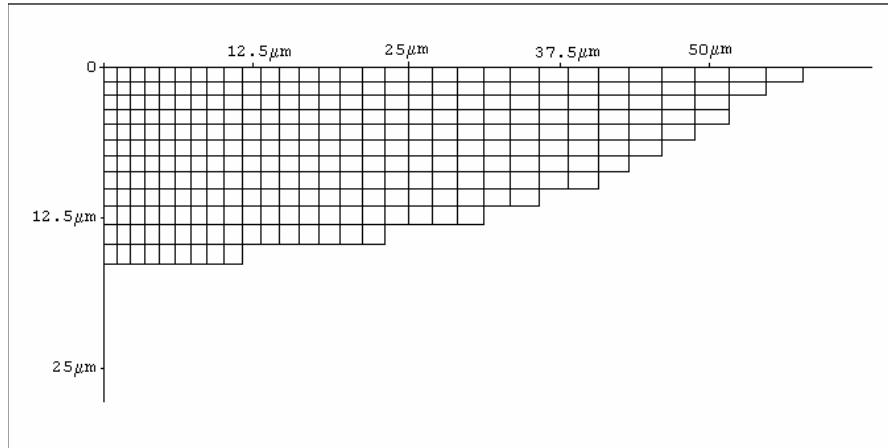


Figure B.19. Removed Elements from the Spark Domain at the End of Pulse.
 ($t_p = 100 \mu\text{s}$, $I_{av} = 16\text{A}$, $R = 95 \mu\text{m}$, $R_w = 0.08$, $R_{wp} = 0$)

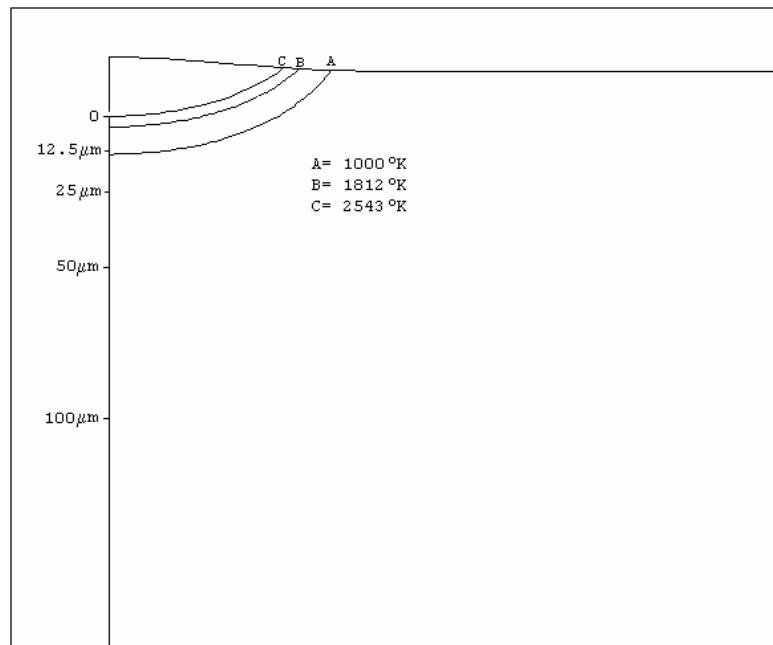


Figure B.20. Temperature at the End of Pulse.
 ($t_p = 100 \mu\text{s}$, $I_{av} = 16\text{A}$, $R = 95 \mu\text{m}$, $R_w = 0.08$, $R_{wp} = 0$)

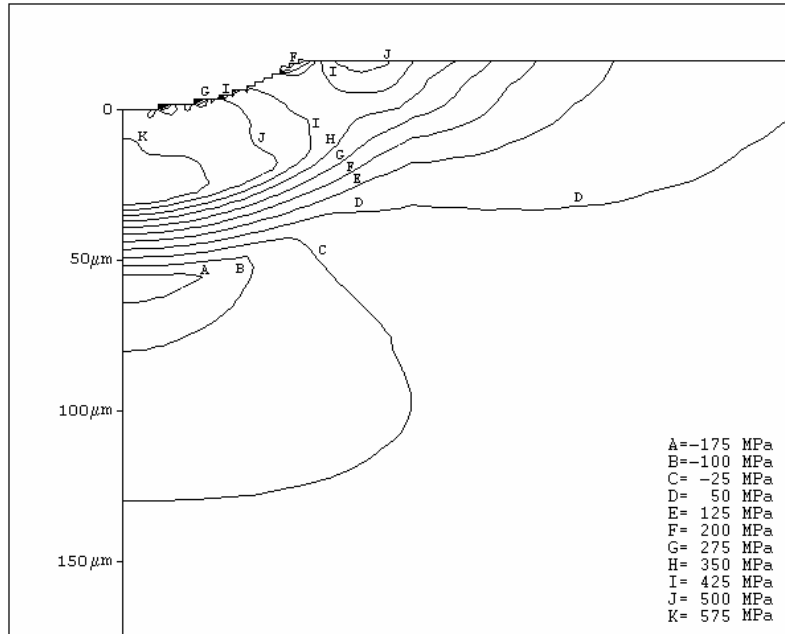


Figure B.21. Radial Component of Residual Stresses (σ_{rr}).
 ($t_p=100 \mu s$, $I_{av}=16A$, $R=95 \mu m$, $R_w=0.08$, $R_{wp}=0$)

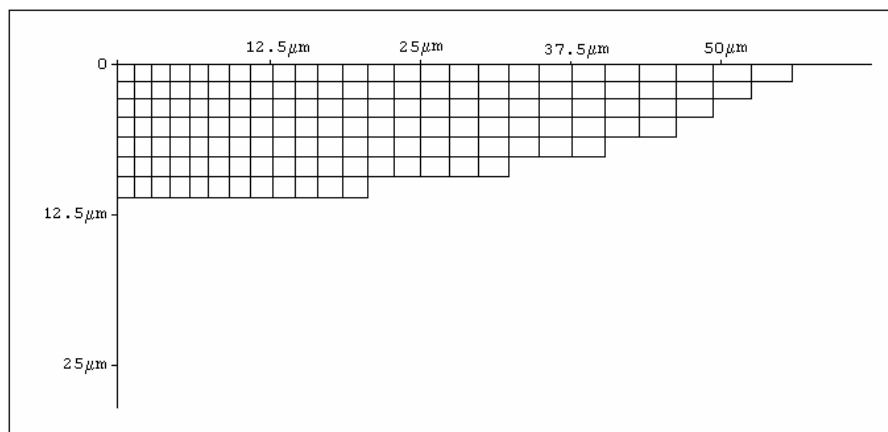


Figure B.22. Removed Elements from the Spark Domain at the End of Pulse.
 ($t_p=100 \mu s$, $I_{av}=16A$, $R=125 \mu m$, $R_w=0.08$, $R_{wp}=0$)

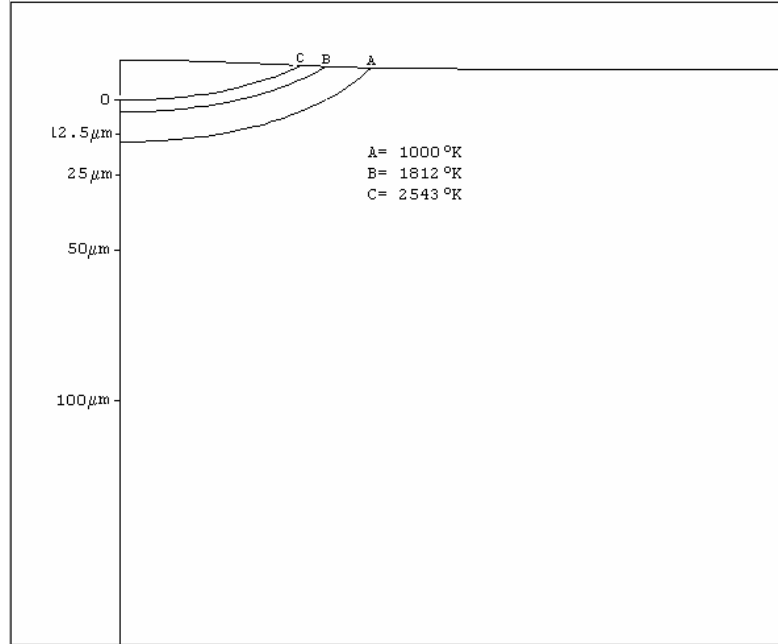


Figure B.23. Temperature at the End of Pulse.
 ($t_p = 100 \mu s$, $I_{av} = 16 A$, $R = 125 \mu m$, $R_w = 0.08$, $R_{wp} = 0$)

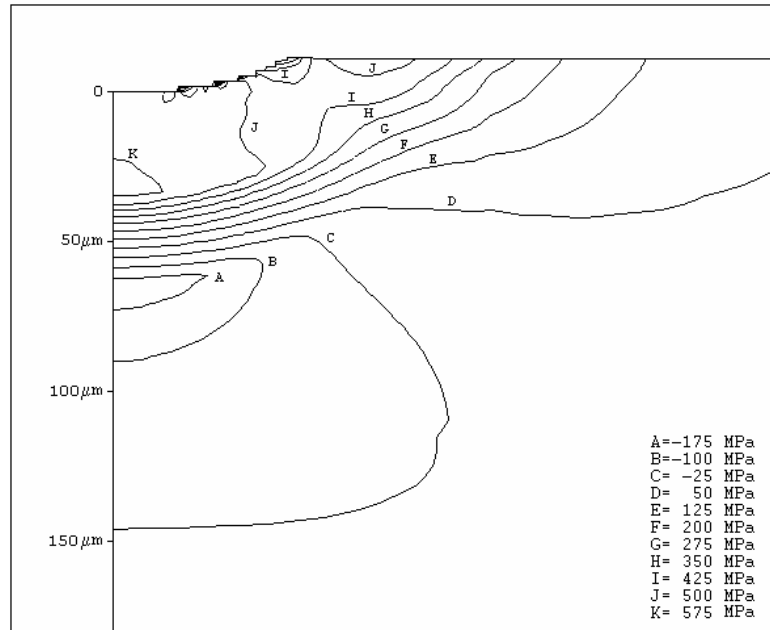


Figure B.24. Radial Component of Residual Stresses (σ_r).
 ($t_p = 100 \mu s$, $I_{av} = 16 A$, $R = 125 \mu m$, $R_w = 0.08$, $R_{wp} = 0$)

APPENDIX C

COMMAND LISTING FOR THE FEM ANALYSIS OF
SINGLE SPARK MODEL

```

/BATCH
!*****
!           FEM Model for Electric Discharge Machining
! Single Spark Solution.....
! Gaussian heat flux and pressure distribution over spark incident surface...
! Convection over non-incident surface and off time period.....
! Temperature dependent bilinear plasticity.....
!
!           Written by Bulent Ekmekci
!*****
!*****INPUT VARIABLES*****
!
PTime=100                !Pulse Time (Micro Second)
UB=47.25                 !Pulse Voltage (Volt)
I=16                     !Current (Amper)
h=10                     !Convection Film Coeficent(KW/mK)
AmbTemp=300              !Ambient Temperature (Kelvin)
R=110                    !Channel Radius (Micro Meters)
RW=8                     !Heat Transformation (%)
RPW=0                    !Pressure Transformation (%)
!
Div=40                   !Time division
CMultip=40               !Cooling Multiplication Factor
MeshDiv=40               !No of elements within Spark Channel
LMultip=8                !Edge Multiplication Factor
KOpt=1                   !Element Killing Option(on=1,Off=0)
BTemp=2513               !Boiling Temperature(Kelvin)
!
!*****UNIT CORRECTION*****
OnTime=PTime*1e-6
R=R*1e-6
RW=RW/100
RPW=RPW/100
h=h*1e3

```

```

Length=Lmultip*R
*ASK,fname,File Name,'SingleSpark'
/FILNAME,fname,0
/TITLE,Single Spark Solution
KEYW,PR_SET,1
KEYW,PR_STRUC,1
KEYW,PR_THERM,1
KEYW,PR_FLUID,0
KEYW,PR_ELMAG,0
KEYW,MAGNOD,0
KEYW,MAGEDG,0
KEYW,MAGHFE,0
KEYW,MAGELC,0
KEYW,PR_MULTI,0
KEYW,PR_CFD,0
/COM,Preferences for GUI filtering have been set to display:
/COM, Structural
/COM, Thermal
/PREP7
!
!*****ELEMENT TYPE AND OPTIONS*****
!
ET,1,PLANE13
KEYOPT,1,1,4
KEYOPT,1,2,0
KEYOPT,1,3,1
KEYOPT,1,4,0
KEYOPT,1,5,0
KEYOPT,1,6,0
!
!*****SET REFERENCE TEMPERATURE*****
!
UIMP,1,REFT,,AmbTemp
!
!*****MATERIAL PROPERTIES*****
!
!Set Density...
UIMP,1,DENS, , ,7850,
!
!Set Temperature Dependent Thermal Expansion Coefficient...
MPTEMP,,,,,,,,
MPTEMP,1,293
MPTEMP,2,393
MPTEMP,3,473
MPTEMP,4,573
MPTEMP,5,673
MPTEMP,6,773
MPTEMP,7,873

```

MPDE,ALPX,1
 MPDE,ALPY,1
 MPDE,ALPZ,1
 MPDATA,ALPX,1,,1.1e-5
 MPDATA,ALPX,1,,1.1e-5
 MPDATA,ALPX,1,,1.25e-5
 MPDATA,ALPX,1,,1.27e-5
 MPDATA,ALPX,1,,1.33e-5
 MPDATA,ALPX,1,,1.4e-5
 MPDATA,ALPX,1,,1.41e-5
 !
 ! Set Temperature Dependent Specific Heat...
 MPTEMP,,,,,,,,
 MPTEMP,1,343
 MPTEMP,2,483
 MPTEMP,3,1025
 MPTEMP,4,1543
 MPTEMP,5,1548
 MPTEMP,6,1698
 MPTEMP,7,1703
 MPTEMP,8,3273
 MPDE,C,1
 MPDATA,C,1,,573.2
 MPDATA,C,1,,598.7
 MPDATA,C,1,,611.4
 MPDATA,C,1,,917.9
 MPDATA,C,1,,917.9
 MPDATA,C,1,,917.9
 MPDATA,C,1,,917.9
 MPDATA,C,1,,917.9
 !
 ! Set Temperature Dependent Thermal Conductivity...
 MPTEMP,,,,,,,,
 MPTEMP,1,300
 MPTEMP,2,600
 MPTEMP,3,882
 MPTEMP,4,1476
 MPTEMP,5,1626
 MPDE,KXX,1
 MPDE,KYY,1
 MPDE,KZZ,1
 MPDATA,KXX,1,,49
 MPDATA,KXX,1,,41.7
 MPDATA,KXX,1,,24.88
 MPDATA,KXX,1,,13.807
 MPDATA,KXX,1,,10.863
 !
 ! Set Temperature Dependent Young's Modulus...

```

MPTEMP,,,,,,,,
MPTEMP,1,300
MPTEMP,2,600
MPTEMP,3,900
MPTEMP,4,1200
MPDE,EX,1
MPDE,EY,1
MPDE,EZ,1
MPDE,NUXY,1
MPDE,NUYZ,1
MPDE,NUXZ,1
MPDE,PRXY,1
MPDE,PRYZ,1
MPDE,PRXZ,1
MPDE,GXY,1
MPDE,GYZ,1
MPDE,GXZ,1
MPDATA,EX,1,,2.1E+011
MPDATA,EX,1,,1.93E+011
MPDATA,EX,1,,1.65E+011
MPDATA,EX,1,,1.2E+011
MPDATA,NUXY,1,,0.28
MPDATA,NUXY,1,,0.3
MPDATA,NUXY,1,,0.31
MPDATA,NUXY,1,,0.33
!
!Set Temperature dependent Bilinear Isotropic Hardening...
TB,BISO,1,4, , ,
TBMODIF,1,1,300
TBMODIF,1,2,600
TBMODIF,1,3,900
TBMODIF,1,4,1200
TBMODIF,2,1,450000000
TBMODIF,2,2,230000000
TBMODIF,2,3,140000000
TBMODIF,2,4,30000000
TBMODIF,3,1,995260000
TBMODIF,3,2,14775120000
TBMODIF,3,3,9428570000
TBMODIF,3,4,497930000
!
!*****GEOMETRIC MODEL AND MESHING*****
!
!If Element Kill Option is not Selected...
*IF,KOpt,EQ,0,THEN
!
!Create Key Points...
K,1,0,-Length,0,

```

```

K,2,0,0,0,
K,3,Length/LMultip,0,0,
K,4,Length,0,0,
K,5,Length,-Length,0,
!Create Lines...
LSTR, 1, 2
LSTR, 2, 3
LSTR, 3, 4
LSTR, 4, 5
LSTR, 5, 1
!
!Create Areas...
FLST,2,5,4
FITEM,2,1
FITEM,2,2
FITEM,2,3
FITEM,2,4
FITEM,2,5
AL,P51X
APLOT
!
!Mesh Areas...
FLST,5,3,4,ORDE,3
FITEM,5,1
FITEM,5,4
FITEM,5,-5
CM,_Y,LINE
LSEL, , , P51X
CM,_Y1,LINE
CMSEL,_,_Y
LESIZE,_Y1, , ,LMultip*MeshDiv, , , ,1
FLST,5,1,4,ORDE,1
FITEM,5,2
CM,_Y,LINE
LSEL, , , P51X
CM,_Y1,LINE
CMSEL,_,_Y
LESIZE,_Y1, , ,MeshDiv, , , ,1
FLST,5,1,4,ORDE,1
FITEM,5,3
CM,_Y,LINE
LSEL, , , P51X
CM,_Y1,LINE
CMSEL,_,_Y
LESIZE,_Y1, , ,(LMultip-1)*MeshDiv, , , ,1
MSHAPE,0,2D
MSHKEY,0
CM,_Y,AREA

```

```

ASEL, , , , 1
CM,_Y1,AREA
CHKMSH,'AREA'
CMSEL,S,_Y
AMESH,_Y1
CMDELE,_Y
CMDELE,_Y1
CMDELE,_Y2
!
!If Element Kill Option is Selected...
*ELSEIF,KOpt,EQ,1,THEN
!
!Create Key Points...
K,1,0,0,0,
K,2,0,(LMultip-1)*Length/LMultip,0,
K,3,0,Length,0,
K,4,Length/LMultip,Length,0,
K,5,Length,Length,0,
K,6,Length,0,0,
K,7,Length/LMultip,(LMultip-1)*Length/LMultip
!
!Create Lines...
LSTR, 1, 2
LSTR, 2, 3
LSTR, 3, 4
LSTR, 4, 5
LSTR, 5, 6
LSTR, 6, 1
LSTR, 4, 7
LSTR, 7, 2
LSTR, 7, 6
!
!Create Areas...
FLST,2,4,4
FITEM,2,2
FITEM,2,3
FITEM,2,7
FITEM,2,8
AL,P51X
FLST,2,4,4
FITEM,2,4
FITEM,2,5
FITEM,2,9
FITEM,2,7
AL,P51X
FLST,2,4,4
FITEM,2,9
FITEM,2,8

```

```

FITEM,2,1
FITEM,2,6
AL,P51X
!
!Mesh Areas...
FLST,5,2,4,ORDE,2
FITEM,5,5
FITEM,5,-6
CM,_Y,LINE
LSEL, , , P51X
CM,_Y1,LINE
CMSEL,_,_Y
LESIZE,_,_Y1, , ,MeshDiv, , , ,1
FLST,5,4,4,ORDE,4
FITEM,5,2
FITEM,5,-3
FITEM,5,7
FITEM,5,-8
CM,_Y,LINE
LSEL, , , P51X
CM,_Y1,LINE
CMSEL,_,_Y
LESIZE,_,_Y1, , ,MeshDiv,4, , , ,1
FLST,5,2,4,ORDE,2
FITEM,5,2
FITEM,5,8
CM,_Y1,LINE
LSEL, , , P51X
*GET,_,_z1,LINE,,COUNT
*SET,_,_z2,0
*DO,_,_z5,1,_,_z1
*SET,_,_z2,LSNEXT(,_z2)
*GET,_,_z3,LINE,_,_z2,ATTR,NDNX
*GET,_,_z4,LINE,_,_z2,ATTR,SPNX
*get,_,_z6,line,_,_z2,attr,kynd
*IF,_,_z3,GT,0,THEN
*IF,_,_z4,NE,0,THEN
LESIZE,_,_z2,,_,_z3,1/_,_z4,,_,_z6
*ENDIF
*ENDIF
*ENDDO
CMSEL,S,_,_Y1
CMDELE,_,_Y1
FLST,5,3,4,ORDE,3
FITEM,5,1
FITEM,5,4
FITEM,5,9
CM,_Y,LINE

```

```

LSEL, , , ,P51X
CM,_Y1,LINE
CMSEL,,_Y
LESIZE,_Y1, , ,MeshDiv/3,8, , , ,1
FLST,5,1,4,ORDE,1
FITEM,5,1
CM,_Y1,LINE
LSEL, , , ,P51X
*GET,_z1,LINE,,COUNT
*SET,_z2,0
*DO,_z5,1,_z1
*SET,_z2,LSNEXT(_z2)
*GET,_z3,LINE,_z2,ATTR,NDNX
*GET,_z4,LINE,_z2,ATTR,SPNX
*get,_z6,line,_z2,attr,kynd
*IF,_z3,GT,0,THEN
*IF,_z4,NE,0,THEN
LESIZE,_z2,,,z3,1/_z4,,,,_z6
*ENDIF
*ENDIF
*ENDDO
CMSEL,S,_Y1
CMDELE,_Y1
MSHAPE,0,2D
MSHKEY,0
FLST,5,3,5,ORDE,2
FITEM,5,1
FITEM,5,-3
CM,_Y,AREA
ASEL, , , ,P51X
CM,_Y1,AREA
CHKMSH,'AREA'
CMSEL,S,_Y
AMESH,_Y1
CMDELE,_Y
CMDELE,_Y1
CMDELE,_Y2
*ELSE
/UIS,MSGPOP,2
*MSG,WARN,'KOpt must be 0 or 1'
%C
/WAIT,3
/UIS,MSGPOP,3
*ENDIF
/UI,MESH,OFF
FINISH
!
!*****APPLY BOUNDARY CONDITIONS AND SOLUTION*****

```

```

/SOLU
EPLOT
FLST,2,1,4,ORDE,1
*IF,KOPT,EQ,0,THEN
FITEM,2,3
*ELSE
FITEM,2,4
*ENDIF
/GO
!
!Set Convection heat transfer, symmetry and displacement boundary conditions...
SFL,P51X,CONV,h, , ,
DL, 1, ,SYMM
*IF,KOpt,EQ,1,THEN
DL, 2, ,SYMM
*ENDIF
FLST,2,1,4,ORDE,1
*IF,KOPT,EQ,0,THEN
FITEM,2,5
*ELSE
FITEM,2,6
*ENDIF
/GO
DL,P51X, ,UX,0
FLST,2,1,4,ORDE,1
*IF,KOPT,EQ,0,THEN
FITEM,2,5
*ELSE
FITEM,2,6
*ENDIF
/GO
DL,P51X, ,UY,0
!
!Generate Gaussian Heat flux Distribution Function...
*DEL,_FNCNAME
*DEL,_FNCMTID
*DEL,_FNC_C1
*DEL,_FNC_C2
*DEL,_FNC_C3
*DEL,_FNC_C4
*SET,_FNCNAME,'HeatFlux'
*DIM,_FNC_C1,,3
*DIM,_FNC_C2,,3
*DIM,_FNC_C3,,3
*DIM,_FNC_C4,,3
*SET,_FNC_C1(2),RW
*SET,_FNC_C2(2),UB
*SET,_FNC_C3(2),I

```

```

*SET,_FNC_C4(2),R
*SET,_FNC_C1(3),h
*SET,_FNC_C2(3),AmbTemp
!/INPUT, heat.func
*DIM,%_FNCNAME%,TABLE,6,21,3
!
! Begin of equation: {TIME}
*SET,%_FNCNAME%(0,0,1), 0.0, -999
*SET,%_FNCNAME%(2,0,1), 0.0
*SET,%_FNCNAME%(3,0,1), 0.0
*SET,%_FNCNAME%(4,0,1), 0.0
*SET,%_FNCNAME%(5,0,1), 0.0
*SET,%_FNCNAME%(6,0,1), 0.0
*SET,%_FNCNAME%(0,1,1), 1.0, 99, 0, 1, 1, 0, 0
*SET,%_FNCNAME%(0,2,1), 0
*SET,%_FNCNAME%(0,3,1), 0
*SET,%_FNCNAME%(0,4,1), 0
*SET,%_FNCNAME%(0,5,1), 0
*SET,%_FNCNAME%(0,6,1), 0
*SET,%_FNCNAME%(0,7,1), 0
*SET,%_FNCNAME%(0,8,1), 0
*SET,%_FNCNAME%(0,9,1), 0
*SET,%_FNCNAME%(0,10,1), 0
*SET,%_FNCNAME%(0,11,1), 0
*SET,%_FNCNAME%(0,12,1), 0
*SET,%_FNCNAME%(0,13,1), 0
*SET,%_FNCNAME%(0,14,1), 0
*SET,%_FNCNAME%(0,15,1), 0
*SET,%_FNCNAME%(0,16,1), 0
*SET,%_FNCNAME%(0,17,1), 0
*SET,%_FNCNAME%(0,18,1), 0
*SET,%_FNCNAME%(0,19,1), 0
*SET,%_FNCNAME%(0,20,1), 0
*SET,%_FNCNAME%(0,21,1), 0
! End of equation: {TIME}
!
! Begin of equation: 4.45*RW*UB*I*exp(-4.5({X}/R)^2)/({PI}*R^2)
*SET,%_FNCNAME%(0,0,2), OnTime, -999
*SET,%_FNCNAME%(2,0,2), 0.0
*SET,%_FNCNAME%(3,0,2), %_FNC_C1(2)%
*SET,%_FNCNAME%(4,0,2), %_FNC_C2(2)%
*SET,%_FNCNAME%(5,0,2), %_FNC_C3(2)%
*SET,%_FNCNAME%(6,0,2), %_FNC_C4(2)%
*SET,%_FNCNAME%(0,1,2), 1.0, -1, 0, 4.45, 0, 0, 17
*SET,%_FNCNAME%(0,2,2), 0.0, -2, 0, 1, -1, 3, 17
*SET,%_FNCNAME%(0,3,2), 0, -1, 0, 1, -2, 3, 18
*SET,%_FNCNAME%(0,4,2), 0.0, -2, 0, 1, -1, 3, 19
*SET,%_FNCNAME%(0,5,2), 0.0, -1, 0, 0, 0, 0, 0

```

```

*SET,%_FNCNAME%(0,6,2), 0.0, -3, 0, 1, 0, 0, -1
*SET,%_FNCNAME%(0,7,2), 0.0, -4, 0, 1, -1, 2, -3
*SET,%_FNCNAME%(0,8,2), 0.0, -1, 0, 1, 2, 4, 20
*SET,%_FNCNAME%(0,9,2), 0.0, -3, 0, 2, 0, 0, -1
*SET,%_FNCNAME%(0,10,2), 0.0, -5, 0, 1, -1, 17, -3
*SET,%_FNCNAME%(0,11,2), 0.0, -1, 0, 4.5, 0, 0, -5
*SET,%_FNCNAME%(0,12,2), 0.0, -3, 0, 1, -1, 3, -5
*SET,%_FNCNAME%(0,13,2), 0.0, -1, 0, 1, -4, 3, -3
*SET,%_FNCNAME%(0,14,2), 0.0, -1, 7, 1, -1, 0, 0
*SET,%_FNCNAME%(0,15,2), 0.0, -3, 0, 1, -2, 3, -1
*SET,%_FNCNAME%(0,16,2), 0.0, -1, 0, 2, 0, 0, 20
*SET,%_FNCNAME%(0,17,2), 0.0, -2, 0, 1, 20, 17, -1
*SET,%_FNCNAME%(0,18,2), 0.0, -1, 0, 3.14159265358979310, 0, 0, -2
*SET,%_FNCNAME%(0,19,2), 0.0, -4, 0, 1, -1, 3, -2
*SET,%_FNCNAME%(0,20,2), 0.0, -1, 0, 1, -3, 4, -4
*SET,%_FNCNAME%(0,21,2), 0.0, 99, 0, 1, -1, 0, 0
! End of equation: 4.45*RW*UB*I*exp(-4.5*({X}/R)^2)/({PI}*R^2)
!
!Begin of equation: -1*h*({TEMP}-AmbTemp)
!Surface is exposed to convection Boundary Condition After Pulse Time...
*SET,%_FNCNAME%(0,0,3), CMultip*OnTime, -999
*SET,%_FNCNAME%(2,0,3), 0.0
*SET,%_FNCNAME%(3,0,3), %_FNC_C1(3)%
*SET,%_FNCNAME%(4,0,3), %_FNC_C2(3)%
*SET,%_FNCNAME%(5,0,3), 0.0
*SET,%_FNCNAME%(6,0,3), 0.0
*SET,%_FNCNAME%(0,1,3), 1.0, -1, 0, -1, 0, 0, 17
*SET,%_FNCNAME%(0,2,3), 0.0, -2, 0, 1, -1, 3, 17
*SET,%_FNCNAME%(0,3,3), 0, -1, 0, 1, 5, 2, 18
*SET,%_FNCNAME%(0,4,3), 0.0, -3, 0, 1, -2, 3, -1
*SET,%_FNCNAME%(0,5,3), 0.0, 99, 0, 1, -3, 0, 0
*SET,%_FNCNAME%(0,6,3), 0
*SET,%_FNCNAME%(0,7,3), 0
*SET,%_FNCNAME%(0,8,3), 0
*SET,%_FNCNAME%(0,9,3), 0
*SET,%_FNCNAME%(0,10,3), 0
*SET,%_FNCNAME%(0,11,3), 0
*SET,%_FNCNAME%(0,12,3), 0
*SET,%_FNCNAME%(0,13,3), 0
*SET,%_FNCNAME%(0,14,3), 0
*SET,%_FNCNAME%(0,15,3), 0
*SET,%_FNCNAME%(0,16,3), 0
*SET,%_FNCNAME%(0,17,3), 0
*SET,%_FNCNAME%(0,18,3), 0
*SET,%_FNCNAME%(0,19,3), 0
*SET,%_FNCNAME%(0,20,3), 0
*SET,%_FNCNAME%(0,21,3), 0
! End of equation: -1*h*({TEMP}-AmbTemp)

```

```

!
FLST,2,1,4,ORDE,1
*IF,KOPT,EQ,0,THEN
FITEM,2,2
*ELSE
FITEM,2,3
!
*ENDIF
/GO
!
SFL,P51X,HFLUX, %HeatFlux%
!
! Generate Distribution Function for Pressure...
*DEL,_FNCNAME
*DEL,_FNCMTID
*DEL,_FNC_C1
*DEL,_FNC_C2
*DEL,_FNC_C3
*DEL,_FNC_C4
*SET,_FNCNAME,'Press'
*DIM,_FNC_C1,,3
*DIM,_FNC_C2,,3
*DIM,_FNC_C3,,3
*DIM,_FNC_C4,,3
*SET,_FNC_C1(2),RPW
*SET,_FNC_C2(2),UB
*SET,_FNC_C3(2),I
*SET,_FNC_C4(2),R
!
*DIM,%_FNCNAME%,TABLE,6,21,3
!
! Begin of equation: {TIME}
*SET,%_FNCNAME%(0,0,1), 0.0, -999
*SET,%_FNCNAME%(2,0,1), 0.0
*SET,%_FNCNAME%(3,0,1), 0.0
*SET,%_FNCNAME%(4,0,1), 0.0
*SET,%_FNCNAME%(5,0,1), 0.0
*SET,%_FNCNAME%(6,0,1), 0.0
*SET,%_FNCNAME%(0,1,1), 1.0, 99, 0, 1, 1, 0, 0
*SET,%_FNCNAME%(0,2,1), 0
*SET,%_FNCNAME%(0,3,1), 0
*SET,%_FNCNAME%(0,4,1), 0
*SET,%_FNCNAME%(0,5,1), 0
*SET,%_FNCNAME%(0,6,1), 0
*SET,%_FNCNAME%(0,7,1), 0
*SET,%_FNCNAME%(0,8,1), 0
*SET,%_FNCNAME%(0,9,1), 0
*SET,%_FNCNAME%(0,10,1), 0

```

```

*SET,%_FNCNAME%(0,11,1), 0
*SET,%_FNCNAME%(0,12,1), 0
*SET,%_FNCNAME%(0,13,1), 0
*SET,%_FNCNAME%(0,14,1), 0
*SET,%_FNCNAME%(0,15,1), 0
*SET,%_FNCNAME%(0,16,1), 0
*SET,%_FNCNAME%(0,17,1), 0
*SET,%_FNCNAME%(0,18,1), 0
*SET,%_FNCNAME%(0,19,1), 0
*SET,%_FNCNAME%(0,20,1), 0
*SET,%_FNCNAME%(0,21,1), 0
! End of equation: {TIME}
!
! Begin of equation: 4.45*RPW*UB*I*exp(-4.5({X}/R)^2)/({PI}*R^2)
*SET,%_FNCNAME%(0,0,2), OnTime, -999
*SET,%_FNCNAME%(2,0,2), 0.0
*SET,%_FNCNAME%(3,0,2), %_FNC_C1(2)%
*SET,%_FNCNAME%(4,0,2), %_FNC_C2(2)%
*SET,%_FNCNAME%(5,0,2), %_FNC_C3(2)%
*SET,%_FNCNAME%(6,0,2), %_FNC_C4(2)%
*SET,%_FNCNAME%(0,1,2), 1.0, -1, 0, 4.45, 0, 0, 17
*SET,%_FNCNAME%(0,2,2), 0.0, -2, 0, 1, -1, 3, 17
*SET,%_FNCNAME%(0,3,2), 0, -1, 0, 1, -2, 3, 18
*SET,%_FNCNAME%(0,4,2), 0.0, -2, 0, 1, -1, 3, 19
*SET,%_FNCNAME%(0,5,2), 0.0, -1, 0, 0, 0, 0, 0
*SET,%_FNCNAME%(0,6,2), 0.0, -3, 0, 1, 0, 0, -1
*SET,%_FNCNAME%(0,7,2), 0.0, -4, 0, 1, -1, 2, -3
*SET,%_FNCNAME%(0,8,2), 0.0, -1, 0, 1, 2, 4, 20
*SET,%_FNCNAME%(0,9,2), 0.0, -3, 0, 2, 0, 0, -1
*SET,%_FNCNAME%(0,10,2), 0.0, -5, 0, 1, -1, 17, -3
*SET,%_FNCNAME%(0,11,2), 0.0, -1, 0, 4.5, 0, 0, -5
*SET,%_FNCNAME%(0,12,2), 0.0, -3, 0, 1, -1, 3, -5
*SET,%_FNCNAME%(0,13,2), 0.0, -1, 0, 1, -4, 3, -3
*SET,%_FNCNAME%(0,14,2), 0.0, -1, 7, 1, -1, 0, 0
*SET,%_FNCNAME%(0,15,2), 0.0, -3, 0, 1, -2, 3, -1
*SET,%_FNCNAME%(0,16,2), 0.0, -1, 0, 2, 0, 0, 20
*SET,%_FNCNAME%(0,17,2), 0.0, -2, 0, 1, 20, 17, -1
*SET,%_FNCNAME%(0,18,2), 0.0, -1, 0, 3.14159265358979310, 0, 0, -2
*SET,%_FNCNAME%(0,19,2), 0.0, -4, 0, 1, -1, 3, -2
*SET,%_FNCNAME%(0,20,2), 0.0, -1, 0, 1, -3, 4, -4
*SET,%_FNCNAME%(0,21,2), 0.0, 99, 0, 1, -1, 0, 0
! End of equation: 4.45*RPW*UB*I*exp(-4.5({X}/R)^2)/({PI}*R^2)
!
! Begin of equation: 0
*SET,%_FNCNAME%(0,0,3), CMultip*Ontime, -999
*SET,%_FNCNAME%(2,0,3), 0.0
*SET,%_FNCNAME%(3,0,3), 0.0
*SET,%_FNCNAME%(4,0,3), 0.0

```

```

*SET,%_FNCNAME%(5,0,3), 0.0
*SET,%_FNCNAME%(6,0,3), 0.0
*SET,%_FNCNAME%(0,1,3), 1.0, 99, 0, 0, 0, 0, 0
*SET,%_FNCNAME%(0,2,3), 0
*SET,%_FNCNAME%(0,3,3), 0
*SET,%_FNCNAME%(0,4,3), 0
*SET,%_FNCNAME%(0,5,3), 0
*SET,%_FNCNAME%(0,6,3), 0
*SET,%_FNCNAME%(0,7,3), 0
*SET,%_FNCNAME%(0,8,3), 0
*SET,%_FNCNAME%(0,9,3), 0
*SET,%_FNCNAME%(0,10,3), 0
*SET,%_FNCNAME%(0,11,3), 0
*SET,%_FNCNAME%(0,12,3), 0
*SET,%_FNCNAME%(0,13,3), 0
*SET,%_FNCNAME%(0,14,3), 0
*SET,%_FNCNAME%(0,15,3), 0
*SET,%_FNCNAME%(0,16,3), 0
*SET,%_FNCNAME%(0,17,3), 0
*SET,%_FNCNAME%(0,18,3), 0
*SET,%_FNCNAME%(0,19,3), 0
*SET,%_FNCNAME%(0,20,3), 0
*SET,%_FNCNAME%(0,21,3), 0
! End of equation: 0
!
FLST,2,1,4,ORDE,1
*IF,KOPT,EQ,0,THEN
FITEM,2,2
*ELSE
FITEM,2,3
*ENDIF
/GO
SFL,P51X,PRES, %Press%
!
!Solve Time dependent Problem
!Solve the First Load Step(Sparking)...
ANTYPE,4
TRNOPT,FULL
LUMPM,0
NLGEOM,1
DELTIM,OnTime/div,OnTime/div,0,1
TIME,OnTime
AUTOTS,-1
SSTIF,1
NROPT,FULL, ,
EQSLV, , ,0,
PRECISION,0
MSAVE,0

```

```

KBC,0
TOFFST,AmbTemp,
TUNIF,AmbTemp,
TREF,AmbTemp,
CNVTOL,HEAT, , ,2,1e-12,
CNVTOL,F, , ,2,1e-6,
CNVTOL,U, , ,2,1e-12,
OUTRES,ALL,ALL,
RESCONT,,ALL,ALL
/WAIT,5
/UIS,MSGPOP,3
SOLVE
!
!Kill Boiled Elements If Wanted...
*IF,KOpt,EQ,1,THEN
/POST1
ETABLE,LTemp,TEMP
ESEL,S,ETAB,LTEMP,BTemp,1E9, ,0
/SOLU
ANTYPE,,RESTART,1,div
EKILL,ALL
EPlot
/WAIT,5
!
NSEL,S,EXT
NPlot
SF,ALL,CONV,h,AmbTemp
/WAIT,5
!
ALLSEL,ALL
*ENDIF
!
!Solve the First Cooling Cycle...
DELTIM,OnTime/div,OnTime/div,0,1
TIME,4*OnTime
SOLVE
!
! Solve the Second Cooling Cycle...
ANTYPE,,RESTART,2,div
DELTIM,OnTime,OnTime,0,1
TIME,(CMultip)*OnTime
OUTRES,ALL,ALL,
SOLVE
!
/UIS,MSGPOP,2
*MSG,UI,'Solution is done!'
%C

```

VITA

Bülent Ekmekçi was born in Ankara on January 02, 1972. He received his B.S degree in Mechanical Engineering from the University of Gaziantep in July 1993. He worked as a graduate assistant and received his M.E degree in Mechanical Engineering from Steven's Institute of Technology in January 1997. He worked as graduate assistant in the Department of Mechanical Engineering at Zonguldak Karaelmas University from 1997 to 1999. Since then he has been working as an Instructor at the same university. His main areas of interest are untraditional production process, electric discharge machining, experimental stress analysis and finite element method.